Dynamics and Energetics of Walking with Prostheses

With the Department of Mechanical Engineering
at the University of Stuttgart for the achievement
of a Doctor's Degree of Engineering (Dr.-Ing.)
submitted treatise

by

Marko Ackermann

born in São Paulo (Brazil)

First reviewer: Prof. Dr.-Ing. Prof. E.h. Dr. h.c. W. Schiehlen
Second reviewer: Prof. Dr. phil. habil. W. Alt

Date of Submission: 22. March 2007
Date of Oral Exam: 02. July 2007

Institute of Engineering and Computational Mechanics
University of Stuttgart

2007

Marko Ackermann

Dynamics and Energetics of Walking with Prostheses

Acknowledgements

To my wife, Priscila,
and my parents, Valika and Helgo

Contents

Symbols

Capital letters

$\boldsymbol{A}$	matrix of moment arms
$\boldsymbol{A}_{eq}$	matrix for linear equality constraints (EID)
$\boldsymbol{C}$	Jacobian matrix of contraints
E	total metabolic cost
$\boldsymbol{E}$	identity matrix
$\dot{E}_w$	metabolic cost rate per body mass
$\boldsymbol{F}^m$	global vector of muscle forces (EID)
$\dot{H}$	muscle heat production rate
$\boldsymbol{I}_i$	inertia tensor body i
$\bar{\boldsymbol{J}}$	global Jacobian matrix
J_{EID}	cost function (EID)
$\boldsymbol{J}_{Ri}$	Jacobian matrix of rotation for body i
J_s	cost function for the Static Optimization
J_{SDO}	cost function (SDO)
$\boldsymbol{J}_{Ti}$	Jacobian matrix of translation for body i
L_l, L_r	step sizes
$\boldsymbol{M}$	mass matrix
$\bar{\bar{\boldsymbol{M}}}$	block diagonal matrix
$PCSA$	muscle physiological cross-sectional area
$\boldsymbol{R}$	matrix transforming muscle forces into generalized forces
$\boldsymbol{S}_i$	rotation matrix of body i
T_{ph}	time duration of phase ph
$\dot{W}$	muscle CE mechanical power

Small letters

a	muscle activation
$\boldsymbol{b}_{eq}$	vector for linear equality constraints (EID)
$\boldsymbol{c}$	kinematic constraints
$\boldsymbol{c}_{ph}$	active constraints in phase ph
$\boldsymbol{e}_j$	incompatibility between muscle forces and kinematics
$e_{sq,j}$	euclidian norm of $\boldsymbol{e}_j$
f	number of degrees of freedom
f^{ce}	muscle CE force
f^m	muscle force
$\boldsymbol{f}^{gr}$	vector of ground reaction forces
$\boldsymbol{f}^m$	vector of muscle forces
f^{pe}	muscle PE force
f_c	cut-frequency of a discrete filter
f_e	degrees of freedom after additional constraints
$\boldsymbol{f}_i^e$	vector of applied forces body i
$\boldsymbol{f}_i^r$	vector of reaction forces body i
f_{max}^m	muscle maximal isometric force

f_{iso}	muscle isometric force	q	number of constraints
$\tilde{f}_i^m$	approximation of muscle force i by splines	$\boldsymbol{q}$	vector of generalized forces
ft	percentage of fast twitch fibers	q_c	number of additional kinematic constraints
$\dot{h}$	total heat rate per unit of muscle mass	$\bar{\boldsymbol{q}}_c$	vector of Coriolis forces
$\dot{h}_a$	activation heat rate per unit of muscle mass	$\bar{\boldsymbol{q}}_e$	vector of applied forces
$\dot{h}_m$	maintenance heat rate per unit of muscle mass	$\boldsymbol{q}_r$	vector of generalized forces other than the ones by muscles
$\dot{h}_{sl}$	shortening/lengthening heat rate per unit of muscle mass	$\bar{\boldsymbol{q}}_r$	vector of reaction forces
$\boldsymbol{k}$	vector of generalized Coriolis forces	$\boldsymbol{r}$	vector of residuals
		$\boldsymbol{r}_h$	position vector of hip joint
k_c	dimension of vector $\boldsymbol{\tau}$	$\boldsymbol{r}_i$	position vector of body i
l^m	total muscle length	$\boldsymbol{s}_i$	vector of infinitesimal rotation
l^{ce}	length of the CE	$\boldsymbol{t}$	vector of time instants
l^{se}	length of the SE	$\tilde{t}$	scaled time between uniformly distributed nodes
l_{slack}	tendon slack length		
l_i^e	vector of applied moments body i	t_a	activation constant
l_i^r	vector of reaction moments body i	t_d	de-activation constant
l_{opt}^{ce}	CE optimal length	u	neural excitation
m	number of muscle groups considered	v^{ce}	CE shortening velocity
		v^m	muscle shortening velocity
m_i	mass of body i	v^{se}	SE shortening velocity
n	number of time steps	$\boldsymbol{v}_i$	velocity of body i
n_a	number of active constraints	v_w	average walking velocity
n_b	number of joint moments	v_{max}^{ce}	CE maximal shortening velocity
n_i	number of markers attached to body i (chap. 3)	$\boldsymbol{x}$	vector of state variables
n_c	number of control points	x_{hip}	position of hip joint in x-axis
n_n	number of nodes	x_k	simulated value for variable k
		$\hat{x}_k$	measured value for variable k
n_r	number of rigid bodies in the model	z_{hip}	position of hip joint in z-axis
p	number of rigid bodies in the multibody system	$\boldsymbol{y}$	vector of generalized coordinates
		$\tilde{y}_n$	approximation of generalized coordinate n by splines
$\boldsymbol{p}^m$	set of muscle-specific parameters	$width$	parameter for CE force-length relation

Greek letters

α	thigh rotation angle	μ	coefficient of friction
$\bar{\boldsymbol{\alpha}}_i$	local angular acceleration for body i	ρ^m	muscle density
α_p	pennation angle	σ_k	standard deviation for variable k
β	knee flexion	$\boldsymbol{\tau}$	vector of joint moments
γ	ankle plantar flexion	φ	approximating polynomial for generalized coordinates
Δt	time step size		
ε_m	compatibility muscle forces/kinematics	$\boldsymbol{\chi}$	design variables for optimization
ε_k	fulfillment kinematic constraints	ψ	approximating polynomial for muscle forces
ε_o^T	tendon strain for $f^{ce} = f_{max}^m$	$\boldsymbol{\omega}_i$	angular velocity for body i
$\boldsymbol{\lambda}$	Lagrangian multipliers	$\bar{\boldsymbol{\omega}}_i$	local angular velocity for body i

Some operators

$diag\left\{\cdot\right\}$ diagonal matrix $Tr\left\{\cdot\right\}$ trace of a matrix

Abbreviations

CE	contractile element	GRF	ground reaction forces
CNS	central nervous system	MSO	modified static optimization
CWS	comfortable walking speed	ODE	ordinary differential equation
DAE	differential algebraical equation	PE	parallel elastic element
DO	dynamic optimization	SE	series elastic element
SDO	state dynamic optimization	SO	static optimization
EID	extended inverse dynamics	SQP	sequetial quadratic programming

Abstract

In Biomechanics, a science evolved from the study of biological systems using mechanics, locomotor system models have been proposed and increasingly used to investigate human walking by means of computational simulations. The skeletal system is often modeled by multibody systems composed of rigid bodies. The biological actuator is almost exclusively modeled by the so-called Hill-type muscle model due to its suitability to computational investigations. The study of normal and pathological walking necessarily involves the consideration of the energetic demand, since it was shown that the energetic demand per unit of distance traveled is the primary performance criterion during walking. Energetics can be assessed by means of recently proposed energy expenditure models used in conjunction with Hill-type muscle models.

These models are used to investigate walking, for instance, by computing moments at the joints required to perform an observed motion using inverse dynamics, by estimating muscle forces from joint moment using optimization techniques, and by generating optimal normal and pathological walking patterns. In spite of the increasing use of computational simulation of gait, the large-scale musculoskeletal models required lead frequently to a prohibitive computational effort, in particular when optimization procedures are involved, preventing its wider use in clinical applications. This dissertation covers part of this wide spectrum of problems in biomechanics focusing on the investigation of normal and pathological walking, in particular prosthetic walking, and on the development of methods that offer alternatives to conventional approaches that either require overwhelming computational effort or deliver unrealistic estimations.

In order to investigate the burden caused by lower limb assistive devices experiments are designed to emulate typical deviations of the mechanical properties of the lower limbs caused by prosthetic and orthotic devices, namely alterations in the inertial properties of the lower limbs and in the mobility of the joints. The experiments are performed in a gait analysis laboratory, and the kinematics is reconstructed from markers attached on anatomical landmarks of two subjects. The reconstructed kinematics and measured ground reaction forces are then used to estimate joint moments by inverse dynamics. The results for the kinematics and joint moments for all experiments and subjects are compared and discussed concerning possible contributions to the understanding of prosthetic and

orthotic walking. A framework is presented, where all important steps to compute the kinematics and joint moments are explained in details and the many sources of errors are presented and discussed.

The determination of individual muscle forces has many applications including the assessment of muscle coordination and internal loads on joints and bones, useful for instance, for the design of endoprostheses or the assessment of risk of damage of ligaments during sport activities. Because muscle forces cannot be directly measured without invasive techniques, they are often estimated from joint moments by means of optimization procedures that search for a unique solution among the infinite solutions for the muscle forces that generate the same joint moments. The conventional method to solve this problem, the static optimization approach, is computationally efficient but neglects the dynamics involved in muscle force generation and requires the use of an instantaneous cost function, leading often to unrealistic estimations of muscle forces. An alternative is using dynamic optimization associated with a motion tracking, which is, however, computationally very costly.

Two alternative approaches are proposed to overcome the limitations of static optimization delivering more realistic estimations of muscle forces while being computationally less expensive than dynamic optimization. One approach, named extended inverse dynamics, delivers physiological estimations of muscle forces by considering the muscle activation and contraction dynamics and by permitting the use of time-integral cost functions as total metabolic cost. Although the improvements provided by this approach makes it computationally much more expensive than static optimization, it is less expensive than dynamic optimization, because it does not require any numerical integration of the state equations. The second proposed approach, named modified static optimization, offers a viable alternative to static optimization by considering the muscle activation and contraction dynamics while requiring a similar low computational effort. The two proposed approaches are used to estimate muscle force histories for the measured normal and disturbed gaits of the subjects using a musculoskeletal model of their lower limbs, and compared to static optimization.

One of the great challenges in biomechanics of human walking is the use of the complex, large-scale models of the musculoskeletal system in predictive investigations of pathological gait, for instance, to help on the design of assistive devices, therapies or surgical interventions. The prohibitive computational effort required by dynamic optimization, the conventional approach used to generate optimal walking patterns, prevents a wider use of dynamic simulation of gait for clinical applications. An alternative to avoid the many integrations of the state equations, the major cause for the high computational effort, is the use of inverse dynamics-based methods. Such methods have been used, for instance, in robotics and character animation, but have been poorly explored in biomechanics. Therefore, an inverse dynamics-based approach to simulate human motion that

deals with the overdeterminacy of muscle actuation and uses Hill-type muscle models is proposed, too.

This third approach is based on the parameterization of the motion and muscle forces using polynomials that interpolate nodal values, which are incorporated to the optimization variables. The neural excitations are computed by inverting the muscle contraction and activation dynamics. The optimization problem is formulated as a search for optimal skeleton motion and muscle forces that minimize a time-integral cost function, and is subject to constraints that ensure bounded neural excitations, fulfillment of the kinematic constraints between feet and ground, and fulfillment of the equations of motion throughout the gait cycle.

The third approach is applied to generate normal walking patterns, to investigate the gait with a bilateral 2 kg-increase in feet mass, and to predict skeleton motion, muscle coordination and metabolic cost of walking with three different bilateral transtibial prostheses, characterized by their ankle moment versus ankle angle curves. Furthermore, improved parameters describing the prosthetic ankle stiffness curve are determined by incorporating them to the optimization variables. The observed improvements in the overall performance of walking with the optimal transtibial prostheses evidence the potential of this approach for helping on the design of assistive devices.

Kurzfassung

Der menschliche Bewegungsapparat besteht hauptsächlich aus einen Skelett sowie aus Muskeln, die Kräfte auf das Skelett ausüben und damit Bewegungen hervorrufen. Die Muskeln werden durch das zentrale Nervensystem angeregt, so dass bestimmte aktivitätsabhängige Kriterien optimiert werden. Während zum Beispiel bei Sprungbewegungen die maximale erreichte Höhe das wichtigste Kriterium darstellt, können bei anderen Aktivitäten die Minimierung von Muskelermüdung oder Schmerz von primärer Bedeutung sein. Experimentelle Hinweise zeigen, dass der Energieaufwand während der Gehbewegung von großer Bedeutung ist. Aus diesem Grund wird bei Untersuchungen der menschlichen Gehbewegung der Energieaufwand häufig berücksichtigt.

Funktionsstörungen des neurologischen oder Muskel-Skelett-Systems verursachen Abweichungen der Kinematik, Kinetik und Muskelerregungen von normalen Mustern und führen zu einem erhöhten Energieaufwand. Insbesondere die Abweichungen, die während des Gehens mit Beinprothesen entstehen, werden in dieser Dissertation betrachtet. Der hohe Energieaufwand zeigt die große Belastung, die durch eine Amputation verursacht wird. Das Verständnis dieser Abweichungen und Störungen kann einen wesentlichen Beitrag zur Entwicklung von Prothesen und Orthesen, zur Planung von chirurgischen Interventionen und zur Verbesserung von Therapien leisten.

In der Biomechanik, einer Wissenschaft, die durch die Untersuchung von biologischen Systemen mit den Methoden der Mechanik entstanden ist, werden Modelle des menschlichen Bewegungsapparates entwickelt und zunehmend auf die Untersuchung von Gehbewegung mit Hilfe von rechnergestützten Simulationen angewandt. Dabei wird das Skelett-System häufig durch ein Mehrkörpersystem bestehend aus starren Körper modelliert. Die biologischen Aktoren werden durch Modelle nach Hill repräsentiert, die aus einem kontraktilen Element bestehen, welches die aktive Krafterzeugung der Muskelfasern wiedergibt, und Elementen, welche die passive Eigenschaften des Gewebes modellieren. Außerdem kann in Verbindung mit Muskelmodellen nach Hill der Energieaufwand bei der Krafterzeugung durch neuerdings entwickelte Modelle abgeschätzt werden. Diese Modelle werden beispielsweise für die Berechnung von Momenten an den Gelenken aus der experimentell erfassten Kinematik, für die Bestimmung von Muskelkräften aus Gelenkmomenten, und für die Bestimmung von normalen und pathologischen Gehbewegungsmustern verwendet.

Trotz der zunehmenden Anwendung von Computersimulationen für die Untersuchung der Gehbewegung führt die hohe Ordnung des Muskel-Skelett-Modells in der Regel zu einem enormen Rechenaufwand, insbesondere wenn das Modell für Optimierungsrechnungen herangezogen wird. Dieser Aufwand schränkt eine häufigere Benutzung der Computersimulation für die Untersuchung von pathologischen Gehbewegungen ein, oder erfordert eine so starke Vereinfachung der Modelle, dass unrealistische Ergebnisse entstehen. Vor diesem Hintergrund sind die in dieser Dissertation enthaltenen Arbeiten zu sehen. So werden einerseits alternative Methoden zur Berechnung der Kinematik, der Kinetik, der Muskelansteuerung sowie des Energieaufwands der menschlichen Bewegung entwickelt, die im Vergleich zu den herkömmlichen Methoden eine bessere Abbildung der natürlichen Gehbewegungen des Menschen bei geringerem Rechenaufwand bieten. Andererseits leistet diese Dissertationen einen Beitrag zum Verständnis der pathologischen Gehbewegung und zur Entwicklung von Beinorthesen und -prothesen.

Zunehmend werden Ganganalyselabore, ausgerüstet mit Kraftmeßplatten, Gehstrecken und Kameras zur 3-D Erfassung der Körperbewegung, verwendet, um Gehbewegungen zu untersuchen. Die erforderlichen Momente an den Gelenken lassen sich mittels der inversen Dynamik aus den gemessenen Bewegungen und Bodenreaktionskräften berechnen. In dieser Arbeit wurde eine Reihe von Experimenten konzipiert und durchgeführt, um die Funktionseinschränkung und Änderungen der mechanischen Eigenschaften der unteren Extremitäten zu simulieren, die durch Beinprothesen und -orthesen hervorgerufen werden. Dabei werden vor allem die Änderungen der Massenverteilung des Beines und die Beeinträchtigung der Mobilität der Gelenke berücksichtigt. Die Messung der kinematischen und kinetischen Größen erfolgte an der Versuchsstrecke des Instituts für Sportwissenschaft der Universität Stuttgart. Dabei wurden passive Markers eingesetzt, die an anatomische Landmarken zweier Probanden befestigt werden. Aus den 3-D Trajektorien dieser Marker lassen sich Position und Drehung der einzelnen Körpersegmente berechnen. Damit erhält man die benötigten Momente an den Gelenken mittels der inversen Dynamik für alle Versuche.

Die Ergebnisse zeigen, dass die Modifikation der Massenverteilung der unteren Extremität durch Anbringen von zusätzlichen Massen am Fuß und die Fixierung der Gelenke zu erheblichen Abweichungen in der Kinematik und Kinetik des Gehens im Vergleich zu normalen Mustern führt. Die Natur und das Ausmaß dieser Abweichungen werden in großem Maße abgeschätzt, und können zur Modellierung des Gehens mit Prothesen und Orthesen und zur Interpretation von Simulationsergebnissen beitragen. Alle benötigten Schritte zur Berechnung der Bewegung des Körpers und der Momente an den Gelenken werden ausführlich erklärt und hergeleitet. Außerdem werden Strategien zur Reduktion der Ungenauigkeiten in der berechneten Kinematik und Kinetik diskutiert, die teilweise durch unvermeidbare Fehler in den Messungen verursacht werden. Damit bietet diese Arbeit viele Hinweise für zukünftige Untersuchungen dieser Art.

Obwohl die Berechnung der Momente an den Gelenken einen Einblick in das Ausmaß der Muskelaktivität ermöglicht, erhält man keine Auskünfte über die Intensität der einzelnen Kräfte an Muskeln, Bändern und anderen Geweben, die die Gelenke spannen. Dabei ist die Kenntnis der einzelnen Kräfte wichtig, um Muskelsteuerungsmuster zu studieren, oder um interne Belastungen an Knochen und Bändern abzuschätzen, die beispielsweise den Entwurf von künstlichen Endoprothesen unterstützen oder Hinweise über mögliche Beschädigungen der Bänder bei Sportaktivitäten geben. Da Muskelkräfte nicht direkt ohne invasive Messungen am lebenden menschlichen Körper bestimmt werden können, werden sie häufig aus den mittels der inversen Dynamik berechneten Momenten an den Gelenken abgeschätzt. Wegen der redundanten Anordnung der Muskeln, gibt es im Prinzip unendlich viele verschiedene Aufteilungen der Muskelkräfte, welche die selben Momente an den Gelenken und damit die selbe Bewegung des Skelettes hervorrufen. Um eine einzige Lösung für die Muskelkräfte zu bestimmen, werden Optimierungsverfahren angewandt unter der Annahme, dass das zentrale Nervensystem die Muskeln so ansteuert, dass ein bestimmtes Kriterium wie z.B. der Energieaufwand optimiert wird. Die gängige Methode, um dieses Problem zu lösen, ist die sogenannte statische Optimierung. Diese benötigt einen geringen Rechenaufwand, weist jedoch zwei bedeutende Beschränkungen auf, die zu einer ungenauen Berechnung der Muskelkräfte führen kann. So wird zum einen das dynamische Verhalten der einzelnen Muskeln bei der Krafterzeugung vernachlässigt, was zu unrealistischen Muskelkraftverläufen führen kann. Weiterhin wird eine momentane Gütefunktion vorausgesetzt, was die Benutzung integraler Zielfunktionen, wie etwa den gesamten Energieaufwand einer Bewegung, ausschließt. Dieser Aufwand spielt jedoch eine wichtige Rolle während des Gehens.

Eine alternative Methode zur statischen Optimierung ist die dynamische Optimierung, welche die gemessene Bewegung berücksichtigt. Dabei werden optimale parametrisierte neuronale Erregungen gesucht, die eine integrale Zielfunktion optimieren. Diese Methode benötigt jedoch einen sehr hohen Rechenaufwand, weil die Zustandsgleichungen des komplexen Muskel-Skelett-Modells immer wieder numerisch integriert werden müssen. Zwei alternative Methoden zur Bestimmung von Muskelkräften werden in dieser Dissertation entwickelt, die die Beschränkungen der statischen Optimierung überwinden und effizienter als die dynamische Optimierung sind. Die erste Methode, erweiterte inverse Dynamik genannt, ermöglicht die Bestimmung realistischer Muskelkräfte, indem das dynamische Verhalten der Muskeln berücksichtigt und die Benutzung integraler Zielfunktionen ermöglicht wird. Diese Methode basiert auf der Inversion der Muskeldynamik, so dass keine numerische Integration der Zustandsgleichungen nötig ist. Damit reduziert sich der Rechenaufwand im Vergleich zur dynamischen Optimierung erheblich. Die zweite Methode, modifizierte statische Optimierung genannt, bietet eine Alternative zur statischen Optimierung mit vergleichbar reduziertem Rechenaufwand, die aber realistischere Muskelkräfte liefert, weil die Dynamik bei der Muskelkrafterzeugung berücksichtigt wird.

Die beide entwickelten Methoden werden auf die Berechnung von Muskelkräften bei der

gemessenen normalen Gehbewegung der zwei Probanden angewendet. Die Methoden werden mit der statischen Optimierung bezüglich Rechenaufwand und Erfüllung der oberen und unteren Grenzen für die neuronalen Erregungen verglichen, deren Verletzung auf unphysiologische Muskelkräfte hindeutet. Die erweiterte inverse Dynamik wird durch zwei verschiedene Arten validiert: durch einen Vergleich der Ergebnisse für die Muskelaktivierungen mit Hüllkurven (linear envelopes) für gemessene EMG aus der Literatur, und durch die Verwendung von berechneten neuronalen Erregungen als Eingang für die numerische Integration der Zustandsgleichungen des Muskel-Skelett-Modells und den anschließenden Vergleich der so berechneten Bewegung des Skelettes mit der gemessenen Bewegung.

In der Entwurfsphase neuartiger Prothesen, Orthesen, operativer Eingriffe und Rehabilitationstherapien werden prädiktive Modelle des Gehens benötigt, die in der Lage sind, die Einflüsse bestimmter Entwürfe auf die Kinematik, die Kinetik, die Muskelansteuerung und den Energieaufwand des Gehens vorauszusagen. Rechenergestützte Simulation und Optimierung der Gehbewegung werden dazu zunehmend verwendet. Die oben erwähnte dynamische Optimierung wird erfolgreich angewandt und ermöglicht nicht nur die Berücksichtigung der Dynamik bei der Muskelkrafterzeugung, sondern auch die Benutzung integraler Zielfunktionen wie etwa des gesamten Energieaufwands und führt zu vollständigere Gangmustern. Der sehr hohe Rechenaufwand verhindert jedoch eine breite Verwendung der dynamischen Optimierung, insbesondere in klinischen Anwendungen und in der Entwicklung von Prothesen und Orthesen.

Einen Ausweg aus diesem Dilemma bieten Optimierungsmethoden, die auf inverser Dynamik basieren, und das Potenzial haben, den hohen Rechenaufwand zu reduzieren, da sie keine numerische Integration der Zustandsgleichungen des Muskel-Skelett-Modells benötigen. Dabei werden Zustände des mechanischen Systems mittels Funktionen approximiert, die durch eine feste Anzahl von Parametern charakterisiert werden, welche in der Optimierungsaufgabe als Entwurfsvariablen eingehen. Zu den Anwendungsbereichen gehören zum Beispiel die Robotik und die Computeranimation. Trotzdem wurden diese Methoden bislang selten in der Biomechanik verwendet. Ein Ziel dieser Arbeit ist, eine Methode zur Erzeugung von optimalen Gehbewegungen zu entwickeln, die auf inverser Dynamik basiert, für die Anwendung mit den weit verbreiteten Muskelmodellen nach Hill geeignet ist, und die redundante Anordnung der Muskeln berücksichtigt.

Die dritte in dieser Arbeit entwickelte Methode, dynamische Zustandsoptimierung genannt, erfordert die Parametrisierung der Bewegung des Skelettes und der Muskelkräfte mit Polynomen, die Knoten interpolieren, welche zu Entwurfsvariablen in der Optimierungsaufgabe werden. Die neuronalen Erregungen sind aus der Inversion der Dynamik der Muskelkrafterzeugung bekannt. Das Optimierungsproblem besteht in der Suche nach optimalen parametrisierten Muskelkräften und Bewegungen des Skelettes, die ein integrales Gütekriterium minimieren, z.B. den gesamten Energieaufwand und die Abwei-

chung von der gemessenen Bewegung. Dabei müssen Nebenbedingungen erfüllt sein, unter anderem die kinematischen Bedingungen zwischen den Füßen und dem Boden und die Konsistenz zwischen der Bewegung und den Muskelkräften, welche die Erfüllung der Bewegungsgleichungen verlangen. Die Erfüllung der Nebenbedingungen wird dabei nur an diskreten Kontrollpunkten geprüft.

Die dritte Methode wird für die Erzeugung optimaler Gehbewegungen verwendet, welche mit normalen gemessenen Mustern verglichen werden. Die gute Übereinstimmung zeigt, dass die Methode in Verbindung mit dem verwendeten Modell in der Lage ist, physiologische Gehbewegungsmuster zu liefern. Die Methode wird außerdem für die Untersuchung des Gehens mit bilateralen Gewichten an den Füßen und für die Bestimmung der Kinematik, der Kinetik, der Muskelansteuerung und des Energieaufwands während des Gehens mit drei verschiedenen transtibialen Prothesen verwendet, welche durch die Steifigkeitskennlinie des prothetischen Knöchels charakterisiert werden. Darüber hinaus werden optimale Parameter, welche die Steifigkeitskennlinie des prothetischen Knöchels beschreiben, durch Einbeziehung in die Entwurfsvariablen der Optimierung bestimmt. Ein Vergleich der Ergebnisse des Modells mit optimierten Steifigkeitskennlinien mit denen dreier herkömmlicher Prothesen für drei verschiedene Gehgeschwindigkeiten zeigt eine wesentliche Verbesserung des prothetischen Ganges hinsichtlich des Energieaufwandes, und der Abweichungen der Kinematik und der Bodenreaktioneskräfte vom natürlichen Gang. Die Verbesserungen durch die optimierten Prothesen zeigen das Potenzial, welches diese Methode für den Entwurf verbesserter Prothesenkonstruktionen aufweist.

Chapter 1

Introduction

Biomechanics is the science that emerged from the attempt to study biological structures using mechanics. The prefix "bio" is from Greek and means "life". Among the many definitions of biomechanics, one that fits well to the subject of this work reads as

> "Biomechanics is the science which studies structures and functions of biological systems using the knowledge and methods of mechanics"

according to Hatze [42] and Nigg [84]. This work focuses on the part of biomechanics dealing with human normal and pathological walking.

Normal walking is a nearly periodic and symmetric motion, where the patterns occurring in one side of the body repeat in the other side, 180° out of phase. The walking cycle can be divided into phases characterized by the contacts occurring between feet and ground. The stance phase corresponds to the period in which the considered foot is in contact with the ground, while during the swing phase this foot is free. In the double support phase both feet are in contact with the ground, and in the single support phase only one of the feet is contacting the ground. The increase of walking velocity is accompanied by a relative decrease in the double stance phase until it completely disappears in the transition from walking to running giving place to a phase where both feet are free.

The human locomotor system is composed by the skeleton that provides support, and the muscles that apply the forces to the skeleton required to cause motion. The muscles are recruited by the central nervous system (CNS) according to underlying performance criteria which are activity-dependent. While for jumping the maximal height achieved might be the primary performance criterion, for other tasks the minimization of time expended, fatigue, or pain might be of primary importance. There are experimental evidences showing that during walking the energetic expenditure per unit of distance traveled play a key role, Ralston [88]. For this reason, the study of human normal and pathological walking necessarily involves energetic considerations.

Neurological or musculoskeletal disorders cause deviations from normal patterns and lead to an increase in the energetic demand during walking. Indeed, data from many literature sources show the burden caused by such disturbances with respect to energetic requirements, refer to Waters and Mulroy [121] for a review. In particular the deviations in the kinematics, kinetics and energetics occurring during the walking with lower limb prostheses are focused in this dissertation. The severity of the burden caused by such handicaps due to the removal of the amputated part together with the loss of the functionality of the muscles spanning the affected joints and the alterations of the inertial properties of the lower limb in comparison to the normal gait is indicated by an oxygen uptake 20% higher for unilateral transtibial amputes, Waters and Mulroy [121], and an energetic demand per unit of distance traveled 30% higher for unilateral transfemoral amputes, Jaegers et al. [55].

The understanding of these disorders and the ways they affect the biomechanics of walking can contribute to the design of therapies and assistive devices or to the planning of surgical interventions to reduce the burden imposed. For instance, the understanding of the muscle coordination during walking and of the biomechanics of the prosthetic gait led to the development of surgical procedures that reduce muscle function loss after amputation and improve prosthetic socket fitting, see e.g. Radcliffe [87]. Furthermore, it contributed to the design and selection of prosthetic components that reduce energetic demand, enhance comfort and reduce pain, see e.g. Michael [75] and Schmalz et al. [99].

A typical problem in biomechanics is the determination of muscle forces required to perform a given motion. The knowledge of muscle forces is important not only to assess muscle coordination but also to estimate internal loads on bones and joints, useful, for example, for the design of endoprostheses or for the analysis of sport activities, see e.g. Alt et al. [6]. However, the direct measurement of muscle forces requires invasive techniques whose implementation is difficult and rarely viable. In order to overcome this problem non-invasive techniques are used to estimate the muscle forces from joint moments by means of models of the musculoskeletal system.

Gait analysis laboratories equipped with motion capture systems and force plates are increasingly being used to measure body motion and ground forces non-invasively. Gas analysis systems to estimate energy expenditure through measurements of oxygen consumption are also often available in these laboratories. The capture of the body motion is most frequently performed by tracking the 3-D trajectories of markers attached to specific landmarks on the body, Cappozzo et al. [21], by means of a set of previously calibrated digital cameras. The computation of the motion of the body segments is referred to as body pose reconstruction and is based on a segmentation of the body and on the assumption that the resulting segments are rigid bodies. This permits the estimation of the translations and rotations of the segments throughout the gait cycle based on the 3-D trajectories of the markers attached to them. Because the markers on one segment move

with respect to each other and to the underlying bones due to skin movement and due to experimental errors, the rigid body assumption is violated. This is overcome by the use of optimization techniques aiming at best fitting the reference marker arrangement to the current measured one, see e.g. Söderkvist and Wedin [102], Lu and O'Connor [65], and Reinbolt et al. [89].

Besides delivering assess to the kinematics of gait, the measured motion and ground forces arising during walking can be used to estimate the moments at the joints required to perform the movement by means of inverse dynamics, refer, e.g., to Siegler and Liu [101] or Winter [123]. This technique requires a mechanical model of the body, which, in biomechanics of gait, is often a multibody system composed by rigid bodies. Indeed, the method of multibody systems is adequate to study mechanical systems that undergo large, nonlinear motions, Schiehlen [95], as occurring during walking. With the mechanical models of the body and the information about the kinematics and ground forces, the dynamics of the skeletal system, described by its equations of motion, can be inverted to determine the total joint moments. An important issue in performing inverse dynamics is the reduction of experimental errors arising from: 1) skin movement (skin artefacts), and 2) errors in the capture and discretization of marker positions. Noise and errors in the position of the markers are amplified by the necessary numerical differentiation of the position, what might cause substantial errors in the moments estimated by inverse dynamics. There is a series of techniques to reduce these errors taking advantage of the fact that more information is available than necessary for the inverse dynamics, and considering the higher accuracy of ground force measurement compared to kinematics measurements, Kuo [61], Vaughan [118].

Although the total moments at the joints give valuable clues on muscle effort, they do not deliver information on individual forces applied by muscles and other tissue spanning the joints. Since there are much more muscles spanning the joints than actuated degrees of freedon, there is an infinite number of solutions for the muscle forces that generate the same moments at the joints. In order to estimate a unique solution for the muscle forces from the moments at the joints obtained by inverse dynamics optimization approaches are used, based on the assumption that the central nervous system minimizes some intrinsic performance criterion. Although straightforward and computational efficient, the traditional strategy to solve this problem, reviewed in Tsirakos [114] and da Silva [26] and referred to as static optimization, suffers from two important limitations. First, it neglects the biochemical and mechanical processes leading to muscle contraction and force generation. Second, it relies on instantaneous performance criteria, for example, the cost function based on muscle fatigue as proposed by Crowninshield et al. [25], which often do not reflect the underlying performance criterion adopted by the CNS. Specially the total energy expenditure, which is the key performance criterion during walking, cannot be described by an instantaneous cost function. These limitations can compromise the correctness of the muscle force estimations.

In order to better account for the complex process of force generation, see e.g. Zaha-lak [131], muscle models with varying degrees of complexity and accuracy have been proposed, refer, for example, to Winters [124] for a review. Models based on the cross-bridge theory of Huxley (Huxley [52]) are accurate, but are computationally expensive and require many parameters that are difficult to assess. These drawbacks prevent their use in studies involving musculoskeletal models with many muscles, van den Bogert and Nigg [116]. In such applications phenomenological, Hill-type muscle models, first proposed by Hill [49], are almost exclusively used, refer, e.g., to Zajac [132]. These models represent well the salient features of the force generation process while being computationally tractable for large-scale applications. The mathematical description of these models often result in second-order dynamics that includes the first-order activation dynamics and the first-order contraction dynamics. Moreover, physiological energy expenditure models that can be used in conjunction with Hill-type muscle models were recently proposed, Umberger et al. [115] and Bhargava at al. [17]. Therefore, computationally tractable models of the musculoskeletal system, of the muscle force generation process, and of the corresponding energetics involved are available in the literature and can be used to study and simulate human walking.

More realistic muscle force estimations can be obtained by considering the muscle force generation process and using physiological cost functions as the energy expenditure per unit of distance traveled. This can be achieved using the so-called dynamic optimization, in opposition to static optimization. Dynamic optimization relies on the parameteriza-tion of the neural excitations by means of nodal points, Pandy et al. [85], and on the multiple numerical integration of the differential equations describing the dynamics of the musculoskeletal model. This strategy has been used to predict muscle coordination by tracking prescribed kinematics, e.g. in Neptune and Bogert [82], Neptune and Hull [80], Strobach [107], Davy and Audu [27]. Because the approach requires several integrations of the often high-dimensional system equations the resulting computational effort turns into prohibitive, preventing its wider use and compromising its implementation in clinical applications.

For this reason, much effort has been recently expended to develop approaches that reduce the computational effort while still considering the muscle force generation process and allowing for the use of physiological cost functions. Indeed, Menegaldo et al. [74] propose a dynamic optimization approach to track moments at the joints obtained by inverse dy-namics instead of the kinematics of the skeleton. This avoids the necessity of integrating the skeletal system dynamics, substantially reducing the computational effort. However, it requires the use of an additional tracking term in the cost function what compromises the interpretation of the results. Thelen and colleagues (Thelen et al. [112] and Thelen and Anderson [111]) propose an approach based on a control algorithm to track measured kinematics and ground forces, the computed muscle control (CMC). The CMC requires a unique integration of the system differential equations dramatically reducing the compu-

tational effort. An important drawback of CMC is the necessity of using an instantaneous cost function to solve the muscle force distribution problem, what prevents the use of time-integral cost functions such as the total energy expenditure. In this context, two novel approaches are proposed in this dissertation to efficiently compute physiological muscle forces, see also Ref. [3], [4], [5], while avoiding the drawbacks mentioned above.

Determining muscle forces from measured kinematics and ground forces is of great importance to estimate internal loads and understand muscle coordination during prescribed or measured motions of the skeleton. However, in the design of new assistive devices, surgical interventions and rehabilitation therapies it is desirable to predict the effect of a specific design, intervention or therapy on the walking patterns, including the motion. In order to achieve this predictive capability computational simulations of the human motion using the available models of the musculoskeletal system, of the muscle force generation process, and of the corresponding energetics are increasingly being used.

The dynamic optimization mentioned previously is being successfully used, permitting the use of time-integral cost functions and the consideration of the dynamics of the muscle force generation process. For instance, dynamic optimization together with models of the musculoskeletal system is used to investigate specific tasks as human walking by Gerritsen et al. [34] and Neptune et al. [81], running by Neptune et al. [83], cycling by Neptune and Hull [80], vertical jumping by Anderson and Pandy [7] and Nagano and Gerritsen [78], and time-optimal kick motion by Spägele [103]. One of the most remarkable applications of dynamic optimization is delivered by Anderson and Pandy [8], who could predict fairly well walking kinematics, muscle coordination and energy expenditure using metabolic cost per unit of distance traveled as cost function. Hase and Yamazaki [41], Umberger et al. [115], and Anderson and Pandy [9] also use dynamic optimization to simulate human walking through minimization the metabolic cost per unit of distance traveled. In spite of the growing use of dynamic optimization, the extremely high computational effort arising from the several numerical integrations of the large-scale state equations required prevents it from being more widely used. For instance, the optimization of Anderson and Pandy [8] needed 10000 hours of CPU time to find a solution. Computationally less expensive approaches to simulate motion are, therefore, essential to allow for design and clinical applications.

The use of approaches based on inverse dynamics have the potential to reduce the high computation effort by avoiding the necessity of numerically integrating the state equations, but have been poorly explored in biomechanics. Such approaches consist in transforming the optimal control problem into a parameter optimization, where the design variables are the parameters of functions that approximate the motion of the mechanical system. The differential equations describing the dynamics of the mechanical system are inverted to find the controls. The use of different approximation functions is reported in the literature, for example, Fourier series by Nagurka and Yen [79], splines of class C^2 by

Saidouni and Bessonnet [93], or splines of class C^3 by Bessonnet et al. [15]. The application fields range from robotics (Stryk [108]) and bipedal walking machines (Bessonnet et al. [15]) to character animation (Witkin and Kass [125]). The development of an inverse dynamics-based approach to generate optimal human walking patterns that deals with the overdeterminacy of muscle actuation and is adequate to the use in conjunction with Hill-type muscle models is proposed in this dissertation. Furthermore, this approach is implemented and used to investigate pathological gaits and to design components of transtibial prostheses.

1.1   Aims and Contents of the Work

The general aim of this dissertation is twofold. On the one hand, the objective is to develop techniques that enable a computationally efficient prediction of the kinematics, kinetics, muscle coordination and energetics of normal and pathological gaits. On the other hand, this dissertation aims at investigating abnormal gait, in particular the prosthetic gait, and at contributing to the design of assistive devices by using conventional and novel optimization-based techniques.

Chapter 2 introduces the models of the musculoskeletal system, of the muscle actuator, and of its corresponding energetics available in the literature, which are used throughout this dissertation to test the approaches proposed and to investigate pathological gaits. In order to provide a basis to the understanding of these models, a brief explanation of the biological system including the biochemical processes leading to muscle contraction is delivered. The characteristic phases of walking are shortly introduced, too.

Chapter 3 presents the experiments designed to study normal walking and the effects of changes in the joints mobility and inertial properties of the lower limb typically occurring due to the use of lower limb assistive devices, in particular lower limb prostheses. First, the design and experimental setup are explained, followed by the processing of the 3-D trajectories of the markers and the ground reaction forces obtained for two subjects wearing different lower limb mechanical disturbances. From this information the kinematics of the body segments, according to the model of the skeleton adopted, is reconstructed using optimization techniques. The results for the kinematics are presented and discussed. Then, the moments at the joints are determined from the measured kinematics and ground forces using inverse dynamics. Different techniques to solve the inverse problem of dynamics and to reduce the errors arising from the skin artefacts and measurement errors are presented. The results obtained for the moments at the joints for both subjects and the different experiments are compared and discussed.

Chapter 4 is devoted to the problem of muscle force distribution in biomechanics. After an introduction to the problem, different methods to solve it are presented together with a

discussion of their limitations. Two alternative approaches are then proposed to overcome the limitations of other methods recently proposed to find muscle forces considering the dynamics of muscle force generation and physiological cost functions. First, an approach named extended inverse dynamics is proposed to allow for the use of time-integral cost functions and to consider the dynamics of the muscle force generation process while being computationally much less expensive than dynamic optimization. A second alternative approach, named modified static optimization, is also proposed based on the static optimization approach but, additionally, considering the muscle force generation process while being computationally very efficient. The approaches are compared to the static optimization approach with respect to computational effort and fulfillment of constraints that guarantee the consideration of the dynamics involved in the muscle force generation process. Applications to the normal and disturbed gait are presented and discussed. The extended inverse dynamics approach is validated through two different ways: a comparison of the results for the muscle activations with the linear envelopes of electromyograms from the literature for the normal gait, and the use of the computed neural excitations as input to a forward-dynamics simulation, with the subsequent comparison of the kinematics obtained with the originally measured one. The estimations of energy expenditure obtained through both ways are compared, too.

Chapter 5 is devoted to the search for optimal normal and pathological walking patterns and to the design of transtibial prostheses. It begins with a comprehensive overview of dynamic simulation and optimization of human walking. In order to avoid the prohibitive computational effort required by dynamic optimization to find optimal human walking patterns, an alternative, inverse dynamics-based approach, named state dynamic optimization, is proposed. This approach is explained in details. Then, the proposed approach is tested and used to study the normal walking, the walking with a bilateral foot weight, and the amputee walking with different transtibial prostheses. Finally, the approach is used to estimate near-optimal prosthetic ankle stiffness curves in the sense of energy expenditure and proximity of the prosthetic gait to normal patterns. The results of the dissertation are concluded in a short summary followed by an extensive list of references.

Chapter 2

Modelling of the Musculoskeletal System

In order to study human gait, a basic understanding of the biological system specially of the human locomotor system is necessary. Furthermore, the simulation of the phenomena occurring during gait requires models of the locomotor system, its energetics and its interaction with the environment. In this context, this chapter presents a short introduction on the biological systems and phenomena involved in gait and of the corresponding models that are employed throughout the work. Since the skeletal system is modeled as a multibody system composed of rigid bodies linked by ideal mechanical joints, a brief overview on multibody systems is delivered in section 2.1. The mechanics, physiology and energetics of the biological actuator, the muscle, as well as corresponding models are briefly described in section 2.2. Section 2.3 presents the model of the entire musculoskeletal system dynamics obtained by integrating the skeletal system dynamics, the contraction dynamics and the activation dynamics. Finally, section 2.4 briefly describes human normal walking and its phases.

2.1   Multibody Systems Models of the Skeleton

During gait the body segments undergo large, nonlinear motions, while the effects of soft tissue motion on the overall dynamics may be neglected. For these reasons the use of the method of multibody systems composed of rigid bodies linked by ideal joints turned out to be an adequate model for the skeletal system during walking. Furthermore, the method of multibody systems is computationally efficient, what is a fundamental issue in biomechanics, since large-scale, highly complex models are often required to accurately describe biological systems, the simulation of which leads frequently to a high computational effort.

A multibody system is typically composed of rigid bodies, particles, joints, bearings,

springs, dampers, force actuators and position actuators. The rigid bodies and particles are connected by joints resulting in a system with chain, tree or loop topology. A loop topology is characterized by the occurrence of kinematic loops and requires a special treatment as explained further on. Multibody systems with loop topology are useful for modeling the double stance phase of the gait, in which both feet are contacting the ground. The modeling of multibody systems as well as the derivation of the corresponding equations of motions are explained in details in Schiehlen [95] and in Schiehlen and Eberhard [97], and are briefly presented in the following sections. Recent developments in multibody dynamics as well as applications are presented in Schiehlen [96].

2.1.1 Kinematics

The kinematics of a multibody system consisting of p rigid bodies subject to q holonomic constraints is fully characterized by a set of $f = 6p - q$ generalized coordinates

$$\boldsymbol{y} = \begin{bmatrix} y_1 & y_2 & \ldots & y_f \end{bmatrix}^T, \tag{2.1}$$

whose number corresponds to the number of degrees of freedom of the multibody system.

The position and orientation of the ith rigid body in an inertial coordinate system I is described by the 3×1-position vector $\boldsymbol{r}_i$ of its center of mass and by the 3×3-rotation matrix $\boldsymbol{S}_i$ of a body-embedded coordinate system, respectively, as

$$\boldsymbol{r}_i = \boldsymbol{r}_i(\boldsymbol{y}, t), \quad \boldsymbol{S}_i = \boldsymbol{S}_i(\boldsymbol{y}, t). \tag{2.2}$$

The translational velocity of the center of mass is obtained by differentiating the position vector yielding

$$\boldsymbol{v}_i = \dot{\boldsymbol{r}}_i = \frac{\partial \boldsymbol{r}_i}{\partial \boldsymbol{y}^T} \, \dot{\boldsymbol{y}} + \frac{\partial \boldsymbol{r}_i}{\partial t} = \boldsymbol{J}_{Ti}(\boldsymbol{y}, t) \, \dot{\boldsymbol{y}} + \bar{\boldsymbol{v}}_i(\boldsymbol{y}, t), \tag{2.3}$$

where $\boldsymbol{J}_{Ti}$ is the $3 \times f$-Jacobian matrix of translation, and $\bar{\boldsymbol{v}}_i$ is the local velocity, which vanishes for scleronomic systems. Analogous to the translational velocity, the angular velocity vector $\boldsymbol{\omega}_i$ is the time derivative of the infinitesimal rotation vector $\boldsymbol{s}_i$ as

$$\boldsymbol{\omega}_i = \dot{\boldsymbol{s}}_i = \frac{\partial \boldsymbol{s}_i}{\partial \boldsymbol{y}^T} \, \dot{\boldsymbol{y}} + \frac{\partial \boldsymbol{s}_i}{\partial t} = \boldsymbol{J}_{Ri}(\boldsymbol{y}, t) \, \dot{\boldsymbol{y}} + \bar{\boldsymbol{\omega}}_i(\boldsymbol{y}, t), \tag{2.4}$$

where $\boldsymbol{J}_{Ri}$ is the $3 \times f$-Jacobian matrix of rotation, and $\bar{\boldsymbol{\omega}}_i$ is the local angular velocity, which vanishes for scleronomic systems. The angular velocity vector $\boldsymbol{\omega}_i = [\omega_1 \, \omega_2 \, \omega_3]^T$ can be obtained from the corresponding skew-symmetric rotation tensor $\tilde{\boldsymbol{\omega}}_i$ computed as

$$\tilde{\boldsymbol{\omega}}_i = \begin{bmatrix} 0 & -\omega_3 & \omega_2 \\ \omega_3 & 0 & -\omega_1 \\ -\omega_2 & \omega_1 & 0 \end{bmatrix} = \dot{\boldsymbol{S}}_i \boldsymbol{S}_i^T. \tag{2.5}$$

The translational and angular accelerations follow by differentiation of (2.3) and (2.4), respectively, yielding

$$\dot{\boldsymbol{v}}_i = \frac{\partial \boldsymbol{r}_i}{\partial \boldsymbol{y}^T} \ddot{\boldsymbol{y}} + \frac{\partial \boldsymbol{v}_i}{\partial \boldsymbol{y}^T} \dot{\boldsymbol{y}} + \frac{\partial \boldsymbol{v}_i}{\partial t} = \boldsymbol{J}_{Ti}(\boldsymbol{y}, t)\, \ddot{\boldsymbol{y}} + \bar{\boldsymbol{v}}_i(\dot{\boldsymbol{y}}, \boldsymbol{y}, t)\,, \tag{2.6}$$

$$\dot{\boldsymbol{\omega}}_i = \frac{\partial \boldsymbol{s}_i}{\partial \boldsymbol{y}^T} \ddot{\boldsymbol{y}} + \frac{\partial \boldsymbol{\omega}_i}{\partial \boldsymbol{y}^T} \dot{\boldsymbol{y}} + \frac{\partial \boldsymbol{\omega}_i}{\partial t} = \boldsymbol{J}_{Ri}(\boldsymbol{y}, t)\, \ddot{\boldsymbol{y}} + \bar{\boldsymbol{\omega}}_i(\dot{\boldsymbol{y}}, \boldsymbol{y}, t)\,, \tag{2.7}$$

where $\bar{\boldsymbol{v}}_i$ and $\bar{\boldsymbol{\omega}}_i$ are the local translational and angular accelerations, respectively.

2.1.2 Kinetics

The motion of the rigid bodies in the multibody system is determined by the acting forces and moments. The Newton's and Euler's equations describe the relation between the motion of rigid body i and the forces and moments acting on it as

$$m_i \dot{\boldsymbol{v}}_i = \boldsymbol{f}_i^e + \boldsymbol{f}_i^r\,, \tag{2.8}$$

$$\boldsymbol{I}_i \dot{\boldsymbol{\omega}}_i + \tilde{\boldsymbol{\omega}}_i \boldsymbol{I}_i \boldsymbol{\omega}_i = \boldsymbol{l}_i^e + \boldsymbol{l}_i^r\,, \tag{2.9}$$

where m_i is the mass of body i, $\boldsymbol{I}_i$ is the 3×3-inertia tensor with respect to the center of mass, $\boldsymbol{f}_i^e$ and $\boldsymbol{l}_i^e$ are, respectively, the 3×1 vectors of the resultant applied force and moment with respect to the center os mass, and $\boldsymbol{l}_i^e$ and $\boldsymbol{l}_i^r$ are, respectively, the 3×1 vector of resultant constraint (or reaction) forces and moments with respect to the center of mass. Applied forces and moments are due the weight, actuator forces and moments, and elements such as springs and dampers, and are determined by laws relating them to the motion of the multibody system. Reaction forces and moments, in contrast, are due to kinematic constraints imposed by elements such as joints, bearings and supports.

Newton's (2.8) and Euler's (2.9) equations can be rewritten in matrix-form as

$$\bar{\bar{\boldsymbol{M}}} \bar{\boldsymbol{J}} \ddot{\boldsymbol{y}} + \underbrace{\begin{bmatrix} m_1 \bar{\boldsymbol{a}}_1 \\ \vdots \\ m_p \bar{\boldsymbol{a}}_p \\ \boldsymbol{I}_1 \bar{\boldsymbol{\alpha}}_1 + \tilde{\boldsymbol{\omega}}_1 \boldsymbol{I}_1 \boldsymbol{\omega}_1 \\ \vdots \\ \boldsymbol{I}_p \bar{\boldsymbol{\alpha}}_p + \tilde{\boldsymbol{\omega}}_p \boldsymbol{I}_p \boldsymbol{\omega}_p \end{bmatrix}}_{\bar{\boldsymbol{q}}^c} = \underbrace{\begin{bmatrix} \boldsymbol{f}_1^e \\ \vdots \\ \boldsymbol{f}_p^e \\ \boldsymbol{l}_1^e \\ \vdots \\ \boldsymbol{l}_p^e \end{bmatrix}}_{\bar{\boldsymbol{q}}^e} + \underbrace{\begin{bmatrix} \boldsymbol{f}_1^r \\ \vdots \\ \boldsymbol{f}_p^r \\ \boldsymbol{l}_1^r \\ \vdots \\ \boldsymbol{l}_p^r \end{bmatrix}}_{\bar{\boldsymbol{q}}^r}\,, \tag{2.10}$$

where $\bar{\boldsymbol{q}}^c$, $\bar{\boldsymbol{q}}^e$ and $\bar{\boldsymbol{q}}^r$ represent the $6p \times 1$-vectors of Coriolis forces, of applied forces and of reaction forces, respectively, and $\bar{\bar{\boldsymbol{M}}}$ is a $6p \times 6p$-block diagonal matrix structured as

$$\bar{\bar{\boldsymbol{M}}} = diag\{m_1 \boldsymbol{E} \ \dots \ m_p \boldsymbol{E} \quad \boldsymbol{I}_1 \ \dots \ \boldsymbol{I}_p\}\,, \tag{2.11}$$

where $\boldsymbol{E}$ is the 3×3-identity matrix, while the global $6p \times f$ Jacobian matrix $\bar{\boldsymbol{J}}$ in (2.10) is constructed as

$$\bar{\boldsymbol{J}} = \begin{bmatrix} \boldsymbol{J}_{T1}^T & \dots & \boldsymbol{J}_{Tp}^T & \boldsymbol{J}_{R1}^T & \dots & \boldsymbol{J}_{Rp}^T \end{bmatrix}^T\,. \tag{2.12}$$

2.1.3   Equations of Motion

Newton's and Euler's equations (2.10) deliver $6p$ equations for the f degrees of freedom and q constraints. Using a matrix formulation of the d'Alembert's principle, refer, e.g., to Schiehlen and Eberhard [97], the equations (2.10) are reduced to their minimal form and the reaction forces are eliminated by premultiplication of (2.10) with $\bar{\boldsymbol{J}}^T$ yielding the f equations of motion

$$\boldsymbol{M}(\boldsymbol{y},t)\,\ddot{\boldsymbol{y}} + \boldsymbol{k}(\boldsymbol{y},\dot{\boldsymbol{y}},t) = \boldsymbol{q}(\boldsymbol{y},\dot{\boldsymbol{y}},t)\,, \tag{2.13}$$

where $\boldsymbol{M} = \bar{\boldsymbol{J}}^T \bar{\bar{\boldsymbol{M}}} \bar{\boldsymbol{J}}$ is the symmetric, positive definite $f \times f$-mass matrix, $\boldsymbol{k} = \bar{\boldsymbol{J}}^T \bar{\boldsymbol{q}}^c$ is the $f \times 1$-vector of generalized Coriolis forces, and $\boldsymbol{q} = \bar{\boldsymbol{J}}^T \bar{\boldsymbol{q}}^e$ is the $f \times 1$-vector of generalized applied forces. Note that the reaction forces and moments in $\bar{\boldsymbol{q}}^r$ vanish, since $\bar{\boldsymbol{J}}^T \bar{\boldsymbol{q}}^r = \boldsymbol{0}$ according to the principle of virtual work.

The motion of a multibody system can be further constrained by q_c additional kinematic constraints described implicitly by a $q_c \times 1$-vector

$$\boldsymbol{c}(\boldsymbol{y},t) = \boldsymbol{0}\,. \tag{2.14}$$

These additional constraints reduce the number of degrees of freedom of the original multibody system to $f_e = f - q_c$, so that the coordinates in $\boldsymbol{y}$ are no longer independent. The equations of motion of the reduced multibody system can be derived by adding a term to (2.13) as

$$\boldsymbol{M}(\boldsymbol{y},t)\,\ddot{\boldsymbol{y}} + \boldsymbol{k}(\boldsymbol{y},\dot{\boldsymbol{y}},t) = \boldsymbol{q}(\boldsymbol{y},\dot{\boldsymbol{y}},t) + \boldsymbol{C}^T \boldsymbol{\lambda}\,, \tag{2.15}$$

where $\boldsymbol{\lambda}$ is the $q_c \times 1$-vector of Lagrangian multipliers containing generalized reaction forces arising from the addition of the new constraints, and $\boldsymbol{C}$ is the $q_c \times f$-Jacobian matrix of the constraints obtained as

$$\boldsymbol{C} = \frac{\partial \boldsymbol{c}}{\partial \boldsymbol{y}^T}\,. \tag{2.16}$$

This leads to a set of differential algebraical equations (DAEs) composed of (2.15) and (2.14). These equations can be in many cases reduced to a set of f_e pure differential equations of minimal form by means of the d'Alembert's principle, see e.g. Schirm [98]. However, when kinematical loops arise in the multibody system, this reduction is not always possible or straightforward, so that, in many cases, the solution of the differential algebraical set of equations is required. Furthermore, for some applications the DAEs given in (2.15) and (2.14) can be advantageous as explained in chapter 5.

2.1.4   Direct Dynamics and Inverse Problem of Dynamics

The equations of motion are differential equations relating the forces and moments applied on the multibody system and its motion. Figure 2.1 illustrates two methods used to

investigate the dynamics of a multibody system, depending on the application. A $k_c \times 1$-vector $\boldsymbol{\tau}$ is introduced to represent the actuator forces and moments. If all forces and moments applied are known, the motion of the multibody system $\boldsymbol{y}(t)$ and $\dot{\boldsymbol{y}}(t)$ can be computed by numerically integrating the equations of motion as shown on the upper part of Fig. 2.1. Standard numerical integrators often require the state space representation of the equations of motion in the form $\dot{\boldsymbol{x}} = \boldsymbol{g}(\boldsymbol{x}, \boldsymbol{\tau}, t)$, where $\boldsymbol{x} = \begin{bmatrix} \boldsymbol{y}^T & \dot{\boldsymbol{y}}^T \end{bmatrix}^T$, and specifying the initial state of the multibody system $\boldsymbol{x}_0 = \begin{bmatrix} \boldsymbol{y}_0^T & \dot{\boldsymbol{y}}_0^T \end{bmatrix}^T$ is needed for the numerical integration of the equations of motion. This computation is called direct dynamics, because it follows the natural cause (actuator forces) and effect (motion) as the sequence of events.

On the contrary, when the motion quantities, $\boldsymbol{y}$, $\dot{\boldsymbol{y}}$ and $\ddot{\boldsymbol{y}}$, are predescribed or measured, the resulting algebraic set of equations can be solved for $\boldsymbol{\tau}$ to determine the actuator forces and moments required to cause the observed motion as illustrated on the lower part of Fig. 2.1. This computation is called inverse dynamics in opposition to direct dynamics. Because it involves the solution of a set of algebraic equations, which are often linear, performing inverse dynamics is computationally much less time consuming than performing direct dynamics. An important issue concerns the number of unknown components of vector $\boldsymbol{\tau}$. If the number of equations f is greater than the number of unknowns k_c the system is underactuated, and a unique solution can in general not be found. If the number of unknowns k_c is greater than that of equations f the system is overactuated and there is an infinite number of solutions.

<div align="center">

direct dynamics

$$\ddot{\boldsymbol{y}} = \boldsymbol{M}(\boldsymbol{y}, t)^{-1} \left(\boldsymbol{q}(\boldsymbol{y}, \dot{\boldsymbol{y}}, \boldsymbol{\tau}, t) - \boldsymbol{k}(\boldsymbol{y}, \dot{\boldsymbol{y}}, t) \right)$$

</div>

| actuator forces and moments | $\boldsymbol{\tau}$ | Equations of Motion $\boldsymbol{M}(\boldsymbol{y},t)\,\ddot{\boldsymbol{y}} + \boldsymbol{k}(\boldsymbol{y},\dot{\boldsymbol{y}},t) = \boldsymbol{q}(\boldsymbol{y},\dot{\boldsymbol{y}},\boldsymbol{\tau},t)$ | $\boldsymbol{y}$ | kinematics |

<div align="center">

$$\boldsymbol{q}(\boldsymbol{\tau}, \boldsymbol{y}, \dot{\boldsymbol{y}}, t) = \boldsymbol{M}(\boldsymbol{y})\,\ddot{\boldsymbol{y}} + \boldsymbol{k}(\boldsymbol{y}, \dot{\boldsymbol{y}}, t)$$

inverse dynamics

</div>

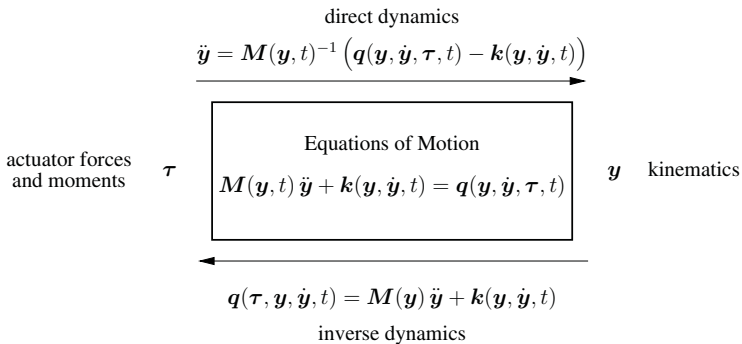Figure 2.1: Schematic representation of the direct and inverse dynamics.

Both methods are applied in biomechanics. While inverse dynamics is widely employed to estimate net joint moments from body kinematics and ground reaction forces measured in gait analysis laboratories, direct dynamics is increasingly being used to investigate the effects of muscle recruitment strategies, musculoskeletal pathologies and design of assistive

devices on motion. The use of inverse dynamics in biomechanics of gait is addressed in details in chapter 3.

2.2 Muscles - The Biological Actuators

The actuators of the locomotor system are the skeletal muscles. Skeletal muscles are basically composed of fibers that generate force and tendons that connect the fibers to the skeleton. Through the corresponding moment arms the forces applied by the muscles originate moments about the articulations or joints, respectively, promoting motion and support of the body. Muscles can span one joint (uniarticular muscles), two joints (biarticular muscles) or more joints, and work in synergy to assure an efficient motion. Since muscles can only pull, muscle groups often work in pairs (antagonistic pairs) to generate joint moments in opposite directions. While one group of muscles (agonists/antagonists) generate moment in one direction, e.g. the knee flexor muscles, the other group (antagonists/agonists) generate moments in the opposite direction, e.g. the knee extensor muscles.

The dynamics of the processes that lead to force generation in the muscle are of fundamental importance to the dynamics of the entire musculoskeletal system. In section 2.2.1 the morphology of the muscle and the biochemical processes leading to force generation and contraction are briefly described. The factors that influence the force generation capabilities of the muscle are briefly discussed, too. With this framework, in section 2.2.2 models of the muscle mechanics and force generation dynamics are presented that are both computationally tractable for large-scale applications and representative of the salient features of the muscle morphology and of the force generation process.

2.2.1 Biological Actuator

Skeletal muscles are composed of structural units of decreasing size, see e.g. Herzog [47]. The muscle is formed by fascicles, which consist of muscle fibers. A muscle fiber is a cell with a diameter of about 100 μm and contains myofibrils lying parallel to each other. The myofibrils contain sarcomeres, the basic contractile structure of a muscle, in series as shown in Fig. 2.3. The arrangement of the filaments (protein molecules) encountered in the sarcomeres gives the skeletal muscle its typical striated pattern, visible with a microscope. Concerning the arrangement of the fibers in the muscle with respect to its line of action (direction of applied force), muscles can be classified as parallel-fibred or fusiform muscles, for which the fibers are aligned with the line of action of the muscle, and pennate muscles, for which the fibers make an angle with the line of action of the entire muscle. Figure 2.2 shows an schematic illustration of a pennate muscle with a pennation angle α_p applying a force f^m on the skeleton.
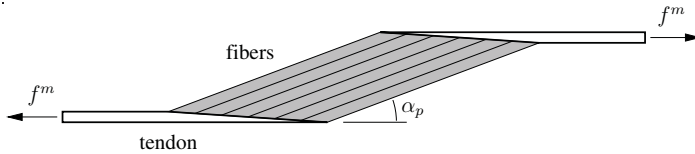
Figure 2.2: Schematic illustration of an unipennate muscle with a pennation angle α_p.

Motor units are the smallest controlable units in a muscle, see Winter [123]. A motor unit is a set of fibers innervated by the same motoneuron and can contain from a few fibers to as many as 2000 fibers according to Herzog [47]. When a motoneuron is stimulated all fibers of the corresponding motor unit generate force. The force applied by the entire muscle is increased either by increasing the firing frequency of the already recruited motor units, or by recruiting a further motor unit. According to the accepted size principle, smaller motor units containing less fibers are recruited first to allow for a finer force control, followed by larger motor units. This process of recruiting increasingly larger motor units and increasing firing frequency proceeds until all motor units at their respective maximal firing frequencies are recruited, for which state the muscle develops its maximal voluntary force, Winter [123].
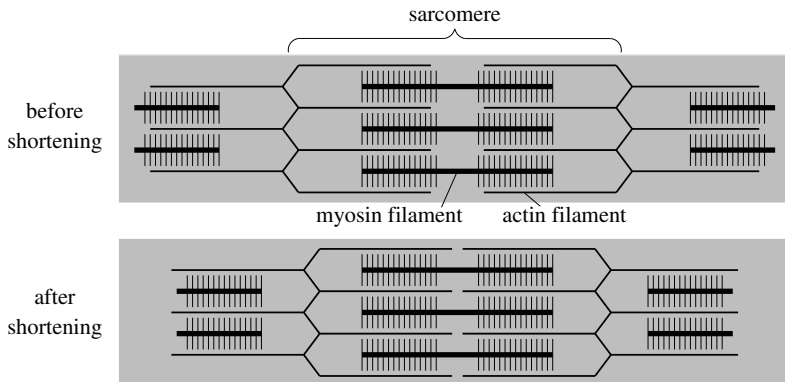
Figure 2.3: Schematic representation of the contractile elements, sarcomers, and the change in length caused by the sliding of the myofilaments past one another.

According to the sliding-filament theory, first suggested by H. E. Huxley (Hanson and Huxley [40], Huxley and Hanson [53]), the changes in muscle length are due to a relative sliding of the two sets of filaments schematically represented in Fig. 2.3, the actin (thin) filaments, and the myosin (thick) filaments, without a significative change in the length of the filaments themselves. The projections from the thick filaments in Fig. 2.3

represent the heads of the myosin molecules (also called cross-bridges), which attach to binding sites on the actin filaments generating force. The cross-bridge then moves pulling the actin filament past the myosin filament, where the necessary energy is provided by the breakdown of adenosinetriphosphate (ATP) into adenosinediphosphate (ADP) and a phosphate ion (P_i), see Herzog [47]. The detachment of the cross-bridge from the actin binding site is enabled by the attachment of an ATP to the myosin head, so that it can attach to another binding site on the actin filament. This process repeats cyclically during contraction.

In 1957 A. V. Huxley (Huxley [52]) formulated the 'cross-bridge theory' of muscle contraction to describe the interaction between the myosin and actin filaments, whose main features are still widely accepted among scientists, Herzog [48]. According to the original 'cross-bridge theory', the cross-bridges are connected to the myosin filaments by elastic elements and vibrate around neutral equilibrium positions, when not bound to actin sites. The cross-bridge eventually binds to a nearby actin site and, due to the stretch of the elastic element, an elementary force arises between the myosin and actin filaments. The sum of all forces generated at all the cross-bridges of the contractile tissue is the total active force applied by the muscle. According to the Huxley's theory the probabilities of attachment and detachment are functions of the displacement of the cross-bridges from their neutral positions. These functions are such that the probability of binding when the displacement is positive, i.e. a pulling force is generated, is greater than the one for a negative displacement, for which a pushing force is generated. For this reason, the total force applied by an entire muscle is a pulling force that tends to shorten the tissue.

The contraction process described above is regulated by an activation process. A neural action potential is generated in a motoneuron. The arrival of the neural action potential at the neuromuscular junction initiates a sequence of biochemical processes that leads to muscle contraction, see e.g. Zahalak [131]. The action potential causes liberation of acetylcholine into the gap between the nerve terminal and the motor end-plate, a region of the muscle fiber. The acetylcholine binds to receptors in the muscle fiber membrane generating a muscle action potential that travels along the muscle fiber and achieves the membranes of the sarcoplasmic reticulum (SR) in the interior of the fiber via structures that invaginate the fiber, called transverse tubules (TT), see Fig. 2.4. This electrical stimulus causes the release of calcium ions (Ca^{2+}) stored in the sarcoplasmic reticulum into the sarcoplasm, where they bind to tropomin molecules located on the thin actin myofilaments. In the absence of calcium ions, tropomin causes an inhibition against the binding of myosin cross-bridges and binding sites on the actin filament. The binding of the calcium to the tropomin removes this inhibition effect and the actin-myosin interaction explained above can take place. The muscle tissue is then said to be activated. In the absence of electrical stimulation, the calcium ions are pumped back to the sarcoplasmic reticulum in an ATP-driven process. With reduced calcium concentration in the sarcoplasm, the calcium dissociates from the tropomin, and the interaction between actin and myosin is

inhibited, leading to the relaxation of the muscle tissue.
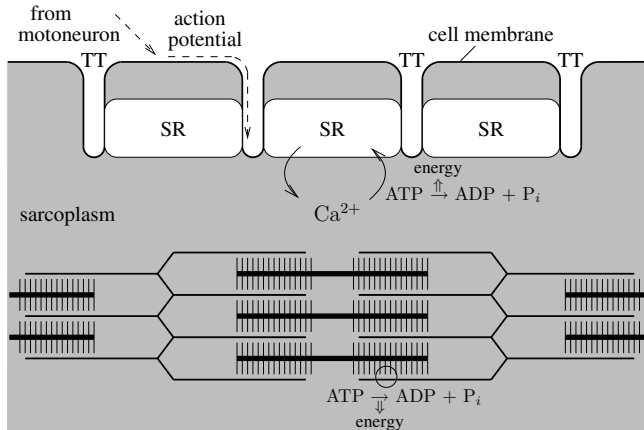
Figure 2.4: Schematic illustration of the activation process, of the contractile elements and of the processes requiring energy consumption. The sarcoplasmic reticulum and the transverse tubules are indicated by SR and TT, respectively.

During the activation and contraction processes described chemical energy is consumed. The source of energy is the hydrolysis of ATP to ADP. In the activation process this energy is consumed to pump calcium ions back to the sarcoplasmic reticulum. In the contraction process, one ATP is thought to be hydrolyzed for each cycle of cross-bridge attachment and detachment. Figure 2.4 schematically shows the consumption of energy in these two processes.

There is a series of factors that influence the muscle force capabilities and which are of fundamental importance for the proper modeling of the muscle force generation process explained in the next section. The force applied by a muscle depends on the number of fibers stimulated, what is controlled by the motor units recruited. The force at the stimulated fibers depend on their activation state, which is influenced by the concentration of calcium ions in the sarcoplasm, which, in turn, is regulated by the firing frequency. At the molecular level the force capabilities of a sarcomere are strongly influenced by its current length and shortening velocity. These two effects are described by the so-called force-length and force-velocity relations.

The relation between the maximal force a fiber can apply and its length is described by the force-length curve. This curve arises due to the structure of the myofibrils in the sarcomers. The force generated depends on the number of cross bridges bound to binding sites on the actin filament, see Fig. 2.3. Therefore, the maximal force that can be exerted occurs at sarcomere lengths for which the myosin heads and the actin filaments

fully overlap. This occurs at about the so called resting length of the sacomere. When the sarcomere lengthens beyond this region the overlapping reduces and the number of bound cross-bridges decrease together with the force applied until the force achieves zero when the position of no overlapping is reached. On the other hand, when the sarcomere is shortened beyond the optimal region, the force applied decreases, first due to interference between actin filaments as they overlap and, after further shortening, also due to deformation of the myosin filaments.

The relation between the maximal force a fiber can apply and its shortening velocity is described by the force-velocity curve. This relation describes the reduction of fiber force as it shortens an the increase of force when it lengthens. The force decreases with increasing shortening velocity until it achieves zero at the so-called maximal velocity of shortening, which depends on the type of the fiber (slow twitch fiber or fast twitch fiber). A classical force-velocity curve for shortening have been proposed by Hill [49] in 1938. There is much less knowledge about the precise nature of the force-velocity curve at lengthening velocities (Winter [123]). The force increases with lengthening velocity until it reaches an asymptotic value that ranges from 1.1 to 2 times the maximal isometric force f_{max}^m.

Another influencing factor on the force a muscle exert is the connective tissue that surrounds the contractile elements. This tissue, that includes the tendon, see Fig. 2.2, plays an important role in the biomechanics of the whole muscle and, in some movements, are responsible for storing and releasing large amounts of energy contributing to a more efficient motion. This tissue is traditionally modeled by springs and dampers in series and in parallel to the contractile element. The modeling of the muscle tissue mechanics and of the factors that influence the force a muscle exert is the focus of the next section.

2.2.2   Muscle Models

As explained in the previous section, models of the muscle force generation process based on the cross-bridge theory of Huxley can describe accurately the mechanical and chemical phenomena during contraction. These kind of models are, therefore, mainly used to interpret mechanical and biochemical outcomes of experiments with isolated muscles (Zahalak [131]). However, these models are inadequate to studies of muscle coordination involving many muscles, since their high complexity compromises the interpretation and computational tractability. Furthermore, these models require a series of parameters that are difficult to assess accurately. As a result, these models are rarely used to study muscle coordination (van den Bogert and Nigg [116]).

In simulations of the musculoskeletal system dynamics involving coordination of many muscles, variations of the classical model of muscle first proposed by Hill [49] are almost always used (Zajac [132]). These models are phenomenological models based on the interpretation of the input-output behavior of muscles obtained experimentally (Win-
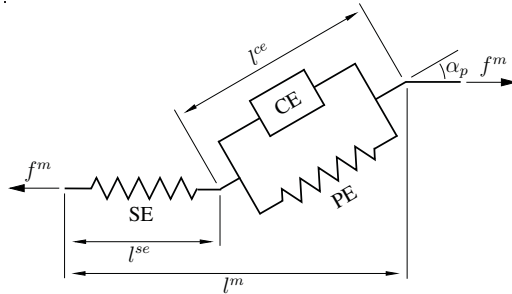
Figure 2.5: Three-element Hill-type muscle model composed of a contractile element (CE), a parallel elastic element (PE), and a series elastic element (SE). The pennation angle of the muscle fibers α_p, the total muscle (muculotendon) length l^m, the SE length l^{se}, the CE length l^{ce} and the muscle force f^m are also indicated.

ters [124]). There exist many different levels of complexity, but in movement simulation the three-component Hill-type muscle model is almost exclusively used (van den Bogert and Nigg [116]). Refer to Zajac [132] and Winters [124] for extensive reviews. The three component Hill-type muscle model is composed by a contractile element (CE) representing the muscle fibers, a parallel elastic element (PE) representing the nonlinear stiffness of connective tissue in parallel to the contractile elements, and a series elastic element (SE) representing the nonlinear stiffness of tissue in series with the contractile elements, including the tendon, see Fig. 2.5. The CE possess the force-length and force-velocity features described in the last section and its force is modulated by an activation state related to the concentration of Ca ions. The average pennation angle of a muscle is also frequently modelled by an angle α_p as depicted in Fig. 2.5.

In some variations of this basic model a damping element is added in parallel to the CE and an additional elastic element (SEE) is added in series to the CE, representing the stiffness of tissue in series with the muscle fibers. A simplification of these models, which will be used here is composed by a CE in series with a series elastic element (SE) and an elastic element in parallel to both. This permits that the parallel elastic element be lumped into the stiffness of a joint, that incorporates the stiffness of the parallel elastic elements of all the muscles and the stiffness of all the other elastic structures spanning the joint. Expressions for these joint stiffnesses can be found in the literature, for example, in Riener and Edrich [90], Mansour and Audu [69] and in Yoon and Mansour [130].

Activation Dynamics

Since the force generated by the fibers of all active motor units sum up resulting in the total active muscle force applied by the muscle tissue, it is reasonable and convenient

to assume a normalized neural excitation $u(t)$ that represents both the number of fibers excited (depending on the motor units stimulated) and the corresponding firing frequencies (Zajac [132]). For a muscle contracting isometrically (without length change), after the steady state is achieved in the biochemical processes leading to muscle contraction, the total muscle force f^m is proportional to the neural excitation u. A neural excitation $u = 1$ represents the excitation of all motor units at their maximal firing frequencies and causes, under isometric conditions at the optimal length of the fibers, and after steady state is reached, the so-called maximal isometric force f^m_{max}.

As explained in section 2.2.1, the stimulation of the muscle fibers leads to an active muscle state representing the ability of the myosin heads to interact with the actin myofilaments after Ca ions bind to tropomin. This process leading to an activation state $a(t)$ of the muscle is frequently modeled by a first order differential equation and is called activation dynamics. This differential equation can be, for example, of the form presented in Nagano and Gerritsen [78] (originally proposed by He et al. [46])

$$\dot{a}(t) = (u(t) - a(t))(t_1 u(t) + t_2) , \qquad (2.17)$$

where $t_2 = 1/t_d$ and $t_1 = 1/(t_a - t_2)$ are time constants, $u(t)$ is the neural excitation $0 \leq u \leq 1$, $a(t)$ is the muscle activation $0 \leq a \leq 1$, t_d is the time constant for de-activation and t_a is the time constant for activation. The activation occurs faster than the de-activation, see Zajac [132], therefore, the time constant for activation t_a is smaller that the time constant for de-activation t_d. Here (2.17) is adopted with muscle-dependent t_a and t_d as functions of the percentage of fast fibers in the muscle ft, refer to Appendix A.1. In Fig. 2.6 an example of the activation response to a stepwise neural excitation using (2.17) is illustrated.

(a)   (b)
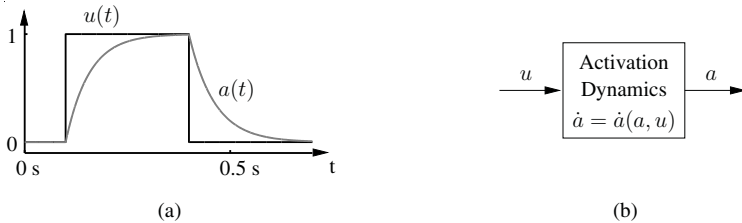
Figure 2.6: a) Example of the activation response $a(t)$ for a muscle subject to step neural excitation; b) schematic representation of the activation dynamics.

Contraction Dynamics

The force generated by the contractile element f^{ce} is a function of the muscle CE length l^{ce} and shortening velocity v^{ce} according to the force-length and force-velocity relations of

the muscle fibers, refer to section 2.2.1, and is further modulated by the activation $a(t)$ resulting in

$$f^{ce} = f^{ce}(a, v^{ce}, l^{ce}) .\qquad(2.18)$$

The force-length relation describing the CE force of a muscle contracting isometrically and fully activated ($a = 1$) presents a maximum at the optimal CE length l_{opt}^{ce}. For lengths greater or less than the optimal length ($l^{ce} > l_{opt}^{ce}$ or $l^{ce} < l_{opt}^{ce}$) the force capability of the CE decreases, refer to the example in Fig. 2.7a. The force-velocity relation describes the muscle CE force as a function of its shortening velocity v^{ce} for a fully activated muscle ($a = 1$) and at the fibers optimal length l_{opt}^{ce}, refer to the example in Fig. 2.7b. The combination of these two relations results in the force-length-velocity relation, illustrated in Fig. 2.7c. In Appendix A.1 the expression for the force-length-velocity relation adopted throughout this work is presented together with the employed muscle parameters. The scaling of the muscle CE force with the activation can be performed by simply scaling the force-length-velocity relation with a. However, in order to better account for the dependence of the maximal shortening velocity v_{max}^{ce}, indicating the velocity for $f^{ce} = 0$, on the activation level, modifications of the general force-length-velocity relation form at submaximal activations are also used (van Soest and Bobbert [117] and Umberger et al. [115]).
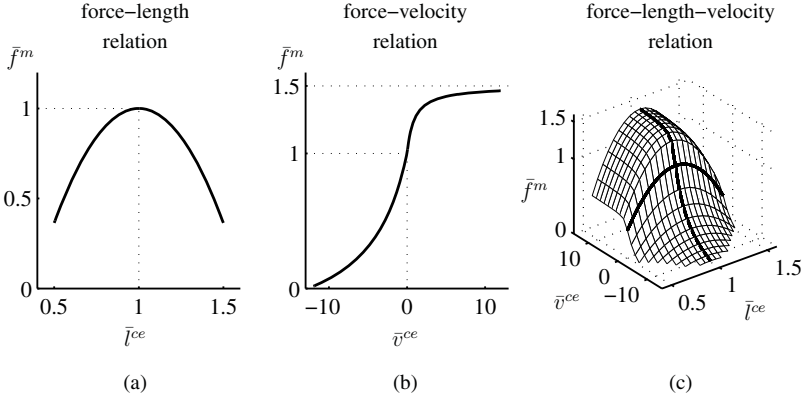
Figure 2.7: (a) force-length relation model, where $\bar{f}^{ce} = f^{ce}/f_{max}^m$ and $\bar{l}^{ce} = l^{ce}/l_{opt}^{ce}$; (b) force-velocity relation model, where $\bar{v}^{ce} = v^{ce}/l_{opt}^{ce}$; (c) force-length-velocity model. The curves are for the expressions presented in Nagano and Gerritsen [78] with $a = 1$, $ft = 50\%$, and $width = 0.627$.

The properties of the tendon are complex, but for the purpose of studying muscle coordination, this tissue can be modeled as an elastic element, as shown by the SE in Fig. 2.5, with a generic force-strain relation according to Zajac [132]. The tendon can be modeled by a simple quadratic force-strain curve characterized by a strain ε_o^T of 3% to 5% occurring

at the maximal isometric muscle force f^m_{max}, see Winters [124], yielding the force-length curve

$$f^{se}(l^{se}) = \begin{cases} k^T(l^{se} - l_{slack})^2 & \text{if} \quad l^{se} \geq l_{slack} \\ 0 & \text{if} \quad l^{se} < l_{slack} \end{cases} \qquad (2.19)$$

where $k^T = f^{ce}_{max}/(\varepsilon^T_o l_{slack})^2$, and l_{slack} is the tendon slack length for which the tendon or SE, respectively, just begin to resist lengthening. For tendon lengths less that the slack length no force is transmitted to the skeletal system. Here $\varepsilon^T_o = 4\%$ is adopted.

Since the force-length curve of the SE is known, its length l^{se} can be computed from the muscle force f^m, and then the time derivative of the muscle force $\dot{f}^m$ can be found as function of the shortening velocity of the series elastic element v^{se} as

$$l^{se} = l^{se}(f^m) \,, \qquad (2.20)$$
$$\dot{f}^m = \dot{f}^m(v^{se}) \,. \qquad (2.21)$$

From the muscle model considered, with constant pennation angle $\alpha_p \approx$ constant, it follows, according to Fig. 2.5,

$$v^{se} = v^m - \frac{v^{ce}}{\cos\alpha_p} \,, \qquad (2.22)$$
$$f^{ce} = \frac{f^m}{\cos\alpha_p} - f^{pe}(l^{ce}) \,, \qquad (2.23)$$
$$l^{ce} = \frac{l^m - l^{se}}{\cos\alpha_p} \,, \qquad (2.24)$$

where the force-length relation for the muscle parallel elastic element $f^{pe}(l^{ce})$ can be obtained, for example, in Delp [29]. In the application examples in this dissertation the force of this element is set to zero as explained further on.

Finally, from (2.18-2.24) the contraction dynamics for the muscle model results in a relation as

$$\dot{f}^m = \dot{f}^m(a, v^m, l^m, f^m) \,, \qquad (2.25)$$

which describes the muscle contraction dynamics and arises due to the elastic element in series to the CE. This dynamics depends on the muscle activation $a(t)$, and on the total muscle length and shortening velocity, $l^m(t)$ and $v^m(t)$, respectively, which are directly computed from the skeletal system generalized coordinates $\boldsymbol{y}(t)$ and their derivatives $\dot{\boldsymbol{y}}(t)$. The skeletal system dynamics described by (2.13) and the muscle contraction dynamics described by (2.25) are, therefore, coupled.

As can be observed, the models of the activation dynamics, of the force-length-velocity relation and of the force-length curve for the tendon can be scaled by a few muscle-specific parameters such as the maximal isometric muscle force f^m_{max}, the optimal muscle fiber length l^{ce}_{opt}, the pennation angle of the fibers α_p, the maximal shortening velocity v^{ce}_{max}, a parameter to adjust the force-length relation named *width*, the percentage of fast

fibers ft, the activation constant t_a, the de-activation constant t_d, the tendon slack length l_{slack}, and the tendon strain ε_o^T for $f^{ce} = f_{max}^{ce}$. These parameters can be experimentally measured and are available in the literature, what facilitates the application of these models in simulations of the musculoskeletal dynamics involving many muscles (Delp and Loan [30]). Numerical values for these parameters adopted in this work can be found in Appendix A.1.

2.2.3 Energetics

The function of the muscle and the origin of its 'fuel' is described by Wasserman et al. [120] as analogous to a machine: "Skeletal muscle may be considered to be a machine that is fueled by chemical energy of substrates derived from ingested food and stored as carbohydrates and lipids in the body". As explained in section 2.2.1, the energy required during contraction to enable cyclic interaction between the heads of the myosin myofilaments and the actin myofilaments, and to pump the Ca ions back to the sarcoplasmic reticulum, see Fig. 2.4, is supplied by the breakdown of ATP into ADP and a phosphate ion (P_i). This chemical energy is called metabolic energy and is believed to play an important role in human locomotion. For instance, Ralston [88] observed that people walk at speeds that minimize metabolic cost per unit of distance traveled. This quantity is, therefore, important to understand and study human locomotion.

Estimations of metabolic cost can be obtained experimentally using metabolic gas analysis systems (Macfarlane [67]), which measure the oxygen uptake and the carbondioxide output by the lungs. These quantities are related to the regeneration of ATP in the muscle, so that the rate of ATP consumption can be inferred (Wasserman et al. [120]). Indeed, many studies assess the energetic requirements imposed by an specific disability or assistive device by measuring the oxygen uptake rate after steady state is achieved and for aerobic regeneration of ATP.
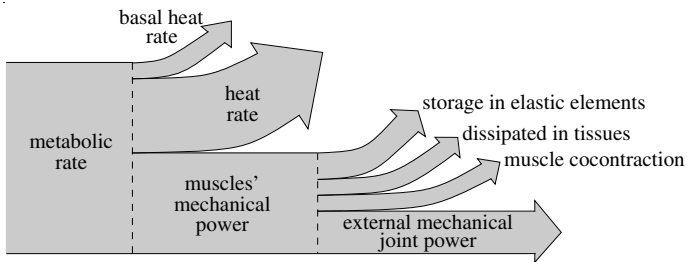
Figure 2.8: Scheme of the energy flow from the metabolic energy level.

Figure 2.8 shows an schematic illustration of the energy flow from the metabolic energy

level to the external mechanical energy in a musculoskeletal system. Note that only a reduced percentage of the metabolic energy rate is transformed into mechanical power at the joints expended to perform external mechanical work on the environment and to modify the mechanical energy of the body segments. A part of the metabolic energy rate called basal heat rate is expended to keep the tissue alive. A substantial percentage is transformed into heat (heat rate) during the contraction process at the molecular level and dissipated at the tissue surrounding the muscle fibers, while the remaining energy rate is transformed into mechanical power applied by the muscle fibers (muscles' mechanical power). From this energy rate a part is stored in elastic tissue surrounding the fibers, e.g. the tendon, a part is dissipated due to friction, a part is expended due to antagonistic muscles working against each other (cocontraction) and only the remaining energy rate is available to perform external joint mechanical power.

Estimation of Metabolic Cost

This section briefly introduces models of muscle energy expenditure available in the recent literature, pointing out some of their advantages and drawbacks. The most simple approach consists in the computation of the net joint mechanical energy. The main advantage of this method is its simplicity. However, the energy expenditure estimations obtained are poorly correlated to the metabolic cost, refer, e.g., to Martin et al. [70] and Neptune and van den Bogert [82]. The percentage of the metabolic cost converted into external mechanical joint power, see Fig. 2.8, varies strongly depending on the state of the muscle actuator. This is illustrated by the fact that metabolic energy is expended even if a muscle applies force without changing its length (isometric contraction), i.e. no external mechanical work is applied.

Minetti and Alexander [76] proposed an elegant method to estimate metabolic cost from joint net moments and angular velocities, based on properties of the underlying muscles. Their model was sufficient to identify basic principles correctly, but it was not able to predict quantitatively the locomotion behavior and the metabolic energy cost as pointed out by the authors and underlined by a strong underestimation of the metabolic cost of transport.

Therefore, in order to assess more accurate estimations of muscle energy expenditure, more detailed models are required, taking the process of force generation of each muscle involved into account. Accurate predictions of energy expenditure could be obtained by models based on the cross-bridge theory by Huxley [52] since in these models the mechanical processes are directly related to the energetic ones, see also Zahalak [131]. However, these models require many parameters whose values are uncertain. Furthermore, because of their complexity, these models would be difficult to implement in a large-scale musculoskeletal model, as explained previously in section 2.2.2.

A compromise is achieved with phenomenological muscle energy expenditure models. These models have the advantage of being used in conjunction with the widely employed Hill-type muscle models, see Fig. 2.5. Furthermore, these empirical models are able to deliver relatively accurate estimations of metabolic energy cost, although the contraction processes are not directly related to the energetic ones. Indeed, Umberger et al. [115] and Bhargava et al. [17] proposed independently phenomenological muscle energy consumption models, that were able to predict reliable characteristics of human normal walking in simulation results obtained by dynamic optimizations that minimized metabolic cost of transport. Both models are similar in their mathematical form and were based to a great extent on the work of Hatze and Buys [45].

The model proposed by Umberger and colleagues is adopted here, because it gives better predictions of energy expenditure for walking and was designed to better account for the muscle heat production during submaximal and eccentric muscle activities, conditions that are prevalent in human movement. In addition, the authors based their model entirely on mammalian or human experimental data, in opposition to other models.

This model subdivides the total metabolic cost rate $\dot{E}$ into the muscle CE work rate or power $\dot{W}$ and the muscle CE heat production rate $\dot{H}$ as $\dot{E} = \dot{H} + \dot{W}$. The heat rate is traditionally further subdivided, refer to Appendix A.1. The work rate is simply the mechanical work performed by the muscle CE,

$$\dot{W} = -f^{ce}v^{ce} \; , \tag{2.26}$$

resulting in a positive rate if v^{ce} is negative due to shortening. The complete algebraic expression for the muscle heat rate is presented in Umberger et al. [115] depending on four variables and five muscle parameters $\dot{H} = \dot{H}(u, a, v^{ce}, l^{ce}, f^m_{max}, l^{ce}_{opt}, ft, PCSA, width)$. The muscle heat rate, described by this expression, is a function of the muscle neural excitation u, the muscle activation a, the muscle CE shortening velocity v^{ce}, the muscle CE length l^{ce}, and a set of muscle-dependent parameters comprising the muscle maximal isometric force f^m_{max}, the muscle CE optimal length l^{ce}_{opt}, the muscle fiber composition in percentage of fast twitch fibers ft, the muscle physiological cross-sectional area $PCSA$, and an additional parameter introduced to adjust the force-length relation for each muscle $width$, see Gerritsen et al. [34]. The total metabolic energy cost rate for a muscle is, therefore,

$$\dot{E} = \dot{E}(u, a, v^{ce}, l^{ce}, f^{ce}, \boldsymbol{p}^m) \; , \tag{2.27}$$

where the muscle parameters are summarized in the vector $\boldsymbol{p}^m$. The expressions of Umberger et al. [115] for $\dot{E}$ are reproduced in Appendix A.1.

2.3 Musculoskeletal System Dynamics

In this section the models of the subsystems described above are integrated resulting in a model of the dynamics and energetics of the whole musculoskeletal system, which is used throughout this work to study and simulate normal and pathological gaits. The first-order activation dynamics (2.17), the first-order contraction dynamics (2.25) and the second-order skeletal system dynamics (2.13) give rise to the dynamics of the entire musculoskeletal system, see Fig. 2.9. The vectors $\boldsymbol{u}$, $\boldsymbol{a}$ and $\boldsymbol{f}^m$, are the $m \times 1$-vectors of neural excitations, muscle activations and muscle forces, respectively, of all m muscle groups considered in the model. The muscle contraction dynamics is coupled to the skeletal system dynamics because it depends on the muscle lengths in the vector $\boldsymbol{l}^m$ and on the muscle shortening velocities in the vector $\boldsymbol{v}^m$. These values are defined by the geometry of the musculoskeletal system (e.g. muscle lever arms) and are modeled as functions of the generalized coordinates $\boldsymbol{y}$ and their derivatives $\dot{\boldsymbol{y}}$ as $\boldsymbol{l}^m(\boldsymbol{y})$ and $\boldsymbol{v}^m(\boldsymbol{y}, \dot{\boldsymbol{y}})$. For instance, the measured values presented in Delp [29] for 43 lower-limb musculotendon actuators are fitted by regression equations by Menegaldo et al. [73], based on the generalized coordinates of the joints spanned by each muscle. The shortening velocity $\boldsymbol{v}^m$ can be obtained by differentiating $\boldsymbol{l}^m$. Here the expressions presented in Gerritsen et al. [34] are adopted, see Appendix A.1. As illustrated in Fig. 2.9, the phenomenological muscle energy expenditure models described in section 2.2.3 can be used to estimate the total metabolic cost rate $\dot{E}$ from the neural excitations in $\boldsymbol{u}$, the muscle activations in $\boldsymbol{a}$ and the muscle forces in $\boldsymbol{f}^m$, which again depend on $\boldsymbol{y}$ and $\dot{\boldsymbol{y}}$, too.
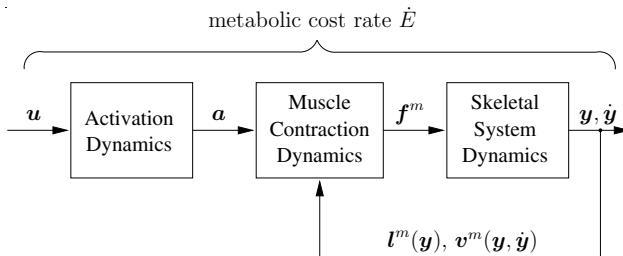
Figure 2.9: Scheme of the musculoskeletal system dynamics.

As for the dynamics of the skeletal system alone, refer to section 2.1.4 and Fig. 2.1, mainly two methods are used in biomechanics to study the dynamics of the entire musculoskeletal model depicted in Fig. 2.9, the direct dynamics and the inverse dynamics. Direct dynamics is used to study the effects on kinematics of changing muscle coordination by varying the neural excitations. As explained in section 2.1.4, this requires the numerical integration of the differential equations describing the dynamics. Standard numerical integrators often require the representation of the differential equations in the form $\dot{\boldsymbol{x}} = \dot{\boldsymbol{x}}(\boldsymbol{x}, \boldsymbol{u}, t)$, where

$\boldsymbol{u}(t)$ is the vector of controls, here represented by the neural excitations, and $\boldsymbol{x}(t)$ is the vector of state variables which, for the model of the musculoskeletal system adopted, reads as

$$\boldsymbol{x} = \begin{bmatrix} \boldsymbol{a}^T & \boldsymbol{f}^{mT} & \boldsymbol{y}^T & \dot{\boldsymbol{y}}^T \end{bmatrix}^T , \tag{2.28}$$

From the first-order activation dynamics (2.17) for all muscles considered, the first-order contraction dynamics (2.25) for all muscles considered, and the second-order skeletal system dynamics (2.13) the differential equations for the dynamics of the musculoskeletal system can be written in the state-space form as

$$\dot{\boldsymbol{x}} = \dot{\boldsymbol{x}}(\boldsymbol{x}, \boldsymbol{u}) = \begin{bmatrix} \dot{\boldsymbol{a}}(\boldsymbol{a}, \boldsymbol{u}) \\ \dot{\boldsymbol{f}}^m(\boldsymbol{a}, \boldsymbol{l}^m(\boldsymbol{y}), \boldsymbol{v}^m(\boldsymbol{y}, \dot{\boldsymbol{y}}), \boldsymbol{f}^m) \\ \dot{\boldsymbol{y}} \\ \boldsymbol{M}^{-1} \left(\boldsymbol{q}(\dot{\boldsymbol{f}}^m, \boldsymbol{y}, \dot{\boldsymbol{y}}) - \boldsymbol{k}(\boldsymbol{y}, \dot{\boldsymbol{y}}) \right) \end{bmatrix} . \tag{2.29}$$

Also here it is necessary to specify the initial state of the system $\boldsymbol{x}_0 = \boldsymbol{x}(t_0)$ at the initial time $t = t_0$. Note that the number of differential equations in (2.29) is $2m + 2f$. Musculoskeletal models of the body during walking typically have 10 to 50 degrees of freedom actuated by 10 to 50 muscle groups. This illustrates the high dimension of (2.29), what leads to a high computational cost to simulate gait, which turns prohibitive when optimization procedures are involved. An alternative to solve this problem using the less expensive inverse dynamics is proposed and exploited in chapter 5.

As discussed in section 2.1.4, the inversion of the skeletal system dynamics to estimate net joint moments from measured kinematics obtained in gait analysis laboratories is widely used in biomechanics mainly due to its relative simplicity and computational efficiency. The further computation of muscle forces from the moments at the joints is less straightforward, since there are many muscles spanning each joint and, therefore, an infinite number of muscle forces that cause the same joint moments. To solve the resulting so-called muscle "force-sharing problem" and find a unique solution for the muscle forces, an optimization problem is formulated and it is assumed that the central nervous system optimizes some underlying performance criterion. The traditional approach can lead to unphysiological solutions for the muscle forces, because it does not consider the activation and contraction dynamics. In chapter 4 this problem is addressed and alternative approaches to compute physiologically correct muscle forces are proposed.

2.4   Phases of Human Gait

The human walking is bipedal. While it seems a natural and simple task bipedal walking requires a complex neural control and is plagued by an implicit instability due to its

inverted pendulum nature. It is well accepted that the muscles are recruited in such a way as to provide an efficient locomotion in terms of energy requirements per unit of distance traveled, refer e.g. to Ralston [88]. Although a considerable variability in the walking pattern between different individuals (inter-subject variability) and even for the same individual in a stride-to-stride basis (intra-subject variability) exists, there are events and general patterns that are observable for all, see Inman et al. [54].
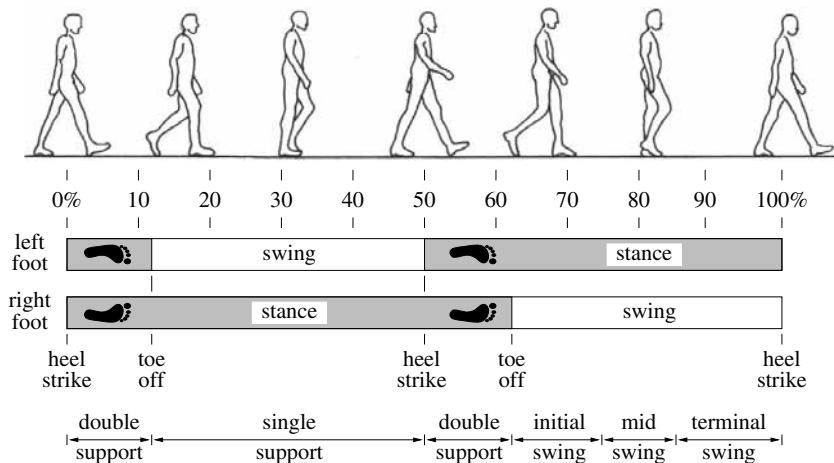
Figure 2.10: Phases of human gait.

Walking is a nearly periodic motion with patterns that repeat in every walking cycle. The description of a single cycle is, therefore, sufficient to characterize walking. Normal walking is nearly symmetric, being the motion of the limbs in one side of the body equal to the ones in the opposite side but 180° out of phase. In order to facilitate the study of the human gait it is common to describe the cycle in terms of percentage. The beginning of the cycle (0%) is defined as occurring at heel strike of the right foot (HSr), which is the instant the right foot touches the ground, and ends at the second heel strike of the right foot (100%), see Fig. 2.10. This convention is used throughout this dissertation, except in chapter 3, where, due to experimental constraints, the beginning of the cycle occurs at toe off (TO), which is the instant the foot just leaves the ground.

The cycle is divided into phases depending on events as shown schematically in Fig. 2.10. The stance phase designates the interval of time in which the foot is in contact with the ground and takes about 62% of the gait cycle period at normal walking velocities according to Sutherland et al. [109]. It starts with the heel strike (HS) and ends with the toe off (TO). In the remaining time the foot is in the air not contacting the ground. This phase is named swing phase and takes approximately 38% of the gait period. The swing

phase starts at toe off (TO), and ends at heel strike (HS).

A feature of the walking in opposition to running is the existence of double support phases, in which both feet are in contact with the ground, see Fig. 2.10. In running the double support phase disappears giving place to a brief phase in which neither foot is in contact with the ground. The double support phase begins with heel strike and ends with toe off of the opposite foot. The gait is further subdivided into phases. The names of some of these phases and the events that delimite them are shown in Fig. 2.10 according to Sutherland et al. [109].

Chapter 3

Experiments on Mechanically Disturbed Walking

The aim of the study described in this chapter is to investigate the influence of mechanical disturbances to the lower limb of a person on the kinematics, dynamics and energetics of the gait. This analysis extends the understanding of the factors determining the observed variations in the gait caused by the use of a lower limb prosthetic or orthotic device. Understanding how these factors influence the kinematics, dynamics and energetics of the gait will lead finally to the development of better prostheses and orthoses in terms of energy expenditure, comfort and aesthetics.

Although direct measurements with amputees or persons presenting gait anomalies could be performed, in experiments with these subject groups it is difficult to isolate the different factors influencing the gait. Moreover, as pointed out by Royer and Martin [92], these populations have other confounding factors such as muscular deficits and instabilities that influence the experimental outcomes. In order to overcome these drawbacks, the experiments are performed with subjects presenting a normal gait. The mass-distribution and joint constraints of the lower limb are then artificially manipulated in a controlled way. This procedure permits an isolated analysis of each one of the considered disturbances and the direct comparison with the undisturbed or normal gait. The experiments were designed in such way as to take into account typical deviations of the mechanical properties of the lower limb that arise by wearing orthotic and prosthetic devices. These deviations are of two basic types:

- alterations of the inertial properties of the lower limb segments, and

- loss of mobility of the lower limb joints.

There are clear evidences that the modification of the inertial properties of the lower limb segments or the introduction of restrictions to the joints, as the ones typically caused by

the use of a prosthesis or orthosis, can dramatically change the energetic efficiency and the aesthetics of the gait. The physiological energy expenditure per unit of distance traveled or metabolic cost of transport, respectively, is a suitable measure of the gait efficiency to quantitatively assess the burden caused by gait disability. In order to exemplify the magnitude of the energetic variations imposed by selected disabilities, some studies that compare the normal walking with the disabled one are briefly described in the following. The metabolic cost in these studies is found by measurements of the oxygen consumption.

Hanada and Kerrigan [38] observed an increase of about 20% in the metabolic cost of transport when the knee of healthy subjects is immobilized. Hsu et al. [51] showed that the energy expenditure per meter walked is significantly higher for transtibial amputees with respect to subjects presenting a nonpathological gait, for all five different walking velocities and different prosthetic foot types tested. Jaegers et al. [55] found a much higher metabolic cost of transport in transfemoral amputees compared to normal subjects, up to 30%. The extensive review of Waters and Mulroy [121] shows clearly the burden imposed by mechanical disturbances added to the lower limb and the significantly higher energy expenditure of pathological gait in comparison to the normal one. Among many other results, they report a 30% increase in the energy expenditure rate when 2 kg loads are placed on each foot and a 20% higher rate of O_2 uptake of transtibial amputees in comparison to non-amputees.

Another interesting note in the paper of Waters and Mulroy [121] refers to the fact that walking speed, rate of O_2 consumption and metabolic cost of transport were very similar between traumatic transtibial amputees and patients with an ankle joint fusion indicating that these two groups of patients have a similar biomechanical penalty, namely the loss of the ankle joint mobility. This latter observation shows the potential of artificially simulating a biomechanical penalty to predict the effect of "real" disabilities, what is the approach adopted here.

The higher metabolic cost of the pathological gait can be significantly reduced by means of the development of improved prostheses and orthoses and by the adoption of other compensation measures. Indeed, Abdulhadi et al. [1] reports a reduction of 7% in the metabolic cost of transport of subjects with a unilateral knee immobilization when a half-inch shoe-lift is added to the sole of the contralateral foot. Schmalz et al. [99] observed that transfemoral amputees wearing an electronically controlled hydraulic knee joint expended less energy than amputees wearing conventional hydraulic transtibial prostheses. These results show that significant improvement in the gait quality can be achieved by improvements in the design of assistive devices.

In order to analyze the effects of the introduction of different constraints to the lower limb, the net joint moments of a mechanical model of the body are computed by inverse dynamics for each one of the experiments designed. The results are then compared to the reference normal gait. This chapter describes all the steps required to achieve estimations

of the net moments applied at the joints, from the capture of the motion by means
of markers attached to the body and the measurements of the ground reaction forces,
through the processing of the raw data, the reconstruction of the body segments' pose,
the adoption of a mechanical model of the body and the computation of its anthropometric
parameters, till the solution of the equations of motion for the moments applied at the
joints.

Section 3.1 explains the experimental design, the experimental setup and equipment, and
the processing of the measured raw data. The experiments were performed in the labo-
ratory of the Institut fuer Sportwissenschaft of the Universitaet Stuttgart. In section 3.2
the adopted kinematical model of the body is presented and in section 3.3 techniques to
reconstruct the body segments positions and orientations and the generalized coordinates
of the model, from the 3-D coordinates of the markers are explained and implemented. In
the latter section the results obtained for the reconstruction are presented and discussed.
In section 3.4 the net moments applied at the joints are computed by inverse dynamics
for all the different experiments performed with both subjects. This section contains a
discussion of the results obtained, too.

3.1   Experiments

This section contains an explanation of the experimental design, describes the equipment
employed to measure the kinematics and ground reaction forces during normal and dis-
turbed walking, discusses the processing of the measured raw data, and presents some of
the results for the processed data.

3.1.1   Experimental Design

The experiments are designed to account for the typical deviations of the lower limb
properties by the use of a lower limb prosthesis or orthosis, namely changes in the mobility
of the joints and in the inertial properties of the segments. In order to simulate these
deviations, the following experiments are designed:

1. subjects walk in their comfortable walking speed (CWS) wearing their usual shoes;

2. subjects walk in their CWS with a unilateral ankle weight;

3. subjects walk in their CWS with a unilateral knee immobilization;

4. subjects walk in their CWS with a unilateral ankle immobilization; and

5. subjects walk in their CWS wearing a ski boot on one of the feet.

Experiments 1 serve as a reference for the normal gait to which the results of the other experiments are compared. In experiments 2 the effects of increasing mass and moment of inertia of the lower limb are simulated. Experiments 3 and 4 are expected to deliver clues on the effects of the loss of mobility of the knee and ankle joints, respectively. Finally, experiments 5 are intended to simulate the net effect of both, loss of mobility of the ankle joint and increase of the lower limb mass and moments of inertia, what occurs for certain orthopedic shoes or in the case of using a transtibial prosthesis. All the experiments are performed in the subject's comfortable walking speed (CWS) for the specific experiment. All the constraints are imposed unilaterally, i.e. to one lower limb only. The scenarios are designed to permit a separate analysis of each one of the main restrictions imposed to the lower limb by wearing assistive devices.

During the experiments the arms of the subjects are kept crossed over their chests. This measure simplifies the analysis and contributes to its straightforwardness by restricting the relatively complex movement of the arms and reducing the degrees of freedom of the mechanical model of the body. Studies showed that the influence of the arm movement during walking is marginal with respect to energy consumption, refer e.g. to Hanada and Kerrigan [38], where the restriction of the arm movement is shown to cause no significant difference in the amount of metabolic cost of transport during walking. On the other hand, Gruber and Ludwig [36] show small influences of the movement of the arms on the ground reaction forces and on the total vertical angular momentum of the body, which, however, can be neglected when compared to the major constraints imposed to the lower limb in this study.

3.1.2   Equipment

During the experiments the kinematics of the walking as well as the reaction forces acting on the right foot during a complete cycle are measured. The experiments were performed in the Laboratory of the Institut fuer Sportwissenschaft of the Universitaet Stuttgart, where a 3-D motion capture system of the company Reality Motion Systems GmbH is installed. A picture of the Laboratory is shown in Fig. 3.1. The photo shows an elevated stage made of wood, on which the subjects walk. A force plate is embedded in approximately the middle of the elevated stage in such a way as no step arises. Four digital cameras are placed at the upper corners of the room directed to a region in the space situated over the force plate in a height of circa one meter from the stage, as schematically depicted in Fig. 3.2.

The ground reaction forces are measured by a KISTLER force plate type 9281B with dimensions $400 \times 600 \ mm^2$ and a sample frequency of $1000 \ Hz$. The 8 piezoelectric sensors placed in the four corners deliver information to compute the resultant force and moments acting on the origin of the coordinate system, situated in the middle of the upper

Figure 3.1: Laboratory of the Institut fuer Sportwissenschaft of the University of Stuttgart, where the experiments were performed.
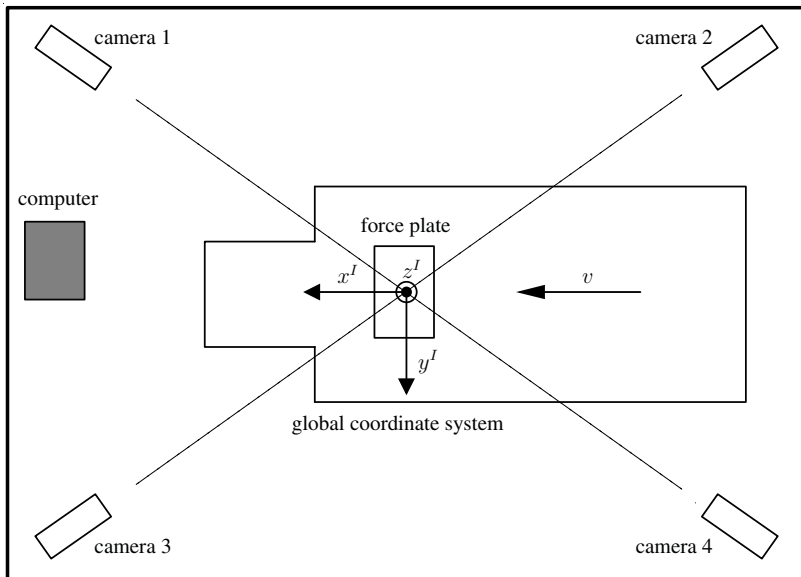
Figure 3.2: Upper view sketch of the Laboratory.

surface of the force plate as shown in Fig. 3.2. If the pressure distribution on the force plate is purely compressive, which is the case during walking, the corresponding point of application of the resultant force on the surface and a perpendicular moment with respect to this point, called free moment, can be computed from the resultant force and moment on the origin. These set of information together with the components of the resultant force describe the load being applied on the force plate by the foot.

The four cameras (Model 1394 - Basler AG) are digital with a resolution of 640×480 pixels and a sample frequency of up to 100 Hz. The data from the cameras and the force plate is received and synchronized by a dedicated hardware installed in a computer with a 2.6 GHz INTEL XEON Processor. The experiment and data managing is assisted by the specialized software SIMI°Motion (Reality Motion Systems GmbH).

The spacial position and orientation of the body segments can be reconstructed through the 3-D positions of markers attached to them. This procedure will be explained further on. The markers produced for the experiment are spheric of diameter 30 mm and are covered by a rectroreflective material, i.e. capable of reflecting light in the same direction from which it comes. This property of the markers is exploited to significantly increase their contrast relative to their surroundings on the images by placing light sources in the adjacencies of the cameras. For this purpose, four spotlights with halogen lamps of 1000 W mounted on stands with adjustable heights are used. Figure 3.3 shows pictures of one of the subjects with the rectroreflective spheric markers attached to his body. The markers are fixed to the skin of the subjects by double-faced adhesive tapes.
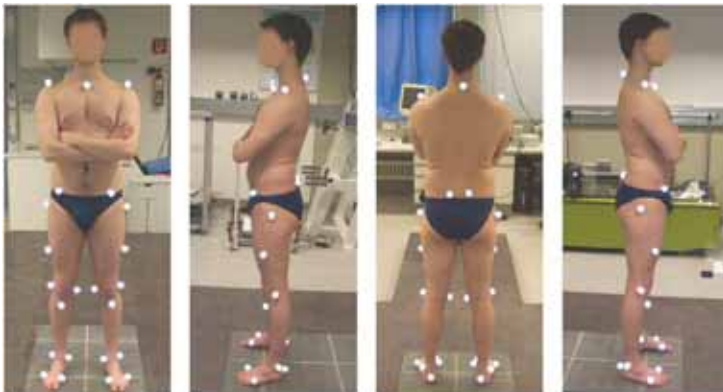
Figure 3.3: Markers attached to the skin of subject 2.

The software SIMI°Motion is used to manually digitize the position of the markers on the images of the four cameras and to compute their 3-D coordinates in the laboratory

global coordinate system.This software is utilized to assist on the management of the experiments and of the data, too.

As explained in section 3.1.1, mechanical disturbances are introduced to constrain the lower limb movements. For the knee immobilization a knee orthosis (Genu Immobil Vario 8065 - Otto Bock Health Care GmbH) is used, which is fixed to the lower limb by Velcro fasteners. A therapeutic pair of shoes (Vario-Stabil - Orthotech GmbH) for treating the rupture of the Achilles tendon is used to immobilize the right ankle joint. The weight attached to the ankle is implemented with an adjustable ankle weight band (Active) fixed to the shank just above the ankle joint by Velcro fasteners. The ski boot as well as the shoes were brought by the subjects. Figure 3.4 shows pictures of one of the subjects wearing the different mechanical disturbances, whose masses and moments of inertia are listed in the Tabs. A.2 and A.3 of Appendix A.2.

Figure 3.4: Mechanical disturbances on subject 1 from left to right: undisturbed, weight attached to the right ankle, right knee immobilization, right ankle immobilization, and ski boot on right foot.

3.1.3 Experimental Setup

Two subjects presenting no gait anomaly were recruited. The anthropometric parameters of both subjects, partially estimated by means of anthropometric tables and regression equations, as explained further on, are presented in Tabs. A.4 and A.5 of Appendix A.3.

The motion capture system was calibrated by means of a 3-D structure with approximate dimensions $1.5 \times 1.5 \times 2 \; m$ positioned on the force plate and containing 14 nodes, whose positions in the space were known with respect to a global coordinate frame. After the calibration the motion capture system is able to reconstruct the 3-D position of points in space from their 2-D coordinates in the camera frames, provided that the positions and orientations of the cameras are not changed after the calibration.

After a series of preparation and testing sessions, each subject was asked to come in a different day for the final experiments. The subjects were asked to wear bathing suits, so that all the markers could be positioned directly on the skin. The markers were placed before the beginning of the trials in predefined anatomical and technical landmarks, following guidelines given in Cappozzo et al. [21], see Appendix A.4 for details about the markers' positioning and designation. The positions of some few markers were slightly modified for each experiment to accommodate for the mechanical disturbances, see Fig. 3.4.

Subsequently to the placement of the spotlights near the cameras, in such a way as to optimize the reflection of light from the markers to the cameras, and to the testing of the equipments, the following experimental procedure, which was repeated for each different disturbance, was initiated:

1. subject wear the disturbance;

2. markers are placed on the skin of the subjects or position of markers is changed to conform to new disturbance;

3. subject walk with the disturbance for some minutes to get used to it;

4. subject stands on the force plate so that a reference position for the body can be captured and his total body mass can be measured by the force plate;

5. subjects stand in the beginning of the platform and walk in the direction depicted in Fig. 3.2 in a comfortable self-selected velocity;

6. the trial is repeated beginning from different initial positions until fully incidence of the right foot upon the force plate is achieved;

7. the same procedure is also performed for fully incidence of the left foot upon the force plate;

8. after saving the measured data, the same procedure is repeated for the experiments with the next disturbance.

The measured force data and the synchronous videos are saved for further processing.

3.1.4   Processing of Experimental Data

This section describes the computation and conditioning of the 3-D coordinates of the markers attached to the body and the filtering of the measured force data obtained by the force plate. The 3-D coordinates of markers can be computed from two or more pairs of 2-D image coordinates of the cameras, provided that the system is previously calibrated.

The 2-D image coordinates are obtained by manually digitizing all the frames of the four videos for all markers in an environment provided by the software SIMI°Motion. The same procedure is performed for the reference postures of the subjects for each different experiment. The software also provides the possibility of performing interpolation of the image coordinates when markers are not visible for a short period of time due to occlusion by a body segment. Finally the raw 3-D coordinates of the markers are computed from the 2-D image coordinates using the calibration performed as explained in section 3.1.3.

If the marker is not visible from three or four cameras, i.e. less than two pairs of image coordinates are available, the 3-D coordinates of this marker cannot be computed. In this case the lacking data in the time histories of the marker's 3-D coordinates can be estimated by interpolation or extrapolation. This operations are, however, only meaningful for short periods of lacking data. If the interpolation or extrapolation of the data is not possible the marker is simply ignored in the pose reconstruction of the segment in the corresponding time steps. Ignoring a limited number of markers is admissible because of the use of a redundant number of markers per segment, as explained in section 3.3.

For the computation of the position and orientation of the body segments from the positions of the markers attached to the skin accurate marker positions are required. This process is subject to many sources of errors, which are divided in two major groups: 1) the ones caused by errors in the measurements of the position of the markers, and 2) the ones due to the movement of the skin with respect to the underlying bone.

The first group of errors are caused by an erroneous determination of the position of the markers in space. This group contains the errors caused by an imperfect calibration of the system, for instance due to image distortions, the ones caused by the digitizing of the image, because of the limited resolution of the digital cameras (640×480 pixels), and the ones caused by human errors in the manual digitizing of the markers. The latter two errors arise from the fact that the markers with diameter of 30 mm are seen in the images as groups of a few bright pixels, what hinder the exact location of their centroids during the digitizing process.

The second group contains the errors caused by the movement of the skin and consequently of the markers with respect to the underlying bones, the so called *skin artefacts*. The errors due to the *skin artefacts* generally overwhelm the ones of the first group and can assume values in the range 10-30 mm during walking, see Cappello et al. [20] for a quantitative study of the effects of this artefact.

The above mentioned errors might cause substantial innacuracies in the determination of the position and orientation of the segments and should, therefore, be minimized. Among the techniques to reduce these errors, three are of great importance: 1) filtering of the 3-D coordinates of the markers, as explained in the following; 2) adequate positioning and distribution of the markers to prevent propagation of errors and to avoid the occurrence

of ill-determined rotations (guidelines provided in Cappello et al. [20] are used); and 3) exploitation of the excess of information in terms of marker's coordinates by means of the implementation of optimization techniques, as explained in section 3.3.

The errors due to the *skin artefacts* and the digitizing procedure can be reduced by smoothing the 3-D coordinates by means of discrete filters. Similarly, the force plate measurements are superposed by a high frequency noise due to the sensitive piezoelectric sensors of the force plate and to the digitizing of the measured analog signal. Since these noise and disturbances are to a great extent of higher frequencies than the ones of the phenomena measured, they can be effectively damped by the use of low-pass filters. The choice of a proper cut-frequency f_c for the low-pass filter is of great importance. On the one hand, a too high cut-frequency leads to a weak damping of the noise. On the other hand, a too low cut-frequency causes the loss of information about the phenomena measured. Winter [123] observes that for normal walking 97.7% of the signal power is contained in frequencies below 6 Hz, what justifies the use of cut-frequencies of about this value. Therefore, a cut-frequency of 6 Hz to filter all the experimental data is adopted.

Another important feature of a filter is the phase shift it generates in the output signal, which is frequency-dependent. This phase lag may cause severe distortions of the signal mainly in the frequency range about the cut-frequency and should, therefore, be avoided. In order to cancel this distortion, the data can be filtered a second time in the reverse direction of time leading to a net-zero lag filter.

In this work a second-order discrete Butterworth filter is adopted and the procedure of filtering the data a second time in the reverse direction of time is implemented. The resulting fourth-order filter has a net cut-frequency of 6 Hz and causes no phase lag in the output signal. Note that for achieving a net cut-frequency of 6 Hz for the zero-phase-lag filter the original Butterworth filter has a cut-frequency of $6Hz/0.802 = 7.48\ Hz$. Refer to Ackermann and Gros [2] for further details about the filter adopted.

3.1.5 Processed Ground Forces and Marker Trajectories

In this section some results for the filtered trajectories of the markers and the filtered measured ground reaction forces are presented. The complete set of results for both subjects and all experiments can be found in Ackermann and Gros [2]. Figure 3.5 shows the filtered 3-D trajectories of selected markers, which are used to reconstruct the position and orientation of the body segments. Figures 3.6 and 3.7 show, respectively, the vertical and x-axis component of the measured and filtered ground reaction forces for both subjects and all experiments acting on the right and left feet.
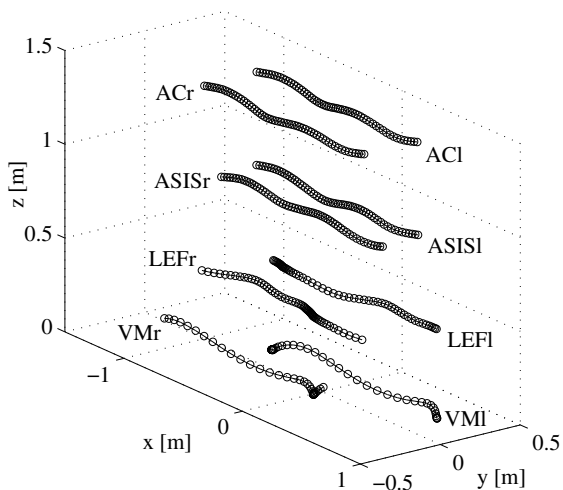
Figure 3.5: Filtered 3-D trajectories of selected markers for barefooted, normal walking of subject 1. Refer to Appendix A.4 for marker positions and designations.
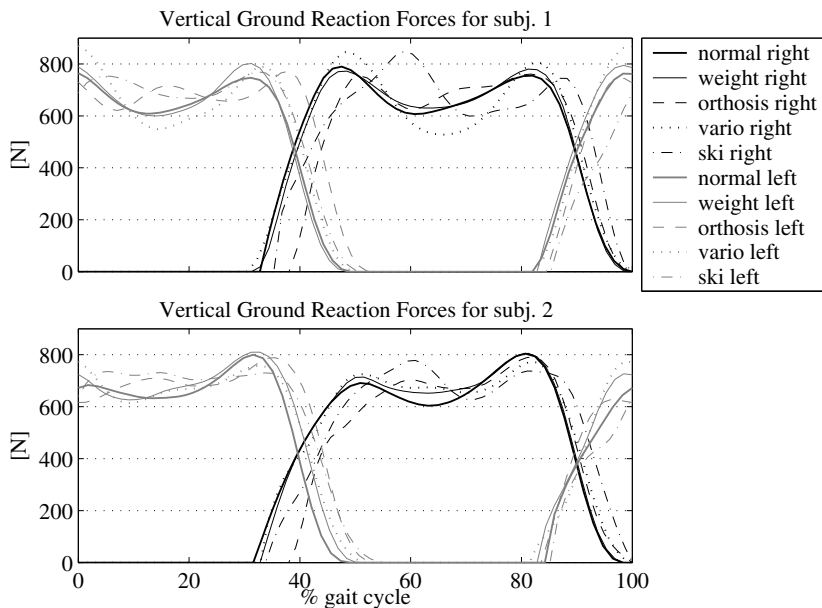
Figure 3.6: Filtered measured vertical ground reaction forces for both subjects.
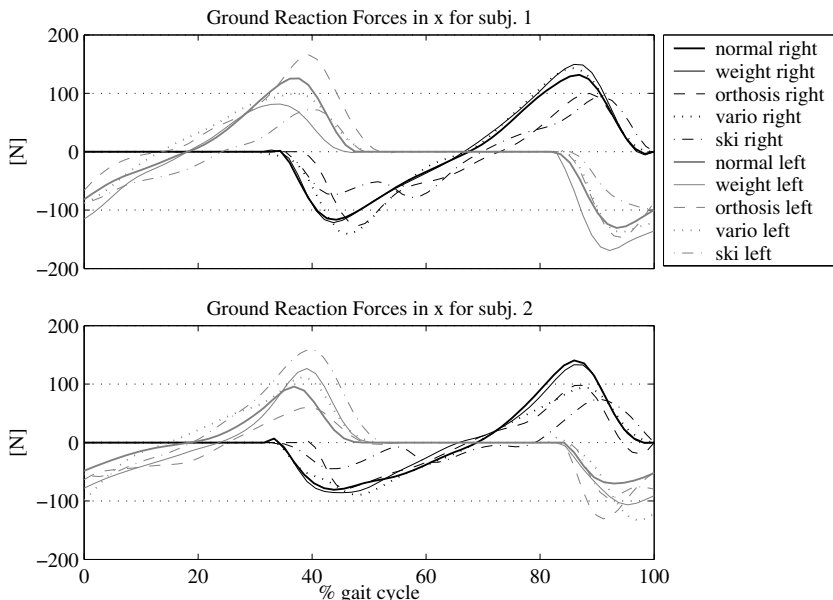
Figure 3.7: Filtered measured ground reaction forces in x^I for both subjects.

3.2 Mechanical Model of the Body Adopted

The human musculoskeletal system, responsible for the locomotion, is composed by about 200 bones and more than 300 muscles. The development of models of such a complex system is a nontrivial task that involves the traditional compromise between straightforwardness and accuracy. On the one hand, the models should be complex enough to deliver accurate estimations of the phenomena studied. On the other hand, the models should be simple enough to keep the problem tractable and the results and analysis straightforward. In the following section the mechanical model of the skeletal system adopted is detailed and justified. In section 3.2.2, the procedures adopted to estimate the body segments anthropometric parameters are presented and discussed.

3.2.1 Kinematical Model

The human body is here modeled as a multibody system composed by rigid bodies linked by ideal joints, approach which is widely used to analyze the human normal and pathological gaits by means of inverse dynamics, see, for example, Gruber [35], Lutzenberger [66] and da Silva [26]. Figure 3.8 shows a schematic drawing of the model adopted. Numerical

values adopted for the geometrical parameters in Fig. 3.8 are listed in Tabs. A.4 and A.5 of Appendix A.3.
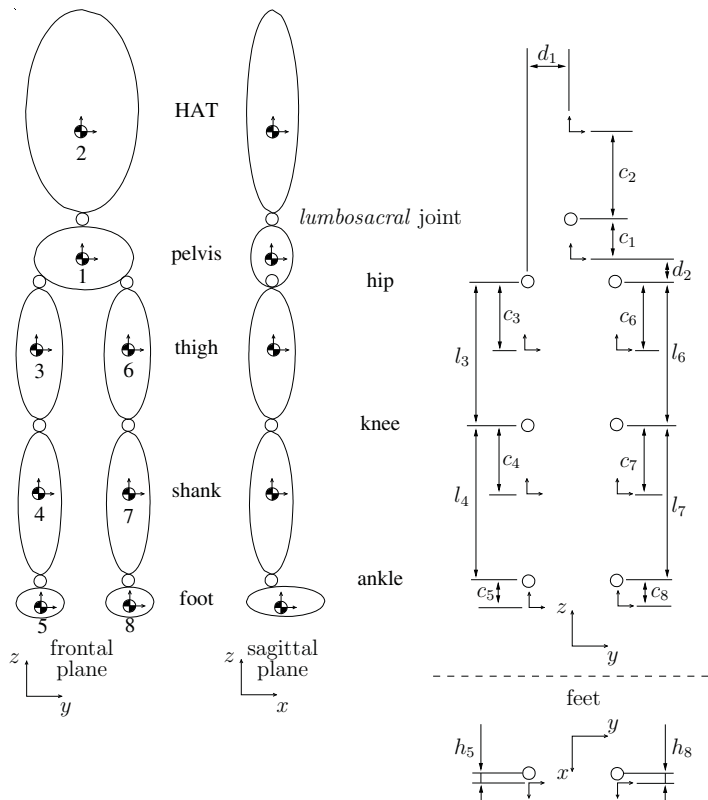
Figure 3.8: Mechanical model of the human body on the right hand side, and some geometrical anthropometric parameters on the right hand side.

The use of rigid bodies to model the body segments is reasonable for big movements, which are not subject to strong impacts, as the movements occurring during normal walking. In this case, the effect of the movement of the soft tissue surrounding the bones is small. The rigid bodies are the two feet, the two shanks, the two thighs, the pelvis and the HAT, as shown on the left hand side of Fig. 3.8. The latter contains the head, the arms crossed over the chest and the trunk without the pelvis in a single rigid body, since the movements among this body segments during walking are reduced.

The real joints arise from complex surface contacts, presenting translation and moving

instantaneous center of rotation between the adjacent segments. However, for big movements, like the ones occurring during walking, the joints can be properly modeled as ideal, spherical joints that allow no translation and feature a fixed center of rotation with acceptable errors. Some specificities of each body joint considered are discussed in the following.

Some segmentation of the trunk is important to represent the motion along the vertebra and decouple the movement of the pelvis from the rest of the trunk, as explained in Yamaguchi [128]. In order to model the net flexion-extension, lateral flexion and axial rotation allowed by the spine, a 3-degree-of-freedom joint is positioned in the lumbar region between the vertebrae L3 and L4, where the range of motion in flexion-extension is specially high, see Zatsiorsky [135] and Lutzenberger [66]. This joint between the pelvis and the trunk is referred to as *lumbosacral* joint. The location of this joint in the model is achieved with the help of the anthropometric tables given in de Leva [28].

The hip joint is well modeled by a 3-degree-of-freedom ball and socket joint permitting movements of flexion-extension, abduction-adduction and internal-external rotation of the thigh with respect to the pelvis. The position of the center of rotation of the hip joint is determined using a relation proposed by Bell et al. [12] and [13] from the positions of the markers ASIS.

The knee joint motion can be characterized by a flexion-extension motion with a varying instantaneous center of rotation, presenting limited, flexion-dependent ranges of motion in abduction-adduction and in axial rotation, see, e.g., Zatsiorsky [135]. To account for the variability in the natural abduction-adduction position for different subjects (varus-valgus position of the knee) and the limited but existent range of external and internal rotation, the knee joint is modeled as a ball and socket joint, what is reasonable for big movements where the influence of the varying position of the instantaneous center of rotation is small. The knee joint center is assumed to be the midpoint between the femoral epicondyles, whose positions are estimated by the external markers LEF and MEF (Zatsiorsky [135]).

The ankle joint complex is a combination of two joints, the talocrural and the subtalar joints, refer, e.g., to Zatsiorsky [135]. These two joints are basically hinge joints, whose axes of rotation are oblique to the anatomical axes. Because of the difficulty in locating these axes by means of external markers, the ankle joint is modeled as a 3-degree-of-freedom spherical joint as well. It should be noted, however, that the three successive rotations that describe the rotation of the foot with respect to the shank are dependent, since two coordinates would be enough to describe the movement. The position of the ankle joint center in the model is determined from the external markers lateral and medial malleoli (MM and LM) using the anthropometric tables proposed in de Leva [28].

The complete model adopted contains, therefore, 8 bodies (HAT, pelvis, two thighs, two shanks and two feet), and 27 degreee of freedom (6 DoFs of the pelvis + 7 joints × 3 DoFs).

Thus, the kinematics of the model is described by $f = 27$ generalized coordinates, that are chosen as follows. The position of the pelvis is described by the position of its center of mass in the global coordinate system, $x_{I,1}$, $y_{I,1}$ and $z_{I,1}$. The rotation of the pelvis is described by three Cardan angles, $\alpha_{I,1}$, $\beta_{I,1}$ and $\gamma_{I,1}$, defined as finite, successive rotations about the axes x, y and z with respect to the global coordinate system. The positions of all the other segments are defined by their relative rotation to the immediately more proximal segment, allowed by the spherical joints that connect the segments. The relative rotation is described by Cardan angles, $\beta_{i,j}$, $\alpha_{i,j}$ and $\gamma_{i,j}$, defined as finite successive rotations about the axes y, x and z, where the index i, j refers to the rotation of segment j with respect to segment i. The segments are numbered as shown in Fig. 3.8 and the global coordinate frame is denoted by the index I. This sequence of rotations is anatomically meaningful and coincides with the *Joint Rotation Convention* (Zatsiorky [135]). For this sequence, the three Cardan angles denote, respectively, flexion-extension, abduction-adduction and internal-external rotation. The vector of generalized coordinates that will be used to derive the equations of motion reads as

$$\boldsymbol{y} = [x_{I,1}\ y_{I,1}\ z_{I,1}\ \alpha_{I,1}\ \beta_{I,1}\ \gamma_{I,1}\ \alpha_{1,2}\ \beta_{1,2}\ \gamma_{1,2}\ \alpha_{1,3}\ \beta_{1,3}\ \gamma_{1,3}\ \alpha_{3,4}\ \beta_{3,4}\ \gamma_{3,4}$$
$$\alpha_{4,5}\ \beta_{4,5}\ \gamma_{4,5}\ \alpha_{1,6}\ \beta_{1,6}\ \gamma_{1,6}\ \alpha_{6,7}\ \beta_{6,7}\ \gamma_{6,7}\ \alpha_{7,8}\ \beta_{7,8}\ \gamma_{7,8}]^T . \tag{3.1}$$

3.2.2 Anthropometric Parameters

An important step to the later computation of the moments at the joints by means of the equations of motion is not only the determination of the topology of the model, as shown in Fig. 3.8, but also the identification of the inertial properties of the segments of the subjects: mass, moments of inertia and locations of the center of masses.

Although there is an extensive literature about this topic, data provided differ considerably among authors (Dempster [31], Chandler et al. [22], Zatsiorsky et al. [94], de Leva [28]). The differences can achieve up to 30% in some cases, see Volle [119] for a comparison, and occur mainly due to the different segmentations of the body used (Zatsiorsky [136]). Other sources of errors are the different methods used to measure the body segment parameters and the considerable variability among populations that differ for example in gender, age, race or body type (Shan and Bohn [100], Durkin and Dowling [32]).

The relations presented in de Leva [28] are adopted, which are based on data for 100 young, male subjects measured by means of a gamma-ray scanning technique by Zatsiorky et al. [94]. The work of de Leva [28] adjusts the data reported in Zatsiorsky et al. [94] to refer them to the joint centers so that they can be used for body models, whose segmentation is based on the position of the joint centers. As mentioned previously, the lengths of the thigh and shanks are estimated directly from the positions of anatomical markers. All the other lengths shown in Fig. 3.8, including the positions of the center of masses, and the masses and moments of inertia of the segments, are estimated using the

anthropometric tables reported in de Leva [28]. Numerical values for the body segment inertial parameters of both subjects computed as explained are presented in Tabs. A.4 and A.5 of Appendix A.3.

3.3   Body Pose Reconstruction

This section deals with the problem of determining the position and orientation of the body segments for each instant of time from the 3-D positions of markers attached to them. Determining the positions and orientation of the body segments permits the computation of the time history of the vector of generalized coordinates (3.1), which is used in section 3.4 to compute the moments at the joints.

The position and orientation of a body segment is characterized by the position of the origin and the orientation of a coordinate frame embedded in the underlying bone in the global coordinate frame. Here two kinds of bone-embedded coordinate systems are used, both having its origin coinciding with the center of mass of the segment and defined in the reference posture, in which the subjects are standing on the force plate as shown in Fig. 3.3. The orientation of one frame, referred to as reference frame, is defined as the one in which its axes are aligned with the corresponding axes of the global coordinate frame in the reference posture. The orientation of the other orthogonal frame, referred to as anatomical frame, is defined by the position of anatomical bony landmarks as explained in Cappozzo et al. [21].

The use of anatomical frames favors the comparison of the results with literature sources using the same anatomical frames to describe orientation and joint moments. However, the orientation of the anatomical frame is very sensitive to a precise location of the anatomical bony landmarks, what is not easy using markers attached to the skin. On the other hand, the orientation of the reference frames is straightforward and independent of the markers position. However, it is dependent on the position of the segments on the reference posture and therefore can vary slightly from experiment to experiment. Since both frames are defined in the reference posture frame and the relative orientation does not change over the trial, it is possible to convert the results from one frame to the other.

The 6 DoFs of a rigid body can be determined from the 3-D coordinates of at least three markers attached to it. However, the marker clusters of the segments deform during the movement due to the *skin artefacts* and the measurement errors explained in section 3.1.4, what violates the assumption of rigid segments. Optimization techniques are used to handle this deformation of the marker clusters and to reduce the errors in the bone pose reconstruction. In the following section the optimization technique adopted is described. In section 3.3.2 other alternative optimization schemes are briefly presented.

3.3.1 Local Optimization

This section describes the technique adopted to reconstruct the position and orientation of the body segment i, i.e. to determine the rotation matrix $\boldsymbol{S}_i$ of the bone-embedded frame and the position of the origin of the segment $\boldsymbol{r}_i$ for each time step considered. The method is based on a least squares pose estimator, i.e. the position and rotation of the original or reference configuration of the cluster of markers is fitted to the current configuration of the markers in a least squares sense.

Least squares pose estimator

In the case of a perfectly rigid body segment, the position of the marker j in the global frame is described by the position vector

$$\boldsymbol{r}_{Mj} = \boldsymbol{S}_i\,\boldsymbol{r}^i_{OMj} + \boldsymbol{r}_{Oi}, \tag{3.2}$$

where $\boldsymbol{S}_i$ is the rotation matrix of a body-embedded frame, $\boldsymbol{r}_{Oi}$ is the position vector of the origin of this frame, and $\boldsymbol{r}^i_{OMj}$ is the reference position vector of marker j in the body-embedded coordinate system, see Fig. 3.9. Because the segments are not perfectly rigid and the cluster of markers deforms due to the *skin artefacts* and the measurement errors, a rest vector $\boldsymbol{r}_{Rj}$ is subtracted from the left hand side of (3.2) yielding

$$\boldsymbol{r}_{Mj} = \boldsymbol{S}_i\,\boldsymbol{r}^i_{OMj} + \boldsymbol{r}_{Oi} - \boldsymbol{r}_{Rj}. \tag{3.3}$$

The extent of the deviation of the current marker position to the corresponding one in the reference configuration is given by the Euclidean norm of the rest vector

$$||\boldsymbol{r}_{Rj}|| = \sqrt{\boldsymbol{r}^T_{Rj}\boldsymbol{r}_{Rj}}. \tag{3.4}$$

Now, the rotation matrix $\boldsymbol{S}_i$ and the position vector $\boldsymbol{r}_{Oi}$ are searched that optimize the position and orientation of the reference configuration with respect to the current configuration of the markers, in a least squares sense, this means to minimize the sum of the norms of all the rest vectors. An interesting analogy to this problem can be formulated as minimizing the elastic potential energy stored in linear springs connecting the markers of the current and reference configurations, as shown in Fig. 3.9. With (3.3) and (3.4) the optimization problem is expressed as

$$\min\left\{ \frac{1}{n_i}\sum_{j=1}^{n_i} ||\boldsymbol{r}_{Rj}||^2 \right\} = \min\left\{ \frac{1}{n_i}\sum_{j=1}^{n_i}(\boldsymbol{S}_i\,\boldsymbol{r}^i_{OMj} + \boldsymbol{r}_{Oi} - \boldsymbol{r}_{Mj})^T(\boldsymbol{S}_i\,\boldsymbol{r}^i_{OMj} + \boldsymbol{r}_{Oi} - \boldsymbol{r}_{Mj}) \right\}, \tag{3.5}$$

where n_i represents the number of markers attached to body i and used in the reconstruction.
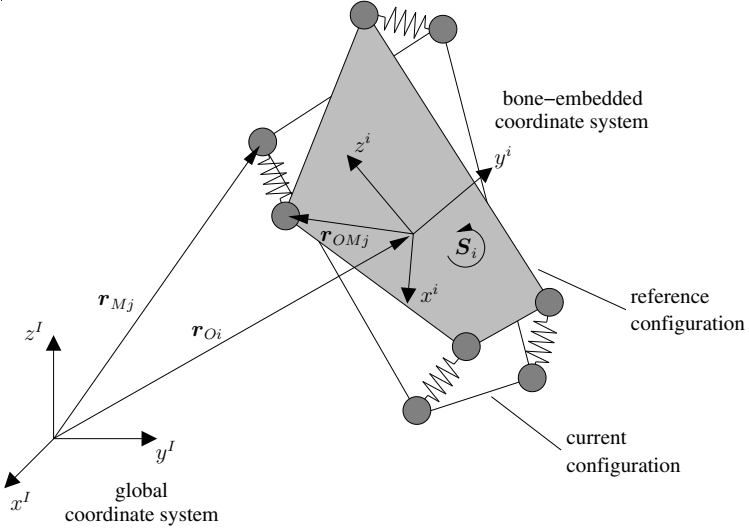
Figure 3.9: Scheme of the "fitting" of the reference configuration of the markers to the current one in a least squares sense.

In order to eliminate the vector $\boldsymbol{r}_{Oi}$ from the expression, the centroids of the positions of the markers in the body-embedded and global coordinate systems, respectively, are introduced as

$$\bar{\boldsymbol{r}}_{OM} = \frac{1}{n_i} \sum_{j=1}^{n_i} \boldsymbol{r}_{OMj}^i \qquad \text{and} \qquad \bar{\boldsymbol{r}}_M = \frac{1}{n_i} \sum_{j=1}^{n_i} \boldsymbol{r}_{Mj}. \tag{3.6}$$

From (3.6) and (3.2) it yields

$$\boldsymbol{r}_{Oi} = \bar{\boldsymbol{r}}_M - \boldsymbol{S}_i \bar{\boldsymbol{r}}_{OM}, \tag{3.7}$$

and (3.5) is rewritten as

$$\min \left\{ \frac{1}{n_i} \sum_{j=1}^{n_i} (\boldsymbol{S}_i \boldsymbol{r}_{OMj}^i + \bar{\boldsymbol{r}}_M - \boldsymbol{S}_i \bar{\boldsymbol{r}}_{OM} - \boldsymbol{r}_{Mj})^T (\boldsymbol{S}_i \boldsymbol{r}_{OMj}^i + \bar{\boldsymbol{r}}_M - \boldsymbol{S}_i \bar{\boldsymbol{r}}_{OM} - \boldsymbol{r}_{Mj}) \right\}. \tag{3.8}$$

After some mathematical manipulation of (3.8), refer to Gruber [35] or Ho Hoang [50], the optimization problem reads as follows

$$\max \left\{ \text{Tr}\{\boldsymbol{S}_i^T \boldsymbol{D}\} \right\}, \tag{3.9}$$

where $\boldsymbol{D}$ is the correlation matrix defined as

$$\boldsymbol{D} = \frac{1}{n_i} \sum_{j=1}^{n_i} (\widetilde{\boldsymbol{r}}_{Mj} \widetilde{\boldsymbol{r}}_{OMj}^T), \tag{3.10}$$

and

$$\widetilde{\boldsymbol{r}}_{OMj} = \boldsymbol{r}_{OMj}^i - \bar{\boldsymbol{r}}_{OM} \qquad \text{and} \qquad \widetilde{\boldsymbol{r}}_{Mj} = \boldsymbol{r}_{Mj} - \bar{\boldsymbol{r}}_M. \tag{3.11}$$

Singular value decomposition

A straightforward and computationally efficient way to solve the optimization problem (3.9) is to perform a singular value decomposition of the correlation matrix $\boldsymbol{D}$, see Söderkvist and Wedin [102], as follows

$$\boldsymbol{D} = \boldsymbol{U}\boldsymbol{W}\boldsymbol{V}^T, \tag{3.12}$$

where $\boldsymbol{U}$ and $\boldsymbol{V}$ are 3×3-orthogonal matrices, $\boldsymbol{W} = diag\{\sigma_1 \ \sigma_2 \ \sigma_3\}$ and $\sigma_1 \geq \sigma_2 \geq \sigma_3 \geq 0$ are the singular values of matrix $\boldsymbol{D}$. Substituting (3.12) into (3.9) and considering that the trace of a matrix is invariant to a similarity transformation gives

$$\max\left\{ \mathrm{Tr}\{\boldsymbol{S}^T\boldsymbol{U}\boldsymbol{W}\boldsymbol{V}^T\} \right\} = \max\left\{ \mathrm{Tr}\{\boldsymbol{V}^T\boldsymbol{S}^T\boldsymbol{U}\boldsymbol{W}\} \right\}, \tag{3.13}$$

where the index i denoting the segment is omitted for simplicity. Combining the first three matrices into the matrix $\boldsymbol{Q}$ yields

$$\max\left\{ \mathrm{Tr}\{\boldsymbol{Q}\boldsymbol{W}\} \right\}. \tag{3.14}$$

Since $\boldsymbol{W}$ is a diagonal matrix and $\boldsymbol{Q}$ is an orthogonal matrix, $\mathrm{Tr}\{\boldsymbol{Q}\boldsymbol{W}\}$ is maximal for $\boldsymbol{Q} = \boldsymbol{V}^T\boldsymbol{S}^T\boldsymbol{U} = \boldsymbol{E}$, where $\boldsymbol{E}$ is the identity matrix. Therefore, the optimal rotation matrix reads simply as

$$\boldsymbol{S} = \boldsymbol{U}\boldsymbol{V}^T. \tag{3.15}$$

Once the optimal rotation matrix of the bone-embedded frame is known, the position vector can be computed with (3.7).

This procedure is implemented in a Matlab® function, "soder.m", written by Ron Jacobs and adapted by Ton van den Bogert, which is available for download from the homepage of the International Society of Biomechanics[1] and is used in this work to perform body pose reconstruction from the positions of the markers.

---

[1]www.isbweb.org/software/index.html

Kinematics

A rotation in the space can be described by three coordinates, so that the nine coordinates of the rotation matrix depend on these three coordinates. In this work the absolute rotation of the pelvis is described by Cardan angles denoting consecutive finite rotations, α, β and γ, about the axes x, y and z, or equivalently, about the axes e_1, e_2 and e_3. The rotation matrix of the pelvis is a function of these Cardan angles and reads as

$$
S_{pelvis}(\alpha, \beta, \gamma) = \alpha_1\beta_2\gamma_3 = \begin{bmatrix} 1 & 0 & 0 \\ 0 & c\alpha & -s\alpha \\ 0 & s\alpha & c\alpha \end{bmatrix} \begin{bmatrix} c\beta & 0 & s\beta \\ 0 & 1 & 0 \\ -s\beta & 0 & c\beta \end{bmatrix} \begin{bmatrix} c\gamma & -s\gamma & 0 \\ s\gamma & c\gamma & 0 \\ 0 & 0 & 1 \end{bmatrix}
$$
$$
= \begin{bmatrix} c\beta c\gamma & -c\beta s\gamma & s\beta \\ c\alpha s\gamma + s\alpha s\beta c\gamma & c\alpha c\gamma - s\alpha s\beta s\gamma & -s\alpha c\beta \\ s\alpha s\gamma - c\alpha s\beta c\gamma & s\alpha c\gamma + c\alpha s\beta s\gamma & c\alpha c\beta \end{bmatrix}.
$$

$$(3.16)$$

Moreover, it is efficient to describe the human motion by means of the relative motion of adjacent segments, corresponding to the movement around the joints connecting them. As explained in section 3.2.1, the generalized coordinates of the model adopted are composed by 6 coordinates describing the position and the rotation of the pelvis with respect to the global coordinate frame and 21 coordinates describing the relative rotation of adjacent segments, see (3.1). The relative rotation of two adjacent segments, a more proximal segment referred to as p and a more distal segment referred to as d, is described by the relative rotation matrix S_{rel} as

$$
S_{rel} = S_p^{-1}S_d = S_p^T S_d \tag{3.17}
$$

because rotation matrices are orthogonal and $SS^T = E$, where S_p and S_d are the rotation matrices of segments p (proximal) and d (distal), respectively, in the global coordinate frame, computed using the body pose reconstruction method explained.

As explained in section 3.2.1, the elementary rotations that describe the relative motion between adjacent segments are chosen such that they are anatomically meaningful, representing consecutive finite rotations, β, α and γ, about the axes y, x and z, or equivalently, about the axes e_2, e_1 and e_3. The relative rotation matrix between two adjacent body segments is a function of these finite rotations as

$$
S_{rel}(\alpha, \beta, \gamma) = \beta_2\alpha_1\gamma_3 = \begin{bmatrix} c\beta & 0 & s\beta \\ 0 & 1 & 0 \\ -s\beta & 0 & c\beta \end{bmatrix} \begin{bmatrix} 1 & 0 & 0 \\ 0 & c\alpha & -s\alpha \\ 0 & s\alpha & c\alpha \end{bmatrix} \begin{bmatrix} c\gamma & -s\gamma & 0 \\ s\gamma & c\gamma & 0 \\ 0 & 0 & 1 \end{bmatrix}
$$
$$
= \begin{bmatrix} c\beta c\gamma + s\alpha s\beta s\gamma & -c\beta s\gamma + s\alpha s\beta c\gamma & c\alpha s\beta \\ c\alpha s\gamma & c\alpha c\gamma & -s\alpha \\ -s\beta c\gamma + s\alpha c\beta s\gamma & s\beta s\gamma + s\alpha c\beta c\gamma & c\alpha c\beta \end{bmatrix}.
$$

$$(3.18)$$

3.3.2 Global Optimization

The local optimization explained in the previous section treats each segment separately, in such a way that the joint constraints are not considered during the optimization. Only after the determination of the rotation matrices the segments are moved translationally until the joint constraints are matched. This procedure can lead to unrealistic positions of the segments, what can be observed, for example, by comparing the reconstructed position of distal segments like the feet with their original position. In order to reduce these errors, global optimization techniques were proposed, which take the joint constraints into account. The performance criterion for the optimization is the distance between the reference and reconstructed positions of the markers in a least squares sense.

For instance, Lu and O'Connor [65] propose a global optimization that searches the optimal pose of a multi-link model for each time step, which minimizes the over-all distances between the measured and reconstructed positions of the markers for a predefined topology of the model. An extended approach is proposed by Reinbolt et al. [89], where, additionally to the pose, also the topology of the multi-link model is optimized. This technique is based on a two-level optimization composed by an outer level, that modifies the model parameters, and an inner one corresponding to the optimization proposed by Lu and O'Connor [65]. Because the described global optimization approaches require a higher computational effort and are more difficult to implement, while algorithms for the local optimimization are readily available, in this work the local optimization technique explained in section 3.3.1 is used.

3.3.3 Results and Discussion

In this section some results for the kinematics of the body for the different experiments obtained by means of the body pose reconstruction are presented and discussed. Table 3.1 shows the general features of the gaits observed for both subjects. The normal gait velocities observed for both subjects, 1.05 m/s and 1.17 m/s, are significantly lower than values reported in the literature for self-selected walking velocities, like 1.38 m/s as average for the normal gait of 26 subjects measured in the "Orthopaedischen Universitaetsklinik Heidelberg", Wolf and Rettig [126], and about 1.50 m/s reported by Sutherland et al. [109]. The stride lengths for the normal experiment, 1.28 m for subject 1 and 1.34 m for subject 2, are also lower than values reported in the literature, 1.41 m measured in the "Orthopaedischen Universitaetsklinik Heidelberg" and about 1.55 m reported by Sutherland et al. [109].

The stance and swing phase durations differ for both subjects slightly from the values measured in the "Orthopaedischen Universitaetsklinik Heidelberg" and reported by Sutherland et al. [109], 61% and 39%, respectively. Note that the data duration is nor-

Table 3.1: General features of the gait patterns observed during the experiments.

	Stride Length $[m]$	Period $[s]$	Aver. Vel. $[m/s]$	Stance Right $[\%]$	Stance Left $[\%]$	Swing Right $[\%]$	Swing Left $[\%]$	Double Stance $[\%]$
subject 1								
normal	1.28	1.22	1.05	65.6	65.6	34.4	34.4	31.1
weight	1.36	1.28	1.06	67.2	65.6	32.8	34.4	32.8
orth.	1.34	1.42	0.94	60.6	69.0	39.4	31.0	29.6
vario	1.34	1.12	1.20	67.9	66.1	32.1	33.9	33.9
ski	1.40	1.36	1.03	63.2	64.7	36.8	35.3	27.9
subject 2								
normal	1.34	1.14	1.17	66.7	63.2	33.3	36.8	29.8
weight	1.28	1.28	1.00	65.6	67.2	34.4	32.8	32.8
orth.	1.30	1.58	0.82	60.8	70.9	39.2	29.1	31.6
vario	1.31	1.40	0.93	65.7	68.6	34.3	31.4	34.3
ski	1.25	1.48	0.85	64.9	68.9	35.1	31.1	33.8

malized by the whole duration of the cycle in order to facilitate the comparison among experiments. These observed discrepancies may be due to the non-optimal length of the walking track in the laboratory, which is about 5 m long, while the minimum length recommended in the literature is 8 m. This limitation is expected to inhibit the development of higher velocities and induce changes in the patterns of the gait.

The comparison among the different experiments reveals a tendency of the velocity to reduce as the kinematic constraints are imposed, as demonstrated by the consistently lower walking speeds for the experiments orthosis, vario and ski compared to the ones for the experiment normal. Subject 2 also presents a significantly lower velocity for the experiment weight in relation to the normal experiment. An exception is the walking velocity of subject 1 during the vario experiment, which may be considered to be an outlier.

The relative duration of the swing phase of the right leg for the experiments orthosis and ski is consistently and significantly higher for both subjects with respect to the duration of the corresponding swing phases of the left leg and also with respect to the duration of the swing phases of the right leg in all the other experiments as shown by the swing columns of Tab. 3.1. This observation can be explained by the higher moments of inertia of the right leg introduced by the disturbances in these two experiments. In the ski experiment the mass moment of inertia is increased mainly by the addition of a 2.4 kg mass around the foot, while the increase for the orthosis experiment is mainly caused by fixating the knee joint in full extension, what maintains the leg mass distribution more distal over

the swing phase. An increase in the moment of inertia of the leg decreases the natural frequency of the swinging leg. In order to reduce the moments required at the hip joint, the subjects naturally respond to this increase in the moment of inertia by increasing the swing phase duration, i.e. by decreasing the swing frequency. These observation reinforces the thesis that the gait kinematics naturally adapts to handicaps in order to reduce the overall effort required.

A comparison of the reconstructed kinematics for subject 1 and subject 2 with kinematics obtained for 26 subjects in the gait analysis laboratory of the "Orthopädischen Universitätsklinik Heidelberg" in Figs. A.3 and A.4 of Appendix A.5 shows an overall good agreement. A discussion of the possible reasons for the few discrepancies observed can be found in Appendix A.5. Figures 3.10 and 3.11 show the kinematics of the right lower limb joints for subject 1 and subject 2, respectively. The values for the generalized coordinates in (3.1) are obtained by using reference bone-embedded frames for the HAT, pelvis and feet, and anatomical bone-embedded frames for the thighs and shanks. Appendix A.5 briefly describes the anatomical and reference frames adopted for the segments while further information can be obtained in Ackermann and Gros [2]. The kinematics of the pelvis, of the HAT with respect to the pelvis, and the kinematics of the left lower limb joints are not shown here and can also be found in Ackermann and Gros [2].

The results give a series of insights into the intensity of the burden imposed by the mechanical disturbances investigated. For instance, a remarkable low variation of the kinematics for the experiment weight in comparison to experiment normal is observed, what might be explained by the fact that the weight handicap is the only one to impose no kinematic constraints to the joints. On the other hand, the most salient alterations in the kinematics of the gait occur for the experiments orthosis and ski, not only on the affected side of the body but also considerably in the non-affected one. This observation is justified by the severeness of the handicap imposed by these two disturbances concerning the kinematics. The orthosis immobilize the very mobile knee joint, which plays an important role to facilitate foot clearance during the swing phase and in the acceptance of body weight in the beginning of the stance phase. The ski boot immobilizes the ankle joint and the metatarsophalangeal joints, besides imposing a 2.4 kg weight to the foot and causing modifications on the geometry of the foot, which together strongly affects the roll-over mechanism during the stance phase of the gait and the normal course of the point of application of the ground reaction forces.

The kinematics of the non-affected joints of the lower limbs in the sagittal plane shows clear adaptations required for the orthosis and ski experiments. For the orthosis experiments discrepant patterns for the trajectories of the right hip joint flexion angle mainly during the swing and terminal stance phases can be observed, see Figs. 3.10 and 3.11, namely a significantly reduced hip flexion in the beginning of the swing phase. Note that the names in these figures correspond to positive values. Negative values change the

Right Lower Limb Kinematics for Subject 1
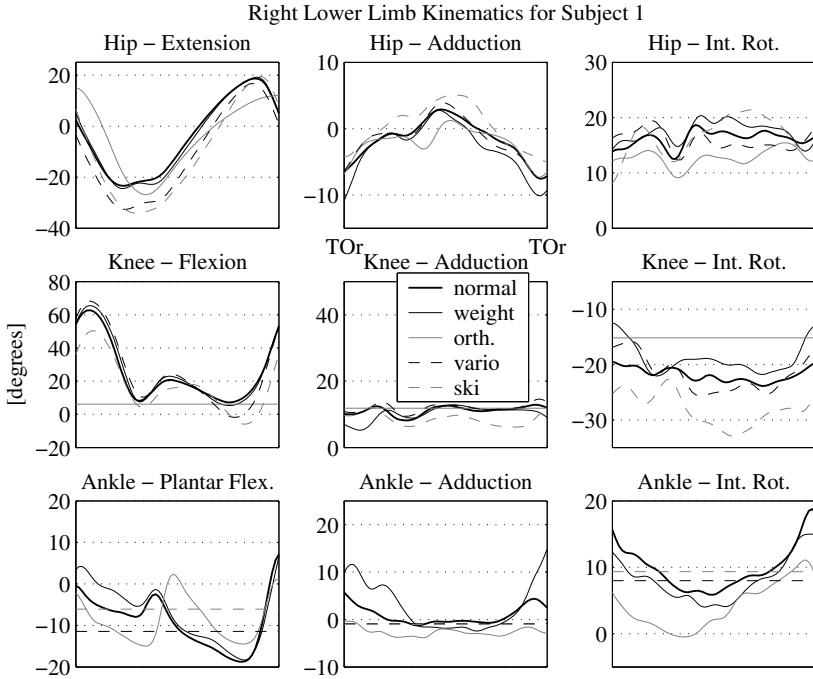
Figure 3.10: Rotations at the right hip, knee and ankle joints of subject 1. The elementary consecutive rotations about axis y (flexion/extension or plantar/dorsiflexion), x (ab/adduction) and z (int./ext. rotation or plantar/dorsiflexion), respectively, are shown. Reference coordinate frames are used for the pelvis and feet, and anatomical frames are use for thighs and shanks.

names, for example, from flexion to extension and vice versa. Also the right ankle joint flexion angles for this experiment show an abnormal pattern to compensate for the loss of knee mobility. For the experiment ski a significantly reduced flexion of the right knee occurs during swing phase and terminal stance, and also a higher extension of the knee can be observed in the terminal swing and terminal stance phases of the right lower limb.

Variations are also observed for the non-affected side, although they are less prominent than the ones in the right, affected lower limb. As for the right side, the kinematics of the ski and orthosis experiments are the ones with more distinct kinematics in the sagittal plane. Furthermore, for the experiments orthosis, vario and ski a strategy to avoid contact of the right foot with the ground during the right swing phase is noticeable. During the swing phase of the right leg a lower flexion of the left knee, a higher plantar flexion of the left ankle and a higher pelvis obliquity to the left can be observed. The net effect of

Right Lower Limb Kinematics for Subject 2
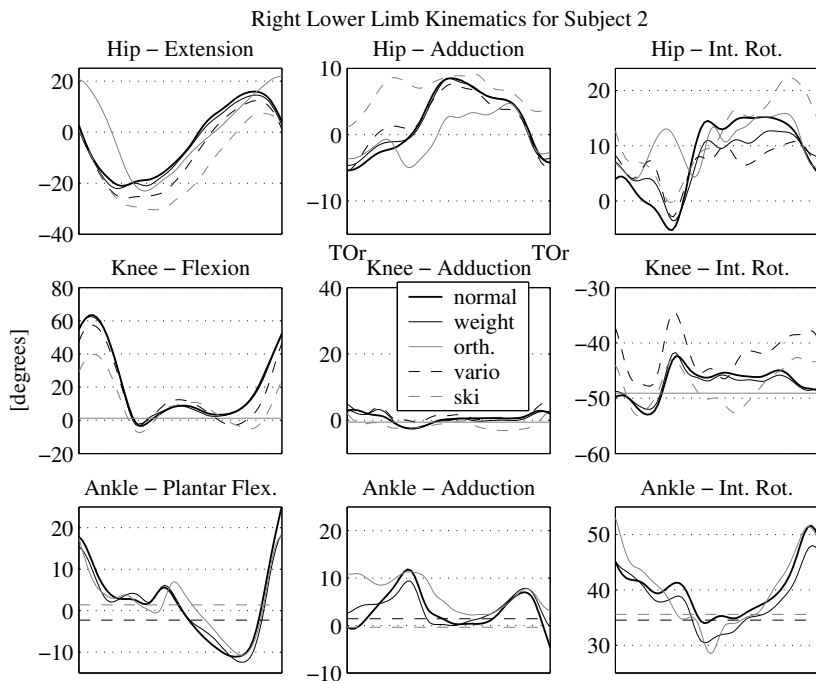
Figure 3.11: Rotations at the right hip, knee and ankle joints of subject 2. The elementary consecutive rotations about axis y (flexion/extension or plantar/dorsiflexion), x (ab/adduction) and z (int./ext. rotation or plantar/dorsiflexion), respectively, are shown. Reference coordinate frames are used for the pelvis and feet, and anatomical frames are use for thighs and shanks.

these measures is to elevate the right hip joint. A higher value of the z-coordinates of the center of mass of the pelvis, up to 2 cm, during the swing phase of the right lower limb is indeed observed. These measure compensates for the increased effective length of the affected limb caused by the joint immobilizations, and guarantees foot clearance during the swing phase of the right lower limb.

As a response to the excessive obliquity of the pelvis to the left, an increase of the HAT obliquity to the right is observed, what approximates the vertical projection of the center of mass of the whole body to the support base of the left foot, thus guaranteeing a more stable posture.

3.4   Computation of Joint Moments

The net joint moments caused by muscles and other passive structures spanning the joints of the body can be estimated by means of the equations of motion of the mechanical model adopted. This calculation is known as inverse dynamics, refer to section 2.1.4, and is a powerful tool in biomechanics, since it permits the determination of the net moments that must be applied at the joints to cause the observed motion. As shown in Fig. 3.12, information about the kinematics of the movement, the ground reaction forces acting on the feet and anthropometric data of the subject are necessary. Refer to Siegler and Liu [101] for a brief overview on inverse dynamics in human locomotion.
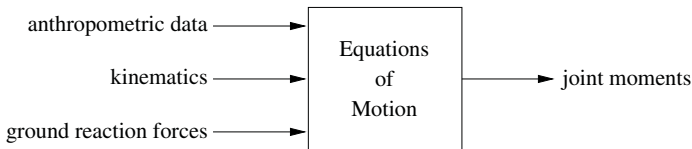
Figure 3.12: Diagram illustrating the inverse dynamics in biomechanics.

As mentioned previously, the goal is to investigate the muscular effort for different lower limb mechanical disturbances. The moments applied at the joints give insights into the variations of the forces applied by all the muscles spanning the joints. Since performing inverse dynamics is computationally efficient, it is reasonable to start the analysis by observing the fluctuation on the net moments applied at the joints.

It is important to note, however, that the net moment alone does not provide the intensity of the forces applied by individual muscles and passive structures like ligaments spanning the joint. Moreover, the moments applied by passive structures contribute to the net joint moments. Thus, the net moments can become a rather inaccurate estimator of the "active" moments requiring energy consumption, specially in the proximity of the joints full extension and flexion, where passive moments often become significant, refer, for example, to Riener and Edrich [90]. Furthermore, because many muscles span two or more joints, conclusions about muscle activity based on moments applied at the joints have to be made very carefully (Zajac et al. [133]).

3.4.1   Solving the Inverse Dynamics in Biomechanics

Inverse dynamics requires the equations of motions of the skeletal model, see Fig. 2.1 and Fig. 3.12. In section 3.2 the mechanical model adopted is presented and explained in details. The equations of motion (2.13) are obtained in symbolic form based on the Newton-Euler formalism, refer to Schiehlen and Eberhard [97], using the software

NEWEUL (Kreuzer and Leister [60]). The equations of motion are exported to Matlab®, where the inverse dynamics computations for all experiments and subjects are performed. The general form of the resulting nonlinear equations of motion are shown in (2.13) and is rewriten here as

$$\boldsymbol{M}(\boldsymbol{y})\,\ddot{\boldsymbol{y}} + \boldsymbol{k}(\boldsymbol{y}, \dot{\boldsymbol{y}}) = \boldsymbol{q}(\boldsymbol{y}, \dot{\boldsymbol{y}}, \boldsymbol{f}^{gr}, \boldsymbol{\tau}), \qquad (3.19)$$

where $\boldsymbol{y}$ is the $f \times 1$-vector of generalized coordinates (3.1), and f is the number of degrees of freedom of the mechanical model. The vector $\boldsymbol{f}^{gr}$ contains the ground reaction forces measured for both feet, which are modeled as external applied forces, and $\boldsymbol{\tau}$ is a vector containing the moments at the joints. As explained in section 3.2 the model has $p = 8$ rigid bodies, 7 joints, and $f = 27$ degrees of freedom. The symbolic equations of motion obtained are documented in Ackermann and Gros [2].

Solving (3.19) for $\boldsymbol{\tau}$ leads usually to an overdetermined system of equations. Overdeterminacy often occurs because the ground reaction forces, i.e. the external forces during walking, are generally measured, since most gait analysis laboratories are equipped with force plates. This measurements reduce the number of unknowns lonely to the joint moments. These overdeterminacy can be treated and exploited in many ways, which will be briefly explained in this section.

A simple way to solve the inverse dynamics problem is explained in Winter [123]. In this method the Newton-Euler equations are applied for each body segment. The equations are solved for each body in a recursive way beginning with one of the extreme bodies of the chain. This method permits the calculation of both, the reaction forces/moments and the applied forces/moments. The exceeding information, e.g. the ground reaction forces, is ignored, so that the overdeterminacy is not exploited.

The ground reaction forces measurements are less error-prone than the reconstructed kinematics, obtained from the 3-D trajectories of markers attached to the skin, which are subject to many sources of error as explained in section 3.3. For this reason, the ground reaction forces should be always considered whenever possible leading to more accurate joint moments estimations. The inverse dynamics problem for the case of measured ground reaction forces can be solved by simply reducing the number of equations to match the number of unknowns. The six first equations in (3.19), "corresponding" to the six coordinates of the pelvis, are chosen as residual equations. Equations (3.19) are split into two sets, the residual equations and the reduced equations, respectively, as

$$\boldsymbol{M}_{res}\,\ddot{\boldsymbol{y}} + \boldsymbol{k}_{res} = \boldsymbol{q}_{res}, \qquad (3.20)$$

$$\boldsymbol{M}_{red}\,\ddot{\boldsymbol{y}} + \boldsymbol{k}_{red} = \boldsymbol{q}_{red}. \qquad (3.21)$$

The matrix $\boldsymbol{M}$ and the vectors $\boldsymbol{k}$ and $\boldsymbol{q}$ are split as follows, $\boldsymbol{M} = \begin{bmatrix} \boldsymbol{M}_{res}^T & \boldsymbol{M}_{red}^T \end{bmatrix}^T$, $\boldsymbol{k} = \begin{bmatrix} \boldsymbol{k}_{res}^T & \boldsymbol{k}_{red}^T \end{bmatrix}^T$ and $\boldsymbol{q} = \begin{bmatrix} \boldsymbol{q}_{res}^T & \boldsymbol{q}_{red}^T \end{bmatrix}^T$. The 6 residual equations (3.20) "correspond" to the 6 generalized coordinates of the pelvis and are composed by the $6 \times f$-matrix $\boldsymbol{M}_{res}$,

the 6×1-vector $\boldsymbol{k}_{res}$ and the 6×1-vector $\boldsymbol{q}_{res}$. The $f - 6$ equations (3.21) are composed by the $(f - 6) \times f$-matrix $\boldsymbol{M}_{red}$, the $(f - 6) \times 1$-vector $\boldsymbol{k}_{red}$ and the $(f - 6) \times 1$-vector $\boldsymbol{q}_{red}$.

Equations (3.21) are used to calculate the $(f - 6) \times 1$-vector $\boldsymbol{\tau}$ of unknown moments applied at the joints. Since the number of equations equals the number of unknowns and the set of equations are linear in the components of $\boldsymbol{\tau}$, the resulting system of equations can be easily and efficiently solved. Equations (3.20) are disregarded for the computation of the moments applied at the joints, but they are useful to assess both, the fidelity of the mechanical model and the quality of the input data, as pointed out by Hatze [44]. Rearranging (3.20) and introducing a vector of residuals $\boldsymbol{r}$ yields

$$\boldsymbol{r} = \boldsymbol{M}_{res} \ddot{\boldsymbol{y}} + \boldsymbol{k}_{res} - \boldsymbol{q}_{res}. \qquad (3.22)$$

It is clear that the 6×1-vector $\boldsymbol{r}$ of residuals would equal zero if the mechanical model reproduces perfectly the real system and if there were not errors in the input data. Since the models are far from perfect and the input data always contain some amount of error, the vector of residuals is always unequal zero. The magnitude of the vector of residuals gives an idea of the inconsistency between the model and the input data. The values of $\boldsymbol{r}$ alone provide, however, no information about the extension to which the model inaccuracies and the input data errors contribute to the inconsistency observed. The physical interpretation of the vector $\boldsymbol{r}$ of residuals in the model used are the, in reality not existent, external forces and moments that would have to be applied to the pelvis of the subject in order to make the input data and the model compatible.

As mentioned previously, the occurrence of overdeterminacy in the inverse dynamics problem is frequent in biomechanics. In order to take advantage of this overdeterminacy optimization techniques can be used. In the following paragraphs some of these techniques are briefly commented for the sake of completeness. For instance, Vaughan et al. [118] determine body segment parameters in such a way as to minimize the difference between the measured and calculated external forces. Kuo [61] exploits the overdeterminacy using optimization methods to extract the best joint torques estimates and angular accelerations from imperfect measurements by means of a least-squares approach.

Another possibility to solve the inverse dynamics problem is to use dynamic optimization to find the joint moments that make the simulated kinematics and ground reaction forces best fit the observed ones by performing several forward integrations of the equations of motion. Performing dynamic optimization is, however, extremely costly in terms of computational effort. In chapter 5 a novel approach is proposed to obtain optimal gait patterns, which is computationally more efficient than dynamic optimization.

In order to avoid the implementation of a dynamic optimization, but still enforce the equations of motion over time, the Computed-Torque Control can be used, refer to Lewis et al. [64]. This method is in fact a control scheme, used for example to make the

manipulator of a robot follow a pre-planned desired trajectory. The ground reaction forces are incorporated to the equations of motion as known external forces.

3.4.2   Results and Discussion

In this section the joint moments computed by inverse dynamics for both subjects and all experiments are presented and discussed. A comparison of the normal experiment results for the lower limb with joint moments obtained for 26 subjects in the gait analysis laboratory of the "Orthopaedischen Universitaetsklinik Heidelberg" is presented in Appendix A.6 along with a discussion. Here, only results for the joint moments of the right lower limb for both subjects and all experiments are shown, in Figs. 3.13 and 3.14. Note that the moments are normalized by the subjects' total body mass and the duration is normalized by the total duration of the cycle in order to facilitate the comparison among experiments. The complete set of joint moments are documented in Ackermann and Gros [2].

The observation of Figs. 3.13 and 3.14 reveals remarkable small differences between the joint moments for the normal and weight experiments. Similar patterns are also found for the kinematics of these two experiments as mentioned in section 3.3.3. Some variations that occur consistently for both subjects can be observed. Note that the big variations of the moments at the right ankle joint for the vario and ski experiments are applied mainly by the vario shoe and the ski boot structures, respectively, so that the moments observed do not reflect the active moments applied by the muscles at these joints.

During the initial and middle stance phases high knee extension moments are observed for the experiments vario and ski for both subjects. During the terminal stance phase, in opposition, higher flexion moments for these experiments are found. These abnormal moment patterns can be explained by the immobilization of the ankle joint in these two experiments, what prevents the normal ankle flexion-extension pattern during the stance phase. This normal pattern can be observed in Figs. 3.10 and 3.11 and consists of a smooth transition of the foot position to a plantar flexion in the initial stance phase by "rolling" of the foot over its heel till the full contact of its plant with the floor is achieved, passing trough a dorsiflexion of the ankle to permit the forward motion of the lower limb and ending with a new plantar flexion at the terminal stance as a preparation for the swing phase, when the metatarsophalangeal joint functions as a pivot for the rotation of the foot before *toe off*. The inhibition of this mechanism by the immobilization of the ankle joint causes the necessity for applying higher knee extension moments to avoid the premature and excessive flexion of the knee in the initial stance as the foot and the shank, rigidly connected, tends to rotate towards the full contact of the sole with the floor. The higher knee flexion moments at the terminal stance, in turn, might be caused by the necessity of applying more torque to the shank in order to achieve heel off when

Joint Moments for the Right Lower Limb of Subject 1
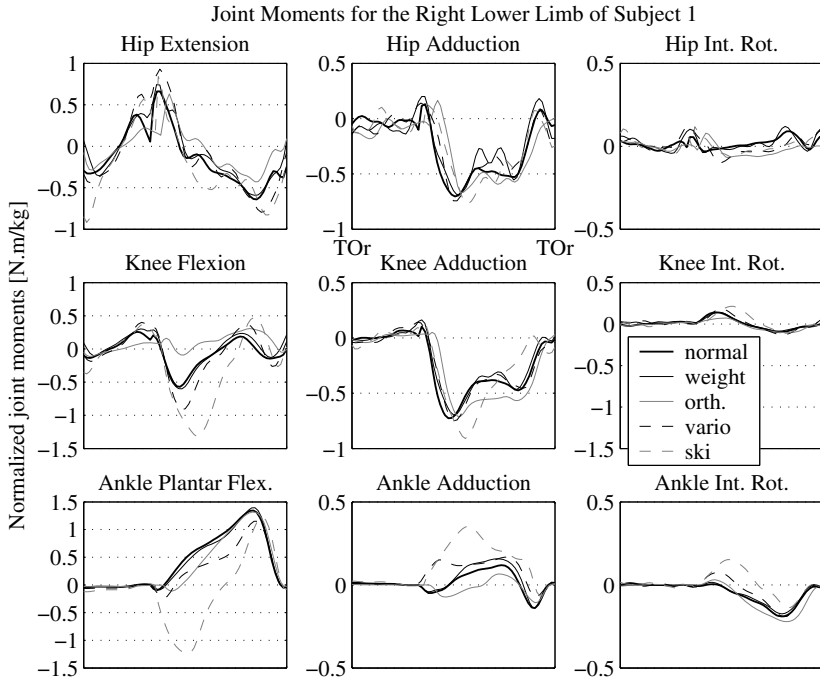
Figure 3.13: Joint moments at the right hip, knee and ankle of subject 1. The hip moment is expressed in the reference frame of the pelvis. The knee and ankle moments are expressed in the anatomical frames of the thigh and of the shank, respectively.

both segments, shank and foot, are maintained in a relative flexion angle of about 0°.

In the same experiments, ski and vario, a higher right hip flexion moment in the beginning of the swing phase can be noticed. This can be explained as a measure to contribute to the knee flexion, since the foot plantar flexion just before *toe off* which normally contributes to the knee flexion in the initial swing, does not occur due to the ankle joint immobilization. The significantly higher abduction moments acting at the knee joint of subject 1 compared with the ones of subject 2 may be attributed to the slight outward deviating knee (genu varus) of subject 2.

The joint moments of the left, non-affected lower limb presents considerable differences with respect to the ones of the right, affected lower limb. A similar pattern variation for both subjects, which would indicate a consistent pattern variation, could, however, not be identified. However, some plausible justifications for the absence of clear pattern variations of the moment curves for the joints of the left lower limb are mentioned. One reason
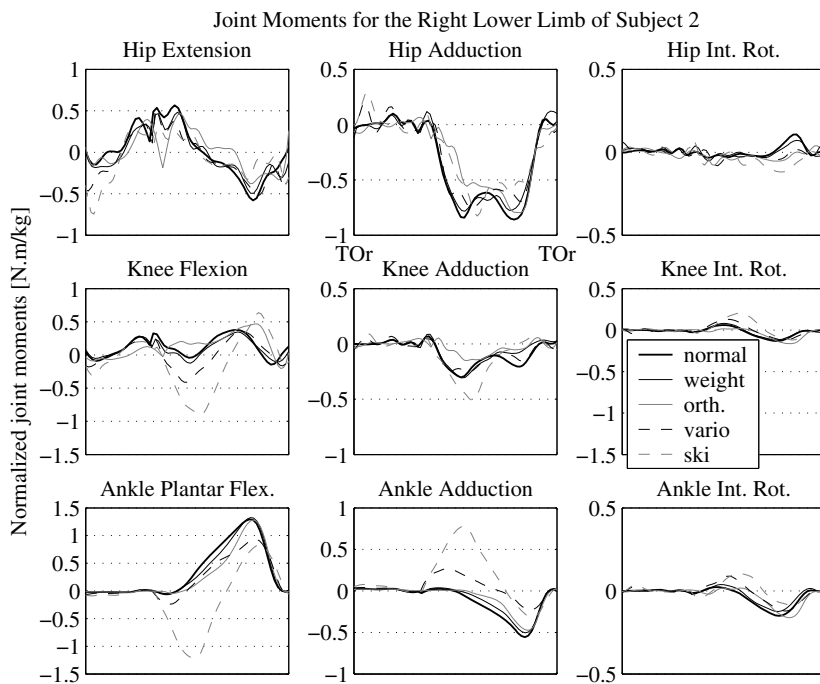
Figure 3.14: Joint moments at the right hip, knee and ankle of subject 2. The hip moment is expressed in the reference frame of the pelvis. The knee and ankle moments are expressed in the anatomical frames of the thigh and of the shank, respectively.

may be the inaccuracy of the ground reaction forces applied at the left foot, which are not measured for the same trial, because only one force plate was available. Instead, the ground reaction forces were measured in another trial with the same disturbances, so that there is no guaranty that the ground reaction forces are totally consistent with the motion observed in the original trial, since the gait kinematics of a person can vary considerably even from step to step. Another reasonable explanation might be the simply adoption of different gait compensation strategies in the left leg by the subjects. Furthermore, the normalization of the cycle duration masks the different velocities with which the subjects walked in the different experiments, what further complicates the direct comparison among experiments. A last possible explanation is that the measurement errors and the errors caused by the *skin artefacts*, amplified by the many numerical manipulation steps necessary for the inverse dynamics, overwhelm the eventually slight variation patterns for the joint moments of the left lower limb. Probably all these factor affect to some extent the results obtained.

The observation of the curves plotted provides important information for the development of models for handicapped gaits. The high rotation and mainly abduction/adduction moments computed indicates the importance of considering motion planes other than the sagittal. Specially the hip joint ad/abduction moments and moment variations, which are mainly applied by muscles spanning the hip, and which are even higher in magnitude than the flexion/extension moments, show the strong limitations of 2-D models constrained to the sagittal plane.

The clearly recognizable variations in the moments and in the kinematics of the non-affected leg indicates the importance of using whole-body models also to model unilateral handicaps. The use of one-lower limb models neglect the compensations occurring at the non-affected side and might lead to incorrect conclusions. Although the magnitude of some of the variations observed achieve high values, in the most cases they are small and insufficient to change the overall pattern of the curves. These observation shows that the compensation for disturbances arises from a summation of small kinematic and kinetic adaptation measures along all the body joints and segments, rather than from a concentrated adaptation in the proximity of the handicap. This reinforces the value of a whole-body model and indicates the necessity of using complex models able to account for a set of small variations. The use of quantities that account for net performance, like the total energy consumption, might be more apropriate to evaluate the adaptations caused by a handicap than the analysis of isolated segments or joints.

Many of the variations observed, though substantial, are not occurring consistently for both subjects so that no direct conclusions can be drawn. Some variations, however, as the ones explained above are so important that they could be observed consistently for both subjects, in spite of the measurement errors discussed and the possibly different adaptation strategies adopted by the subjects. The detection of slighter variations and a complete statistical analysis would require a higher number of subjects and was not the aim of this project.

It was shown that the variations caused by the introduction of mechanical disturbances typically introduced by lower limb prostheses, like modification of the inertial properties of segments and introduction of kinematical constraints to the joints of the lower limb, do cause significant changes in the kinematics and kinetics of the whole body. Also the nature and the magnitude of the changes caused could be to a great extent assessed. The information and analyses delivered here are expected to contribute to the modeling process and the interpretation of simulation results for handicapped gaits. Another expected contribution of this study is providing a frame for further investigations of this type, where all the important steps to compute the kinematics and the moments at the joints are explained in detail and the many sources of errors are presented and discussed.

Chapter 4

Extended Inverse Dynamics Approach

In the previous chapter inverse dynamics is used to compute the net joint moments required to generate a measured motion. Although giving a clue about the intensity of the actuation required to accomplish the observed motion, net joint moments fail in delivering information on the forces applied by the individual muscles and other structures spanning the joints. Because the skeletal system is redundantly actuated by muscles, i.e. there are many more muscles than actuated degrees of freedom, and many muscles are multi-articular, spanning more that one joint, the direct translation of net moments into muscle forces is not possible. Therefore, conclusions about muscle activity from net joint moments are not very reliable (Zajac et al. [133]). Furthermore, the energy consumption involved, represented by the metabolic cost during human motion, refer to section 2.2.3, cannot be accurately assessed.

In order to solve the mathematically indeterminate problem and assess muscle forces, optimization approaches are employed. The classical static optimization approach is characterized by the search for muscle forces that minimize a cost function and fulfill constraints, given basically by bounded muscle forces and by the equations of motion or joint moments computed by inverse dynamics, respectively. The cost functions are mathematical expressions assumed to model some physiological criterion optimized by the central nervous system during a particular activity.

In spite of being computationally efficient, the static optimization approach assumes an instantaneous optimal distribution of muscle forces suffering from two important limitations. Firstly, it neglects the muscle contraction and activation dynamics, refer to sections 2.2.2, what might lead to unphysiological estimations of muscle forces. Secondly, the cost functions must be an instantaneous measure of performance, what excludes the possibility of using time-integral criteria as for example total metabolic cost expended. The latter limitation is specially important for the analysis of human walking, since metabolic cost

is accepted to play an important role during locomotion.

The muscle activation and contraction dynamics can be taken into account by using dynamic optimization associated with the tracking of the prescribed kinematics. This approach is based on the search for optimal controls, in this case the neural excitations, that drive a forward-dynamics model of the musculoskeletal system to track the prescribed motion. Due to the several numerical integrations of the differential equations necessary, a prohibitive computational effort is required to achieve a solution. This drawback prevents this approach from being widely used and stimulated recent efforts to reduce the computational burden. Some strategies based on dynamic optimization are presented in more details in section 4.1.2.

A novel approach to solve the distribution problem in biomechanics is proposed in section 4.3. It considers the muscle contraction and activation dynamics and permits the use of time-integral cost functions as the total metabolic cost. This approach is called extended inverse dynamics (EID) because it requires, in addition to the inversion of the skeletal system dynamics, the inversion of the muscle contraction and activation dynamics. Because no numerical integration of the differential equations is required, the extended inverse dynamics is computationally less costly than the dynamic optimization. An alternative, simplified approach to permit computation of muscle forces that fulfill the constraints given by the activation and contraction dynamics is also proposed and presented in section 4.4. Although the latter approach maintains computational effort similar to the ones for static optimization, it does not permit the use of time-integral cost functions.

4.1 Muscle Force-Sharing Problem in Biomechanics

The knowledge of loads in individual joint structures is important in fields like medicine, sport science or prosthesis design. For instance, the determination of muscle and ligament forces is required for an analysis of the risk of damage of the ACL (anterior cruciate ligament) in specific sport activities, for the design of hip and knee endoprostheses or for the planning and evaluation of orthopedic surgeries, see Delp [29]. However, muscle forces cannot be measured directly in-vivo without invasive techniques. This stresses the importance of techniques that permit the estimations of tissue loads from the skeletal system motion and the external applied forces, quantities that can be measured in-vivo as shown in the previous chapter.

The problem of finding the muscle forces for a prescribed or measured motion is also called the 'Redundant Problem in Biomechanics', see e.g. Yamaguchi et al. [129]. Since many muscles span each joint of the skeletal system, a redundant system arises because muscle forces may contribute differently to the same joint moments, i.e. muscle forces cannot be uniquely determined from joint moments. Under a mathematical point of view, there are

more unknown muscle forces than equilibrium equations available, i.e. there is an infinite number of solutions for the muscle forces that fulfill the equilibrium equations and can generate the same observed motions of the skeletal system.

Equation (3.19) describes the dynamics of the skeletal system. Splitting the vector of generalized forces $\boldsymbol{q}$ into a vector of generalized forces caused exclusively by muscles and a vector of generalized forces caused by other structures spanning the joints and the ground forces yields

$$\boldsymbol{M}(\boldsymbol{y})\,\ddot{\boldsymbol{y}} + \boldsymbol{k}(\boldsymbol{y}, \dot{\boldsymbol{y}}) = \boldsymbol{q}(\boldsymbol{y}, \dot{\boldsymbol{y}}, \boldsymbol{f}^{gr}, \boldsymbol{\tau}) = \boldsymbol{q}_r(\boldsymbol{y}, \dot{\boldsymbol{y}}, \boldsymbol{f}^{gr}) + \boldsymbol{R}(\boldsymbol{y})\,\boldsymbol{f}^m \ , \qquad (4.1)$$

where $\boldsymbol{q}_r$ is the $f \times 1$-vector of generalized forces other than the ones caused by the muscles, $\boldsymbol{f}^m$ is the $m \times 1$-vector of muscle forces, $\boldsymbol{R}$ is the $f \times m$-matrix that transforms the muscle forces into generalized forces, and $\boldsymbol{\tau} = \boldsymbol{A}\,\boldsymbol{f}^m$, where $\boldsymbol{A}$ is a $k \times m$-matrix that contains the muscles moment arms. The vector $\boldsymbol{q}_r$ includes the vector of ground reaction forces $\boldsymbol{f}^{gr}$ for both feet since the contact forces between feet and ground are modeled as external applied forces.

If the kinematics of the movement $\boldsymbol{y}(t)$, $\dot{\boldsymbol{y}}(t)$, $\ddot{\boldsymbol{y}}(t)$ and the ground forces applied $\boldsymbol{f}^{gr}(t)$ are known, (4.1) can be solved for $\boldsymbol{\tau}$, since the number of degrees of freedom of the mechanical system f is greater or equal to the number k of unknown joint moments in the vector $\boldsymbol{\tau}$. On the other hand, the number of muscles m is always greater than the number of degrees of freedom of the skeletal system f, what leads to the mentioned underdetermination. It is reasonable to assume that the central nervous system distributes the muscle forces $\boldsymbol{f}^m$ in such a way as to optimize some physiological criteria, for instance, energy, fatigue or pain. This assumption is the basis for the optimization procedures to determine muscle forces presented in the following sections.

A typical formulation of the optimization is as follows: find $\boldsymbol{f}^m(t)$ that minimizes the cost function J, subject to equality constraints given by the equations of motion in the form $\boldsymbol{R}\,\boldsymbol{f}^m = \boldsymbol{b}(\boldsymbol{y}, \dot{\boldsymbol{y}}, \ddot{\boldsymbol{y}}, \boldsymbol{f}^{gr})$, which represent linear constraints on the muscle forces, where $\boldsymbol{b} = \boldsymbol{M}\ddot{\boldsymbol{y}} + \boldsymbol{k} - \boldsymbol{q}_r$. Additionally, inequality constraints are given either by bounded muscle forces or by bounded neural excitations as explained further on. Muscle forces are positive, since muscles cannot push, and are limited by upper bounds. Neural excitations are bounded by 0 and 1, refer to section 2.2.

4.1.1 Static Optimization Approach

The static optimization approach is a computationally efficient approach to solve the muscle force-sharing problem presented in the previous section. Static optimization is based on the assumption of an instantaneous cost function. This allows the solution of the force-sharing problem for each time instants t_j independently. The vector of muscle forces $\boldsymbol{f}_j^m$ at the instant t_j is searched that minimizes a cost function $J_s(\boldsymbol{f}_j)$. The optimization

is subject to physiological lower and upper bounds for the muscle forces and constraints given by the equations of motion (4.1) as

$$\boldsymbol{R}(\boldsymbol{y}_j)\,\boldsymbol{f}_j^m = \boldsymbol{M}(\boldsymbol{y}_j)\,\ddot{\boldsymbol{y}}_j + \boldsymbol{k}(\boldsymbol{y}_j, \dot{\boldsymbol{y}}_j) - \boldsymbol{q}_r(\boldsymbol{y}_j, \dot{\boldsymbol{y}}_j, \boldsymbol{f}_j^{gr}) \; , \tag{4.2}$$

where the index j denotes the values of the measured or prescribed variables at the time instant t_j.

Some variations of this approach were proposed in the literature mainly to better account for muscle physiology, refer to Tsirakos et al. [114], but the basic strategy remains the same. Several instantaneous cost functions J_s were proposed to solve the muscle force-sharing problem, refer, e.g. to Tsirakos et al. [114] and da Silva [26] for extensive reviews and applications. The cost function proposed by Crowninshield and Brand [25] is one of the most frequently employed due to its physiological background related to muscle fatigue and reads as

$$J_s = \sum_{i=1}^{m} \left(\frac{f_{ij}^m}{PCSA_i} \right)^3 \; , \tag{4.3}$$

where f_{ij}^m is the force applied by muscle i at time instant t_j, $PCSA_i$ is the cross-sectional area of muscle i, and m is the number of muscles considered.

4.1.2   Dynamic Optimization and Alternative Approaches

The investigation of human motion coordination and muscle recruitment by solving the optimal control problem using neural excitations as controls was used in the past, e.g., in Hatze [43], Hatze and Buys [45] and in Davy and Audu [27]. Pandy et al. [85] proposed the use of an alternative computational method for these problems consisting in the convertion of the optimal control problem into a parameter optimization problem, where the neural excitation histories are parameterized using a set of nodal points. This approach is claimed to circumvent the numerical difficulties that arise to solve the two-point boundary-value problem derived from the necessary conditions of optimal control theory. This approach has been successfully implemented to study normal walking using metabolic energy cost per unit of distance traveled as cost function, e.g. in Anderson and Pandy [8], Bhargava et al. [17], Umberger et al. [115]. These studies could mimic human normal walking patterns such as kinematics, optimal walking velocity and metabolic energy cost reasonably, using forward-dynamics models of the musculoskeletal system. Other application fields include simulation of vertical jumping (Spägele [103], Anderson and Pandy [7], Nagano and Gerritsen [78]), and cycling (Neptune and van den Bogert [82]). This approach is denoted dynamic optimization in opposition to static optimization (section 4.1.1).

As mentioned previously, the advantage of using dynamic optimization over static optimization resides in the consideration of the muscle contraction and activation dynamics, and in the possibility of using a time-integral cost function such as total metabolic

cost. However, performing dynamic optimization with large-scale musculoskeletal models is extremely costly in terms of computational effort, requiring as much as weeks for a 2-D musculoskeletal model with a reduced number of degrees of freedom, Menegaldo et al. [72], or months for a 3-D complex musculoskeletal model for walking using parallel super-computing facilities, Anderson and Pandy [8]. The high CPU times result mainly from the several numerical integrations of the differential equations (2.29) required.

The conventional applications of dynamic optimization, as the ones mentioned, look simultaneously for optimal controls, muscle forces and optimal motion patterns that minimize a cost function. For the cases in which the motion and the external applied forces are completely or partially prescribed or measured, the mechanical model must additionally track the known kinematics and apply the prescribed forces on the environment. This is achieved by augmenting the cost function with a term that quantifies the deviation from the prescribed kinematics and applied forces, see e.g. Neptune and van den Bogert [82], Neptune and Hull [80], Strobach et al. [107], Davy and Audu [27]. The introduction of the tracking term to the cost function transforms the problem in a multi-criteria optimization, what compromises the interpretation of the results, since the solution of the problem depend on the weighting factors chosen. Because the objective criteria are usually competing, the use of different weighting factors leads to different solutions.

In order to reduce the prohibitive computational effort required to solve the muscle force distribution problem by dynamic optimization new methods are being proposed. For instance, Menegaldo et al. [74] propose recently a dynamic optimization approach based on the tracking of the moments at the joints, which are computed for example from measured kinematics by conventional inverse dynamics. By avoiding the necessity of forward integration of the skeletal system dynamics, it considerably reduces the computational time required while considering the muscle activation and contraction dynamics and allowing for the use of time-integral cost functions. Although this method seems very promising with respect to computational time, it involves the solution of a multi-criteria optimization leading to the mentioned subjective choice of a solution among many possible ones.

Thelen et al. [112] and Thelen and Anderson [111] propose an algorithm called Computed Muscle Control (CMC) to solve the problem of muscle force distribution for known movement kinematics, based on a control algorithm that tracks the kinematics of a measured movement and uses measured external forces as input. This method is much faster than dynamic optimization approaches, because it requires only one forward integration of the state equations (2.29). It efficiently enforces the musculoskeletal system dynamics, but, in order to solve the muscle redundancy, it still requires the use of an instantaneous cost function. Therefore, in opposition to dynamic optimization, the use of a time-integral cost function such as total metabolic cost is not possible.

In this chapter two alternative methods are proposed, which present some advantages over the other methods described to solve the muscle redundancy problem. Both meth-

ods depend on the inversion of the contraction and activation dynamics. The first one named extended inverse dynamics and described in detail in section 4.3 permits the computation of muscle forces by using time-integral cost functions as total metabolic cost and is computationally more efficient than dynamic optimization. The second method, in fact a simplification of the first one, is described in section 4.4 and is called modified static optimization. It is based on the minimization of an instataneous cost function and characterized by constraints on the muscle forces at the current time step derived from the muscle forces at the previous time step that arise due to the activation and the contraction dynamics.

Table 4.1: Comparison among approaches to solve the muscle force-sharing problem; Static Opt. - static optimization; CMC - Computed Muscle Control; Mod. Static Opt. - modified static optimization; Dyn. Opt. 1 - dynamic optimization with tracking of kinematics; Dyn. Opt. 2 - dynamic optimization with tracking of joint torques; Ext. Inverse Dyn. - extended inverse dynamics.

Method	Act. & Contr. Dynamics	Computation Time	Time-Integral Cost Function	Multi-Criteria Optimization
Static Opt.	no	low	no	no
CMC	yes	low/medium	no	-
Mod. Static Opt.	yes	low	no	no
Dyn. Opt. 1	yes	high	yes	yes
Dyn. Opt. 2	yes	medium	yes	yes
Ext. Inverse Dyn.	yes	medium	yes	no

A comparison of the approaches proposed here with others from the literature is presented in Table 4.1. The approaches can be divided into two major groups depending on the use of instantaneous or time-integral cost functions. The latter methods are computationally more expensive due to the necessity of performing large-scale optimizations. In the first group the modified static optimization (Mod. Static Opt.) takes the activation and contraction dynamics into account and is most probably computationally less expensive than Computed Muscle Control (CMC). Among the methods based on a time-integral cost function, the extended inverse dynamics (Ext. Inv. Dyn.) and the dynamic optimization with tracking of joint torques (Dyn. Opt. 2) are computationally less expensive than dynamic optimization with tracking of kinematics (Dyn. Opt. 1). Because the extended inverse dynamics is completely based on an inversion of the musculoskeletal dynamics, the joint torques are automatically fulfilled, while for the dynamic optimization with tracking of joint torques (Dyn. Opt. 2) this is achieved by augmenting the cost function with a deviation term leading to a multi-criteria optimization. A disadvantage of the approaches based on inverse dynamics is the necessity of estimating time derivatives by finite differences what can lead to inaccuracies if the time steps are not sufficiently small.

Furthermore, methods based on forward integration of the dynamic equations allows a certain accommodation of the results to inconsistencies of the model or measurement errors. The choice of the approach to be used depends on the problem to be solved and is based on the specificities of each method.

4.2 Metabolic Cost as Optimization Criterion in Walking

The optimization techniques discussed in the previous section require the adoption of a cost function assumed to model a physiological criterion expected to be minimized by the central nervous system. The performance criterion adopted by the central nervous systems depends on the task to be accomplished. It is reasonable, for example, to expect that during jumping the muscles are recruited in such a way as to maximize the achieved height, or that people with pain in the knee joint will tend to distribute muscle forces in such a way as to reduce the knee joint forces. During human walking the metabolic cost is believed to play a key role, refer to Rose et al. [91].

Metabolic energy cost is a measurement of effort required from the person to perform a given activity, in particular during walking. For this reason, many studies assess the performance of prosthetic and orthotic devices and the success of therapies oriented to patients presenting gait disorders by experimental measurements of the metabolic energy expenditure (Schmalz et al. [99], Macfarlane et al. [68], Hsu et al. [51]). This quantity can be measured using, for example, metabolic gas analysis systems (see Macfarlane [67]), which are based on the oxygen uptake and the carbon dioxide production by the lungs, when there is a steady state, i.e., oxygen uptake and carbon dioxide output by the lungs equals the ones by the cells. A brief introduction on fundamentals of metabolic cost and a discussion on models to estimate it are found in section 2.2.3.

Experimental evidences show that people tend to walk in such a way as to minimize the metabolic energy expended per unit of distance traveled, i.e. the amount of energy required to walk a given distance. This can be shown, for instance, by data on metabolic cost measured for different walking velocities. Ralston [88] showed that the quadratic equation

$$\dot{E}_w = 32 + 0.0050v_w^2 \quad (cal/kg/min) \tag{4.4}$$

predicts well the metabolic cost rate expended as a function of average walking velocities for walking velocities up to approximately 100 m/min, where $\dot{E}_w$ is the metabolic cost rate per unit of body mass in $cal/kg/min$, and v_w is the average walking velocity in m/min. The dashed curve in Figure 4.1 shows the metabolic cost rate as a function of the walking velocity by (4.4), showing a monotone increase of the metabolic cost rate with the walking velocity. Dividing (4.4) by the average walking velocity v_w results in the

energy cost per unit of distance traveled as

$$E_w^t = \frac{32}{v_w} + 0.0050 v_w \quad (cal/kg/m) \; , \tag{4.5}$$

represented by the solid line in Fig. 4.1. Note that this curve presents a minimum at a walking velocity of 80 m/min ($\approx$ 1.33 m/s), what agrees well with naturally selected walking velocities chosen by humans.
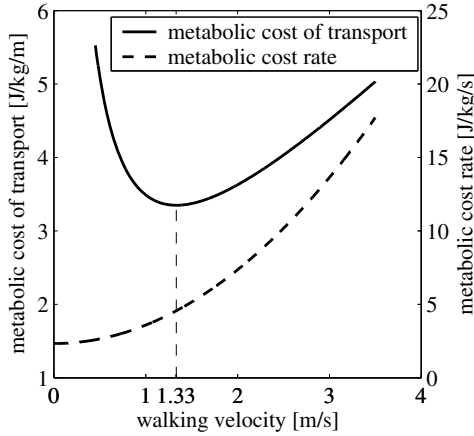
Figure 4.1: Metabolic cost rate and metabolic cost cost of transport during normal walking according to (4.4) and (4.5), respectively.

This experimental evidence contributes to the belief that the central nervous system controls muscle recruitment during walking in such a way as to minimize metabolic cost per unit of distance traveled. For this reason the metabolic cost per unit of distance traveled, or simply metabolic cost of transport, is adopted here as cost function. For the case of prescribed kinematics using total metabolic cost as objective function is equivalent to using metabolic cost of transport, since the walked distance is constant.

4.3 Proposed Optimization Approach

As discussed in section 4.1.1, the static optimization approach does not consider the muscle contraction and activation dynamics what can lead to the calculation of unphysiological muscle force patterns. Furthermore, it does not permit the use of time-integral cost functions such as total metabolic cost, which is assumed to be an important criterion during normal walking (section 4.2). In order to overcome these limitations, dynamic

optimization can be used as explained in section 4.1.2. However, the prohibitive computational effort required to find a solution prevents it from being widely used to solve the muscle-force distribution problem.

In this section we propose a novel optimization procedure that considers the contraction and activation dynamics, and permits the use of time-integral cost functions, while reducing the computation times compared to dynamic optimization. The proposed approach consists in formulating the problem as a large-scale optimization problem, whose optimization variables are the muscle forces at all time steps considered. The optimization is subject to equality constraints given by the equations of motion at all time steps, and lower and upper bounds for the neural excitations. The goal is to minimize a time-integral cost function, which is assumed to be the total metabolic cost, estimated using the recently proposed expressions of Umberger et al. [115], refer to section 2.2.3. Because the approach is based on the inversion of the activation and contraction dynamics it is named extended inverse dynamics.

Figure 4.2 shows the general optimization scheme of the proposed extended inverse dynamics. The optimization variables are parameterized muscle force time histories. The activation and neural excitations for each one of the muscles considered are computed by inverting the contraction and activation dynamics as explained in section 4.3.2 and section 4.3.3, respectively. The approach allows for the use of any time-integral cost function, but in this work the total metabolic cost is adopted for the reasons discussed in section 4.2. In section 4.3.5 the computation of the total metabolic cost from the available information is briefly explained. The optimization is subject to two sets of constraints: 1) the constraints represented by neural excitations bounded by 0 and 1; 2) the constraints given by the equations of motion at all time steps, which ensure the compatibility between the muscle forces and the measured skeletal system motion and ground reaction forces. Thus, optimal (parameterized) muscle force histories are searched for that minimize total metabolic cost, fulfill the constraints given by the equations of motion for the given kinematics and measured ground reaction forces (GRF), and ensure physiological neural excitations bounded by 0 and 1. In the next sections, the elements of the optimization scheme proposed are explained in details.

4.3.1 Parameterization of Muscle Forces

The parameterization of the force $\boldsymbol{f}_i^m(t)$ applied by the ith muscle is illustrated in Fig. 4.3. The discretization is performed using a set of n nodes uniformly distributed along the duration of the motion of interest resulting in a vector of time steps $\boldsymbol{t} = [t_1 \cdots t_j \cdots t_n]$, where $t_j - t_{j-1} = \Delta t$. The optimization variables are the muscle forces f_{ij}^m for all muscles i, $i = 1 \ldots m$, at all nodes j, $j = 1 \ldots n$, summarized in a $mn \times 1$-vector of global muscle
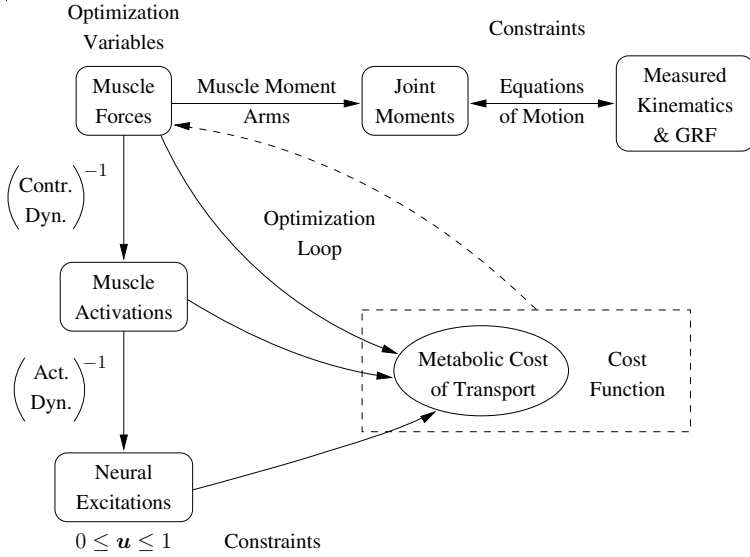
Figure 4.2: Schematic representation of the extended inverse dynamics approach for walking.

forces

$$\boldsymbol{F}^m = [\boldsymbol{f}_1^{mT} \quad \boldsymbol{f}_2^{mT} \quad \cdots \quad \boldsymbol{f}_j^{mT} \quad \cdots \quad \boldsymbol{f}_n^{mT}]^T , \qquad (4.6)$$

where $\boldsymbol{f}_j^m = [f_{1j} \cdots f_{ij} \cdots f_{mj}]^T$ is the vector of muscle forces at the time step t_j.
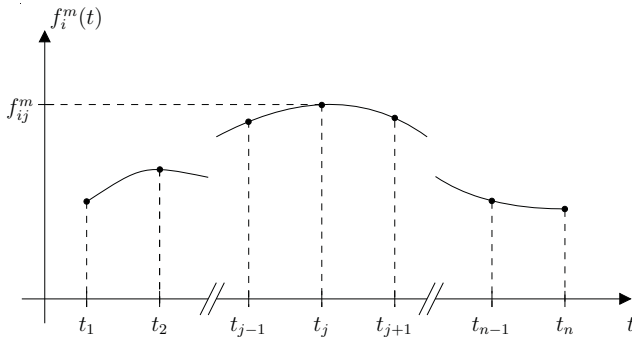
Figure 4.3: Schematic representation of the muscle force parameterization.

4.3.2   Inversion of the Contraction Dynamics

The inversion of the contraction and activation dynamics are important steps for the implementation of the approaches proposed in this chapter. This section shows how to invert the contraction dynamics and find the time history of the muscle activation of the ith muscle $a_i(t)$ from the measured kinematics $\boldsymbol{y}(t)$ and $\dot{\boldsymbol{y}}(t)$, and from the time history of the muscle force $f_i^m(t)$. In order to simplify the notation the index i is omitted.

The contraction dynamics for Hill-type muscle models, illustrated in Fig. (2.9), is mathematically described by a first order ordinary differential equation as

$$\dot{f}^m = \dot{f}^m(a, v^m, l^m, f^m) , \tag{4.7}$$

refer to section 2.2.2, where v^m, l^m and f^m are the muscle shortening velocity, length and applied force, respectively. The first step to invert this dynamics and find the time history of the muscle activation $a(t)$, is to compute the total muscle length l^m (including the tendon) and the total muscle shortening velocity v^m from the generalized coordinates in $\boldsymbol{y}$ and their time derivatives in $\dot{\boldsymbol{y}}$, refer to section 2.3, as

$$l^m = l^m(\boldsymbol{y}) , \tag{4.8}$$
$$v^m = v^m(\boldsymbol{y}, \dot{\boldsymbol{y}}) . \tag{4.9}$$

The second step consists in numerically differentiating the time history of the muscle force $f^m(t)$ obtaining $\dot{f}^m(t)$. Since the value of $f^m(t)$ is only available at discrete time steps t_j, $\dot{f}^m(t)$ is estimated only at these time instants by using the centered finite-divided-difference formula, Chapra and Canale [23], as

$$\dot{f}_j^m \approx \frac{f_{j+1}^m - f_{j-1}^m}{2\Delta t} , \quad j = 2 \ldots n - 1 , \tag{4.10}$$

for internal nodes or by using forward and backward finite-divided-difference formulas for the initial ($j = 1$) and final nodes ($j = n$), respectively,

$$\dot{f}_n^m \approx \frac{f_n^m - f_{n-1}^m}{\Delta t} , \tag{4.11}$$

$$\dot{f}_1^m \approx \frac{f_2^m - f_1^m}{\Delta t} . \tag{4.12}$$

In the case of perfectly periodic motions, centered finite-divided-difference formulas for the extreme nodes are preferred, since they deliver more accurate estimations of the derivatives, see e.g. Chapra and Canale [23]. The reason is that the errors due to the truncation of the Taylor series involved in the approximation of the derivative by centered finite differences are of order of Δt^2, while the errors caused by the use of forward or backward finite differences are of order of Δt.

The muscle serial elastic element (SE) length l^{se} and shortening velocity v^{se} can be then computed, respectively, by

$$l^{se} = l^{se}(f^m) \ , \tag{4.13}$$
$$v^{se} = v^{se}(\dot{f}^m) \ , \tag{4.14}$$

where $l^{se}(f^m)$ models the force-length relation of the SE, refer to section 2.2.2.

The contractile element (CE) shortening velocity, length and force, v^{ce}, l^{ce} and f^{ce}, are computed according to Fig. 2.5 and with $\alpha_p \approx$ constant, respectively, as

$$v^{ce} = (v^m - v^{se}) \cos \alpha_p \ , \tag{4.15}$$
$$f^{ce} = \frac{f^m}{\cos \alpha_p} - f^{pe}(l^{ce}) \ , \tag{4.16}$$
$$l^{ce} = \frac{l^m - l^{se}}{\cos \alpha_p} \ . \tag{4.17}$$

Finally, the muscle activation a is obtained by solving the muscle force-length-velocity relation (2.18) for a as

$$f^{ce} - f^{ce}(a, v^{ce}, l^{ce}) = 0 \ . \tag{4.18}$$

For some models of the muscle force-length-velocity relation, refer to section 2.2.2, a can be written explicitly as function of v^{ce}, l^{ce} and f^{ce}. For other models, this is not possible and a has to be computed numerically through (4.18) using a zero-finder algorithm, what considerably increases the computation time required. The procedure explained is repeated for all n nodes and m muscles considered.

4.3.3   Inversion of the Activation Dynamics

The activation dynamics is described by a first order ordinary differential equation as

$$\dot{a} = \dot{a}(a, u) \ , \tag{4.19}$$

where u is the neural excitation, refer to section 2.2.2. The first step to invert this dynamics and assess the time history of the neural excitation $u(t)$ is to find the time derivative $\dot{a}(t)$ of the muscle excitation $a(t)$. This is achieved by numerical differentiation of $a(t)$ by using finite-divided-difference formulas as the ones used to compute the time derivatives of muscle forces in section 4.3.2. The same considerations regarding the accuracy of the estimations described in section 4.3.2 apply to the computation of the time derivative of the muscle activation.

The values for the muscle activation $a(t)$ and its first time derivative $\dot{a}(t)$ are then inserted into (4.19). This results in an algebraic equation, which is either linear or quadratic in u. If a linear equation in u arises, e.g. for the activation dynamics model of Zajac [132], solving

(4.19) for u is trivial. If a quadratic equation in u arises, e.g. for the activation dynamics model (2.17) presented in Nagano and Gerritsen [78], the two roots of the polynomial are computed and one of them is chosen as solution. The choice of the appropriate root is in most cases straightforward. Checking which root is bounded by 0 and 1 and is most proximal to the muscle activation a proved to be efficient rules.

4.3.4 Constraints

The optimization is subject to two kinds of constraints as depicted in Fig. 4.2, the constraints that ensure the fulfillment of the equations of motion and the lower and upper bounds for the required neural excitations. The fulfillment of the constraints is checked at the nodes considered so that small infringements in the region between nodes might occur. The magnitude of these infringements is dictated by the number of nodes used. A properly chosen Δt leads to negligible inter-node infringements of the constraints.

Fulfillment of Equations of Motion

The vectors of muscle forces $\boldsymbol{f}_j^m$ contained in $\boldsymbol{F}^m$ have to satisfy the equations of motion (4.1) at all time instants t_j considered as

$$\boldsymbol{M}(\boldsymbol{y}_j)\,\ddot{\boldsymbol{y}}_j + \boldsymbol{k}(\boldsymbol{y}_j, \dot{\boldsymbol{y}}_j) = \boldsymbol{q}_r(\boldsymbol{y}_j, \dot{\boldsymbol{y}}_j, \boldsymbol{f}_j^{gr}) + \boldsymbol{R}(\boldsymbol{y}_j)\,\boldsymbol{f}_j^m\,, \quad j = 1 \ldots n\,. \tag{4.20}$$

Since the kinematics of the movement in $\boldsymbol{y}_j$, $\dot{\boldsymbol{y}}_j$, $\ddot{\boldsymbol{y}}_j$ and the ground reaction forces in $\boldsymbol{f}_j^{gr}$ are measured or specified, the only unknowns are the muscle forces $\boldsymbol{f}_j^m$. Rearranging (4.20) yields a set of linear equations in the elements of $\boldsymbol{f}_j^m$,

$$\boldsymbol{R}_j\,\boldsymbol{f}_j^m = \boldsymbol{b}_j\,, \tag{4.21}$$

where $\boldsymbol{b}_j = \boldsymbol{M}(\boldsymbol{y}_j)\,\ddot{\boldsymbol{y}}_j + \boldsymbol{k}(\boldsymbol{y}_j, \dot{\boldsymbol{y}}_j) - \boldsymbol{q}_r(\boldsymbol{y}_j, \dot{\boldsymbol{y}}_j, \boldsymbol{f}_j^{gr})$. Writing all the constraint equations given by the equations of motion at all time steps j in a single matrix equation yields

$$\boldsymbol{A}_{eq}\,\boldsymbol{F}^m = \boldsymbol{b}_{eq}\,, \tag{4.22}$$

where $\boldsymbol{A}_{eq}$ is a $fn \times mn$ block diagonal matrix and $\boldsymbol{b}_{eq}$ is a $fn \times 1$ vector, constructed as

$$\boldsymbol{A}_{eq} = \begin{bmatrix} \boldsymbol{R}_1 & & & & \\ & \boldsymbol{R}_2 & & \boldsymbol{0} & \\ & & \ddots & & \\ & & & \boldsymbol{R}_j & \\ & \boldsymbol{0} & & & \ddots \\ & & & & & \boldsymbol{R}_n \end{bmatrix}, \tag{4.23}$$

$$\tag{4.24}$$

$$\boldsymbol{b}_{eq} = [\boldsymbol{b}_1^T \quad \boldsymbol{b}_2^T \quad \cdots \quad \boldsymbol{b}_j^T \quad \cdots \quad \boldsymbol{b}_n^T]^T. \tag{4.25}$$

Bounds for Neural Excitations

The second group of constraints is represented by neural excitations bounded by 0 and 1 as

$$0 \le u_{ij} \le 1 , \quad i = 1 \ldots m , \quad j = 1 \ldots n . \tag{4.26}$$

The fulfillment of these constraints for the whole period considered guarantees the fulfillment of the lower and upper bounds for the activations and muscle forces. However, although not strictly necessary, constraints on muscle activations and muscle forces can be additionally formulated as

$$0 \le a_{ij} \le 1 , \quad i = 1 \ldots m , \quad j = 1 \ldots n , \tag{4.27}$$

$$0 \le \boldsymbol{f}_j^m \le \boldsymbol{f}_{max}^m , \quad j = 1 \ldots n , \tag{4.28}$$

where $\boldsymbol{f}_{max}^m$ is the vector of maximal achievable muscle forces (for each one of the muscles considered) which occur at the CE optimal length, for an infinite CE lengthening velocity, and for an activation level of 1. This measure, in special the explicit bounds on the optimization variables, reduces the search space of the optimization variables 'visited' during the optimization, what can, depending on the optimization algorithm employed, reduce the number of iterations required to achieve convergence to an optimum.

4.3.5 Cost Function

As mentioned previously, one of the advantages of using the extended inverse dynamics approach over static optimization is the use of time-integral cost functions as for example total energy expenditure. For the simulation results discussed further on, all dealing with normal and pathological gaits, the total metabolic cost is adopted as cost function for the reasons discussed in section 4.2. The total metabolic cost can be estimated by recently proposed phenomenological muscle energy expenditure models, e.g. Umberger et al. [115]. For a discussion refer to section 2.2.3.

With these expressions, metabolic cost rate is computed from the neural excitation u, muscle activation a and muscle CE force f^{ce}, length l^{ce} and shortening velocities v^{ce}, and from a set of muscle specific parameters $\boldsymbol{p}^m$ for all muscles m considered as

$$J_{EID} = \sum_{i=1}^{m} \left(\int_{t_1}^{t_n} \dot{E}_i(u_i(t), a_i(t), v_i^{ce}(t), l_i^{ce}(t), f_i^{ce}(t), \boldsymbol{p}_i^m) dt \right) , \tag{4.29}$$

where $\dot{E}_i$ is the metabolic cost rate for muscle i. The integral in (4.29) is solved numerically using the values of the variables at the discrete time instants t_j. Because all information in (4.29) required to compute $\dot{E}_i(t)$ is calculated from the kinematics $\boldsymbol{y}(t)$ and $\dot{\boldsymbol{y}}(t)$ and the muscle force $f_i^m(t)$, refer to sections 4.3.3 and 4.3.2, $J_{EID} = J_{EID}(\boldsymbol{F}^m, \boldsymbol{y}, \dot{\boldsymbol{y}})$ or $J_{EID} = J_{EID}(\boldsymbol{F}^m)$, because the skeletal system motion is measured or prescribed.

Thus, the extended inverse dynamics approach proposed consists in an optimization scheme formulated as: find the optimal global vector of muscle forces $\boldsymbol{F}_{opt}^{m}$ that minimizes the total metabolic cost (4.29), subject to linear equality constraints given by the equations of motion at all time steps (4.22), to the inequality constraints for the neural excitations (4.26), and, if advantageous, to the additional lower and upper bounds for the activations and muscle forces in (4.27) and (4.28), respectively.

4.3.6 Comments on the Implementation and on Optimization Methods

This section contains some few comments on the implementation and on the optimization method employed that are not included in the previous sections. In the case of non-periodic motions it is recommended to consider some nodes before and after the period of interest. This measure increases the accuracy of the numerical estimations of the time derivatives of the muscle forces and activations (sections 4.3.3 and 4.3.2) at the beginning and at the end of the period of interest. Furthermore, considering some period before and after the period of interest better accounts for the influence of these periods on the behavior of the model in the period of interest. As a general rule, the greater the periods before and after the period of interest, the more accurate the solution is for the period considered. Obviously, the lengths of these additional periods are limited by the availability of experimental data and by the extra computational effort. In the non-periodic motion (swing phase) used as example further on, the use of two additional nodes (corresponding to 0.04 s) proved to be sufficient, but the proper number of additional nodes might depend on the application and a study of the influence of the number of additional nodes on the solution might be necessary. For periodic motions as walking this problem does not occur.

The number of discretization nodes n is an important parameter for the optimization that considerably influences the computational effort and the accuracy of the solution. The number of optimization variables is proportional to n. On the one hand, the number of optimization variables and, therefore, n should be reduced in order to decrease the computational effort. On the other hand, increasing n reduces the errors caused in the numerical derivation using finite differences and improves the fulfillment of the constraints in the inter-node regions. The decision on n is based on the accuracy required and on the computational effort one is ready to accept.

There are many different numerical methods that can be used to solve a nonlinear optimization problem with nonlinear constraints. The Sequential Quadratic Programming (SQP), however, seems to be superior to any other methods with respect to efficiency and accuracy, see, e.g., Bestle [16]. The method consists in the successive solution of Quadratic Programming subproblems (QP), obtained by a quadratic approximation of

the Lagrangian function and a linear approximation of the nonlinear constraints. The solution of the QP subproblem defines a search direction, which is used in a line search procedure to obtain a new iterate for the optimization. Other details involved in the implementation of a SQP, like methods to update the Hessian of the Langrangian function or the choice of merit functions to solve the line search problem are not addressed here. The optimization problem arising from the formulation of the extended inverse dynamics is solved here using the *fmincon* function available in the Optimization Toolbox of Matlab®, which uses a SQP method.

4.4 Modified Static Optimization Approach

The approach to solve the muscle force redundant problem proposed in section 4.3 accounts for the activation and contraction dynamics and uses a time-integral cost function. The price for these desirable features is a computational effort some orders of magnitude higher than the one required in static optimization, although being lower than the one required for dynamic optimization, see Tab. 4.1. The high computational effort is a limiting factor for the use of the more elaborate approaches dynamic optimization and extended inverse dynamics.

Specially in applications in which a rather gross estimation of muscle forces is sufficient and instantaneous cost functions are assumed to be reasonable models of the underlying muscle force distribution laws adopted by the central nervous system (CNS) static optimization will still be the first choice. However, neglecting completely the activation and contraction dynamics, what assumes the muscle as a perfect force generator, capable of delivering the required amount of force instantaneously, can lead to unphysiological solutions. In this section an alternative approach is proposed, which modifies the static optimization approach in such a way as to consider the muscle activation and contraction dynamics, while requiring a similar, reduced computational effort.

The approach, named modified static optimization, formulates the optimization problem in the same way as in the static optimizations for each time step considered, refer to section 4.1.1, with the difference of defining additional nonlinear constraints that ensure neural excitations bounded by 0 and 1. This measure guarantees the compatibility of the current muscle forces with the activation and contraction dynamics. These additional constraints can be interpreted as additional upper and lower bounds on the current muscle forces obtained by the maximal allowed variations of muscle forces that are still compatible with the activation and contraction dynamics. The upper and lower bounds, $f_{j,max}^m$ and $f_{j,min}^m$, respectively, are implicitly formulated depending on the states, muscle forces f_{j-1}^m and activations a_{j-1}, at the previous time instant t_{j-1} as depicted in Fig. 4.4.

Therefore, the formulation of the optimization problem for the time step j is identical to
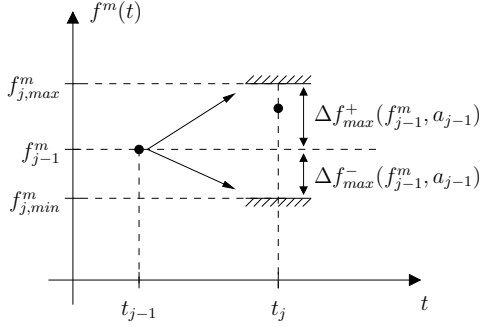
Figure 4.4: Schematic representation of the implicit additional lower and upper bounds on the muscle force f_j^m as a function of the states at the previous time instant t_{j-1} in the modified static optimization approach. (The index i referring to a specific muscle is omitted.)

the one for the static optimization, section 4.1.1, with additional upper and lower bounds for the neural excitations of the muscles considered as

$$0 \leq u_{ij} \leq 1 \,, \quad i = 1 \ldots m \,, \quad j = 2 \ldots n \,. \tag{4.30}$$

The computation of the neural excitations requires the inversion of the contraction and activation dynamics as done for the extended inverse dynamics approach, sections 4.3.2 and 4.3.3, with the difference of using only the information from the previous time steps. The procedure is briefly explained in the following focusing on the differences from the extended inverse dynamics. The index i referring to a specific muscle is omitted.

The first step consists in computing the first derivatives of the muscle forces $\dot{f}_j^m$ from the values of the muscle forces at the previous and current time steps f_{j-1}^m and f_j^m, respectively, using a backward finite-divided formula as, for example,

$$\dot{f}_j^m = \frac{f_j^m - f_{j-1}^m}{\Delta t} \,, \quad j = 2 \ldots n \,. \tag{4.31}$$

The total muscle length l_j^m and shortening velocity v_j^m are computed from the generalized coordinates $\boldsymbol{y}_j$ and their derivatives $\dot{\boldsymbol{y}}_j$ using (4.8) and (4.9), respectively. With this information the contraction dynamics (4.7) is inverted as explained in section 4.3.2 in such a way a_j is computed by

$$a_j = a_j(\dot{f}_j^m, v_j^m, l_j^m, f_j^m) \,, \quad j = 2 \ldots n \,. \tag{4.32}$$

The next step consists in the inversion of the activation dynamics which requires the estimation of the first time derivatives of the activations $\dot{a}_j$ by using also a backward finite-divided formula as

$$\dot{a}_j = \frac{a_j - a_{j-1}}{\Delta t} \,, \quad j = 2 \ldots n \,. \tag{4.33}$$

It follows the computation of the neural excitations, as explained in section 4.3.3, by inserting a_j and $\dot{a}_j$ into (4.19) and solving it for u_j as

$$\dot{a}_j - \dot{a}_j(a_j, u_j) = 0 , \quad j = 2 \ldots n . \tag{4.34}$$

The explained procedure to estimate the neural excitation at t_j shows that u_j is a function of the muscle force f_{j-1}^m and activation a_{j-1} at the previous time step t_{j-1}, of the time step size Δt, of the muscle total length l_j^m and shortening velocity v_j^m at t_j, and of the searched muscle force f_j^m at t_j. This results in implicit constraints on the searched muscle forces f_j^m given by the bounds on the neural excitation in the form

$$0 \leq u_j(f_j^m, f_{j-1}^m, a_{j-1}, \boldsymbol{y}_j, \dot{\boldsymbol{y}}_j, \Delta t) \leq 1 , \quad j = 2 \ldots n , \tag{4.35}$$

for all muscles considered. Therefore, muscle forces at t_j are searched that minimize the instantaneous cost functions of section 4.1.1, and fulfill the nonlinear constraints given by (4.35) and the linear constraints given by the equations of motion (4.20). The first time step in the modified static optimization receives a special treatment. The muscle forces $\boldsymbol{f}_1^m$ at the first time step t_1 are computed by conventional static optimization without the additional constraints on the neural excitations. The activations a_{i1}, $i = 1 \ldots m$, at t_1 are approximately estimated by inversion of the contraction dynamics, as explained in section 4.3.2, with the difference that the required estimations of the derivatives of the muscle forces $\dot{\boldsymbol{f}}_1$ are obtained by a forward finite-divided-difference formula using the muscle forces computed at the first and second time steps, $\boldsymbol{f}_1^m$ and $\boldsymbol{f}_2^m$, respectively, computed by conventional static optimization.

The constraints on the rate of change of the muscle forces can be so restrictive, that infeasibilities may occur at a time instant for which no solution for the muscle forces can be found that fulfills all the constraints. This occurs to a great extent due to the fixed values of the computed muscle forces at the previous time steps. The incidence of such infeasibilities for the extended inverse dynamics approach is much lower, because there the complete time histories of the muscle forces can be accommodated in such a way as to guarantee fulfillment of the constraints at all time steps. One drawback of the modified static optimization is the necessity of using backward finite-divided-difference formulas to estimate derivatives numerically, what causes greater truncation errors in comparison to centered finite-divided-difference formulas. Furthermore, the activations at the initial time step have to be determined approximately, because no values for the muscle forces at the previous time step are available.

4.5 Application to Normal and Pathological Gaits

In this section the approaches to solve the muscle force-sharing problem in biomechanics proposed in this chapter are applied to the normal and to mechanically disturbed gaits

measured in a gait analysis laboratory as explained in chapter 3. The extended inverse dynamics and the modified static optimization are compared to the static optimization and to other approaches proposed in the literature, see Table 4.1. Only the lower limb of the subjects is considered.

4.5.1   Model of the Musculoskeletal System

Although 3-D models of the skeleton can better assess the aspects of gait, specially in the frontal plane, as shown in chapter 3, walking is a motion occuring predominantly in the sagittal plane. For this reason, less complex 2-D models of the musculoskeletal system can still be used to investigate the salient phenomena during walking, while requiring a reduced computational effort and permitting a more straightforward interpretation of the results.

Therefore, a 2-D mechanical model of the skeletal system of the right lower limb is adopted here, composed by three rigid bodies, the thigh, the shank and the foot. The motion is performed in the sagittal plane and is described by three generalized coordinates and two rheonomic constraints, refer to Fig. 4.5b. The generalized coordinates are the angle α describing the rotation of the thigh, the angle β describing the knee flexion, and the angle γ for the ankle plantar flexion. The two rheonomic constraints are the horizontal and vertical positions of the hip joint, x_{hip} and z_{hip}, respectively. The pelvis and trunk are assumed to remain in the vertical position throughout the gait cycle, what is reasonable for normal walking. The masses, center of mass locations, and the mass moment of inertia of the three segments in the sagittal plane are computed for both subjects using the tables in de Leva [28] as functions of the subject's body mass, stature, thigh length and shank length, refer to Appendix A.3. The motion and the ground reaction forces were measured in a gait analysis laboratory as explained in section 3.

Since the motion measured is 3-D, a transformation of the motion and of the ground reaction forces into the sagittal plane is necessary. The motion of the hip joint along the y-axis is simply ignored. The thigh angle α is obtained by describing the rotation of the thigh in the global coordinate system by Euler angles defined as consecutive finite rotations about the axes y, x and z, respectively, and assuming α as equal to the first Euler angle. The angles β and γ are assumed to be equal to the angles $\beta_{3,4}$ $\beta_{4,5}$ of the vector of generalized coordinates for the 3-D inverse dynamics model (3.1), i.e. to the first Euler angles describing the relative rotation of the shank with respect to the thigh, and of the foot with respect to the shank, respectively. The ground reaction forces are transformed by neglecting the y-components of the ground reaction force and of the point of application, and by neglecting the free moment applied about the vertical axis. Thus, the ground reaction forces are characterized by the x and z components of the ground forces f_x^{gr} and f_z^{gr}, respectively, and by their point of application, or center of pressure,
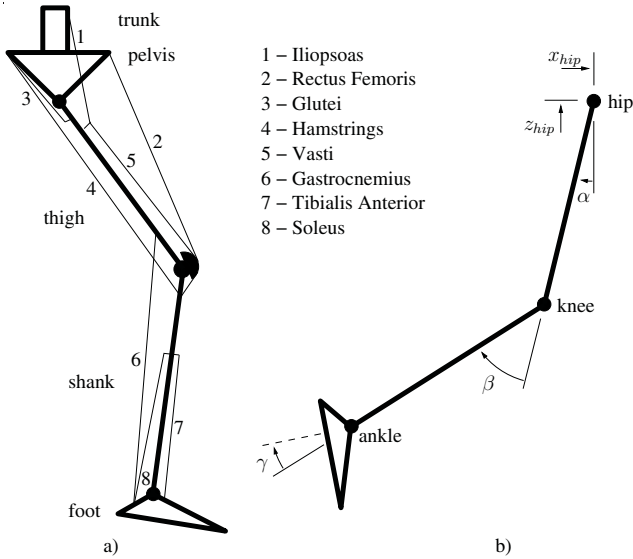
Figure 4.5: Musculoskeletal model of the lower limb adopted.

c_x depicted in Fig. 4.6, all summarized in a vector $\boldsymbol{f}^{gr}$.
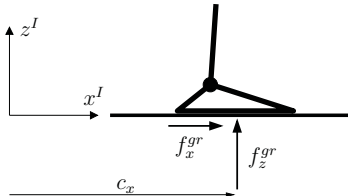
Figure 4.6: Characterization of the ground reaction forces in the sagittal plane.

The eight muscle groups considered in this analysis are shown in Fig. 4.5a. The Hill-type muscle model adopted is composed by a contractile element CE and a series elastic element SE, while the force of the parallel elastic element PE is set to zero, Fig. 2.5. In this model all the structures in parallel to the CE and the SE are represented by total passive moments at the joints, which include the moments generated by all other passive structures crossing the joints, like ligaments, too. The formula for the passive moments at the hip, knee and ankle are functions of α, β and γ as proposed by Riener and Edrich [90]. A linear damping is added to the knee and hip joints and their values are the approximate average values obtained by pendulum experiments performed by Stein et al. [105].

The models adopted for the muscle activation and muscle force-length-velocity relation, refer to section 2.2.2, are based to a great extent on the models in Nagano and Gerritsen [78] with some few modifications. A modification of activation dynamics in Nagano and Gerritsen [78] proposed in Umberger et al. [115] is adopted, where the time constants for activation and de-activation are computed from the muscle fiber type distribution using an empirical formula. The force-length-velocity relation in Nagano and Gerritsen [78] is modified to avoid discontinuities in the cost function and to reduce the computational effort to invert the contraction dynamics. The expressions adopted as well as an explanaition and justification of the modifications done are presented in Appendix A.1. The modifications of the force-velocity relation are small and a significant loss of quality in the results obtained for large-scale musculoskeletal models is unlikely.

4.5.2   Application to the Normal Walking

The muscle forces are computed for the measured kinematics and ground reaction forces of the normal walking for the both subject (chapter 3). The results obtained by using extended inverse dynamics (EID), modified static optimization (MSO) and the static optimization (SO) for the normal gait of both subjects are presented in Tabs. 4.2 and 4.3. For the SO and for the MSO the cost function proposed by Crowninshield and Brand [25] is used, refer to section 4.1.1. The cost function for the EID adopted is the total metabolic cost (4.29). The metabolic cost for the MSO is computed by inverting the contraction and activation dynamics (sections 4.3.2 and 4.3.3) after the computation of optimal muscle forces for each time instant j. In order to consider the periodicity of the gait cycle, although the measured kinematics was not perfectly periodic, a time step is used between the initial time and the final time of the gait cycle. In this way a dependency is introduced between the states at the beginning and at the end of the cycle, without the hard constraints of equal initial and final states, which is not achieved because of the natural variability of the walking motion and because of experimental errors. All the optimization problems were solved using the Sequential Quadratic Programing algorithm implemented in the function *fmincon* available in the Optimization Tollbox of Matlab®, as explained in section 4.3.6. The initial guesses for the muscle forces in the static optimization are zero. The initial guesses used in the many low-dimension optimizations involved in the MSO and in the unique large-scale optimization in the EID are the optimal muscle forces obtained as solutions of the SO.

The analysis of the results in Tables 4.2 and 4.3 shows that the computation time required for the EID approach is four orders of magnitude higher than the computation times required for the SO and MSO. This difference can be explained by the much higher dimension of the optimization problem in the EID with respect to the optimizations in the SO and MSO. While in the EID a unique large-scale optimization problem with several optimization variables is solved, the SO and the MSO require the solution of many

Table 4.2: Comparison among approaches to solve the muscle force-sharing problem for the measured normal walking of subject 1; Static Opt. - static optimization; Mod. Static Opt. - modified static optimization; Ext. Inverse Dyn. - extended inverse dynamics.

Subject 1	Initial Guess	Computation Time (s)	Opt. Variables	Metabolic Cost (J)
Static Opt. (SO)	$\boldsymbol{f}_{j,0}^{m} = 0$	5.3	8 (67x)	-
Mod. Static Opt. (MSO)	solution SO	7.6	8 (67x)	254.8
Ext. Inverse Dyn. (EID)	solution SO	$4.5 \cdot 10^4$	400 (8x50)	201.0

Table 4.3: Comparison among approaches to solve the muscle force-sharing problem for the measured normal walking of subject 2; Static Opt. - static optimization; Mod. Static Opt. - modified static optimization; Ext. Inverse Dyn. - extended inverse dynamics.

Subject 2	Initial Guess	Computation Time (s)	Opt. Variables	Metabolic Cost (J)
Static Opt. (SO)	$\boldsymbol{f}_{j,0}^{m} = 0$	6.0	8 (64x)	-
Mod. Static Opt. (MSO)	solution SO	6.2	8 (64x)	238.7
Ext. Inverse Dyn. (EID)	solution SO	$12.1 \cdot 10^4$	400 (8x50)	168.3

low-dimension optimization problems. This is the cost that has to paid for the use of a time-integral cost function as metabolic cost. Although the computational effort for the EID (33.6 hours) can be considered high with respect to the SO and MSO, it is probably much lower that the required for a dynamic optimization with tracking of the kinematics, which can require as much as weeks or months for a solution, see e.g. Menegaldo et al. [72] and Anderson and Pandy [8], as discussed in section 4.1.2.

The results show the computational efficiency of the MSO. The MSO required a computational effort comparable to the one required by the SO, while considering the activation and the contraction dynamics. This shows the potential of the MSO for applications that need fast and realistic estimations of muscle forces, muscle activation and neural excitations when instantaneous cost function are adopted. The MSO can, however, lead to infeasibilities due to the restrictive constraints imposed by the limitation on the amount of allowable changes in the muscle forces, as discussed in section 4.4. Nevertheless, the possible infeasibilities cannot be attributed to a fail of the method, but rather to inconsistencies arising from errors in the measurements, oversimplification of the models or assumption of an incorrect cost function.

The metabolic cost for the SO cannot be estimated using (4.29), because the muscle forces computed lead to muscle activations and neural excitations that infringe their lower and upper bounds, being out of the range to which these expressions are valid.

This occurs because the SO does not consider the activation and contraction dynamics. On the contrary, the solution for the muscle forces delivered by the MSO can be used to compute muscle activations and neural excitations that fulfill the constraints by inverting the contraction and the activation dynamics. These values can then be inserted into (4.29), which delivers estimations of metabolic cost as shown in Tables 4.2 and 4.3. The metabolic cost estimated from the muscle forces computed with the MSO is 27% and 42% greater than the metabolic cost estimated with the EID, for subject 1 and subject 2, respectively. A difference is expected, since the EID minimizes the metabolic cost, while in the MSO the instantaneous cost function of Crowninshield and Brand [25] is minimized, which is related to muscle fatigue. The relatively big differences show that the cost function of Crowninshield and Brand [25] is not well related to the metabolic energy consumption.

The absolute values of the total metabolic cost of transport obtained with the EID for subjects 1 and 2, assuming the total metabolic cost expended during walking is approximately two times the expended for one of the legs, are 311 J/m and 267 J/m, respectively, which agree well with values computed using the expression (4.5) proposed by Ralston [88], 247 J/m and 264 J/m, respectively. The difference for subject 1 is of reasonable 21%, while the one for subject 2 is of only 1%. The good agreement observed, specially for subject 2, is remarkable, although for design purposes the accurate estimation of absolute values for the metabolic cost is not of primary importance. More important is an estimator that account well for the underlying energetic phenomena and deliver a good basis for comparisons. The fact that the values obtained by expression (4.5) are an average, while the metabolic cost can differ considerably among subjects, can explain in part the greater difference observed for subject 1. Moreover, the strongly simplified model of the complex musculoskeletal system used is expected to cause deviations from the real values.

The optimal muscle forces for the normal gait of subject 1 computed using SO, MSO and EID and the corresponding muscle activations and neural excitations are presented in Figures 4.7, 4.8 and 4.9, respectively. Figure 4.7 shows clearly the infringement of the lower and upper bounds for the neural excitations indicating nonphysiological muscle force histories. Figure 4.8 shows that the MSO smoothes the muscle force curves avoiding unphysiological fast variations, what maintains the neural excitations bounded by 0 and 1. The smoothing effect is specially visible for the muscle groups rectus femoris (RF) and vasti (Vas). Also the results of the EID in Fig. 4.9 fulfill the bounds on the activations and neural excitations.

The constraints on the neural excitations cause cocontraction, even in single joint antagonist muscles, although cocontraction of antagonists is clearly noneconomical. This occurs due to the fact that muscles are not ideal actuators and cannot be switched on and off instantaneously. Indeed, the single joint antagonistic muscle pairs iliopsoas (Ilio) and glutei (Glu), and tibialis anterior (TA) and soleus (Sol) present practically no cocontraction, i.e. almost no simultaneous activation, when SO is used, see Fig. 4.7. On the contrary, if

Figure 4.7: Muscle forces, activations and neural excitations obtained with the static optimization (SO) for the normal gait of subject 1; TOr - toe off of the right foot; HSr - heel strike of the right foot.

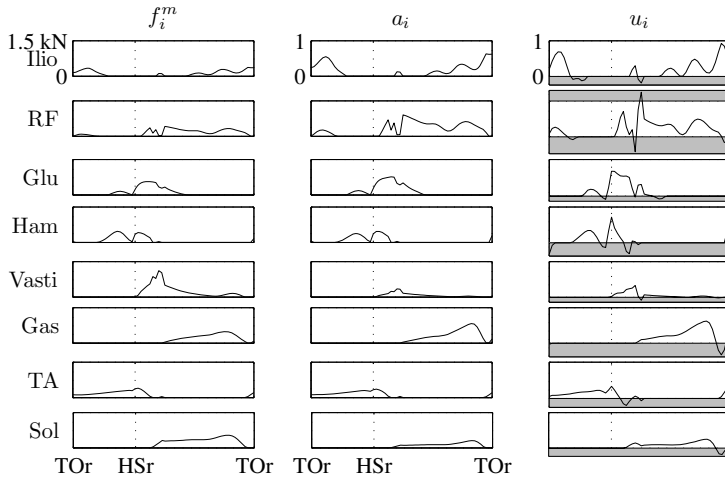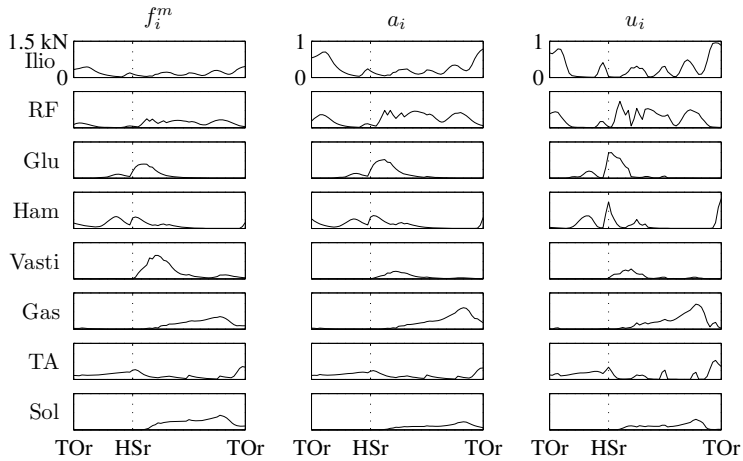Figure 4.8: Muscle forces, activations and neural excitations obtained with the modified static optimization (MSO) for the normal gait of subject 1.

MSO or EID are used cocontraction is observed for these muscles, refer to Figs. 4.8 and 4.9. In order to reduce energy consumption, the results of EID have less cocontraction than the results of MSO, but a considerable amount of cocontraction in the results of EID
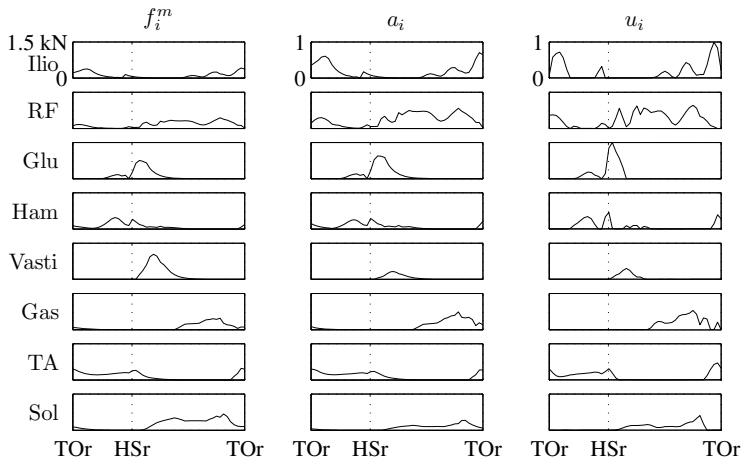
Figure 4.9: Muscle forces, activations and neural excitations obtained with the extended inverse dynamics (EID) for the normal gait of subject 1.

can still be observed for the mentioned muscles, specially at the regions of activation and de-activation. In spite of the relatively reduced differences in the muscle force histories between the results of the MSO and of the EID, the difference in the metabolic cost estimation is of about 21%. This shows a high sensitivity of the metabolic cost with respect to variations in the muscle force histories.

4.5.3 Application to the Walking with Disturbances

In this section the extended inverse dynamics approach is applied for the study of the mechanically disturbed gaits described in chapter 3. Firstly, the walking of subject 2 with a ski boot is compared to his normal walking for the whole gait cycle. It follows a comparison of the swing phase of the gait of subject 2 with and without a weight attached to the ankle joint and a discussion of the adaptations arising when a mechanical disturbance is introduced.

Ski Boot Walking

In this section the burden imposed by the addition of a mass to the foot and the immobilization of the ankle is discussed by means of a comparison between the computed muscle forces and the metabolic cost of transport arising during the normal walking and the walking with a ski boot, refer to section 3.1.1. Figure 4.10 shows the muscle force

histories for the both experiments analyzed for the right leg of subject 2. A considerable change in the muscle force patterns can be recognized.

In the ski boot experiment the tibialis anterior (TA) and the soleus (Sol) are deactivated throughout the gait cycle. This is expected for these uniarticular muscles, since the ski boot represents a kinematic constraint and the moment at the ankle joint required to keep it immobilized is applied by the ski boot structure and by the gastrocnemius (Gas). The Gas is less active in the ski experiment because it does not have to contribute to the ankle plantar flexion moment. The reduced activation observed during the second half of the stance phase arises exclusively due to the contribution to the knee flexion moment.

The activity of all other muscles but he hamstrings (Ham) clearly increases in the ski boot experiment. The most salient difference is observed for the muscle group vasti (Vasti), which is active in the first halve of the stance phase to prevent flexion of the knee at weight acceptance. The increased knee extension moments in the beginning of the stance phase can be attributed to the ankle immobilization as explained in section 3.4.2. During the beginning of the swing phase an increase in the activity of the iliopsoas (Ilio) and rectus femoris (RF) is observed to provide hip flexion after toe off. In the second half of the swing phase the hamstrings (Ham) and the glutei (Glu) act decelerating the flexion of the hip and knee joints and gradually deactivate toward the end of the swing phase while the RF becomes activated to keep knee and hip extended immediately before heel strike.

Figure 4.10: Muscle forces obtained with the extended inverse dynamics approach for the subject 2 walking normally and wearing a unilateral ski boot in the right foot; TOr - toe off of the right foot; HSr - heel strike of the right foot.

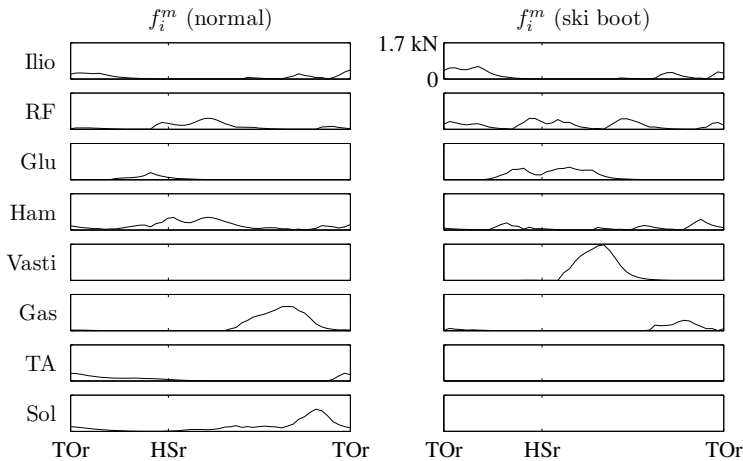The intensive activity of the muscles Ilio, RF, Glu and specially Vasti increases consider-

ably the energy expenditure during the walking with a ski boot. Indeed, the metabolic cost of transport estimated for the affected, right leg increases from 133.5 J/m for the normal walking to 208.0 J/m, what represents an additional cost of about 56%. Therefore, the use of a ski boot, causing an increase in the foot mass and the immobilization of the ankle joint, represents a substantial burden for the walking from the energetic point of view.

Ankle Weight Walking and Adaptation

In this section the effect of adding a 1.7 kg ankle weight during the swing phase of the gait on the metabolic cost is investigated. Furthermore, the natural adaptation of the motion when a disturbance is introduced is shown. The estimations of metabolic cost are obtained using the extended inverse dynamics approach with the total metabolic cost as cost function. The bars in Fig. 4.11 show the metabolic cost estimated for three different scenarios. The first bar from the left shows the metabolic cost for the measured kinematics of the lower limb of subject 2 during the swing phase without weight, 48.3 J. The second bar shows the metabolic cost for the measured kinematics of subject 2 during the swing phase with a 1.7 kg ankle weight, 49.9 J. The third and last bar shows the metabolic cost using the kinematics measured for the normal walking and adding a 1.7 kg ankle weight to the skeletal system model, 59.6 J.

As expected, the swing phase with an ankle weight requires a higher metabolic cost than the normal, although the observed difference of 3% is slight. An interesting result is shown by the third bar from the left. It shows an increase of about 23% in the metabolic cost if the kinematics were maintained the same as for the normal walking when the ankle weight is added. This means that, after the addition of the ankle weight, the subject naturally adapted the motion of the lower limb in such a way as to reduce the metabolic cost required, leading to a slight increase of energy expenditure with respect to the undisturbed gait. If the adaptations in the kinematics were not performed, the increase in the metabolic cost would be much higher (third bar in Fig. 4.11). This observation evidence the importance of the motion adaptations in the reduction of energy expenditure during gait. Chapter 5 is devoted to an extension of the extended inverse dynamics that permits the search for optimal motion patterns in additional to optimal muscle forces.

4.5.4   Validation

In order to validate the extended inverse dynamics approach two studies are performed. In the first study the neural excitations obtained with the EID are used as controls for a forward integration of the musculoskeletal dynamics. The kinematics and metabolic cost estimations are then compared. The second study consists in a comparison between the
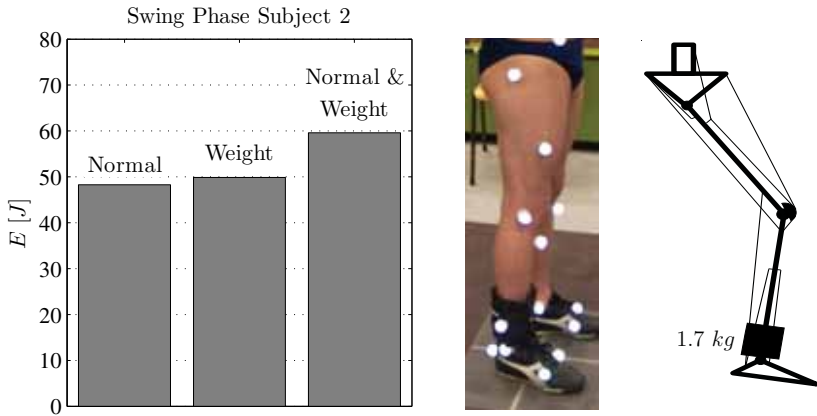
Figure 4.11: The bars in the diagram in the left show the metabolic cost for the swing phase of subject 2, from left to right, during normal walking, during walking with a 1.7 kg ankle weight, and during the walking with the normal kinematics and an added 1.7 kg ankle weight. The estimations are obtained using the extended inverse dynamics approach. In the right a schematic representation of the musculoskeletal model of the lower limb with the ankle weight added is depicted. In the middle a picture of the lower limb of subject 2 with an ankle weight attached to his ankle is shown.

activations obtained by the EID for the normal walking of one subject and EMG-data available in the literature.

Inverse and Direct Dynamics

One way to validate the extended inverse dynamics approach is to use the solution for the neural excitations obtained with the EID as controls for a numerical integration of the differential equations of the musculoskeletal model. If the kinematics obtained in this way agrees well with the measured one, used as input for the EID, it can be concluded that the approach works well and that the discretization adopted is sufficiently fine, i.e. the number n of nodes is enough to guarantee a proper modeling of the phenomenon. Figure 4.12 shows a scheme of the described procedure on the left hand side, and the results of the comparison using the kinematics of the swing phase of subject 1 walking normally on the right hand side.

The kinematics $\boldsymbol{y}_m(t)$ of the lower limb of subject 1 during the swing phase serves as input to the EID approach to compute optimal neural excitations in $\boldsymbol{u}_{EID}$ and total metabolic cost E_{EID}. The neural excitations at the nodes are then linearly interpolated and used as controls to a numerical, forward integration of the differential equations with
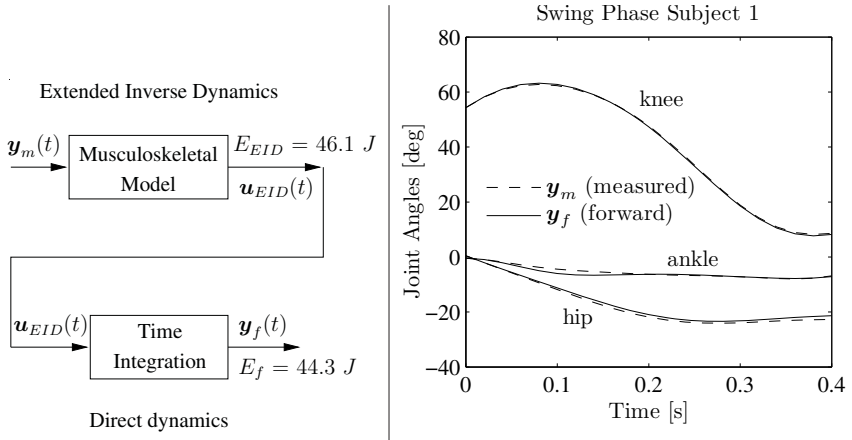
Figure 4.12: Schematic representation of the procedure to validate the EID approach on the left hand side. The right hand side shows a comparison between the measured kinematics $\boldsymbol{y}_m(t)$ of the swing phase of subject 1 walking normally with the kinematics $\boldsymbol{y}_f(t)$ computed by forward-integrating the musculoskeletal dynamics using the neural excitations obtained with the EID as controls.

initial conditions for the states, muscle forces and muscle activations at $t = 0$, given by the values computed with the EID. The integration delivers the time history of the generalized coordinates $\boldsymbol{y}_f(t)$. A new estimation of the total metabolic cost E_f is then computed.

The results of the described procedure are shown in Fig. 4.12. On the left hand side, the metabolic cost estimations obtained with the EID and with the forward integration are shown, 46.1 J and 44.3 J, respectively, representing a small difference of about 4%. The comparison of the kinematics on the right hand side of Fig. 4.12 features a good agreement. The results indicate, therefore, that the method works well and that the discretization is sufficiently fine by showing a good reconstruction of the original measured kinematics and a reasonable match of the metabolic cost estimations. In fact, this comparison would show an even better agreement if the states at all nodes computed with the EID were used for a numerical integration throughout the inter-node times.

Comparison to EMG Data of Literature

As mentioned previously, muscle forces cannot be directly measured in a non-invasive way, so that a direct comparison of the solution of the muscle force-sharing problem with the real muscle forces is in general not possible. In order to assess to some extend the

muscle activity electromyograms (EMG) are used. Electromiograms are the electrical signal associated with the muscle contraction, refer to chapter 9 of Winter [123], and are usually measured by electrodes placed on the skin. The electrodes record the sum of all *motor unit action potentials* transmitted along muscle fibers, refer to section 2.2.2. The difficulties in the interpretation of raw EMG gave rise to processing techniques. The signal obtained by rectification of the raw EMG followed by its filtering by a low-pass filter is called the linear envelope of the EMG. This signal was shown to follow well the variation patterns of muscle force during isometric contraction, i.e. an increase in the magnitude of the linear envelope of the EMG represents an increase in muscle force during isometric contraction. Unfortunately, the relation is not always linear for general contractions and the magnitude of the EMG signal is affected by the distance of the electrode from the motor units. For these reasons a quantitative comparison of the linear envelope of the EMG with muscle activations is not possible. On the other hand, the linear envelope of the EMG can be used in a qualitative analysis giving a clue to the activation and deactivation times and to the general variation patterns of the muscle activations.

The validity of the model employed and of the EID approach, and the correctness of the experimental data can be assessed to some extent by comparing the muscle activations with EMG data available in the literature. If a good agreement is achieved, it can be claimed that reasonable results are delivered with the measured data and with the model and muscle force-sharing approach adopted. Figure 4.13 shows such a comparison for the normal walking of subject 1. On the left the results for the muscle activations obtained with the EID approach are presented. On the right inter-subject averages of the linear envelopes of EMG data published in Winter [122], including the dashed curves indicating one standard deviation, are shown. Note that the magnitude of the linear envelopes of the EMG are normalized by the maximal achieved value of the sum of the average and one standard deviation. Therefore, the magnitudes of the muscle activations on the left, and of the processed EMG on the right cannot be compared.

The comparison of the curves in Fig. 4.13 shows some agreement between the activation patterns and the linear envelopes of the EMG data, despite the use of extremely simplified models of the musculoskeletal system, and the unavoidable errors contained in the experimental data. These results together with the results of the previous section and the reasonable estimation of metabolic cost shown in section 4.5.2 indicate that the adopted model, and the EID approach with the adopted discretization can be employed to study the salient behavior of the musculoskeletal system during walking.
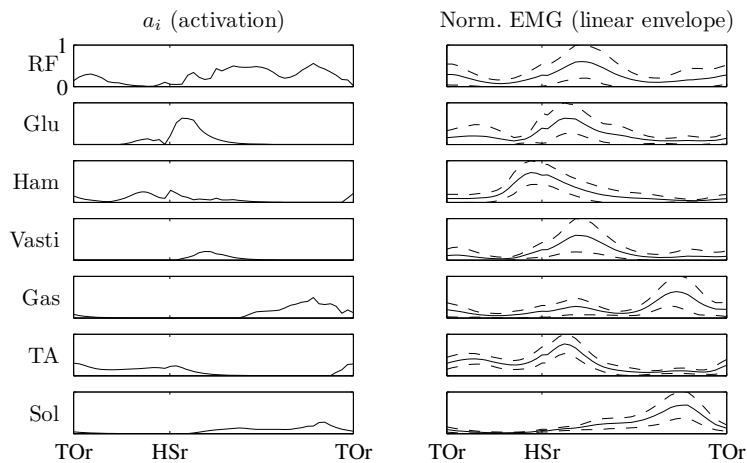
Figure 4.13: Comparison of the activations a_i with the normalized linear envelope of the EMG presented in Winter [122] showing one standard deviation. The data used for the muscle groups in Winter [122] are for the following muscle groups: rectus femoris, gluteus maximus, medial hamstrings, vastus lateralis, lateral gastrocnemius, tibialis anterior, and soleus.

Chapter 5

State Dynamic Optimization

In the previous chapter methods to solve the force-sharing problem in biomechanics are introduced. These methods are applied to predict muscle force histories due to the observed motion of the skeleton and the measured external forces on the environment. The measurement of the motion, of the externally applied forces and of the energetic requirements, and their subsequent processing proved to be of great value to the evaluation of existent assistive devices or therapeutic strategies as shown in the previous two chapters. However, when it comes to the design of new assistive devices or the planning of rehabilitation therapies or surgical interventions on the musculoskeletal system it is desirable to dispose of a dynamic simulation tool capable of predicting motion of the skeletal system besides muscle forces and energy consumption. Indeed, the study of the effects of adding an ankle weight to the leg of a person illustrated in Fig. 4.11 of section 4.5.3 evidences the importance of adapting the motion in order to keep the effort, quantified by the total metabolic cost, as reduced as possible.

This chapter is devoted to the application of dynamic simulation of the musculoskeletal system to the design of assistive devices. Dynamic simulation of human motion driven by physiological muscle models is increasingly used to understand human motion. Indeed, recent research has provided remarkable insights into the coordination of human walking. Because the neural excitations to the muscles are not known a priori, optimization techniques are used based on the assumption that the central nervous system (CNS) recruits muscles in such a way as to optimize some physiological performance criterion. The strategy usually adopted to solve the resulting optimal control problem is called dynamic optimization, which involves several forward integrations of the differential equations describing the dynamics of the musculoskeletal model, as explained in section 4.1.2. This approach has been successfully implemented recently to the human normal walking and has delivered reasonable kinematics and muscle activation patterns at the expense of high complexity and computational cost, refer to Anderson and Pandy [8].

The use of dynamic simulations of the musculoskeletal system to help on the design of

assistive devices, on the evaluation of rehabilitation therapies or on the planning of surgical interventions is promising and has been the focus of much recent research. However, the overwhelming computational effort required does not support clinical applications. The successful application of dynamic simulation to the design of assistive devices depends on the reduction of computational effort to acceptable levels. This can be achieved through simplification of models and through development of computationally efficient strategies. In this context, this chapter is devoted to a novel technique based on inverse dynamics and the parameterization of motion and muscle forces, which is potentially more efficient that the extremely expensive dynamic optimization, because it does not require any numerical integration of the differential equations. The last part of the chapter is dedicated to the application of the proposed technique to the normal and pathological gaits and to the determination of design parameters for transtibial prostheses.

5.1 Dynamic Simulation of Human Motion

Models to simulate human motion range from very-simple, passive mechanical models to highly complex models of the skeletal system actuated by muscles. Numerous approaches have been implemented in conjunction with these models to study human motion, e.g. the search for limit cycles of passive mechanical machines actuated exclusively by gravitational forces, the use of control loops associated with the tracking of measured or predescribed motions, or the implementation of large-scale optimization schemes.

The simplest models of human walking reported are frequently inspired by the work of McGeer [71]. McGeer showed that very simple biped walking machines can present stable passive periodic motions that resamble human walking. The motion is powered exclusively by the gravity when the biped walks on a shallow slope, in such a way the energy lost by friction and collisions is recovered from the gravity. For instance, Garcia et al. [33] use what they call the simplest walking model to study basic features of human walking. Kuo [62] adds an active powering to permit the biped to walk on level ground and study the relationship between metabolic cost, step length and step frequency. Passive dynamic walking have also been employed to determine energy-saving walking trajectories for humanoid robots. Gruber and Schiehlen [37], for example, showed that the use of motion patterns obtained from passive walking machines as reference trajectories for active machines like biped robots significantly reduce energy consumption. These works evidence the inherently passive nature of human walking characterized by periodic cycles. A typical example of a nearly completely passive or ballistic motion is the motion of the swinging lower limb during walking, see e.g. Mochon and McMahom [77]. Although giving some insights into basic dynamic principles underlying human motion, the application of such simple mechanical models powered by gravity to study the locomotion of the complex real biological system is evidently very limited.

Simple models of the lower limb during the swing phase of the gait were employed to help on the design and evaluation of transfemoral prostheses. For instance, Zarrugh and Radcliffe [134] use a planar model of the affected leg in simulations of the behavior of a prosthetic knee system, in which the motions of the hip joint and thigh obtained experimentally are prescribed. Tsai and Mansour [113] extend this approach by predefining hip joint trajectories and moments obtained experimentally and through inverse dynamics, respectively, but allowing the motion of the thigh to be computed by dynamic simulation. In order to evaluate the performance of a specific transfemoral prosthesis, the motions of the thigh and shank are simulated and compared to the normal ones obtained experimentally. These two works neglect the natural adaptations of the kinematics and moments arising to reduce the effort when a new disturbance is introduced. Chapter 3 and section 4.5.3 show the importance of these adaptations to reduce effort.

The works of Zlatnik [137] and Berbyuk [14] can be mentioned as attempts to take these adaptations into account in the design of prostheses by assuming the central nervous system is minimizing some physiological performance criterion. Both works aim at predicting the motion of whole-body models and the corresponding controls by means of optimization schemes that minimize some measure of effort based on moments and on mechanical work at the joints. Parameters of the transfemoral prostheses are incorporated to the optimization as design variables. Zlatnik [137] uses the obtained optimal time histories of prosthetic parameters to design a control scheme for a prosthetic knee system. In fact, Zlatnik [137] and Berbyuk [14] solve the optimal control problem, where the controls are represented by the moments at the joints.

As discussed previously, neglecting the dynamics of the muscle actuators, namely the muscle contraction and activation dynamics, can lead to nonphysiological results. Furthermore, including muscles to the model gives insights into the muscle coordination and a better estimation of the energetic requirements. For these reasons, dynamic simulation of the human motion including models of the muscles are increasingly being used. Hill-type muscle models, refer for example to Zajac [132] or Winters [124], have proved to be computationally tractable and represent fairly well muscle physiology, refer to section 2.2. One of the first attempts to use musculoskeletal models to solve the optimal control problem for the neural excitations can be attributed to Hatze [43] thirty years ago. He solved the optimal control problem for a time-optimal kick motion by means of the optimality conditions derived from the optimal control theory, which requires the solution of a two-point, boundary value problem. This was also the method used by Audu and Davy [11] to analyze the influence of muscle model complexity on the results of dynamic simulations. However, as pointed out by Pandy et al. [85], algorithms to derive the optimal controls are difficult to implement and the approach to solve the two-point, boundary value problem is not robust for the highly nonlinear models of the musculoskeletal system.

An alternative is to convert the optimal control problem into a parameter optimization,

in which the controls are parameterized. This can be performed, for example, by means of nodes linear interpolated, as explained in Pandy et al. [85]. This allows for solving the problem with standard Nonlinear Programming algorithms, e.g. the Sequential Quadratic Programming (SQP), readily available in a series of commercial softwares. In this approach the nodes are the design variables and the system differential equations are numerically integrated using the reconstructed trajectories of the controls. This approach, called dynamic optimization in the present work, refer to section 4.1.2, is being increasingly used to study human muscle coordination.

Indeed, numerous recent studies adopt dynamic optimization to solve the optimal control problem for the neural excitations. For instance, Gerritsen et al. [34] and Neptune et al. [81] applied dynamic optimization to study walking, Neptune et al. [83] to running, Neptune and Hull [80] to cycling, Anderson and Pandy [7] and Nagano and Gerritsen [78] to vertical jumping, and Spägele [103] to vertical jumping and time-optimal kick motion. In particular for human walking, metabolic cost per unit of distance traveled is accepted to be an important performance criterion minimized by the central nervous system, refer to section 4.2. Thus, phenomenological muscle energy expenditure models, which deliver more accurate estimations of metabolic cost, refer to section 2.2.3, have been used recently to find optimal neural excitations, muscle forces, kinematics and kinetics during walking by minimizing metabolic cost per unit of distance traveled, see Hase and Yamazaki [41], Anderson and Pandy [8], Umberger et al. [115], Anderson and Pandy [9].

In spite of the increasing use of dynamic optimization to study human motion, the prohibitive computational effort required prevents a broader use in clinical applications. Achieving a solution can require as much as hundreds of tausends or millions of numeric integrations of the system dynamics, what is computationally very expensive. For this reason, some research effort is being expended toward alternatives to dynamic optimization. One approach consists in using control strategies associated with the tracking of measured kinematics. These techniques are implemented, for instance, by Thelen and Anderson [111] to reconstruct normal walking and by Pheasgood et al. [86] to assist on the design of transtibial prostheses. Although being computationally much more efficient than dynamic optimization, these techniques require the adoption of control laws, which might not correspond well with the control structure of the biological system. Furthermore, the approaches depend on the tracking of measured normal kinematics, which may not be always available or might be bad references for pathological gait patterns.

One promising alternative, which is surprisingly poorly explored in biomechanics, is the use of inverse-dynamics approaches to solve the optimal control problem. For instance, Nagurka and Yen [79] proposed an inverse-dynamics approach that consists in approximating the trajectories of the generalized coordinates of a nonlinear dynamic system with Fourier series, whose coefficients are incorporated to the design parameters. This allows the convertion of the optimal control problem into a parameter optimization, and conse-

quently the use of standard and efficient nonlinear programming algorithms such as SQP. Furthermore, the controls are computed by inverse dynamics by means of the equations of motion from the generalized coordinates and their first and second time derivatives, which are obtained by analytical differentiation. As a result, numerical integrations of the system differential equations are not required and, thus, the computational effort is significantly reduced. A similar approach, although in a different formulation, has been proposed by Witkin and Kass [125] to create character animation in the field of computer graphics. Stryk [108] investigates a method based on piecewise polynomial approximations of the state variables for the determination of optimal trajectories for industrial robots. Recently, Saidouni and Bessonnet [93] and Bessonnet et al. [15] applied a similar approach to determine near-optimal walking trajectories and joint moments for biped robots. Instead of Fourier series, Bessonnet et al. [15] employ splines of class C^3, i.e. approximating polynomials of fourth order, to approximate the time histories of the generalized coordinates. They divide the gait cycle into phases and model contact by means of kinematic constraints that are activated and deactivated along the walking cycle.

The application of inverse-dynamics approaches to transform the optimal control problem into a parameter optimization problem seems promising in biomechanics, having the potential of significantly reducing computational effort while still delivering reasonably accurate results. The application of this approach to human locomotion requires, however, the introduction of physiological models of the muscles and their dynamics. Furthermore, the redundancy in the actuation resulting from the number of muscles being greater than the number of degrees of freedom have to be addressed. In this context, a novel inverse-dynamics approach is proposed that allows for the determination of near-optimal time histories of the generalized coordinates, muscle forces and neural excitations taking the contraction and activation dynamics of the muscles into account. As for the inverse-dynamics methods mentioned above, the trajectories of the generalized coordinates describing the motion of the skeletal system are approximated by parameterized functions. In addition, in order to deal with the redundancy caused by the introduction of muscles, also the time histories of the muscle forces are parameterized. The consistency between the generalized coordinates and the muscle forces is guaranteed by ensuring the fulfillment of constraints given by the equations of motion. The neural excitations, i.e. the controls, are computed by inverting the muscle contraction and activation dynamics. In this way, near-optimal time histories of the generalized coordinates and of the muscle forces are searched that optimize a time-integral cost function, such as minimal metabolic cost of transport or maximal proximity to measured data.

5.2   Proposed Optimization Approach

The approach proposed in this chapter consists in a convertion of the optimal control problem having neural excitations as controls into a parameter optimization by means of inverse-dynamics methods. Direct-dynamics methods are based on the approximations of the control, i.e. neural excitations, by parameterized functions and the numerical integration of the system differential equations (2.29). Inverse-dynamics methods, on the contrary, depend on the parameterization of states while the controls are determined by inverse dynamics. This dispenses with the need for numerically integrating the system differential equations, thus, reducing the computational effort required. In order to deal with the fact that the musculoskeletal system is redundantly actuated, a parameterization of the muscle forces is proposed. The consistency of the muscle forces with the motion is guaranteed by satisfying the equations of motion at discrete control points. From the muscle force histories, the neural excitations are evaluated by inverting the muscle contraction and activation dynamics similarly to the technique proposed for the Extended Inverse Dynamics approach.

The proposed approach can be seen as a fusion of the approaches of Bessonnet et al. [15] to determine near-optimal walking patterns for biped robots with the Extended Inverse Dynamics approach of Ackermann and Schiehlen [3] to determine optimal, physiological muscle forces and energetic requirements for a prescribed motion of the skeleton, as described in the previous chapter. The connection between both approaches occurs at the joint levels by imposing the agreement between joint moments applied by the muscles and joint moments required to generate the parameterized motion. The approach guarantees the determination of optimal motion patters and joint moment histories that are compatible with muscle capabilities. This avoids, for instance, the appearance of discontinuities in the joint moments at the phase transitions as observed in the results of Bessonnet et al. [15]. Furthermore, more accurate estimations of metabolic cost can be assessed by using phenomenological muscle energy expenditure models. In the next sections, the elements of the optimization framework proposed are explained in detail followed by applications to the normal and pathological gaits.

5.2.1   General Optimization Scheme

Figure 5.1 shows a schematic representation of the inverse-dynamics approach proposed for solving the optimal control problem. Basically, the general optimization framework proposed here differs from the Extended Inverse Dynamics approach depicted in Fig. 4.2 by the additional approximation of the kinematics by parameterized functions and the incorporation of the corresponding parameters to the set of design variables to be optimized, as shown by the additional arrow on the right hand side of Fig. 5.1. Note that the

moments at the joints are serving as constraints that ensure the compatibility between muscle forces and motion. Although seemingly trivial, the modification of the Extended Inverse Dynamics approach to allow for motion adaptation during walking requires a series of steps, specially for the appropriate modeling of walking, which will be explained in details further on. For instance, an appropriate inverse-dynamics model of the skeletal system is adopted, whose structure is variant throughout the gait cycle due to the activation and deactivation of kinematic constraints imposed at the foot. This measure is required to allow for the computation of the ground forces as the reaction forces appearing at these constraints due to the walking kinematics.
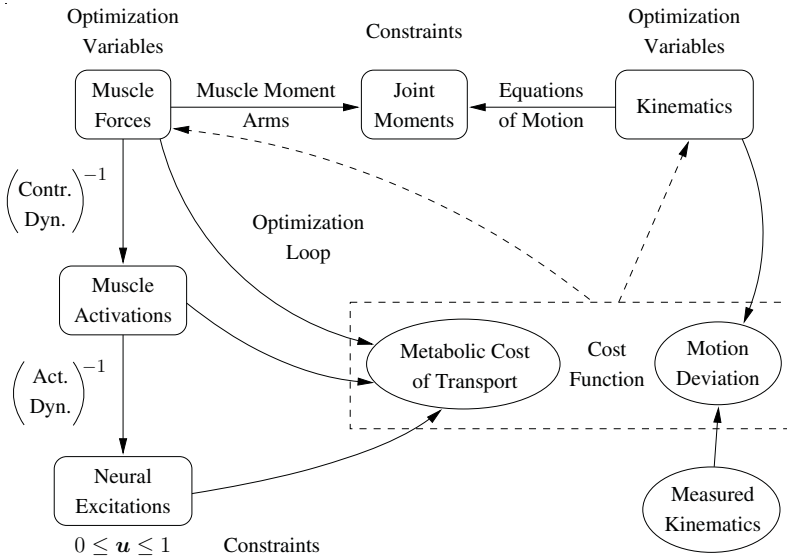
Figure 5.1: Schematic representation of the inverse-dynamics optimization approach.

5.2.2 Adopted Model of the Musculoskeletal System

Here, only the special case of walking will be addressed in detail. However, the basic approach can be easily extended to a large variety of applications in biomechanics. Although 3-D models of the skeletal system offer a more accurate assessment of the determinants of gait as shown in chapter 3, and can better explain muscle coordination (refer e.g. to Jinha et al. [56]), walking is a motion predominantly contained in the sagittal plane. Therefore, 2-D models can still deliver many insights into the phenomena involved, while requiring a significantly lower complexity of the model in terms of number of degrees of freedom and

muscle units needed. For this reason, the planar model of the skeletal system contained in the sagittal plane shown in Fig. 5.2 is adopted to test the approach proposed and to study normal and pathological gaits.

The 'free' model, i.e. without considering the ground contact constraints, is composed by 7 bodies, the HAT, the two thighs, the two shanks and the two feet, and has nine degrees of freedom. The motion of the model is performed in the sagittal plane and is described by nine generalized coordinates as depicted in Fig. 5.2. The pelvis, upper part of the trunk, arms and head are modeled as a single rigid body referred as HAT. The masses, center of mass, and moments of inertia of the segments are computed for both subjects using the tables in de Leva [28] as functions of the subjects' total body mass, stature, thigh lengths and shank lengths, refer to Appendix A.3. The heels, the positions of the metatarsophalangeal joints, and the ankles are denoted by the the capital letter A, B and C, respectively, followed by r for the right or l for left foot. This points will be used further on to define the constraints active at different walking phases. Each lower limb is actuated by the same 8 muscle units considered in chapter 4 totalizing 16 muscle units.

The eight muscle groups considered are shown in Fig. 5.2 for one leg. The Hill-type muscle model is composed by a contractile element CE and a series elastic element SE, while the force of the parallel elastic element PE is set to zero, Fig. 2.5. All the structures in parallel to the CE and the SE are represented by total passive moments at the joints, which include the moments generated by all other passive structures crossing the joints, like ligaments. The model for the passive moments at the joints is adopted from Riener and Edrich [90]. A linear viscous damping is added to the hip and knee joints, whose values are determined by pendulum experiments performed by Stein et al. [105]. In order to account for the moments $l_{mj,r}$ and $l_{mj,l}$ applied at the metatarsophalangeal joints by the muscles *flexor halucis longus* and *flexor digitorum longus*, negative moments up to $-10\ Nm$ are allowed to act at Br and Bl. The limit value of $10\ Nm$ was determined by doubling the maximal moments applied by these muscles at isometric conditions and optimal fiber lengths. The doubling of the maximal moments applied by the muscles is a heuristic assumption to take passive moments into account. Positive moments on the foot at the metatarsophalangeal joint 'pull' the toes upwards having little or no influence on the dynamics of the model during walking. For this reason no positive moments are applied at the metatarsophalangeal joint in the model.

As explained in section 4.5.1, the models for the muscle activations and muscle force-length-velocity relation adopted are based to a great extent on the models presented in Nagano and Gerritsen [78]. The same modifications of the force-length-velocity relation discussed in section 4.5.1 and in Appendix A.1 are adopted. The modification of the force-length-velocity relation is introduced to guarantee continuity of the neural excitations and, thus of the cost function, namely the *slope factor* is set to 1 instead of 2, see Appendix A.1. A *slope factor* of 1 causes the force-velocity relation to be continuous in
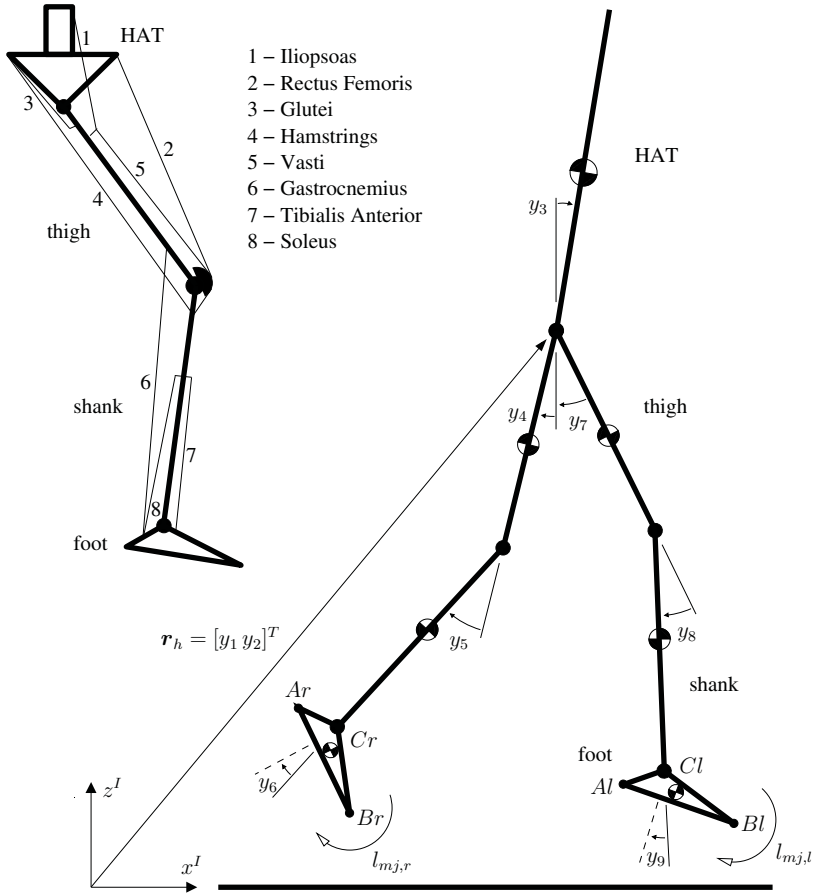
Figure 5.2: Model of the skeletal system adopted contained in the sagittal plane on the right, and muscle units considered for each lower limb.

the first derivative at $v^{ce} = 0$, see Fig. A.1 in Appedix A.1. Discontinuities in the first derivative at the force-velocity relation cause discontinuities in the first derivative of the muscle activations and, thus, discontinuities in the time histories of the neural excitations computed by inverting the contraction and activation dynamics. Due to the use of discrete values of the neural excitations to compute the metabolic cost, discontinuities in the neural excitations can originate discontinuities in the objective function, what can cause problems to gradient-based optimization algorithms. The change in the overall force-velocity relation caused by this modification is small, so that a loss of quality in

the results is unlikely. The phenomenological energy expenditure models of Umberger et al. [115] is employed to estimate metabolic cost. More details about the muscle parameters and the models adopted can be found in Appendix A.1.

5.2.3 Equations of Motion and Contact Conditions During Walking

The equations of motion of the free model shown in Fig. 5.2 are of the form of (4.1) and read as

$$M(y)\,\ddot{y} + k(y,\dot{y}) = q_r(y,\dot{y}) + R(y)\,f^m \,, \tag{5.1}$$

where the vector of generalized coordinates is, according to Fig. 5.2,

$$y = \begin{bmatrix} y_1 & y_2 & y_3 & y_4 & y_5 & y_6 & y_7 & y_8 & y_9 \end{bmatrix}^T . \tag{5.2}$$

During walking contacts occur between the feet and the ground. The contacts can be modeled by means of kinematic constraints as implemented by Bessonnet et al. [15]. The constraints are activated and deactivated throughout the gait cycle leading to a time-varying kinematic topology. The gait cycle is divided into eight phases based on the events observed during normal walking. The phases, shown schematically in Fig. 5.3, are characterized by the corresponding active constraints, indicated by circles at the contact points Ar, Br, Al and Bl. The phases 1, 2, 3 and 4 correspond to the periods delimited by the right heel strike, right toe contact (flat contact of sole), left toe off, right heel off, and left heel strike, respectively, as shown on the left hand side of Fig. 5.3. The phases 5, 6, 7 and 8 correspond to the periods delimited by the left heel strike, left toe contact (flat contact of sole), right toe off, left heel off, and right heel strike, respectively, as shown on the right hand side of Fig. 5.3.

The equations of motion (5.1) of the free model, which are a set of ordinary differential equations (ODEs), are modified as explained in section 2.1.3 to account for the additional kinematic constraints modeling the contacts occurring between the feet and the ground for each one of the phases ph as

$$M(y)\,\ddot{y} + k(y,\dot{y}) = q_r(y,\dot{y}) + R(y)\,f^m + C_{ph}^T\,\lambda_{ph} \tag{5.3}$$

$$c_{ph} = 0\,, \qquad ph = 1\ldots 8\,, \tag{5.4}$$

where c_{ph} is the vector containing the kinematic constraints at the feet corresponding to the phase ph, λ_{ph} is the vector of Lagrangian multipliers, which may be interpreted as the generalized constraint forces required to fulfill the kinematic constraints in c_{ph}, and C_{ph} represents the Jacobian matrix of the constraints active in phase ph, where

$$C_{ph} = \frac{\partial c_{ph}}{\partial y^T}\,, \qquad ph = 1\ldots 8\,. \tag{5.5}$$
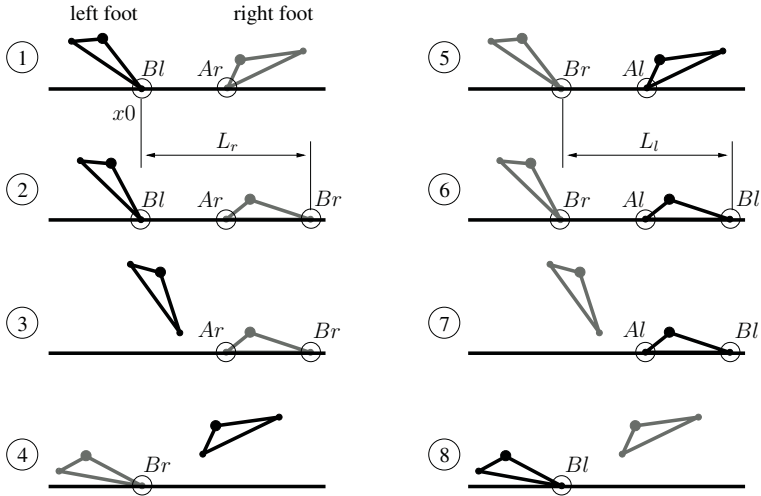
Figure 5.3: Schematic representation of the phases of the gait numbered from 1 to 8, which are characterized by the active constraints indicated by the circles around the contact points *Ar* (right heel), *Al* (left heel), *Br* (right metatarsophalangeal joint), and *Bl* (left metatarsophalangeal joint). The step lengths in first and second halves of the gait cycle are indicated, respectively, by L_r and L_l.

Equations (5.3) and (5.4) represent a set of differential algebraic equations (DAEs), so that the generalized coordinates of the free model in $\boldsymbol{y}$ are no longer independent. In particular during the swing phases, in which the model consists in a tree-like kinematic chain, the reaction forces could be eliminated from the equations of motion by means of a matrix formulation of the principle of virtual work (refer, for example, to Blajer and Schiehlen [18]). However, this reduction of the equations of motion to their minimal form is not necessary here because the explicit appearance of the reaction forces represented by the Langrange multipliers is advantageous for the application of the approach proposed here as clearly shown further on.

The constraints appearing at the heel and metatarsophalangel joints in the vertical direction are unilateral. However, it is sufficient to formulate them as bilateral constraints as in (5.4) and impose constraints to the optimization that ensure positive vertical reaction forces, i.e. as long as the constraints are active only positive vertical reaction forces at these two contact points are allowed. The definition of the constraints depends on foot dimensions using approximate relationships extracted from Winter [123], as shown in Fig. 5.4. One possibility to describe the kinematic constraints active in each one of the

right foot

left foot
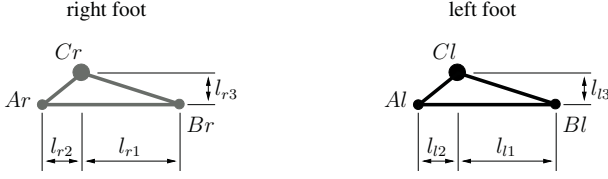
Figure 5.4: Schematic representation of the feet with the dimensions that characterize the positions of the heels (points Ar and Al) and of the metatarsophalangeal joints (points Br and Bl) .

phases in the first half of the gait cycle according to Figs. 5.3 and 5.4 reads as

$$c_1(\boldsymbol{y}, L_r) = \begin{bmatrix} r_{Bl,x}(\boldsymbol{y}) - x0 \\ r_{Bl,z}(\boldsymbol{y}) \\ r_{Ar,x}(\boldsymbol{y}) - (x0 + L_r - l_{r1} - l_{r2}) \\ r_{Ar,z}(\boldsymbol{y}) \end{bmatrix} = \boldsymbol{0}, \tag{5.6}$$

$$c_2(\boldsymbol{y}, L_r) = \begin{bmatrix} r_{Bl,x}(\boldsymbol{y}) - x0 \\ r_{Bl,z}(\boldsymbol{y}) \\ r_{Ar,x}(\boldsymbol{y}) - (x0 + L_r - l_{r1} - l_{r2}) \\ r_{Ar,z}(\boldsymbol{y}) \\ r_{Br,z}(\boldsymbol{y}) \end{bmatrix} = \boldsymbol{0}, \tag{5.7}$$

$$c_3(\boldsymbol{y}, L_r) = \begin{bmatrix} r_{Ar,x}(\boldsymbol{y}) - (x0 + L_r - l_{r1} - l_{r2}) \\ r_{Ar,z}(\boldsymbol{y}) \\ r_{Br,z}(\boldsymbol{y}) \end{bmatrix} = \boldsymbol{0}, \tag{5.8}$$

$$c_4(\boldsymbol{y}, L_r) = \begin{bmatrix} r_{Br,x}(\boldsymbol{y}) - (x0 + L_r) \\ r_{Br,z}(\boldsymbol{y}) \end{bmatrix} = \boldsymbol{0}, \tag{5.9}$$

where $r_{P,x}$ is the x-component and $r_{P,z}$ is the z-component of the position vector $\boldsymbol{r}_P$ of any point P. The kinematic constraints for the second half of the gait cycle are obtained in the same way being functions of the vector of generalized coordinates $\boldsymbol{y}$ and of the step lengths L_r and L_l as $c_5(\boldsymbol{y}, L_r, L_l)$, $c_6(\boldsymbol{y}, L_r, L_l)$, $c_7(\boldsymbol{y}, L_r, L_l)$, and $c_8(\boldsymbol{y}, L_r, L_l)$. Note that the initial position of the left metatarsophalangeal joint $x0$, refer to Fig. 5.3, can be defined freely or based on experimental data when a measured motion is to be tracked.

5.2.4   Parameterization of the Problem

The solution of the optimal control problem by means of the inverse-dynamics approach proposed requires the approximation of the time histories of the muscle forces and of the generalized coordinates of the skeletal model by parameterized functions. Different functions were adopted in the literature to approximate the motion of a mechanical system.

For instance, Nagurka and Yen [79] use Fourier series, while Saidouni and Bessonnet [93] and Stryk [108] use cubic splines. Bessonet et al. [15] observed that using cubic splines results in moments at the joints that are not continuous in the first derivative at the connecting nodes. In order to circumvent this problem they adopt, instead, spline functions of class C^3, i.e. approximating polynomials of fourth order, to interpolate nodal values, what guaranties smoother trajectories for the moments. The interpolating nodal values for the approximating polynomials correspond to the values of the function at the nodal times, which are uniformly distributed along the walking cycle. Note that, in the next section, control points are introduced to verify the fulfillment of the constraints at discrete points, and are independent of the number of nodal points.

Because smooth (differentiable) moments at the joints are more compatible with muscle capabilities, interpolating polynomials of 4th order are adopted to approximate the time histories of the generalized coordinates as

$$y_n(t) \approx \tilde{y}_n(t) \equiv \varphi_{n,k}(\bar{t}), \quad t_k \leq t < t_{k+1}, \quad n = 1 \ldots f, \quad k = 1 \ldots n_n - 1, \qquad (5.10)$$

where $\tilde{y}_n(t)$ is the approximating function for $y_n(t)$, $\varphi_{n,k}$ is the polynomial that interpolates the nodal values $y_{n,k} = y_n(t_k) = \tilde{y}_n(t_k)$ and $y_{n,k+1} = y_n(t_{k+1}) = \tilde{y}_n(t_{k+1})$ of the generalized coordinate y_n as shown in Fig 5.5, f is the total number of generalized coordinates of the free model, n_n is the total number of nodes considered,

$$\varphi_{n,k}(\bar{t}) = p_{0,n,k} + p_{1,n,k}\bar{t} + p_{2,n,k}\bar{t}^2 + p_{3,n,k}\bar{t}^3 + p_{4,n,k}\bar{t}^4, \qquad (5.11)$$

$$\bar{t} = \frac{t - t_k}{\Delta t}, \qquad (5.12)$$

and $\Delta t = t_{k+1} - t_k$ is a constant time step because nodes $y_{n,k}$ are uniformly distributed along the gait cycle.
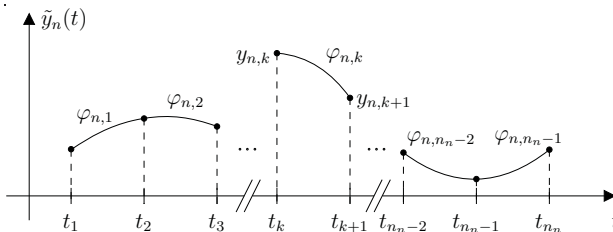

Figure 5.5: Piecewise approximation of the time history of the generalized coordinate y_n using fourth-order polynomials and uniformly distributed nodes $y_{n,k}$ as connecting points.

The polynomials (5.11) with $k = 1 \ldots n_n - 1$ must fulfill the following three sets of conditions. The end-points of the polynomials equal the values of the generalized coordinates

at the nodes as

$$\varphi_{n,k}(0) = y_{n,k} \quad k = 1 \ldots n_n - 1 \,. \tag{5.13}$$

The continuity of the approximating function and of its first, second and third time derivatives at the connecting points, which coincide with the nodes t_k, is ensured by

$$\varphi_{n,k}(1) = \varphi_{n,k+1}(0) \quad k = 1 \ldots n_n - 2 \,, \tag{5.14}$$
$$\dot{\varphi}_{n,k}(1) = \dot{\varphi}_{n,k+1}(0) \quad k = 1 \ldots n_n - 2 \,, \tag{5.15}$$
$$\ddot{\varphi}_{n,k}(1) = \ddot{\varphi}_{n,k+1}(0) \quad k = 1 \ldots n_n - 2 \,, \tag{5.16}$$
$$\dddot{\varphi}_{n,k}(1) = \dddot{\varphi}_{n,k+1}(0) \quad k = 1 \ldots n_n - 2 \,. \tag{5.17}$$

Finally, for periodic motions as walking, the values of the generalized coordinates and their first three time derivatives at the end (t_{n_n}) and at the beginning (t_1) of the gait cycle coincide as

$$\varphi_{n,n_n-1}(1) = \varphi_{n,1}(0) \,, \tag{5.18}$$
$$\dot{\varphi}_{n,n_n-1}(1) = \dot{\varphi}_{n,1}(0) \,, \tag{5.19}$$
$$\ddot{\varphi}_{n,n_n-1}(1) = \ddot{\varphi}_{n,1}(0) \,, \tag{5.20}$$
$$\dddot{\varphi}_{n,n_n-1}(1) = \dddot{\varphi}_{n,1}(0) \,. \tag{5.21}$$

The total number of equations given by the conditions (5.13) to (5.21) totalizing $5(n_n-1)$ coincides with the number of unknown coefficients of the approximating fourth-order polynomials. Furthermore, the resulting set of equations are linear in the coefficients. For these reasons, the solution for the coefficients that fulfill the conditions is unique and can be obtained in a computationally efficient way. Note, that the use of an odd number of nodes when using interpolating polynomial of fourth order for periodic motions should be avoided because it leads to a singular matrix of coefficients for the set of linear equations.

Because the x-coordinate of the hip joint is not purely periodic, a special treatment is required. The motion can be described by a superposition of a periodic motion and a constant average velocity, which coincides with the average walking velocity. This description allows for subtracting the constant velocity from the motion, and then for the piecewise approximation of the remaining periodic part of the motion by polynomials as explained above. Finally the constant velocity motion is added to the approximating periodic functions to reconstruct the original motion.

The time histories of the muscle forces are approximated by cubic splines instead of 4th-order polynomials, because the first derivatives of the neural excitations, also obtained by inverting a second-order dynamics, must not be necessarily continuous in the first derivatives as desirable for the moments at the joints. This measure reduces the computational effort to find the coefficients of the interpolating polynomials and prevents the unnecessary oscillating behavior caused by higher-order polynomial interpolations (Saidouni and Bessonnet et al. [93]).

The approximation of the muscle force histories by cubic splines is carried out following the same basic procedure used for the approximation of the generalized coordinates by fourth-order polynomials as

$$f_i^m(t) \approx \tilde{f}_i^m(t) \equiv \psi_{i,k}(\bar{t}), \quad t_k \leq t < t_{k+1}, \quad i = 1 \ldots m, \quad k = 1 \ldots n_n - 1. \quad (5.22)$$

where $\tilde{f}_i^m(t)$ is the approximating function for $f_i^m(t)$, m is the total number of muscles considered and $\psi_{i,k}$ is the third-order polynomial that interpolates the nodal values $f_{i,k}^m = f^m(t_k)$ and $f_{i,k+1}^m = f_i^m(t_{k+1})$ of the muscle force f_i^m as

$$\psi_{i,k}(\bar{t}) = \hat{p}_{0,i,k} + \hat{p}_{1,i,k}\bar{t} + \hat{p}_{2,i,k}\bar{t}^2 + \hat{p}_{3,i,k}\bar{t}^3. \quad (5.23)$$

The coefficients of the cubic splines in (5.23) are computed by solving the $4(n_n - 1)$ linear equations resulting from the conditions for continuity up to the second time derivatives and from the equality to nodal values of the muscle forces $f_{i,k}^m$. The continuities at the connecting points are guaranteed by equations as (5.14) to (5.16), the continuities at the end-points for periodic muscle force trajectories are ensured by equations as (5.18) to (5.20), and the equality to nodal values of the muscle forces $f_{i,k}^m$ are expressed by equations as (5.13), where the interpolating fourth-order polynomials $\varphi_{n,k}$ are substituted by the third-order polynomials $\psi_{i,k}$.

Besides the nodal values that describe the approximating functions for the generalized coordinates, the durations of the periods are required to characterize completely the kinematics of the model during the walking cycle. The durations of the eight gait phases are denoted by T_{ph} with $ph = 1 \ldots 8$. Thus, the whole kinematics of the model is characterized by the $f \times (n_n - 1)$ nodal values of the f generalized coordinates, and by the 8 time durations of the phases T_{ph}. The muscle force histories are completely characterized by the $m \times (n_n - 1)$ nodal values of forces $f_{i,k}^m$ of the m muscle units considered. All these parameters that characterize muscle forces and kinematics together with the step lengths L_r and L_l shown in Fig. 5.3, necessary to define the kinematical constraints for the foot-ground contact points, refer to (5.6-5.9), are summarized in a vector

$$\chi = \begin{cases} y_{n,k}, & n = 1 \ldots f, \quad k = 1 \ldots n_n - 1 \\ f_{i,k}^m, & i = 1 \ldots m, \quad k = 1 \ldots n_n - 1 \\ T_{ph}, & ph = 1 \ldots 8 \\ L_r, L_l \end{cases}, \quad (5.24)$$

which contains the design variables to be searched for by the optimization algorithm. Thus, the optimal control problem is recast into a parameter optimization problem that aims at determining a finite set of optimal parameters in χ that optimize a cost function to be introduced in section 5.2.7, and that fulfill the constraints presented further on in section 5.2.9.

5.2.5 Control points

In order to ensure the fulfillment of the constraints in the internode regions, control points are introduced independently from the nodal points. The decoupling of the number of nodes required to approximate the trajectories and the number of control points required to ensure fulfillment of constraints at discrete times, allows for the reduction of the number of nodal points without compromising the fulfillment of constraints. This is important to reduce the number of optimization variables as far as possible, thus, decreasing computational effort. Furthermore, a finer grid for the control points permits a better estimation of the time derivatives of the muscle activations, which are computed by finite differences, and are necessary to compute the neural excitations as explained further on.
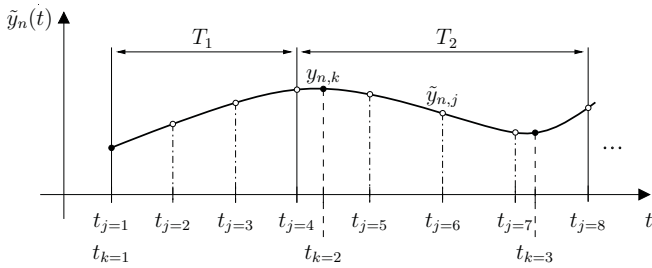
Figure 5.6: Example of the distribution of control points. The figure shows the approximation $\tilde{y}_n(t)$ of the trajectory of a generalized coordinate $y_n(t)$. The nodes serving as connecting points for the interpolating polynomials are denoted by k at the time instants t_k. The two first phases of the cycle are shown with durations T_1 and T_2, respectively, while control points denoted by j at t_j are uniformly distributed within the phases.

For the model of walking adopted, a phase-wise uniformly distribution of control points is superior to a uniformly distribution throughout the walking period. In a gross way, a uniformly distribution of control nodes originates discontinuities in the cost function at regions of the space of design variables for which control points coincide with phase transitions, where kinematic constraints are just activated or deactivated. Because the phase-wise distribution of control points avoids these discontinuities in the cost function, it is more adequate for the use of nonlinear programming algorithms to solve the optimization problem, which require continuous cost functions. The number of control points for each phase of the gait is specified and then uniformly distributed within the phases, as depicted in Figure 5.6. The total number of control points at the time instants t_j is n_c, where $j = 1 \ldots n_c$. The distribution is carried out in such a way that there are always control points at phase transitions, see Fig. 5.6.

5.2.6   Inversion of the Activation and Contraction Dynamics

As depicted in Fig. 5.1, the muscle activations and neural excitations are estimated from
the time histories of the muscle forces by inverting the contraction and the activation
dynamics. The inversion of the contraction dynamics to estimate muscle activations from
muscle forces and the inversion of the activation dynamics to compute neural excitations
from the muscle activations follow the same procedure used for the extended inverse
dynamics approach proposed in chapter 4. The only difference resides in the time grid used
in the methods. A uniform distribution is used in the extended inverse dynamics approach
while in the approach proposed in this chapter a phase-wise uniformly distribution of the
control points is employed. This difference requires small modifications of the procedure
that will be explained in the following.

The inversion of the contraction dynamics to compute muscle forces is explained in details
in section 4.3.2. It consists basically in the numerical differentiation of the muscle force
(4.10) to compute its time derivative, followed by the computation of the shortening
velocity, force and length of the muscle contractile element (CE) using (4.15) to (4.17),
and the computation of the muscle activations by means of the muscle force-length-velocity
relation (4.18). The inversion of the activation dynamics to compute neural excitations
from the muscle activations is explained in details in section 4.3.3. It consists basically in
the numerical differentiation of the muscle activation to estimate its time derivative and
in solving the activation dynamics for the neural excitation (2.17).

In the Extended Inverse Dynamics approach all the information required for the inversion
of the dynamics is computed at discrete time instants uniformly distributed throughout
the motion period. This allows for the use of a centered finite-divided difference formula
as in (4.10). In the approach proposed in this chapter, the control points, which are used
to compute the information required for the inversion of the dynamics, are uniformly
distributed within the phases but not globally. For this reason, centered finite-divided-
difference formulas, which are more accurate than backward or forward finite-divided
formulas, can be applied at internal control points, i.e. at control points inside the phase
that are not at transitions, but they cannot be applied to control points at the transitions,
because the time step in one adjacent phase is in general unequal the time step in the
other adjacent phase, refer to Fig. 5.6. Here alternative formulas obtained by truncation
of Taylor series are used to increase the accuracy of the derivative estimations, instead of
using backward or forward finite-divided difference formulas. The same formulas are used
to compute the time derivatives of the muscle activation $\dot{a}(t)$ from the muscle activation
$a(t)$. The inversion of the contraction and activation dynamics deliver estimations of the
activations and neural excitations at the control points t_j for all m muscles considered as

$$a_{i,j} \quad \equiv \quad a_i(t_j),$$ (5.25)

$$u_{i,j} \quad \equiv \quad u_i(t_j), \quad i = 1 \ldots m, \quad j = 1 \ldots n_c.$$ (5.26)

5.2.7   Cost Function

The importance of the total metabolic cost per unit of distance traveled during walking
was explained in section 4.2. It was shown that humans tend to minimize this quantity
during walking. The metabolic cost rate can be estimated using phenomenological energy
expenditure models for Hill-type muscles as explained in section 2.2.3. The total metabolic
cost due to the action of all muscles considered is computed by (4.29), which is divided
by the distance traveled ΔS yielding the total metabolic cost of transport as

$$E^t = \frac{1}{\Delta S} \sum_{i=1}^{m} \int_{t_1}^{t_{n_c}} \dot{E}(u_i(t), a_i(t), v_i^{ce}(t), l_i^{ce}(t), f_i^{ce}(t), \boldsymbol{p}_i^m) \, dt \ , \tag{5.27}$$

where $\Delta S = L_r + L_l$, m is the total number of muscle units considered, and $\dot{E}$ is the
metabolic cost rate, computed as function of the neural excitations $u_i(t)$, the muscle
activations $a_i(t)$, a set of muscle-specific parameters $\boldsymbol{p}_i^m$, and $v_i^{ce}(t)$, $l_i^{ce}(t)$ and $f_i^{ce}(t)$,
respectively, the shortening velocity, the length and force of the contractile element (CE),
refer to section 2.2.2. The integral is estimated using linear interpolated discrete values
of the metabolic cost rate at the control points t_j. Since all the variables in (5.27) can be
expressed as functions of the design variables in $\boldsymbol{\chi}$ as explained in the previous section,
$E^t = E^t(\boldsymbol{\chi})$.

Besides the metabolic cost other performance criteria play an important role in the per-
ceived quality of the walking with assistive devices as prostheses. Among them, the
aesthetics of the resulting gait cannot be underestimated. Although being a subjective
perception, aesthetics is clearly related to motions that are proximal to normal patterns
and can, thus, be quantified by the proximity of the resulting kinematics to normal stan-
dards. Another essential criterion referred to as comfort is also a subjective perception
difficult to quantify. Comfort can be, however, related to energy expenditure and to the
avoidance of unusual motions or forces. The former is accounted for by the metabolic
cost, while the latter could be quantified by the proximity of the forces exerted on the
environment, in the case of walking the ground contact forces, and of the kinematics to
normal patterns. Therefore, although other criteria such as pain can play a significant
role during pathological walking, the quality of gait can be to a great extend character-
ized by the energy consumption required and by the proximity of the kinematics and of
the ground reaction forces to normal patterns. Indeed, many studies evaluate the perfor-
mance of assistive devices by measuring the proximity of the kinematics and of the ground
reaction forces to standard normal walking patterns (Sutherland et al. [110], Blumentritt
et al. [19] and Johansson et al. [57]).

The deviation of the kinematics and ground reaction forces from the normal measured
values is quantified by the following expression

$$J_{dev} = \sum_{k=1}^{n_d} \int_{t_1}^{t_{n_c}} \frac{(x_k(t) - \hat{x}_k(t))^2}{\sigma_k(t)^2} \, dt \ , \tag{5.28}$$

where x_k is the simulated value for the kth variable, $\hat{x}_k$ is the measured average value for the kth variable, σ_k is the standard deviation for the kth variable obtained experimentally, and n_d is the total number of variables considered. The integral (5.28) is approximated using linear interpolated discrete values of the kinematics at the control points, directly available from the approximated vector of generalized coordinates $\tilde{y}$, and of the ground reaction forces, computed as explained in the next section. The standard deviation of data obtained by experiments with many subjects is a suitable scaling factor since it allows for the comparison of variables with different units and serves as a weighting factor that indicates the relative importance of proximity to measured data among variables and among gait phases. Since the motion and the ground reaction forces can be computed as functions of the design variables of the optimization in $\boldsymbol{\chi}$, is yields $J_{dev} = J_{dev}(\boldsymbol{\chi})$.

In order to take the energy expenditure, the aesthetics and the comfort into account a cost function composed by (5.27) and (5.28) is adopted as

$$J_{SDO}(\boldsymbol{\chi}) = w_1 \frac{E^t(\boldsymbol{\chi})}{100} + w_2 \, J_{dev}(\boldsymbol{\chi}) \; , \qquad (5.29)$$

where the coefficient $1/100$ brings the value of the first term to the same order of magnitude of the second term, and w_1 and w_2 are weighting factors that specify the relative importance of the terms, where $w_1 + w_2 = 2$. The advantage of using a cost function that includes a term for the deviation of measured normal kinematics and ground reaction forces in addition to the metabolic cost of transport term is twofold. On the one hand, aesthetics and comfort are considered as explained. On the other hand, it assists a better convergence of the optimization to a reasonable solution avoiding the convergence to unnatural or unrealistic walking patterns.

The simultaneous use of metabolic cost of transport and deviations from normal patterns as cost functions leads to a multicriteria optimization problem. The scalar cost function (5.29) represents a possible way of dealing with the resulting optimization problem by scalarization, refer to Stadler [104]. A drawback of using cost function (5.29) consists in the difficulty of interpretation of the solutions. The use of different weighting factors in (5.29) lead to different optimal solutions for $\boldsymbol{\chi}$. In order to increase the quality of the conclusions made by using (5.29), a strategy is adopted consisting in the use of sets of weighting factors specifying different relative importances of the metabolic cost of transport term with respect to the deviations term. The weighting factors are chosen such to cover a region of the possible solutions that are reasonable with respect to energy expenditure and kinematics. Although there are many other ways to deal with a multicriteria optimization problem, refer e.g. to Stadler [104], the strategy adopted here is expected to deliver at least conclusions on the superiority of one therapy or design of assistive devices over others, while being straightforward and computationally tractable.

5.2.8 Computation of Ground Reaction Forces

The ground contact forces have to be assessed due to two reasons. Firstly, computed contact forces are part of the cost function (5.29) quantifying the deviation from normal walking patterns. Secondly, their values are constrained to guarantee unilateral contact constraints and avoid slip as explained further on in section 5.2.9. The immediate availability of reaction forces was the main reason for dispensing the reduction of the set of equation of motion (5.3) to their minimal form, and to preserve the Lagrange multipliers explicitly in the equations.

As mentioned previously, the Lagrange multipliers in (5.3) can be interpreted as the ground contact forces required to fulfill the kinematic constraints at the contact points A and B as schematically shown in Fig. 5.3. It is straightforward to verify that, for the specific case of constraints formulated as in (5.6) to (5.9), the Lagrange multipliers in (5.3) coincide with the components of the reaction forces at the corresponding contact points. For instance, the vector of Lagrange multipliers in the first phase $\boldsymbol{\lambda}_{ph=1}$ corresponds to the vector of constraints $\boldsymbol{\lambda}_{ph=1} = [f_{Bl,x} \; f_{Bl,z} \; f_{Ar,x} \; f_{Ar,z}]^T$ in (5.6), where the components are the horizontal contact force at Bl, the vertical contact force at Bl, the horizontal contact force at Ar and the vertical contact force at Ar, respectively.

The reaction forces at the active kinematic constraints can be computed by solving (5.3) for the corresponding Lagrange multipliers from the muscle forces, generalized coordinates and their first and second time derivatives. Since the number of equations f is greater than the number of unknown Lagrange multipliers in all phases, $\boldsymbol{\lambda}_{ph}$ is computed by means of the pseudoinverse of $\boldsymbol{C}_{ph}^T$ for all phases and control points as

$$\boldsymbol{\lambda}_{ph,j}^* = \left(\boldsymbol{C}_{ph,j}^T\right)^+ \left(\boldsymbol{M}(\boldsymbol{y}_j)\,\ddot{\boldsymbol{y}}_j + \boldsymbol{k}(\boldsymbol{y}_j, \dot{\boldsymbol{y}}_j) - \boldsymbol{q}_r(\boldsymbol{y}_j, \dot{\boldsymbol{y}}_j) - \boldsymbol{R}(\boldsymbol{y}_j)\,\boldsymbol{f}_j^m\right), \tag{5.30}$$
$$ph = 1 \ldots 8, \quad j = 1 \ldots n_c,$$

where the index j denotes the value of the variable at the control point, and the pseudoinverse of a matrix $\boldsymbol{Z}$ is denoted by $\boldsymbol{Z}^+$. Equation (5.30) delivers the optimal least squares solution $\boldsymbol{\lambda}_{ph,j}^*$ of the linear system of equations (5.3), i.e. $\boldsymbol{\lambda}_{ph,j}^*$ is the vector that minimizes the error $e_{sq,j} = \|\boldsymbol{e}_j\|$, where

$$\boldsymbol{e}_j = (\boldsymbol{M}\,\ddot{\boldsymbol{y}}_j + \boldsymbol{k} - \boldsymbol{q}_r - \boldsymbol{R}\,\boldsymbol{f}_j^m) - \boldsymbol{C}_{ph,j}^T\boldsymbol{\lambda}_{ph,j}. \tag{5.31}$$

Refer, for example, to Strang [106] for an explanation of the properties of the pseudoinverse and of the corresponding solution of the linear system of equations. Note that, if the muscle forces $\boldsymbol{f}_j^m$ and the kinematics $\boldsymbol{y}_j$, $\dot{\boldsymbol{y}}_j$ and $\ddot{\boldsymbol{y}}_j$ are compatible, there must be a vector of Lagrange multipliers, for which the error $e_{sq,j}$ in (5.31) is zero. In this case, (5.30) delivers the vector of Lagrange multipliers $\boldsymbol{\lambda}_{ph,j}$ that fulfills (5.3). As long as the muscle forces are not completely compatible to the kinematics, the Langrange multipliers, computed using the pseudoinverse of $\boldsymbol{C}_{ph,j}^T$, are just the most compatible reaction forces

for the given kinematics and muscle forces in a least squares sense and $e_j \neq 0$. In the next section, a strategy is proposed to guarantee that the kinematics in $\boldsymbol{y}_j$, $\dot{\boldsymbol{y}}_j$ and $\ddot{\boldsymbol{y}}_j$ and the muscle forces in $\boldsymbol{f}_j^m$ are compatible and, thus, that the equations of motion are fulfilled at all control points j so that $e_{sq,j} \approx 0$ for $j = 1 \ldots n_c$.

5.2.9   Constraint Specification

The optimization problem is subject to a series of constraints, whose specification is the last step required to fully characterize the optimization framework proposed in this chapter. In the following, these contraints are listed and briefly presented. Two groups of contraints are difficult to fulfill and require an extra amount of computational effort, namely the constraints that ensure the fulfillment of the equations of motion and the kinematic constraints due to the ground-feet contacts. These two groups of contraints require a special treatment based on the specification of allowable infringements, following strategies explained in this section.

A first set of constraints for the optimization problem guarantee the physiological or physical feasibility of the solution and enhance the converge of the optimization by limiting the search space of the design variables. The physiological upper and lower bounds for the neural excitations,

$$0 \leq u_{i,j} \leq 1\,, \quad i = 1 \ldots m \quad j = 1 \ldots n_c\,, \tag{5.32}$$

ensure physiological muscle forces that respect the activation and contraction dynamics, refer to section 2.2.2. Note that the constraints are verified at the discrete control points j so that slight infringements can occur between control points.

The physical feasibility of the walking motion is guaranteed mainly by constraints that ensure foot clearance, positive vertical reaction forces and bounded horizontal reaction forces to prevent slipping according to Coulomb's friction law. Foot clearance is achieved by checking the vertical position of the points Ar, Br, Al and Bl, see Figs. 5.2 and 5.3, for both feet at the phases of the gait in which these points are not in contact with the ground. The formulation reads as

$$r_{Ar,z}(t_j) \;>\; 0\,, \quad ph = 4,\,5,\,6,\,7,\,8\,, \tag{5.33}$$
$$r_{Br,z}(t_j) \;>\; 0\,, \quad ph = 1,\,7,\,8\,, \tag{5.34}$$
$$r_{Al,z}(t_j) \;>\; 0\,, \quad ph = 1,\,2,\,3,\,4,\,8\,, \tag{5.35}$$
$$r_{Bl,z}(t_j) \;>\; 0\,, \quad ph = 3,\,4,\,5\,, \tag{5.36}$$

where the vertical position of the point P is denoted by $r_{P,z}$ and the level of the ground is assumed to have zero height.

The vertical ground reaction forces must be positive at the contact points to ensure unilateral constraints at the phases in which the corresponding contacts are activated as

$$f^{gr}_{z,Ar}(t_j) \;\ge\; 0\,, \quad ph = 1, 2, 3\,, \tag{5.37}$$

$$f^{gr}_{z,Br}(t_j) \;\ge\; 0\,, \quad ph = 2, 3, 4, 5, 6\,, \tag{5.38}$$

$$f^{gr}_{z,Al}(t_j) \;\ge\; 0\,, \quad ph = 5, 6, 7\,, \tag{5.39}$$

$$f^{gr}_{z,Bl}(t_j) \;\ge\; 0\,, \quad ph = 1, 2, 6, 7, 8\,, \tag{5.40}$$

where the vertical ground reaction forces at point P is denoted by $f^{gr}_{z,P}$.

The horizontal ground reaction forces satisfy the Coulomb's friction law and their magnitudes are limited to avoid sliding as

$$|f^{gr}_{x,r}(t_j)| \;\le\; \mu \left(f^{gr}_{z,Ar}(t_j) + f^{gr}_{z,Br}(t_j) \right), \quad ph = 1, 2, 3, 4, 5, 6, 7\,, \tag{5.41}$$

$$|f^{gr}_{x,l}(t_j)| \;\le\; \mu \left(f^{gr}_{z,Al}(t_j) + f^{gr}_{z,Bl}(t_j) \right), \quad ph = 1, 2, 3, 5, 6, 7, 8\,, \tag{5.42}$$

where μ is the coefficient of friction between the foot or shoe sole and the ground, $f^{gr}_{x,r}(t_j) = f^{gr}_{x,Ar}(t_j) + f^{gr}_{x,Br}(t_j)$, and $f^{gr}_{x,l}(t_j) = f^{gr}_{x,Al}(t_j) + f^{gr}_{x,Bl}(t_j)$.

Additional constraints can be added to avoid unnatural, although physiological, gait patterns, and to reduce the computational time required to achieve a reasonable solution by reducing the search space of the design variables. Fixing the average walking velocity proved to be an efficient way to avoid convergence to local minima describing unnatural walking patterns. The constraint on velocity is linear on the design variables in $\boldsymbol{\chi}$ as

$$\sum_{ph=1}^{8} T_{ph} - \frac{L_r + L_l}{v_w} = 0\,. \tag{5.43}$$

Specially important to reduce the search space of the design variables is the specification of box constraints (lower and upper bounds) generally represented by

$$\boldsymbol{\chi}_{min} \le \boldsymbol{\chi} \le \boldsymbol{\chi}_{max}\,, \tag{5.44}$$

where $\boldsymbol{\chi}_{min}$ and $\boldsymbol{\chi}_{max}$ denote, respectively, the lower and the upper bounds for the design variables in $\boldsymbol{\chi}$. These constraints specify physiological range of motion of the joints, physiological muscle forces, reasonable durations of the phases, and reasonable step lengths. Note that physiological muscle forces are, in fact, guaranteed by the bounded neural excitations verified at control points in (5.32). However, additional bounds on the parameters for the muscle forces helps on reducing the search space and, thus, the computational effort. The same is valid for the unphysiological range of motion of the joints, which are unlikely to occur even without the direct limitations of the motion range in (5.44). These unphysiological motions are already penalized in the cost function by causing an increase in energy expenditure or infringements of other constraints.

Other constraints that proved to be effective in preventing convergence to unnatural walking patterns are the imposition of a lower bound θ_{knee} for the maximal achieved knee flexion during the swing phase as

$$\max\{y_5(t)\} \geq \theta_{knee}, \quad \text{for } ph = 7,\, 8\,, \tag{5.45}$$

$$\max\{y_8(t)\} \geq \theta_{knee}, \quad \text{for } ph = 3,\, 4\,, \tag{5.46}$$

evaluated at control points $t = t_j$, and the specification of a lower bound θ_{hip} for the maximal achieved hip extension at the end of the stance phase as

$$\max\{y_4(t)\} \geq \theta_{hip}, \quad \text{for } ph = 4,\, 5,\, 6\,, \tag{5.47}$$

$$\max\{y_7(t)\} \geq \theta_{hip}, \quad \text{for } ph = 1,\, 2,\, 8\,, \tag{5.48}$$

evaluated at control points $t = t_j$.

Fulfillment of Equations of Motion

The first group of constraints requiring a special treatment represents the constraints due to the equations of motion. These constraints ensure that the time histories of the muscle forces $\boldsymbol{f}^m(t)$ and of the generalized coordinates $\boldsymbol{y}(t)$ are compatible, i.e. fulfill the equations of motion throughout the gait cycle. As mentioned in the previous section, this is achieved when there is a solution for the Lagrange multipliers $\boldsymbol{\lambda}^*_{ph}$ for which the error $\boldsymbol{e}_j$ in (5.31) is zero. A natural approach would be to constrain all $\boldsymbol{e}_j$ to 0 directly. However, such 'hard' constraints are difficult to satisfy, what can lead to an increased computational effort and even prevent convergence. A solution to overcome this problem is to 'soften' the constraints by allowing slight violations that do not compromise significantly the accuracy required for the analysis.

The amount of violation permitted is specified by control parameters. The vector of errors $\boldsymbol{e}_j$ lacks physical interpretation, so that the determination of meaningful bounds for it is not straightforward. A physically meaningful measure of the incompatibility between kinematics and muscle forces is achieved by comparing the moments at the joints applied by muscles and the moments at the joints computed by inverse dynamics. The moments due to muscle forces are

$$\overline{\boldsymbol{\tau}}^m_j(\boldsymbol{f}^m_j) = \boldsymbol{A}(\boldsymbol{y}_j)\, \boldsymbol{f}^m_j\,, \tag{5.49}$$

where $\boldsymbol{A}$ is the matrix of muscle moment arms. The moments required to produce the current kinematics $\boldsymbol{y}_j$, $\dot{\boldsymbol{y}}_j$, $\ddot{\boldsymbol{y}}_j$ and estimated ground reaction forces in $\boldsymbol{\lambda}^*_{ph,j}$ are computed by inverse dynamics as

$$\boldsymbol{\tau}^{m*}_j(\boldsymbol{y}_j, \dot{\boldsymbol{y}}_j, \ddot{\boldsymbol{y}}_j, \boldsymbol{\lambda}^*_{ph}) = \boldsymbol{B}^+ \left(\boldsymbol{M}(\boldsymbol{y}_j)\, \ddot{\boldsymbol{y}}_j + \boldsymbol{k}(\boldsymbol{y}_j, \dot{\boldsymbol{y}}_j) - \boldsymbol{q}_r(\boldsymbol{y}_j, \dot{\boldsymbol{y}}_j) - \boldsymbol{C}^T_{ph,j}(\boldsymbol{y}_j)\, \boldsymbol{\lambda}^*_{ph} \right), \tag{5.50}$$

where $\boldsymbol{B}^+$ is the pseudoinverse of the matrix $\boldsymbol{B}$, which transforms the moments at the joints into generalized forces. The kinematics and muscle forces are fully compatible if

the differences $\boldsymbol{e}_{m,j} = \boldsymbol{\tau}_j^{m*} - \overline{\boldsymbol{\tau}}_j^m$ at all control points $j = 1 \ldots n_c$ equal zero, what will be proven further on. Instead of the 'hard' constraints $\boldsymbol{e}_{m,j} = 0$ small violations are allowed as

$$max(|\boldsymbol{e}_{m,j}(\boldsymbol{\chi})|) \le \varepsilon_m \,, \quad j = 1 \ldots n_c \,, \tag{5.51}$$

where the vector $\boldsymbol{e}_{m,j}$ is evaluated from the vector of design variables of the optimization $\boldsymbol{\chi}$, and ε_m is the control parameter that specifies the maximal allowed magnitude of the difference between the joint moments due to muscle forces and the joint moments computed by inverse dynamics.

In the following, it will be shown that $\boldsymbol{e}_{m,j} = 0$ implies $\boldsymbol{e}_j = 0$, i.e. guaranteeing agreement of the moments ensures the existence of ground reaction forces that fulfill the equations of motion, see (5.31). From (5.30) and (5.31) it yields

$$\boldsymbol{\lambda}_{ph,j}^* = \left(\boldsymbol{C}_{ph,j}^T\right)^+ \left(\boldsymbol{C}_{ph,j}^T \, \boldsymbol{\lambda}_{ph,j}^* + \boldsymbol{e}_j\right). \tag{5.52}$$

According to Strang [106], if a rectangular matrix $\boldsymbol{Z}$ has independent columns and its rank equals the number of columns, its pseudoinverse $\boldsymbol{Z}^+$ is its left-inverse as $\boldsymbol{Z}^+ = (\boldsymbol{Z}^T \boldsymbol{Z})^{-1} \boldsymbol{Z}^T$ and $\boldsymbol{Z}^+ \boldsymbol{Z} = \boldsymbol{E}$, where $\boldsymbol{E}$ is the identity matrix with dimension of the number of columns of $\boldsymbol{Z}$. Since $\boldsymbol{C}_{ph,j}^T$ always satisfy these conditions, $\left(\boldsymbol{C}_{ph,j}^T\right)^+ \boldsymbol{C}_{ph,j}^T = \boldsymbol{E}$ and from (5.52)

$$\left(\boldsymbol{C}_{ph,j}^T\right)^+ \boldsymbol{e}_j = 0 \,. \tag{5.53}$$

Because the number f of components of $\boldsymbol{e}_j$, corresponding to the number of equation of motion of the free model, is greater than the number of equations in (5.53), which corresponds to the number of active constraints n_a, i.e. $n_a < f$, nontrivial solutions for $\boldsymbol{e}_j$ are possible. This is expected because the compatibility of the kinematics and muscle forces is not guaranteed yet.

From (5.50) and (5.31), and considering (5.49) it yields

$$\boldsymbol{\tau}_j^{m*} = \boldsymbol{B}^+ \left(\boldsymbol{B} \boldsymbol{A} \, \boldsymbol{f}_j^m + \boldsymbol{e}_j\right) = \boldsymbol{B}^+ \left(\boldsymbol{B} \overline{\boldsymbol{\tau}}_j^m + \boldsymbol{e}_j\right), \tag{5.54}$$

were $\boldsymbol{R} = \boldsymbol{B} \boldsymbol{A}$. Since the columns of matrix $\boldsymbol{B}$ are independent and its rank is equal to the number of its columns, $\boldsymbol{B}^+ \boldsymbol{B} = \boldsymbol{E}$ and

$$\boldsymbol{e}_{m,j} = \boldsymbol{\tau}_j^{m*} - \overline{\boldsymbol{\tau}}_j^m = \boldsymbol{B}^+ \boldsymbol{e}_j \,, \tag{5.55}$$

If the equality of the moments applied by the muscles and the moments computed by inverse dynamics is ensured with $\boldsymbol{e}_{m,j} = 0$, then

$$\boldsymbol{B}^+ \boldsymbol{e}_j = 0 \,, \tag{5.56}$$

where the number of equations corresponds to the number of moments at the joints n_b. Because the mechanical model is never underactuated throughout the gait cycle, $n_a + n_b \ge f$, i.e. the number of equations $n_a + n_b$ in (5.53) and in (5.56) is greater than

or equal to the number of elements f in the vector $\boldsymbol{e}_j$. For this reason, the only solution for $\boldsymbol{e}_j$ that satisfies (5.53) and (5.56) is the trivial solution $\boldsymbol{e}_j = 0$. Therefore, it turns out that the agreement of muscle moments with $\boldsymbol{e}_{m,j} = \boldsymbol{\tau}_j^{m*} - \overline{\boldsymbol{\tau}}_j^m = 0$ implies $\boldsymbol{e}_j = 0$. In other words, it is sufficient to verify the compatibility between the moments $\boldsymbol{\tau}_j^{m*}$ and $\overline{\boldsymbol{\tau}}_j^m$ to ensure the compatibility between kinematics and muscle forces and the fulfillment of the equations of motion.

Although it was not formally shown that a small infringement at the muscle moments level, with $\boldsymbol{e}_{m,j} \leq \varepsilon_m$ (5.51), necessarily implies a small infringement $\boldsymbol{e}_j$ of the equations of motion, this is expected based on the demonstration above that $\boldsymbol{e}_{m,j} = 0$ implies $\boldsymbol{e}_j = 0$, and was, indeed, always observed during the numerical experiments performed using the proposed approach.

Fulfillment of Kinematic Constraints

The mathematical description of the walking model adopted is represented by the set of differential algebraic equations in (5.3) and (5.4). The fulfillment of (5.3) is discussed in the previous subsection. It remain the kinematical constraints (5.4), which also require a special treatment based on a 'softening' of the constraints, in order to decrease computational effort and ensure convergence. Instead of considering the 'hard' equality constraints $\boldsymbol{c}_{ph,j} = 0$, a control parameter ε_k is introduced which specifies the maximal allowed infringement as

$$max(|\boldsymbol{c}_{ph,j}(\boldsymbol{\chi})|) \leq \varepsilon_k\,, \quad j = 1\ldots n_c\,, \tag{5.57}$$

where the constraints can be computed as functions of the optimization variables in $\boldsymbol{\chi}$. Because of the formulation of the kinematical constraints as in (5.6) to (5.9), ε_k has a physical interpretation, namely the maximal deviation from the kinematic constraints in units of distance. For this reason, the interpretation of the errors caused by the choice of a specific ε_k is straightforward.

5.2.10 Comments on the Implementation

With the definition of the constraints the optimization framework for the approach proposed in this chapter is fully characterized. Summarizing, the optimization problem consists in finding an optimal vector of design variables $\boldsymbol{\chi}$, described in (5.24), that minimizes a time-integral cost function as in (5.29) subject to the following sets of constraints:

1. bounded neural excitations (5.32);

2. ground clearance (5.33-5.36);

3. positive vertical reaction forces (5.37-5.40);

4. avoidance of sliding according to Coulomb's friction law (5.41-5.42); and

5. constant average walking velocity (5.43).

6. box constraints on design variables (5.44);

7. other constraints that favor fast converge to reasonable walking patterns (5.45-5.48);

8. fulfillment of the equations of motion (5.51);

9. fulfillment of the kinematic constraints (5.57);

The optimization depends on the definition of parameters for the allowed violation of the equations of motion, expressed as maximal error ε_m between moments applied by muscles and moments computed by inverse dynamics, the allowed violation ε_k of the kinematic constraints describing contact conditions, the number n_n of nodes, and the number of control points per phase $n_{c,ph}$, $ph = 1 \ldots 8$. In the examples of application presented in the next section, the following values are adopted for the allowed constraint infringements $\varepsilon_k = 0.002 \ m$ of the kinematic contraints between feet and ground, and $\varepsilon_m = 2 \ Nm$ compared to typical maximal joint moments that range from $50 \ Nm$ to $150 \ Nm$ during normal walking, see results further on. These values proved to ensure accurate fulfillment of the corresponding constraints, while keeping computational time low.

The number of nodes adopted is $n_n = 18$, which was chosen after a study of the influence of the number of nodes on the solution, refer to analysis in section 5.3.1. The number of control points for each phase is $n_{c,ph=1,5} = 5$, $n_{c,ph=2,6} = 10$, $n_{c,ph=3,7} = 21$, and $n_{c,ph=4,8} = 4$. These values were determined based on a study of the influence of the number of control points on the fulfillment of constraints and on the accuracy of numerical differentiation of the muscle activations. The total number of control points adopted is sufficiently high to ensure acceptably accurate estimations of time derivatives obtained by finite differences and to prevent significant infringements of the constraints in the periods between control points. The distribution of control points among phases is performed in such a way as to provide a relatively uniform global distribution with similar time step sizes Δt_{ph} for typical solutions. Furthermore, as lower bound for the maximal knee flexion during the swing phase $\theta_{knee} = 60°$ in (5.45-5.46) is adopted. A lower bound $\theta_{hip} = 5°$ in (5.47-5.48) for the maximal extension of the hip in the end of the stance phase is adopted to guarantee the convergence to natural walking patterns.

As for solving the EID optimization approach proposed in chapter 4, the Sequential Quadratic Programming (SQP) method implemented in the function *fmincon* available in the Optimization Toolbox of Matlab® is employed to solve the optimization problem resulting from the approach proposed in this chapter. Refer to section 4.3.6 or, for example, to Bestle [16] for further details on the SQP method. As last comment regarding the

implementation of the optimization framework, the proper scaling of the design variables in order to ensure similar magnitudes of the components of $\boldsymbol{\chi}$ is mentioned.

5.3   Application to Normal and Pathological Gaits

In this section, the proposed inverse-dynamics approach is applied to the study of normal and pathological gaits. In section 5.3.1, it is shown that the approach delivers reasonable results for the normal walking, with very small infringements of the constraints and realistic estimations of metabolic cost, muscle forces, kinematics and ground reaction forces. Section 5.3.2 illustrates the application of the approach to the study of the effects of introducing bilateral foot weights. Section 5.3.3 is devoted to the analysis of the performance of existent transtibial prostheses with respect to their prosthetic ankle stiffness and the design of optimal stiffness for different walking velocities. In the latter section the results and design considerations for transtibial prostheses are discussed, too.

5.3.1   Normal Walking

In this section the validity of the approach proposed to study human walking is shown. The model of the musculoskeletal system described in section 5.2.2 is adopted. Anthropometric data is taken from subject 1, refer to Appendix A.3. The cost function (5.29) contains a metabolic cost of transport term and a normal-walking tracking term with weighting factors $w_1 = 4/3$ and $w_2 = 2/3$. These weighting factors are chosen here because they proved to deliver realistic solutions for the kinematics and metabolic cost of transport. For the analysis of pathological gaits, the weighting factors are varied to study the effects of valorizing one term over the other. The control parameters that bound the infringement of the equations of motions and of the kinematical constraints adopted, refer to section 5.2.10, are $\varepsilon_m = 2\ Nm$ and $\varepsilon_k = 0.002\ m$, respectively. In order to reduce the number of parameters required and, thus, the computational effort, complete symmetry is assumed, so that the motion of one lower limb in the first half of the cycle coincides with the motion of the other lower limb in the second half, while the motion of hip and HAT at the first and second halves of the cycle are the same. In this first analysis, the average walking velocity is constrained to the one measured for subject 1. Moreover, to assist on the convergence to reasonable results some additional constraints are introduced as explained in section 5.2.10. The number of control points adopted and their distribution among phases correspond to the description in section 5.2.10.

As mentioned previously, the number of nodes is an important parameter to increase accuracy of the results on the one hand, and to reduce computational effort on the other hand. In order to determine a proper number of nodes, a study of its influence on the solutions is performed, whose results are shown in Table 5.1. The table shows a decrease

Table 5.1: Comparison among results obtained using different number of nodes for the total value of the cost function (5.29), the total metabolic cost of transport (5.27) and the deviation from measured kinematics and ground reaction forces (5.28).

Number of Nodes (nn)	Cost Function (J_{ID})	Met. Cost Transp. (E^t [J/m])	Deviation (J_{dev})	Comp. Time [hours]
14	23.8	493.0	22.8	11.3
16	18.7	477.1	17.2	15.9*
18	14.2	432.7	11.9	22.3
20	13.8	415.5	12.3	28.9

*approximate value

in the cost function value with an increase in the number of nodes, caused by a decrease in the metabolic cost of transport and in the deviation from normal data. Since the values tend to stabilize after 18 nodes, this number of nodes is adopted to avoid unnecessary increase in the computational effort. Indeed, the increase of the number of nodes from $nn = 18$ to $nn = 20$ causes a significant increase in the computational time for convergence to a solution, namely from 22.3 hours to 28.9 hours.
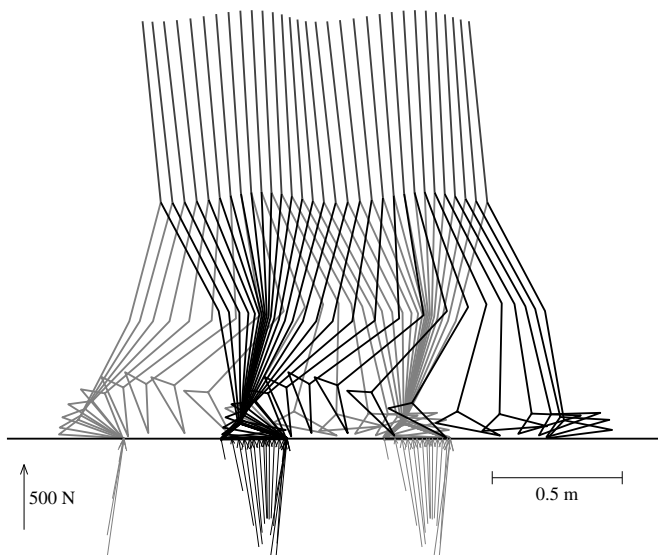

500 N   0.5 m

Figure 5.7: Stick-figure of the complete gait cycle for the normal walking obtained using the proposed approach with weighting factors $w_1 = 4/3$ and $w_2 = 2/3$ in (5.29) for an average walking velocity of 1.1275 m/s. The reaction forces are schematically represented by arrows.

The results obtained for 18 nodes are shown in Figs. 5.7 to 5.12. The kinematics and ground reaction forces obtained for the normal walking are visualized in Fig. 5.7. Note the good fulfillment of the kinematic constraints and the feet clearance during the swing phases of the gait. Also the exclusively positive vertical ground reaction forces can be observed. Figure 5.8 shows the results for the motion of the lower limbs in the first half of the gait cycle, which agrees well with the motion measured for the normal gait of subject 1. The dashed lines denote one standard deviations σ from the measured data obtained from Winter [122] and used in (5.28). Figure 5.9 shows the simulated vertical and horizontal ground reaction forces compared to the measured ground reaction forces for subject 1. One standard deviation from data in Winter [122] is also shown superposed to the measured forces. A good agreement is observed also here, although a higher value at the second peak of the vertical reaction force can be observed. This pattern is recurrent in the further results shown in this chapter and can be partially explained by the collisionless motion pattern used in our approach, see Blajer and Schiehlen [18]. The deceleration of the contralateral heel to guarantee zero velocity at *heel strike* results in an increase in the vertical ground force at the ipsilateral foot, which acts decelerating the descendant motion of the center of mass of the multibody system. An increase in the number of nodes might reduce this effect.

Figure 5.10 illustrates the good agreement between the moments at the joints obtained by inverse dynamics and the moments applied by muscles. As explained in section 5.2.9 this indicates the fulfillment of the equations of motion throughout the gait cycle. At phase transitions slight jumps in the moments obtained by inverse dynamics can be observed, which occur due to the change in the model structure, refer to section 5.2.3. Slight jumps can be also clearly observed in the vertical ground forces at left heel strike (HSl) in Fig. 5.9. The magnitude of these jumps can be reduced by increasing the number of control points or by decreasing the allowed discrepancy in joint moments ε_m at the cost of a higher computational effort.

Figure 5.11 shows the simulated contributions of the muscle forces to the net active moments at the joints of the right lower limb. Figure 5.12 shows the simulated muscle activations and neural excitations for the muscles of the right lower limb. Note that, because of the imposed symmetry, the results for the right lower limb completely characterize the ones for the left lower limb. The results show the fulfillmet of the lower and upper bounds for the neural excitations, 0 and 1, respectively, throughout the gait cycle. Only very slight infringements are observed, which occur between control points. The results for the muscle activations show a fairly good agreement with the overall muscle activity patterns during walking shown on the right hand side of Fig. 4.13. Differences are observed for the muscle glutei (Glu), which is very weakly activated, and for the muscle hamstrings (Ham), which is overactivated specially during the swing phase of the gait.

A last comment about the results refer to the estimation of metabolic cost of transport.
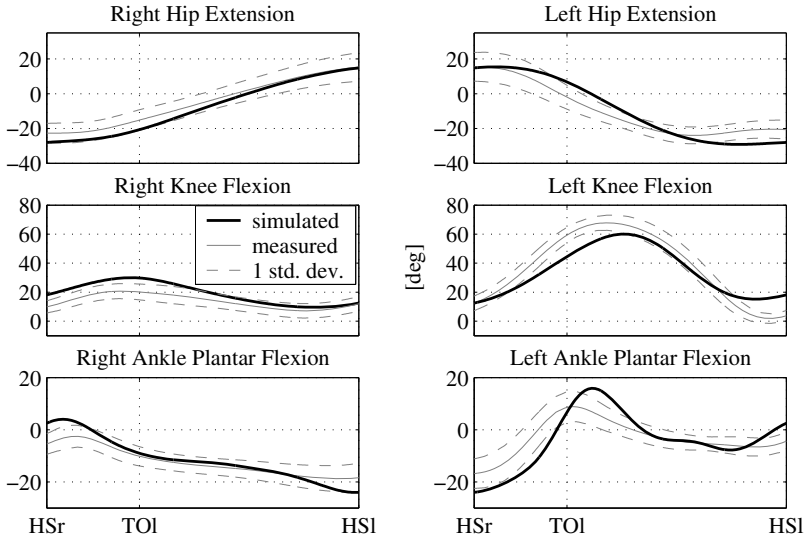
Figure 5.8: Motion of the lower limbs during the first half of the gait cycle. Note that, because of the imposed symmetry, the motion of the right lower limb in the first half of the cycle equals the motion of the left lower limb during the second half and vice versa. The brighter lines denote the measured motion for subject 1 and the dashed lines show one standard deviation (from Winter [122]) superposed to the measured data.

The absolute values obtained, refer to Table 5.1, for 20 nodes for example, is of approximately 415 J/m, while the metabolic cost estimated for the measured normal walking of subject 1 obtained by the EID approach is about 310 J/m (refer to section 4.5.2), thus, about 25% lower. Some possible reasons for this difference are the smoothing effect of the interpolating functions what could be overcome by the use of more nodes, the simple model adopted, inaccuracies in the phenomenological energy expenditure model and the adoption by the central nervous system of other performance criteria during walking, based, for example, on pain, joint loads or smoothness.

The exclusive use of the metabolic cost of transport as objective function leads to solutions, whose most salient feature is an extended knee pattern during the stance phase, which is not observed during normal walking. This observation deserves attention in future investigations, since it might indicate that an extended knee during stance is more economical than a flexed one. A direct conclusion would be that other cost functions that favor a flexed knee might play an important role during walking. This question, however, exceeds the scope of this research. In the design of assistive devices, much more important than a model that delivers accurate absolute values for the energy expenditure
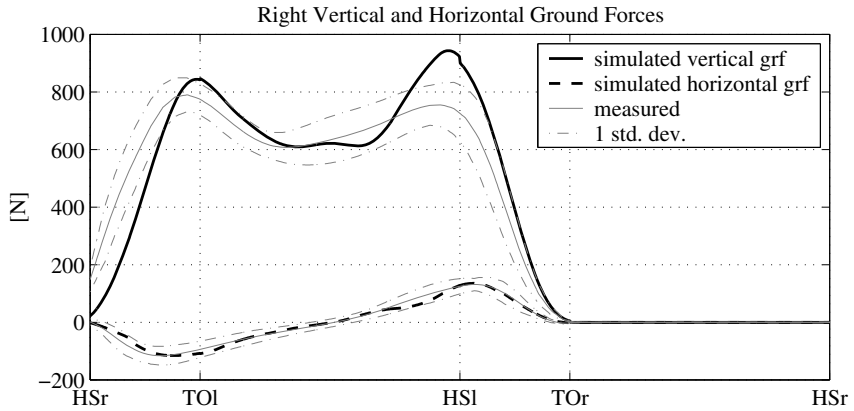
Figure 5.9: Simulated vertical and horizontal ground reaction forces, measured values for normal walking of subject 1, and standard deviations from Winter [122].
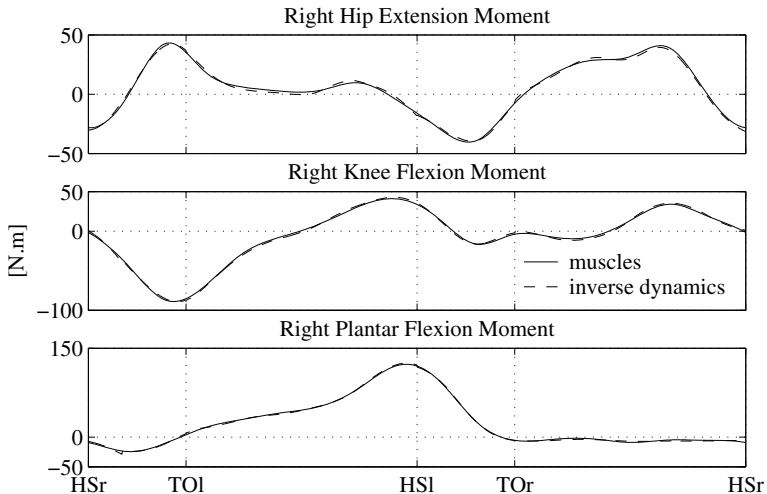
Figure 5.10: Comparison of the moments at the three right joints computed by inverse dynamics and applied by muscles. The good agreement indicates the fulfillment of the equations of motion.

are models that represent well the underlying energetic phenomena and can be used to evaluate the overall performance of one design of the assistive device in comparison to others. As explained in section 5.2.7, the incorporation of the deviation term (5.28) to
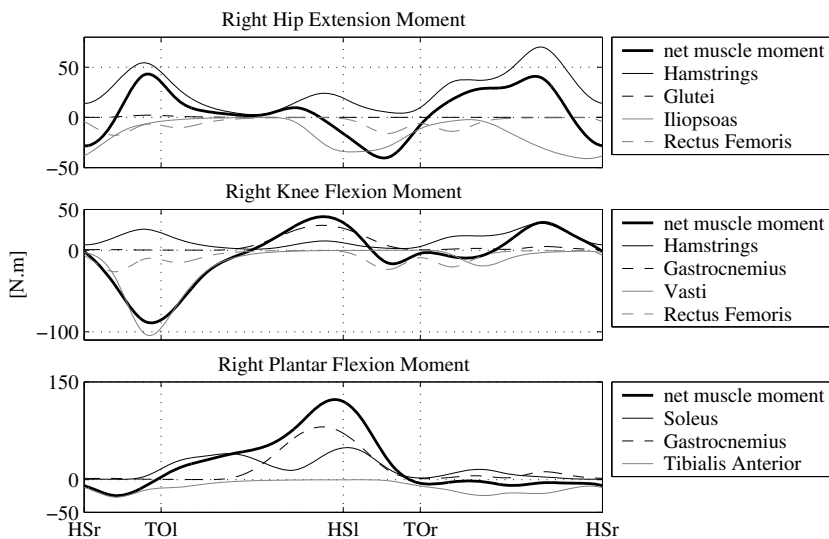
Figure 5.11: Contribution of the muscles to the net muscle moments at the joints.
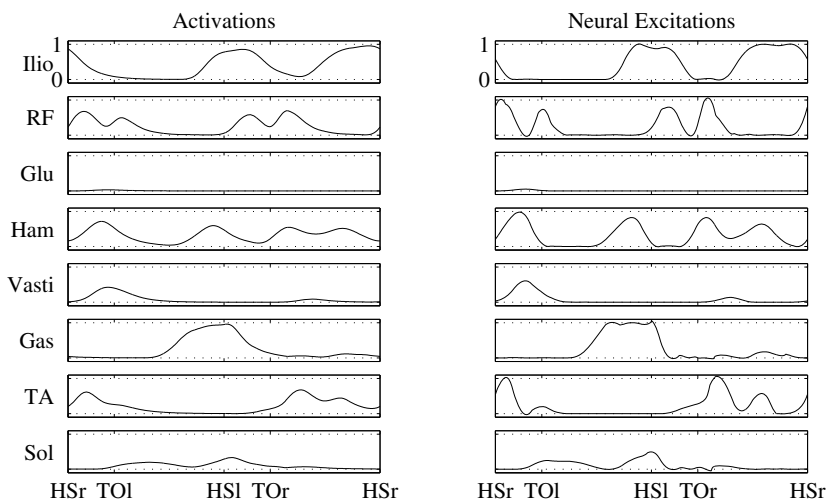
Figure 5.12: Muscle activations and neural excitations for each on the muscle unit considered for the right lower limb.

the cost function (5.29) is an attempt to take other possible performace criteria adopted during walking into account.

5.3.2 Bilateral Foot Weights

In this section, an example for the application of the approach proposed to study the adaptations caused by the introduction of mechanical disturbances is presented. The walking patterns resulting from a bilateral increase of 2 kg in the mass of both feet is simulated. The same model and parameters used in the previous section are employed. Table 5.2 shows the results obtained for the metabolic cost of transport E^t and for the deviation from measured kinematics and ground forces J_{dev} using four different combinations of weighting factors, named a) to d), where $w_1 + w_2 = 2$. The values for J_{SDO} are approximate values obtained using interpolation of values at control points, while the estimations for the metabolic cost of transport and the deviation from the kinematics and ground reaction forces measured for subject 1 are obtained by postprocessing using a fine grid. Walking velocity is constrained to 1.1275 m/s. The results are compared to the ones obtained for normal walking. As expected, for the normal as well as for the weight walking, increasing the importance of the metabolic cost of transport term leads to a decrease in the metabolic cost required and an increase in the deviation from the measured kinematics for the walking pattern found as solution.

Table 5.2: Comparison between normal walking and walking with a 2 kg increase in feet mass using different weighting factors, according to (5.29).

Weighting Factors	Normal			Foot Weight		
($J_{SDO} = w_1 \frac{E^t}{100} + w_2 J_{dev}$)	J_{SDO}	E^t [J/m]	J_{dev}	J_{SDO}	E^t [J/m]	J_{dev}
a) $w_1 = 1$; $w_2 = 1$	14.17	468.8	10.04	22.00	547.2	17.46
b) $w_1 = 4/3$; $w_2 = 2/3$	14.22	432.7	11.86	18.25	489.6	18.41
c) $w_1 = 8/5$; $w_2 = 2/5$	10.57	384.1	11.82	14.07	449.1	18.32
d) $w_1 = 20/11$; $w_2 = 2/11$	8.49	333.9	14.33	10.36	316.7	26.41

The walking with an increased feet weight shows a considerably worse performance J_{SDO} if compared to the undisturbed walking for all weighting combinations due to increases in the metabolic cost of transport E^t and in the deviation J_{dev}. The only exception occurs for the weighting combination d) ($w_1 = 20/11$ and $w_2 = 2/11$), where, in spite of the expected worse overall performance J_{SDO}, there is a decrease in the metabolic cost of transport. This can be explained by a solution for the increased foot weight simulation that is far from the measured kinematics and ground reaction forces, with $J_{dev} = 26.41$, what is compensated by a virtual decrease in metabolic cost of transport.

Figure 5.13 shows the muscle force contributions to the joint moments for the walking

with increased foot weights obtained with the weighting factors combination b). An overall increase in the muscle activity with respect to the results for normal walking shown in Fig. 5.11 is observed, what explains the significantly greater metabolic cost of transport shown in Tab. 5.2. Greater muscle activities and joint moments are observed specially during the swing phase of the gait due to the required acceleration and deceleration of the foot in the beginning and end of the swing phase, respectively. The distal position of the additional weight with respect to the hip and knee joints has a particularly negative effect on the moments required at these joints because of the quadratic growth of the corresponding mass moments of inertia with distance. Indeed, significantly greater hip extension and knee flexion moments are observed in the end of the swing phase to decelerate the lower limb. Furthermore, in the beginning of the swing phase a higher knee extension moment is observed.

Also in the stance phase changes in the joint moment patterns can be recognized. These changes are mainly characterized by increased maximal ankle plantar flexion and hip flexion moments in the second half of the stance phase. These variations occur probably due to the dynamics of the contralateral lower limb and illustrate the importance of considering whole body models to study pathological gaits.
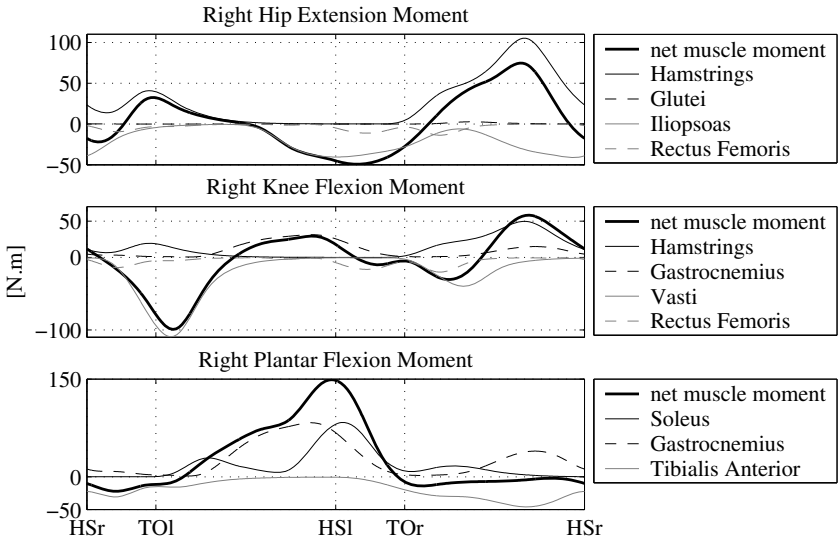

Figure 5.13: Contribution of the muscles to the net muscle moments at the joints for the simulation with additional 2 kg masses at the feet and using weighting factors $w_1 = 4/3$ and $w_2 = 2/3$ in the cost function (5.29).

5.3.3 Bilateral Transtibial Prostheses and Design Considerations

In this section the burden caused by a bilateral transtibial amputation to subjects walking with different bilateral transtibial prostheses is investigated with respect to the deviation from normal gait patterns and to energetic demands by means of simulations using the inverse dynamics-based method proposed in this chapter. This section also includes the determination of prosthetic ankle stiffness curves that improve the performance of the prosthesis compared to three different commercially available prosthetic feet.

A transtibial amputation results in the loss of the biological ankle articulation, the corresponding muscles spanning it and the foot. Prostheses are designed to restore, at least partially, the biomechanical function of these biological structures. Prosthetic ankle mechanical characteristics are primarily designed to substitute the action of plantar flexors (e.g. gastrocnemius and soleus) and of dorsiflexors (e.g. tibialis anterior). Specially the plantar flexors are deemed to play a fundamental role in human walking contributing to support, forward progression and swing initiation, refer e.g. to Neptune et al. [81].

Hansen et al. [39] concluded through analysis of the ankle moment versus ankle angle curve for the normal walking at different velocities that the net moment applied at the ankle joint could be effectively restored by a rotational spring and a damper at slow and normal walking velocities. At fast walking velocities, however, an augmented system would be required to fully restore the function of the biological actuators. Indeed, an appropriate choice of stiffness associated with a series of adaptations, for example, in the muscle coordination as investigated in Zmitrewicz et al. [138], can restore to a great extent normal gait kinematic and kinetic patterns. The adaptations required, however, imply in an increased energy consumption, that for unilateral transtibial prosthesis is characterized by a 20% higher rate of O_2 uptake as reported in Waters and Mulroy [121].

Different prostheses have been designed to improve the gait quality of transtibial amputees (Radcliffe [87]). For instance, the dynamic elastic response feet, e.g. the Seattle foot and the Flex-foot, are designed to store energy in the early stance and midstance and release it in the late stance and pre-swing to partially substitute the function of the plantar flexors (see Zmitrewicz et al. [139]). Therefore, these feet are claimed to provide a superior performance compared to earlier designs as the SACH foot. However, studies that compare these prostheses with respect to energetic demands have been inconclusive as pointed out by Waters and Mulroy [121], although Klute et al. [58] argues that these inconclusive results may be attributed to problems in sample populations or methodological limitations.

Stiffness differences at the prosthetic ankle joint have well-recognized effects on gait biomechanics (Lehman at al. [63]), but as observed by Klute et al. [58] "it remains completely unknown what optimal stiffness profile should be in order to minimize the metabolic cost

of locomotion, increase symmetry, or simply improve patient confort". In this context, the investigation performed here will focus on a comparison of three commercially available prosthetic feet with respect to ankle joint stiffness by means of numerical experiments. Furthermore, ankle joint stiffness curves that improve the gait quality of bilateral trastibial amputees are determined by incorporating parameters that describe the ankle moment versus ankle angle curve to the design variables of the optimization.

The model used is the same as in the previous sections with modifications to account for the bilateral transtibial amputations and prostheses. The masses, moments of inertia and positions of the centers of mass of the body segments are the same as the ones of the intact leg. In fact, the prosthesis alter these properties, which are dependent on the level of amputation and prosthesis type. However, in order to isolate the effect of ankle stiffness and due to the difficulty in determining these quantities accurately, the use of the same inertial properties of the intact leg seemed reasonable. The action of the uniarticular muscles soleus and tibialis anterior, of the biarticular gastrocnemius, and of other structures spanning the intact ankle joint are substituted by a prosthetic ankle moment caused by a damping and a rotational spring with moment versus angle characteristics as

$$
\tau_s = \begin{cases} a_p\, y_{ank}^3 + b_p\, y_{ank}^2 + c_0\, y_{ank}\,, & \text{if } y_{ank} > 0 \\ a_n\, y_{ank}^3 + b_n\, y_{ank}^2 + c_0\, y_{ank}\,, & \text{if } y_{ank} \leq 0 \end{cases}\,,
\tag{5.58}
$$

where τ_s is the moment applied by the rotational spring (in Nm), y_{ank} (in radians) is the prosthetic ankle angle for the right or left foot illustrated in Fig. 5.2 as y_6 or y_9, respectively, and a_p, b_p, c_0, a_n and b_n are the coefficients of the cubic polynomials. Note that, according to this parameterization, the ankle moment τ_s at $y_{ank} = 0$ is always 0, and that (5.58) is continuous up to the first derivative at $y_{ank} = 0$, where the stiffness is c_0. The total moment at the prosthetic ankle is, therefore,

$$
\tau_{prosth} = \tau_s(y_{ank}) - d_{prosth}\, \dot{y}_{ank}\,,
\tag{5.59}
$$

where d_{prosth} is the damping coefficient.

The action of the muscle gastocnemius at the knee joints remains the same, in spite of the amputations, and its length is computed by assuming a neutral intact ankle angle. The maximal isometric forces of all the muscles used in the previous section and shown in Tab. A.1 of Appendix A.1 are increased by 50%. This measure was adopted after convergence difficulties were encountered due to the high burden imposed by the bilateral amputations, specially at higher walking velocities. Since the reference normal walking patterns were also computed with the same increase in maximal isometric force and all the simulations are performed using the same muscle parameters, a reasonable comparison of the performance of the different prostheses and the normal gait is expected. However, an analysis of the sensitivity of the results presented here to variations in these parameters would be desirable, and might be the focus of future studies, since there are evidences

that changes in muscle strength might require a different muscle coordination to achieve optimal performance as investigated, for example, by Nagano and Gerritsen [78]. It is known that the maximal muscle strength is strongly subject-specific and depends on factors such as age, gender, body mass and body height (see e.g. Annegarn [10]) and can be substantially altered by strength training. For instance, Komi et al. [59] reported an increase in 20% in knee isometric extension moment after a 12-week muscle conditioning program. These evidences indicate that conclusive results will probably require the use of subject-specific muscle parameters.

Three different prosthetic feet commercially available are investigated, the conventional low-cost SACH foot, and the dynamic elastic response feet, Seattle foot and Flex-foot, see Fig. 5.14 for examples. The moment angle versus ankle angle curves reported in Klute et al. [58] (adapted from original measurements by Lehman et al. [63]) are adopted to characterize these feet. Please, note that the SACH foot is a solid ankle prosthetic foot and the ankle stiffness curve presented in Klute et al. [58] represents an equivalent stiffness curve derived from data measured by Lehman et al. [63]. For the simulations these curves were fitted using the polynomials in (5.58) resulting in the curves shown in Fig. 5.16. For the obtained coefficients of (5.58) refer to Appendix A.7. In the optimization where optimal stiffness curves for the prosthetic foot are searched, the coefficients of the polynomials in (5.58) are incorporated to the design variables (5.24) with proper scaling to avoid numerical problems. In order to ensure the computation of moment versus angle curves for the springs that are physically meaningful, additional constraints are introduced, that guarantee a monotonically decreasing moment versus angle curve for $\tau_s(y_{ank})$.

Figure 5.14: Picture of the SACH Foot[1] on the left, and illustration of the dynamic elastic response Flex-Foot on the right.

Numerical experiments are performed for three different walking velocities, 1.00 m/s, 1.33 m/s and 1.68 m/s, based on the kinematic data presented in Winter [122] for three difference walking cadences, slow, natural and fast, respectively. The reference normal kinematics, the ground reaction forces and the corresponding standard deviations used in

_____
[1]Photo courtesy of Ohio Willow Wood

the deviation term (5.28) of the cost function (5.29) for each one of the three velocities are also taken from the data reported in Winter [122]. For all velocities and prosthetic feet, the four different value combinations for the weighting factors, w_1 and w_2, introduced in section 5.3.2 that specify the relative importance of the two terms in the cost function (5.29) are used to investigate the influence of changing the relative importance of the terms on the results. As initial guess for the optimization search optimal gait patterns obtained for normal walking are used.

Table 5.3 presents the results obtained for all the numerical experiments performed for the value of the cost function J_{SDO}, for the metabolic cost of transport estimated E^t, and for the deviation J_{dev} of the kinematics of the lower limbs and of the ground reaction forces from the data in Winter [122]. The values for J_{SDO} are approximate values obtained using control points, while the estimations for the metabolic cost of transport E^t (5.27) in J/m and for the deviation from the experimental kinematics and ground reaction forces J_{dev} (5.28) of Winter [122] are obtained by postprocessing using a fine grid. The experiments indicated with stars refer to results surely corresponding to local minima, because the results for other factor combinations lead to lower values for the cost function. This shows the existence of local minima. Indeed, the use of different initial guesses often leaded to different local optima. Gradient-based, deterministic optimization algorithm deliver the local minimum most proximal to the initial guess. This shows the necessity of a careful interpretation of the results and indicates that stochastic optimization algorithms, which are more likely to find the global minimum, might be required to find more representative solutions.

Figure 5.15 clearly shows a much higher cost function value J_{SDO} for the prosthetic gait at the walking velocities $1.00\,m/s$ and $1.33\,m/s$ and for all the weighting factor combinations compared to the normal gait. This shows the expected worse performance of the walking with transtibial prostheses in comparison to the normal walking independently from the walking velocity or the cost function used. The results for the three prosthetic feet for the walking velocity $1.68\,m/s$ are not shown because difficulties to fulfill the constraints, specially the ones specifying maximal muscle neural excitations, were encountered during the optimization procedure. This stresses the high burden caused by a bilateral amputation and indicates that the physiological demands required for walking at this velocity can be hardly achieved with the capabilities of the model adopted.

The results also clearly show the significant improvement in the performance promoted by the use of optimal parameters for the ankle joint stiffness and damping. The values of the cost function, shown in Fig. 5.15, are much lower for the prosthesis with optimal parameters than the ones for the SACH foot, Seattle foot and Flex-foot, and even approximate the performance of the normal gait. This shows the potential impact of a good design of the prosthetic components on the ability of the prostheses to restore normal gait and enhance overall gait performance. In the following the results obtained will be

Table 5.3: Results obtained for the three prosthetic feet investigated, 'SACH', 'Seattle' and 'Flex', for optimal ankle design parameters 'opt. foot', and for the normal gait 'normal' at three walking velocities, 1.00 m/s, 1.33 m/s and 1.68 m/s, and for four weighting factor combinations.

numeric	$v_w = 1.00\ m/s$			$v_w = 1.33\ m/s$			$v_w = 1.68\ m/s$		
experiment	J_{SDO}	E^t	J_{dev}	J_{SDO}	E^t	J_{dev}	J_{SDO}	E^t	J_{dev}
a) $w_1 = 1;\ w_2 = 1$									
SACH	15.97*	467.7*	12.05*	23.79	586.8	18.56	–	–	–
Seattle	15.05	437.2	11.07	25.29*	520.8*	21.00*	–	–	–
Flex	21.96	373.2	18.91	29.71*	489.7*	25.83*	–	–	–
opt. foot	9.87	294.3	7.31	12.46	352.0	9.44	22.46	552.7	22.39
normal	6.94	375.2	3.41	8.57	439.0	4.40	16.53	585.9	11.46
b) $w_1 = 4/3;\ w_2 = 2/3$									
SACH	12.18	350.6	11.85	19.78	550.7	19.34	–	–	–
Seattle	11.93	362.0	11.60	15.00	453.2	14.16	–	–	–
Flex	17.46	341.7	20.31	20.85	417.3	23.95	–	–	–
opt. foot	9.99*	317.9*	9.12*	11.15	323.5	10.88	21.72	475.3	24.26
normal	8.01	310.6	4.36	8.51	401.4	5.13	15.86	505.2	14.35
c) $w_1 = 8/5;\ w_2 = 2/5$									
SACH	10.75*	367.0*	13.19*	16.48	512.2	21.54	–	–	–
Seattle	10.28	350.7	12.21	14.30	425.8	20.16	–	–	–
Flex	12.43	256.1	21.83	14.89	334.7	24.82	–	–	–
opt. foot	6.39	188.7	8.87	10.37*	289.5*	15.42*	17.71*	565.8*	23.44*
normal	6.39	270.5	5.59	7.78	306.3	7.77	13.23	453.8	15.83
d) $w_1 = 20/11;\ w_2 = 2/11$									
SACH	10.37*	391.9*	19.36*	13.01	447.9	27.76	–	–	–
Seattle	8.11	290.2	17.82	10.54*	428.0*	24.61*	–	–	–
Flex	7.68	191.3	24.13	10.03	286.2	27.90	–	–	–
opt. foot	6.08*	199.7*	14.68*	6.44	218.5	14.56	14.68*	543.0*	29.82*
normal	5.42	208.4	9.66	6.76	229.1	15.36	11.73	418.7	23.93

discussed in more details.

Starting with a comparison between the three investigated prosthetic feet at the two investigated velocities, 1.00 m/s and 1.33 m/s, the Flex-foot caused a lower energy consumption if compared to the other two commercially available prosthetic feet as shown in Tab. 5.3. This reduced metabolic cost of transport is visualized in Fig. 5.15 for the weighting factors combination d), for which the metabolic cost of transport is favored with respect to the tracking of normal walking patterns. For all the other weighting fac-
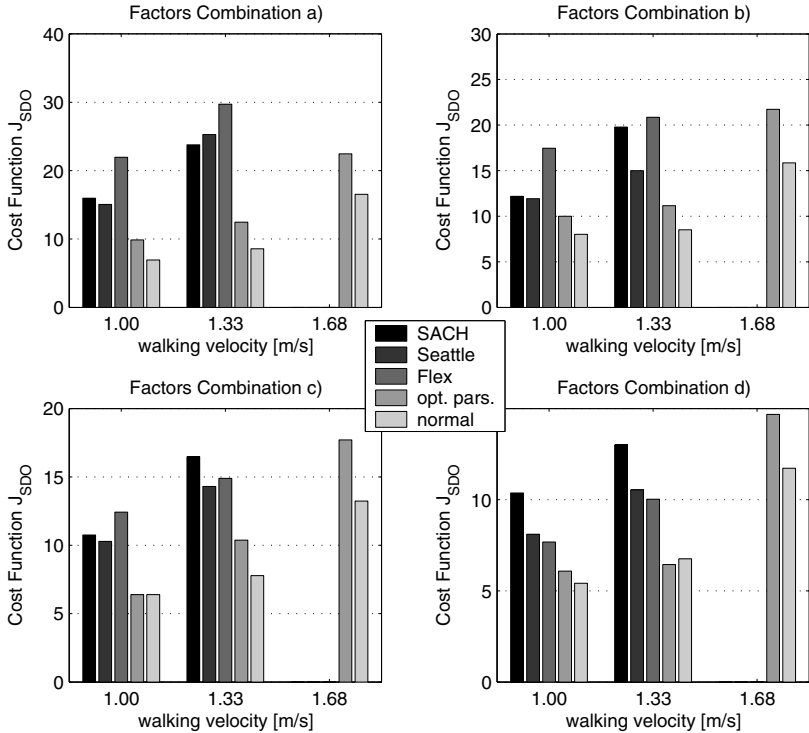
Figure 5.15: Cost function values for the four ankle moment-angle relations and the normal walking for the four factors combinations and the three walking velocities considered.

tor combinations the Flex-foot presents the worst performance due to a greater deviation from the normal walking patterns, although always requiring a reduced energetic demand. This observations can be explained by the lower stiffness of the Flex-foot in dorsiflexion. The required plantar flexion moments at midstance, final stance and pre-swing to promote vertical support and forward progression (Netpune et al. [81]) lead to a greater dorsiflexion for the less stiff Flex-foot than for the SACH and Seattle feet, which surpasses the normal dorsiflexion patterns in these phases contributing to the worse tracking of normal patterns presented by the Flex-foot.

On the other hand, as pointed out in Klute et al. [58], an excessive dorsiflexion stiffness in a prosthetic foot can inhibit the progression of the tibia and hence knee flexion, what could explain in part the higher energy consumption observed for the SACH and Seattle feet, which are stiffer in dorsiflexion. Furthermore, the Flex-foot, being less stiff, permits a
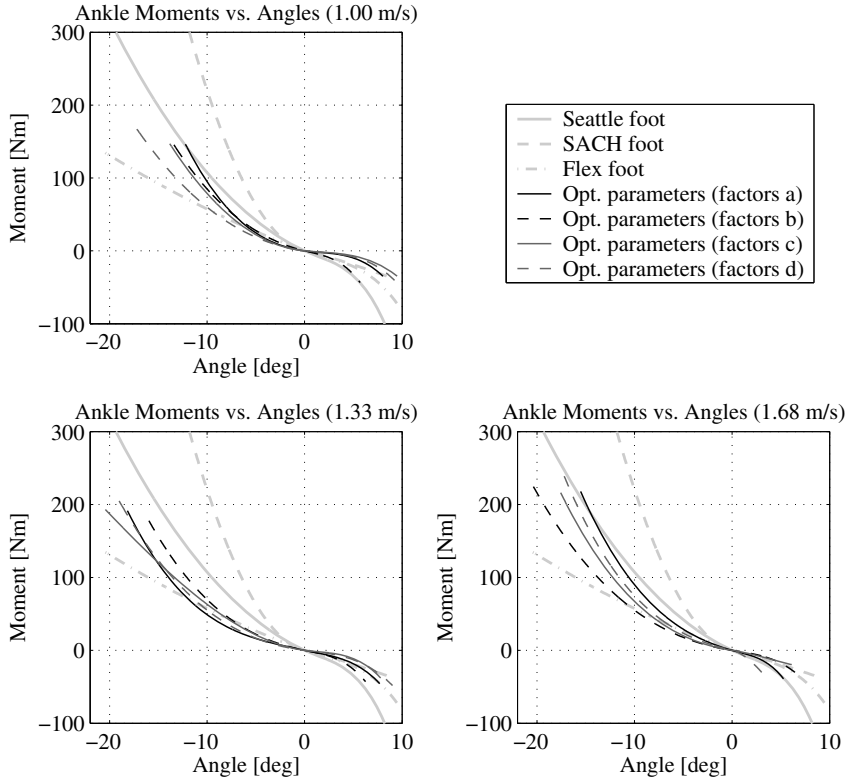
Figure 5.16: Near-optimal moment-angle relations for the prosthetic ankle joint obtained using the optimization approach proposed. The coefficients in (5.58) are determined for the three different walking velocities shown and for the four factor combinations shown in Tab. 5.3.

higher energy storage and realease, what can contribute to the lower energy requirements observed for the Flex-foot. Indeed, Tab. 5.3 shows that, with few exceptions, the metabolic cost of transport grows with the stiffness of the foot in dorsiflexion, from the highest metabolic cost of transport for the SACH foot to the lowest for the Flex-Foot.

The Seattle foot and SACH foot presented better performance with respect to proximity to normal walking patterns, what is indicated by the lower values for the deviation term J_{dev} at all numerical experiments performed shown in Tab. 5.3 and by the lower values for the cost function in Fig. 5.15 for the weighting factor combinations that favor the tracking of normal gait over the metabolic cost of transport (factor combinations a) and b)). The Seattle foot presented the best performance at the two walking velocities for the factor

combinations a), b) and c), with one exception (velocity 1.33 m/s and factors combination a)), which, however, can be disconsidering because it represents a local minimum as indicated by stars in Tab. 5.3. The Seattle foot seems, therefore, to be a reasonable choice when energetic efficiency is not the primary concern, for which the Flex-foot seems to deliver the best outcomes. Nevertheless, the high sensitivity of the performane of these feet to the cost function chosen (different weighting factor combinations) clearly shown in Fig. 5.15 indicates the great importance of defining proper cost functions to compare the performace of assistive devices. This determination is, however, a difficult task since a performance criteria depends on a series of factors that are often subject-dependent, difficult to quantify or to estimate, such as pain, aesthetics, comfort, mobility, energetic efficiency, smoothness, and others.

In order to determine prosthetic ankle features that improve the performance of transtibial prostheses, the coefficients that describe the ankle moment versus ankle angle in (5.58) and the damping coefficient in (5.59) are incorporated to the set of design variables (5.24). Simulations for three different walking velocities, 1.00 m/s, 1.33 m/s and 1.68 m/s, and for all the weighting factors combinations are performed. The optimal results (not necessarily global optima) for the parameterized ankle moment versus angle curves are shown in Fig. 5.16. Numerical values for the coefficients obtained for each one of the numerical experiments are reported in Tab. A.8 of Appendix A.7. The corresponding performance of the optimal prosthetic feet are listed in Tab. 5.3 and illustrated in Fig. 5.15 together with the results for the normal walking and the three prosthetic feet investigated.

The results show a significant improvement in the optimal prosthetic foot performance with respect to the three investigated feet, even approximating the performance to the one of the simulated normal gait. The metabolic cost of transport E^t demanded and the deviation from the normal experimental data J_{dev} are significant lower than the ones for the three investigated feet. This indicates the potential of improving the design of the prosthetic ankle to enhance the overall gait performance of bilateral transtibial amputes.

Although, as expected, the cost function is in all but one experiment lower for the normal gait than for the optimal prosthetic gait, the metabolic cost of transport for the optimal prosthesis is often lower than for the normal walking. This can be partially attributed to the absence of the muscles tibialis anterior and soleus in both lower limbs, and to the use of a multiobjective cost function. The metabolic cost of transport would be most probably lower for the normal walking if E^t alone would be used as cost function, i.e. with $\omega_1 = 2$ and $\omega_2 = 0$. The results might also indicate oversimplication and inaccuracies in the models adopted – the musculoskeletal model, the muscle dynamics models and the energy expenditure model.

Regarding the optimal moment versus angle curves shown in Fig. 5.16, some conclusions that can assist on the design of future improved prosthetic ankle joints can be drawn. In spite of the different walking velocities and weighting factors combinations, surprisingly

similar optimal moment versus angle curves were obtained, specially in dorsiflexion. The curves are characterized by lower stiffnesses for smaller dorsiflexion angles near $y_{ank} = 0$, where they approximate the curve corresponding to the Flex-foot, and by fast increasing moments approximating the torque applied by the Seattle foot at greater dorsiflexion angles. The only clear characteristic recognized for the optimal moments versus angle curves at plantar flexion angles is that the curves are in the range of the moments applied by the three commercially available prosthetic feet investigated. The moment versus angle curve at dorsiflexion seems, therefore, to be the preponderant factor that explains the consistently better performance of the optimal prosthetic feet over the other investigated feet. The better performance of the optimal feet is explained by a moment versus angle curve at dorsiflexion that favors energy storage and tibia progression in mid stance, where the dorsiflexion is still reduced, and by higher moments at greater dorsiflexion angles which guarantee vertical support, forward progression and swing initiation during late stance and pre-swing at normal dorsiflexion angles.

The similarity of the optimal curves obtained indicates that a single stiffness curve could lead to near-optimal gait performance at very different walking velocities and for different cost functions, while presenting a significantly better performance compared to the SACH foot, Seattle foot or Flex-foot. Although the results shown here are specific for the model adopted, an average of the curves obtained for all velocities and weighting factors combinations could be a good initial guess for the design of improved passive prosthetic ankle systems. A rotational nonlinear spring with this average moment versus deflection curve would be a mechanical realization.

The investigation performed in this section demonstrates the potential of the optimization framework proposed in this chapter to evaluate the performance of existing assistive devices and improve the performance of assistive devices in the design phase. Note that the quality of the evaluations and predictions delivered are just as good as the accuracy of the underlying models of the musculoskeletal system and the correctness of the cost function chosen.

Chapter 6

Summary

Locomotor system models are proposed and used to investigate human walking by means of computational simulations. The skeletal system is modeled by multibody systems composed of rigid bodies. The biological actuators, the muscles, are modeled by the so-called Hill-type models, which are composed by a contractile element representing the fibers that generate force, and elastic elements in series and in parallel representing structures in series and in parallel to the muscle fibers. The biochemical processes leading to force generation are modeled by an activation and a contraction dynamics resulting in a second-order dynamics. Furthermore, recently proposed metabolic cost models assess the energetics of muscle contraction in conjunction with Hill-type muscle models. These models are used to investigate gait using techniques to compute moments at the joints from kinematics and ground reaction forces measured in a gait analysis laboratory, to estimate muscle forces non-invasively from the moments at the joints, and to generate optimal normal and pathological walking patterns.

In spite of the increasing use of computational simulation to investigate gait, the high-dimensionality of the musculoskeletal models arising from the many degrees of freedom of the skeletal system models and from the several muscle units involved in motion generation, leads frequently to a prohibitive computational effort, specially when optimization procedures are involved. This prevents its wider use in clinical applications or requires oversimplification of the models leading often to unrealistic estimations. In this context the aim of this dissertation is twofold. On the one hand, approaches to predict kinematics, kinetics, muscle coordination and energetics of normal and pathological gaits are proposed that offer alternatives to conventional techniques that require overwhelming computational effort or result in unphysiological estimations. On the other hand, this dissertation aims at delivering a contribution to the understanding of pathological gaits, and to the design of assistive devices, in particular lower limb prostheses.

The motion and external forces measured in a gait analysis laboratory are used to assess net moments at the joints required to generate the observed motion of the skeleton by

means of inverse dynamics. In order to investigate the burden caused by lower limb assistive devices experiments are designed to simulate typical deviations of the mechanical properties of the lower limb that arise by wearing orthotic and prosthetic devices, namely alterations in the inertial properties and mobility of the lower limbs. The experiments are performed in the laboratory of the Institut fuer Sportwissenschaft of the Universitaet Stuttgart, where the 3-D trajectories of markers attached to anatomical landmarks of two subjects are measured together with the ground reaction forces during the walking with different mechanical disturbances. The translation and rotation of the body segments are computed from the 3-D trajectories by means of reconstruction techniques, and used to estimate net joint moments for all experiment by inverse dynamics.

The results obtained for the kinematics and kinetics are compared and discussed. It was shown that the variations caused by the introduction of mechanical disturbances typically introduced by lower limb prostheses by modification of the inertial properties of segments and by the introduction of kinematic constraints to the joints of the lower limb cause significant deviations in the kinematics and kinetics of the whole body with respect to normal patterns. Also the nature and the magnitude of these deviations are to a great extent assessed. Another contribution of this study is providing a framework for further investigations of this type where all the important steps to compute the kinematics and the moments at the joints are explained in detail, and the many sources of errors are presented and discussed. The information and analyses delivered can also contribute to the modeling process and to the interpretation of simulation results for handicapped gaits.

Although giving some insight into the muscle effort, net joint moments do not deliver information on individual forces applied by muscles and other structures spanning the joints, which are important, for instance, to assess muscle coordination and internal loads on joints and bones, useful for the design of endoprostheses or to assess, e.g., the risk of damage of ligaments during sport activities. Since muscle forces cannot be directly measured without invasive techniques, they are often estimated from joint moments obtained by inverse dynamics. However, because there are many more muscles than actuated degrees of freedom, there is an infinite number of solutions for the muscle forces that generate the same net joint moments. In order to determine a unique solution optimization techniques are used, based on the assumption that the central nervous system distributes muscle forces such as to minimize a performance criterion. The conventional method to solve the resulting so-called muscle force-sharing problem is called static optimization and, although being computationally efficient, suffers from two important limitations: 1) it neglects the dynamics involved in the muscle force generation process, what can lead to unphysiological muscle force histories, and 2) it requires the use of instantaneous cost functions, excluding the possibility of using time-integral cost functions as the total metabolic cost, which was shown to play a key role during walking.

In order to overcome these limitations dynamic optimization associated with a tracking

of the measured kinematics is an alternative. This approach requires, however, extremely high computational costs due to the several numerical integrations of the high-dimensional system equations necessary. Two alternative approaches are proposed to overcome the limitations of static optimization delivering more realistic muscle force estimations while being computationally less expensive than dynamic optimization. One approach named extended inverse dynamics delivers physiological estimations of muscle forces by considering the muscle activation and contraction dynamics and by permitting the use of time-integral cost functions as total metabolic cost. Although the improvements provided by this approach makes it computationally much more expensive than static optimization, it is less expensive than dynamic optimization, because it does not require any numerical integration of the state equations. The second proposed approach, named modified static optimization, offers a viable alternative to static optimization by considering the muscle activation and contraction dynamics while requiring a low computational effort.

The two proposed approaches are applied to estimate muscle force histories for the measured normal gait of the subjects using a musculoskeletal model of their lower limbs. The approaches are compared to the static optimization with respect to computational effort and fulfillment of constraints that guarantee the consideration of the dynamics involved in the process of muscle force generation. Applications to the normal and selected disturbed gaits are presented and discussed. The extended inverse dynamics approach is validated through two different ways: a comparison of the results for the muscle activations with the linear envelopes of electromyograms from the literature for the normal gait, and the use of the computed neural excitations as input to a forward-dynamics simulation, with the subsequent comparison of the kinematics obtained with the originally measured one. The estimations of energy expenditure obtained through both ways are compared, too. Other alternative approaches recently proposed in the literature to solve the muscle force-sharing problem are reviewed. The choice of a proper approach depends on the accuracy required, the computational facilities available, and the particularities of each method.

For the design of new assistive devices, surgical interventions and rehabilitation therapies it is desirable to predict the effect of a specific design, intervention or therapy on the walking patterns, including the motion, too. In order to achieve this predictive capability computational simulations of the human motion using the mentioned available models of the musculoskeletal system are used. In particular, the dynamic optimization is successfully used, permitting the use of time-integral cost functions and the consideration of the dynamics of the muscle force generation process. In spite of the growing use of dynamic optimization to simulate human motion, the extremely high computational effort arising from the several numerical integrations of the large-scale state equations required prevents it from being widely used. Computationally less expensive approaches to simulate motion are, therefore, essential to allow for design and clinical applications.

The use of approaches based on inverse dynamics have the potential to reduce the high

computation effort by avoiding the necessity of numerically integrating the state equations. Such approaches consist in transforming the optimal control problem into a parameter optimization, where the optimization variables are the parameters of functions that approximate the motion of the mechanical system. Although the application fields range from robotics and bipedal walking machines to character animation, this approach has been poorly explored in biomechanics. An inverse dynamics-based approach to simulate human motion that deals with the overdeterminacy of muscle actuation and is adequate to the use in conjunction with Hill-type muscle models widely used in biomechanics is proposed. Because of the parameterization of states the approach is named state dynamic optimization.

This third approach proposed named state dynamic optimization is based on the parameterization of the motion and muscle forces using polynomials that interpolate nodal values, which are incorporated to the design variables. The neural excitations are obtained by inverting the muscle contraction and activation dynamics. The optimization problem is formulated as a search for optimal skeleton motion and muscle forces that minimize a time-integral cost function, e.g., the metabolic cost of transport and the deviations from normal measured patterns, subject to constraints that ensure bounded neural excitations, fulfillment of the kinematic constraints between feet and ground, and consistency between muscle forces and motion by fulfillment of the equations of motions throughout the walking cycle. The fulfillment of the constraints is checked at discrete, properly distributed control points. The approach is used to generate normal walking patterns that are shown to approximate normal measured kinematics and ground reaction forces, proving its viability.

The state dynamic optimization approach is also used to investigate the walking with a bilateral 2 kg-increase in feet mass, and to predict skeleton motion, muscle coordination and metabolic cost of walking with three different bilateral transtibial prostheses, characterized by their ankle moment versus ankle angle curves. Furthermore, improved parameters describing a general prosthetic ankle stiffness curve are determined by incorporating them to the optimization variables. The results show that the optimal prosthetic ankle stiffness curves computed lead to significant improvements compared to the three prosthetic foot investigated with respect to energetic demand and deviation from normal patterns, for the three different walking velocities investigated. This indicates the potential of the proposed approach in helping on the design of assistive devices.

Appendix

A.1   Muscle Parameters

This section presents the models of the musculoskeletal system, its energetics, and the corresponding numerical parameters adopted throughout this work.

Activation dynamics

The model of the activation dynamics, refer to section 2.2.2, is adopted from He at al. [46], refer to (2.17). The time constants for activation t_a and de-activation t_d are computed for each muscle depending on the percentage of fast twitch fibers ft using an expressions proposed in Umberger et al. [115] as

$$t_a = A_{a1} - A_{a2}\, ft\,, \tag{A.1}$$

$$t_d = A_{d1} - A_{d2}\, ft\,, \tag{A.2}$$

where $A_{a1} = 80$ ms, $A_{a2} = 0.47$ ms, $A_{d1} = 90$ ms, $A_{d2} = 0.56$ ms. Numerical values for the percentage of fast twitch fibers ft (adopted from Gerritsen et al. [34]) are presented in Tab. A.1.

Force-length-velocity relation

The model of the force-length-velocity relation scaled by the muscle activation a, refer to section 2.2.2 and Fig. 2.7, is adopted from Soest and Bobbert [117] and from Cole et al. [24]. The expression for a concentric contraction with $v^{ce} < 0$ reads as

$$\frac{f^{ce}}{f^m_{max}} = \frac{aB_r(f_{iso} + A_r) - aA_r(B_r - \frac{\tilde{v}^{ce}}{fac})}{B_r - \frac{\tilde{v}^{ce}}{fac}}\,, \tag{A.3}$$

where $\tilde{v}^{ce} = v^{ce}/l^{ce}_{opt}$, $A_r = 0.41$, $B_r = 5.2$, l^{ce}_{opt} is the muscle fibers optimal length (in Tab. A.1 for each one of the muscles considered), f^m_{max} is the maximal isometric force a muscle generates (see Tab. A.1), and f_{iso} is the muscle isometric force relative to the

maximal muscle force f_{max}^m obtained with

$$f_{iso} = \frac{-1}{width^2} \left(\frac{l^{ce}}{l_{opt}^{ce}}\right)^2 + \frac{2}{width^2} \left(\frac{l^{ce}}{l_{opt}^{ce}}\right) - \frac{1}{width^2} + 1 \,, \qquad \text{(A.4)}$$

where $width$ is a muscle-specific parameter, see Tab. A.1 for the adopted values. The parameter fac follows from $fac = \min(1, 3.33 \times a)$ in Soest and Bobbert [117]. In the applications presented in this dissertation a modification of this expression is used by setting $fac = 1$ in order to reduce the computational effort required to invert the contraction dynamics.

The expression of the force-length-velocity relation scaled by the muscle activation for an eccentric contraction with $v^{ce} \geq 0$ reads as

$$\frac{f^{ce}}{f_{max}^m} = \frac{b_1 a - b_2 a (b_3 - \tilde{v}^{ce})}{b_3 - \tilde{v}^{ce}} \,, \qquad \text{(A.5)}$$

where

$$b_2 = -f_{iso} \, f_{asympt} \,, \qquad \text{(A.6)}$$

$$b_1 = \frac{fac \, B_r (f_{iso} + b_2)^2}{(f_{iso} + A_r) \, slopefactor} \,, \qquad \text{(A.7)}$$

$$b_3 = \frac{b_1}{f_{iso} + b_2} \,, \qquad \text{(A.8)}$$

and $slopefactor$ is the ratio between eccentric and concentric derivatives (derivative of the muscle CE force with respect to the muscle CE shortening velocity) for an isometric contraction, i.e. at a CE shortening velocity $v^{ce} = 0$. The $slopefactor$ adopted in Soest and Bobbert [117] is 2. In this dissertation a $slopefactor = 1$ as shown in Fig. A.1 is used for the applications to avoid discontinuities in the objective function as explained in section 4.5.1. The modification of the force-velocity relation caused by this measure is small and a significant loss of quality in the results obtained for large-scale musculoskeletal models is unlikely.

Muscle total length and moment arm

The muscle lengths l^m and moment arms can be determined as functions of the generalized coordinates using expressions or tables available in the literature (see, for example, Delp [29] and Menegaldo et al. [73]). In this dissertation the simple expression proposed by Gerritsen et al. [34] is adopted, which has the general form

$$l^m = l_0^m + r_a \left(\frac{\pi}{2} - \gamma\right) + r_k \beta - r_h \alpha \,, \qquad \text{(A.9)}$$

where γ is the angle between thigh and trunk (equivalent to $y_4 - y_3$ or $y_7 - y_3$ in Fig. 5.2), β is the angle between shank and knee (equivalent to y_5 or y_8 in Fig. 5.2) and γ is the angle
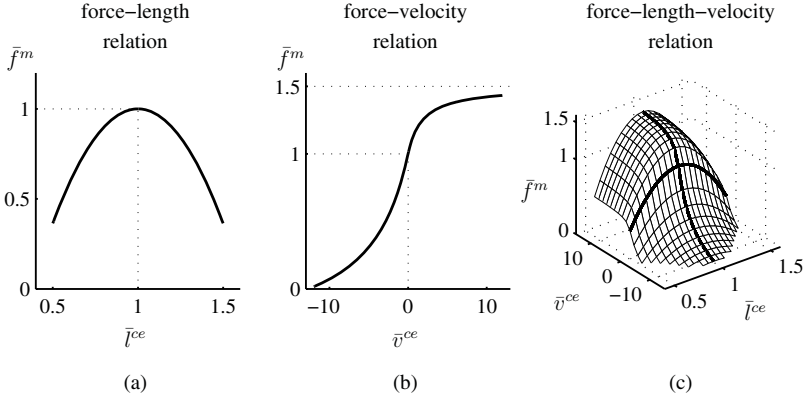
Figure A.1: (a) force-length relation model, where $\bar{f}^{ce} = f^{ce}/f^m_{max}$ and $\bar{l}^{ce} = l^{ce}/l^{ce}_{opt}$; (b) modified force-velocity relation model with *slope factor* = 1 instead of 2, compare to Fig. 2.7, where $\bar{v}^{ce} = v^{ce}/l^{ce}_{opt}$; (c) force-length-velocity model. The curves are for the expressions presented in Nagano and Gerritsen [78] with $a = 1$, $ft = 50\%$, and $width = 0.627$.

between foot and shank (equivalent to angles y_6 or y_9 in Fig. 5.2), and parameters l^m_0, r_a, r_k, and r_h are listed in Tab. A.1. Positive r_k and r_h indicate knee and hip flexor muscles, respectively, while negative r_k and r_h indicate knee and hip extensor muscles, respectively. A positive r_a indicates a plantar flexor muscle, while a negative r_a indicates a dorsiflexor muscle. The muscle lengthening/shortening velocity can be obtained by differentiating (A.9).

Defining the moment arm $r_{i,k}$ of muscle i with respect to joint k as

$$r_{i,k} = \frac{\tau_{i,k}}{y_k}, \tag{A.10}$$

where $\tau_{i,k}$ is the moment at joint k generated by muscle i, and y_k is the coordinate defining the rotation at joint k, then, using the principle of virtual work, the moment arm $r_{i,k}$ can be directly obtained from (A.9) as

$$r_{i,k} = -\frac{\partial l^m_i}{\partial y_k}, \tag{A.11}$$

where l^m_i is the total length of muscle i.

Metabolic cost rate expressions

As explained in section 2.2.3, phenomenological energy expenditure models that can be used in conjunction with Hill-type muscle models have been recently proposed by Bhargava et al. [17] and Umberger et al. [115]. In this dissertation the expressions in Umberger

et al. [115] are used, because, as claimed by the authors, they are adequate for human movements at submaximal contraction conditions, as the ones occurring during walking. In the following the expressions for the metabolic cost rate are reproduced. For a complete clarification of the expressions refer to Umberger et al. [115]

The total muscle metabolic energy expenditure rate $\dot{E}$ is the sum of the muscle CE mechanical power $\dot{W}$ and the muscle CE heat rate $\dot{H}$ as

$$\dot{E} = \dot{W} + \dot{H} = -f^{ce} v^{ce} + m_{musc} \, \dot{h}(u, a, v^{ce}, l^{ce}, f^{ce}, \boldsymbol{p}^m), \tag{A.12}$$

where $\dot{h}$ is the total specific muscle heat rate, $\boldsymbol{p}^m$ contains muscle-specific parameters listed in Tab. A.1, and m_{musc} is the muscle mass computed from the maximal isometric force f^m_{max} with

$$m_{musc} = \rho^m \, l^{ce}_{opt} \, PCSA = \frac{\rho^m \, l^{ce}_{opt}}{\sigma^m} f^m_{max}, \tag{A.13}$$

where $PCSA$ is the muscle physiological cross-sectional area, ρ is the muscle density (for mammalian muscle $\rho^m = 1059.7 \, kg \, m^{-3}$), and σ^m is the muscle specific tension (assumed here to be $\sigma^m = 0.25 \, MPa$).

The specific muscle heat rate $\dot{h}$ is further subdivided into the maintenance heat rate $\dot{h}_m$, the shortening/lengthening heat rate $\dot{h}_{sl}$, both due to the interaction between the myosin and actin filaments, and the activation heat rate $\dot{h}_a$ due to the sarcoplasmic reticular ion transport process, as

$$\dot{h} = \dot{h}_m + \dot{h}_{sl} + \dot{h}_a. \tag{A.14}$$

The expressions for the total specific muscle heat rate $\dot{h}$ read as follows

If $\quad l^{ce} \leq l^{ce}_{opt}$

$$\dot{h} = \dot{h}_{am} \, a_m^{0.6} \, S + \\ + \begin{cases} (-\alpha_{s,st} \, \tilde{v}^{ce} \, (1 - ft/100) - \alpha_{s,ft} \, \tilde{v}^{ce} \, ft/100) \, a_m^{2.0} \, S & \text{if} \quad \tilde{v}_{ce} \leq 0 \\ \alpha_l \, \tilde{v}_{ce} \, a_m \, S & \text{if} \quad \tilde{v}_{ce} > 0 \end{cases} \tag{A.15}$$

If $\quad l^{ce} > l^{ce}_{opt}$

$$\dot{h} = (0.4 + 0.6 \, f_{iso}) \dot{h}_{am} \, a_m^{0.6} \, S + \\ + \begin{cases} (-\alpha_{s,st} \, \tilde{v}^{ce} \, (1 - ft/100) - \alpha_{s,ft} \, \tilde{v}^{ce} \, ft/100) \, f_{iso} \, a_m^{2.0} \, S & \text{if} \quad \tilde{v}_{ce} \leq 0 \\ \alpha_l \, \tilde{v}_{ce} \, f_{iso} \, a_m \, S & \text{if} \quad \tilde{v}_{ce} > 0 \end{cases} \tag{A.16}$$

where

$$
a_m = \begin{cases} u & \text{for} \quad u > a \\ (u + a)/2 & \text{for} \quad u \le a \end{cases} , \tag{A.17}
$$

$$
\dot{h}_{am} = 1.28\, ft + 25 \, , \tag{A.18}
$$

$$
\alpha_{s,st} = \frac{250}{\tilde{v}^{ce}_{max,ft}} \, , \tag{A.19}
$$

$$
\alpha_{s,ft} = \frac{153}{\tilde{v}^{ce}_{max,ft}} \, , \tag{A.20}
$$

$$
\alpha_l = 4\, \alpha_{s,st} \, , \tag{A.21}
$$

where $\tilde{v}^{ce}_{max,ft}$ is the maximal shortening velocity of the fast twitch fibers in optimal CE lengths l^{ce}_{opt} per seconds and is assumed here to be $\tilde{v}^{ce}_{max,ft} = 12\, l^{ce}_{opt}/s$, and S is a scaling factor that specifies the primarily contraction condition: if primarily anaerobic $S = 1$, if primarily aerobic $S = 1.5$. Since walking is a a primarily aerobic exercise $S = 1.5$ is adopted. Equations (A.15-A.16) are supplemented by the following conditions: (1) the total specific heat rate is not allowed to fall below $1.0\ W\ kg^{-1}$; and (2) the term $(-\alpha_{s,st}\, \tilde{v}^{ce}\, (1 - ft/100))$ cannot exceed $100\ W\ kg^{-1}$.

Table A.1: Table of parameters adopted for the muscle groups considered: percentage of fast twitch fibers ft from Gerritsen et al. [34], optimal CE length l^{ce}_{opt} from Gerritsen et al. [34], $width$ from Gerritsen et al. [34], tha maximla isometric muscle force f^m_{max} from Gerritsen et al. [34], tendon slack length l_{slack} from Gerritsen et al. [34], muscle fibers pennation angle α_p from Menegaldo et al. [72]. The muscle groups considered are iliopsoas (Ilio), rectus femoris (RF), glutei (Glu), hamstrings (Ham), vasti (Vas), gastrocnemius (Gas), tibialis anterior (TA), and soleus (Sol).

	ft [%]	l^{ce}_{opt} [m]	$width$	f^m_{max} [N]	l_{slack} [m]	α_p [deg.]	l^m_0 [m]	r_a [m]	r_k [m]	r_h [m]
Ilio	50	0.102	1.298	821	0.142	7.5	0.248	0	0	−0.050
RF	65	0.081	1.443	663	0.398	5.0	0.474	0	0.050	−0.034
Glu	45	0.200	0.625	1705	0.157	3.0	0.271	0	0	0.062
Ham	35	0.104	1.197	1770	0.334	7.5	0.383	0	−0.034	0.072
Vas	50	0.093	0.627	7403	0.223	4.4	0.271	0	0.043	0
Gas	50	0.055	0.888	1639	0.420	14.3	0.404	0.053	−0.020	0
TA	25	0.082	0.442	1528	0.317	6.0	0.464	−0.037	0	0
Sol	20	0.055	1.039	3883	0.245	23.6	0.201	0.053	0	0

A.2   Inertial Parameters of the Mechanical Disturbances

In the following table the masses and moments of inertia of the mechanical disturbances and of the usual shoes of the subjects are listed, see Fig. 3.4. The moments of inertia are given with respect to the center of mass of the bodies and around the three Cartesian axes aligned with the global frame for the reference position of the body, before the start of the trial. The masses were measured with an electronic balance. The moments of inertia were determined by pendulum experiments performed with different arms. Because of inaccuracies in the determination of the position of the center of mass, in the alignment of the axes of rotation with the axes of the disturbances and in the experimental setup errors of up to 30% in the moments of inertia are to be expected. Very small values of the moments of inertia with respect to the ones of the lower limb are neglected.

Table A.2: Masses and moments of inertia of the disturbances.

Disturbance	value	unity
shoes of subject 1		
mass	0.319	kg
moment of inertia about X axis	0	$kg\,m^2$
moment of inertia about Y axis	0.0017	$kg\,m^2$
moment of inertia about Z axis	0.0017	$kg\,m^2$
shoes of subject 2		
mass	0.279	kg
moment of inertia about X axis	0	$kg\,m^2$
moment of inertia about Y axis	0.0014	$kg\,m^2$
moment of inertia about Z axis	0.0014	$kg\,m^2$
weight band		
mass	1.719	kg
moment of inertia about X axis	0.0043	$kg\,m^2$
moment of inertia about Y axis	0.0043	$kg\,m^2$
moment of inertia about Z axis	0.0041	$kg\,m^2$
knee orthosis		
mass	0.924	kg
moment of inertia about X axis	0.026	$kg\,m^2$
moment of inertia about Y axis	0.021	$kg\,m^2$
moment of inertia about Z axis	0.0061	$kg\,m^2$

Table A.3: Masses and moments of inertia of the disturbances (continuation).

Disturbance	value	unity
right vario shoe		
mass	0.999	kg
moment of inertia about X axis	0.014	$kg\,m^2$
moment of inertia about Y axis	0.015	$kg\,m^2$
moment of inertia about Z axis	0.0055	$kg\,m^2$
left vario shoe		
mass	0.497	kg
moment of inertia about X axis	0.0013	$kg\,m^2$
moment of inertia about Y axis	0.0040	$kg\,m^2$
moment of inertia about Z axis	0.0027	$kg\,m^2$
ski boot		
mass	2.431	kg
moment of inertia about X axis	0.020	$kg\,m^2$
moment of inertia about Y axis	0.033	$kg\,m^2$
moment of inertia about Z axis	0.012	$kg\,m^2$

A.3 Anthropometric Parameters of the 3-D Inverse Dynamics Model

The masses, moments of inertia, lengths and positions of the center of mass of the segments of the subjects, corresponding to the model explained in section 3.2, are contained in the following tables, Tabs. A.4 and A.5. Refer to Fig. 3.8 for a schematic drawing of the model and an indication of the lengths considered. The majority of these anthropometric parameters is computed by means of the anthropometric tables proposed by de Leva [28], who adjusted the data measured by Zatsiorky et al. [94] in order to refer them to the joint centers, easily identifiable in mechanical models of the body, rather than to anatomical bony marks. Whenever possible the segment lengths are measured directly from the positions of the markers. These lengths are identified by a star (*) in Tabs. A.4 and A.5. The moments of inertia and position of the center of mass of the HAT, which contains the trunk, head and arms, are computed for the arms crossed over the chest. The position of the hip joint is estimated from the markers ASIS and PSIS using relations proposed by Bell et al. ([12] and [13]). When slightly different values for the right and left sides arise, the average is shown in the tables.

Table A.4: Masses, lengths, center of mass and moments of inertia of the body segments of subjects 1 and 2.

Segment	subj. 1	subj. 2	unity
HAT (trunk, head and arms)			
mass	35.85	36.64	kg
proximal CM (c_2)	0.269	0.268	m
moment of inertia about sagittal axis (X)	1.6061	1.6585	$kg\,m^2$
moment of inertia about frontal axis (Y)	1.1903	1.2064	$kg\,m^2$
moment of inertia about longitudinal axis (Z)	0.5175	0.5539	$kg\,m^2$
pelvis			
mass	8.15	8.33	kg
proximal CM (c_1)	0.092	0.091	m
pelvis CM to hip joints in Y (d_1)	0.080	0.087	m
pelvis CM to hip joints in Z (d_2)	0.058	0.058	m
moment of inertia about sagittal axis (X)	0.0694	0.0719	$kg\,m^2$
moment of inertia about frontal axis (Y)	0.0557	0.0577	$kg\,m^2$
moment of inertia about longitudinal axis (Z)	0.0632	0.0655	$kg\,m^2$

Table A.5: Masses, lengths, center of mass and moments of inertia of the body segments of subjects 1 and 2 (continuation).

Segment	subj. 1	subj. 2	unity
right and left thighs			
mass	10.34	10.56	kg
length (l_3 and l_6)*	0.475	0.4447	kg
proximal CM (c_3 and c_6)	0.195	0.183	m
moment of inertia about sagittal axis (X)	0.2678	0.2450	$kg\,m^2$
moment of inertia about frontal axis (Y)	0.2678	0.2450	$kg\,m^2$
moment of inertia about longitudinal axis (Z)	0.0549	0.0503	$kg\,m^2$
right and left shanks			
mass	3.16	3.23	kg
length (l_4 and l_7)*	0.429	0.405	kg
proximal CM (c_4 and c_7)	0.188	0.178	m
moment of inertia about sagittal axis (X)	0.0400	0.0370	$kg\,m^2$
moment of inertia about frontal axis (Y)	0.0382	0.0353	$kg\,m^2$
moment of inertia about longitudinal axis (Z)	0.0065	0.0061	$kg\,m^2$
right and left feet			
mass	1.00	1.02	kg
proximal CM in Z (c_5 and c_8)	0.043	0.0569	m
proximal CM in X (h_5 and h_8)	0.117	0.117	m
moment of inertia about sagittal axis (X)	0.0011	0.0011	$kg\,m^2$
moment of inertia about frontal axis (Y)	0.0047	0.0047	$kg\,m^2$
moment of inertia about longitudinal axis (Z)	0.0042	0.0043	$kg\,m^2$
total			
mass	73.0	74.6	kg
stature	1.792	1.785	m

A.4 Markers

Table A.6 shows the names and designations of the 28 markers attached to the body of the subjects on the positions approximately shown in Fig. A.2. The majority of the markers are attached to bony anatomical landmarks, what makes the experiments reproducible and facilitates the localization of the anatomical frames for the segments, see Cappozzo et al. [21]. Additional markers, for example the MRFr and MRFl, are attached to positions on the limb that reduced errors due to *skin artefacts* and that avoid the occurrence of ill-determined rotations in the reconstruction process, refer, for example, to Cappello et al. [20]. Whenever possible, the markers were kept at the same place for all the experiments with the same subject. This was not always possible because of the disturbances introduced. In these cases, some markers were replaced by another ones on the disturbances and on the skin on locations assumed to be meaningful. The pictures of Fig. 3.4 show the different positions of some of the markers for the different experiments. Refer to Fig. 3.3 for a picture of subject 2 with attached markers.

Table A.6: Names and designation of the markers attached to the body of the subjects on the positions shown in Fig. A.2 for the normal experiment. Note that the suffix 'r' refers to the markers attached to the right side of the body and the 'l' to the ones attached to the left side.

|	
VMr and VMl	Metatarsal lateralis right and left
FMr and FMl	Metatarsal medialis right and left
LMr and LMl	Malleolus lateralis right and left
MMr and MMl	Malleolus medialis right and left
CAr and CAl	Calcaneous posterior right and left
TTr and TTl	Tuberositas tibiae right and left
LEFr and LEFl	Epicondylus lateralis femoris right and left
MEFr and MEFl	Epicondylus medialis femoris right and left
MRFr and MRFl	Musculus rectus femoris right and left
GTr and GTl	Trochanter major right and left
ASISr and ASISl	Spina iliaca anterior superior right and left
PSISr and PSISl	Spina iliaca posterior superior right and left
ACr and ACl	Acromioclavicular right and left
C7	Vertebra Prominens
ST	Manubrium sterni
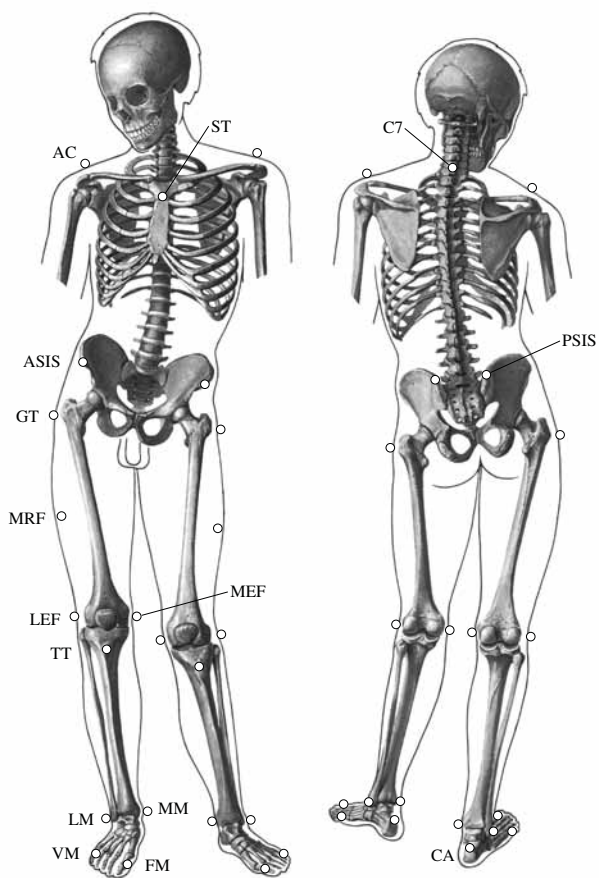
Figure A.2: Location of the markers listed in Tab. A.6 (modified from Wolf-Heidegger [127]).

A.5 Comparison of Reconstructed Kinematic to Data of Heidelberg

Figures A.3 and A.4 show comparisons of the kinematics reconstructed for subject 1 and subject 2, respectively, with kinematics obtained for 26 subjects in the gait analysis laboratory of the "Orthopädischen Universitätsklinik Heidelberg", Wolf and Rettig [126]. The curves show an overall good agreement. Some discrepancies can also be observed. One reason for the differences observed might be the use of different segment-fixed coordinate frames. The discrepancies observed for the longitudinal rotations of the segments of the lower limb are likely to be caused by the high sensitivity of these rotations to the displacements of the markers with respect to the underlying bones due to the *skin artefacts* explained in section 3.1.4. Another possible reason for the discrepancies observed might be the adoption of a slightly different gait pattern by the subjects as a consequence of the reduced walking velocity.

In order to compute the relative kinematics between segments in section 3.3 and to express the joint net moments presented in section 3.4 two distinct segment-fixed coordinate systems are employed – the anatomical frames and the reference frames. As evident from Figs. A.3 and A.4, the choice of the coordinate system can have a very significant influence on the values of the generalized coordinates that describe relative rotations. Also the projection of the moment vector on the three axis of the coordinate system may have significantly different values, although they describe the same relative rotation and the same moment vector at the joints, respectively.

The reference frames are defined as the frames, whose origins are the center of mass of the body segments and whose axes directions coincide with the ones of the global coordinate system for the subject standing in the reference posture. The reference posture corresponds to the standing posture of the subject on the force plate as shown in Fig. 3.3, i.e. standing with the anteroposterior axis aligned with the direction of progression (x-axis of the global coordinate system, see Fig. 3.2). This implies that the rotation matrices describing the relative rotations of the reference frames are identity matrices in the reference posture of the subject.

The anatomical frames are based on the location of anatomical landmarks, like bony saliences. Here, the anatomical frames are determined following guidelines in Cappozzo et al. [21], where standardized orientations of the axes are obtained by the positions of markers placed on specified bony landmarks. For details on the definition of the anatomical frames refer to Ackermann and Gros [2].
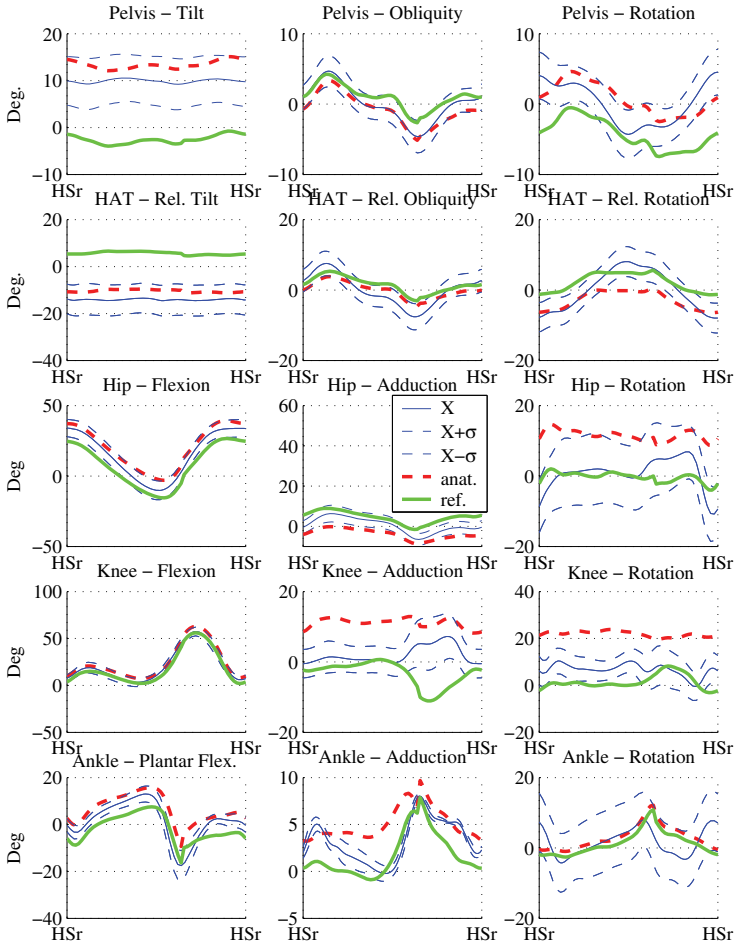
Figure A.3: Comparison between the kinematics for subject 1 with the reference data for 26 subjects obtained in the gait analysis laboratory of the "Orthopädischen Universitätsklinik Heidelberg" (kindly provided by Wolf and Rettig [126]). X is the average of the joint angles of the reference data and σ is the standard deviation. "ref." refers to the curves obtained by using reference frames for the body segments, and "anat." refers to the curves obtained by using anatomical frames, as explained in Ackermann and Gros [2].
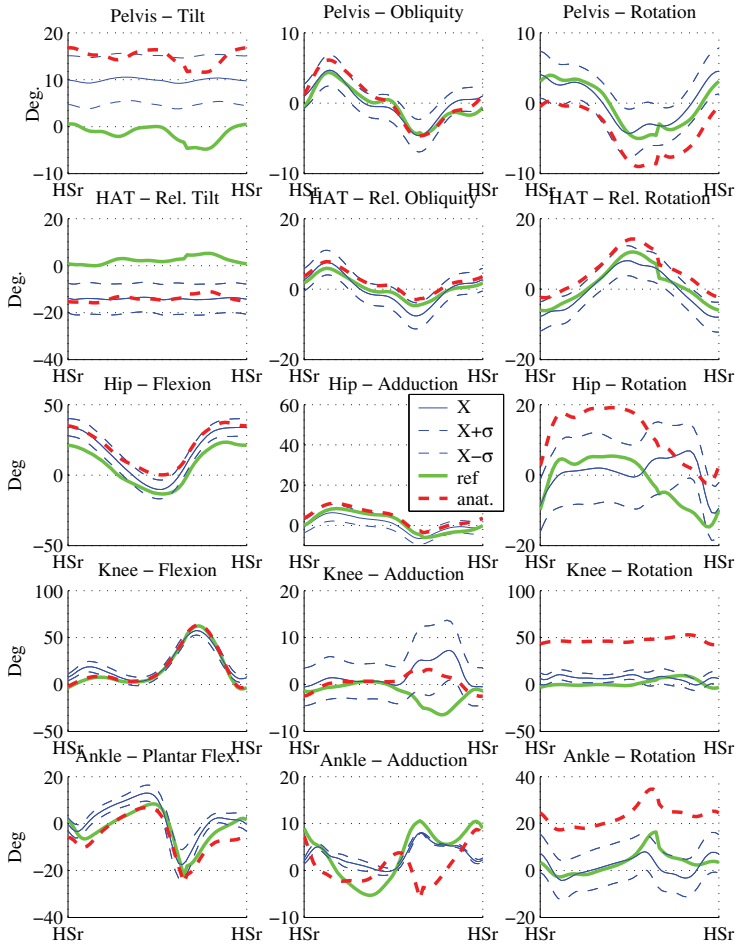
Figure A.4: Comparison between the kinematics for subject 2 with the reference data for 26 subjects obtained in the gait analysis laboratory of the "Orthopädischen Universitätsklinik Heidelberg" (kindly provided by Wolf and Rettig [126]). X is the average of the joint angles of the reference data and σ is the standard deviation. "ref." refers to the curves obtained by using reference frames for the body segments, and "anat." refers to the curves obtained by using anatomical frames, as explained in Ackermann and Gros [2].

A.6   Comparison of Computed Joint Moments to Data of Heidelberg

Figures A.5 and A.6 show a comparison of the joint moments for the lower limb obtained for subject 1 and subject 2, respectively, with data obtained in the gait analysis laboratory of the "Orthopädischen Universitätsklinik Heidelberg" kindly provided by Wolf and Rettig [126]. Note that the moments are normalized by the subject total body mass and the duration is normalized by the total duration of the cycle in order to facilitate the comparison among experiments.
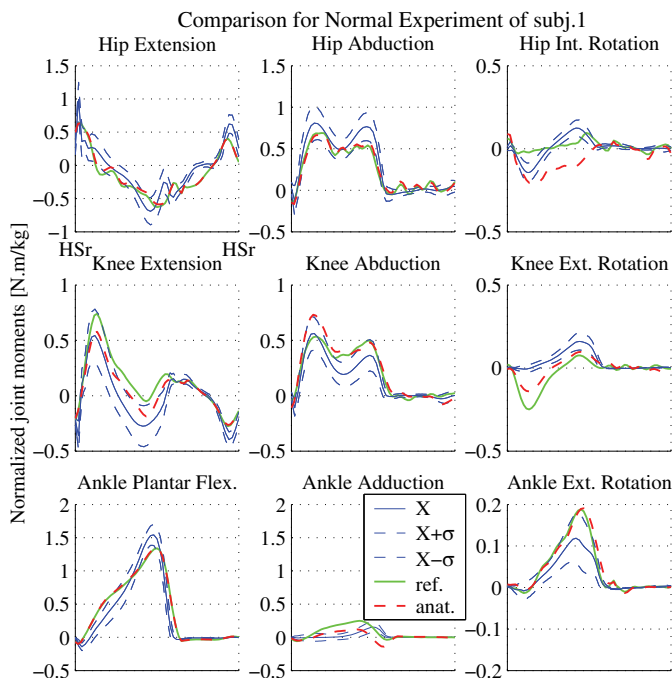

Figure A.5: Comparison between the joint moments of the right lower limb of subject 1 and reference joint moments for 26 subjects obtained in the gait analysis laboratory of the "Orthopädischen Universitätsklinik Heidelberg". X is the average of the joint moments of the reference data and σ is the standard deviation. "ref." refers to moments expressed in reference frames, and "anat." refers to moments expressed in anatomical frames.

The curves show an overall fairly good agreement. Exceptions are the curves for hip internal rotation, for knee external rotation and for ankle adduction. The discrepancies
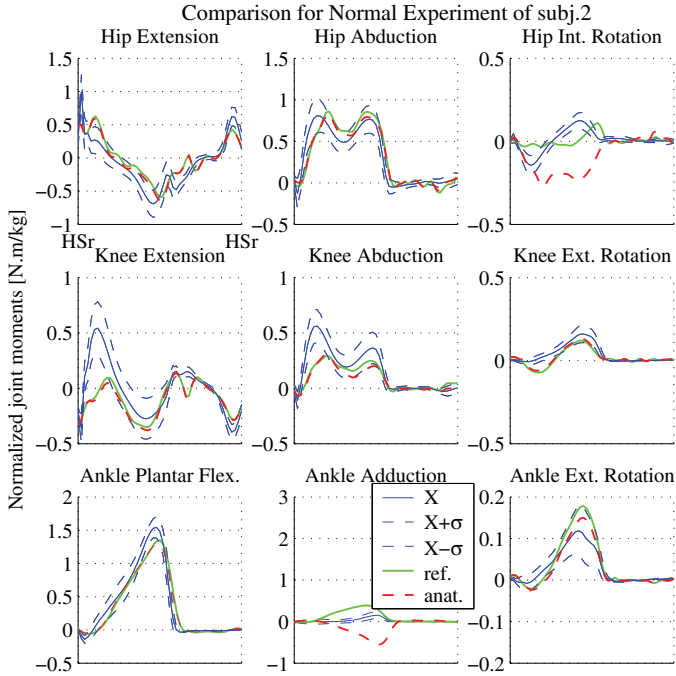
Figure A.6: Comparison between the joint moments of the right lower limb of subject 2 and reference joint moments for 26 subjects obtained in the gait analysis laboratory of the "Orthopädischen Universitätsklinik Heidelberg". *X* is the average of the joint moments of the reference data and σ is the standard deviation.

observed for the longitudinal rotations might occur due to the previously mentioned errors and noise in the kinematics caused mainly by *skin artefacts*, see chapter 3.3. The errors and the part of the noise that is not enough damped during the filtering process are amplified by numerical differentiation to compute the velocities and accelerations needed for the inverse dynamics. This can lead to significant errors in the moments computed.

The discrepancies observed for the ankle adduction can be justified by the adoption of distinct segment-fixed coordinate frames to express the moment vector acting at the ankle joint. Figures A.5 and A.6 show the differences that can be caused by the use of distinct segment-fixed coordinate systems to express the joint moments. For more details on the anatomical and reference frames adopted refer to Appendix A.5.

A.7 Optimal Prosthetic Ankle Moment vs. Angle Curves

In Tab. A.7 the coefficients of (5.58) for the ankle moment versus ankle angle curves for the three prosthetic feet, SACH foot, Seattle foot, and Flex-foot, obtained by fitting the curves reported in Klute et al. [58] are reported together with the damping coefficient adopted. Table A.8 shows the near-optimal coefficients obtained for the three walking velocities investigated and the four weighting factor combinations adopted in the cost function (5.29).

Table A.7: Coefficients of (5.58) for the ankle moment versus ankle angle curves for the three prosthetic feet, SACH foot, Seattle foot, and Flex-foot, obtained by fitting the curves reported in Klute et al. [58]. The damping coefficient d_{prosth} adopted for (5.59) in $(N.m.s/rad)$ is also presented.

Prosth. Foot	a_p	b_p	c_0	a_n	b_n	d_{prosth}
SACH	1534	−640.0	−174.2	914.8	6396	1.000
Seattle	−34020	2496	−354.3	−524.9	1402	1.000
Flex	−17090	1889	−281.5	15.64	274.2	1.000

Table A.8: Near-optimal coefficients of (5.58) and (5.59) obtained for the three walking velocities investigated and the four weighting factor combinations investigated.

Opt. Ankle	a_p	b_p	c_0	a_n	b_n	d_{prosth}
$v_w = 1.00\ m/s$						
a)	-17360	1375	-100.0	-5231	1630	0.372
b)	-36150	1099	-190.4	-2532	1254	0.035
c)	-9340	695	-68.8	-726	2064	0.000
d)	-13850	1310	-103.2	-1092	1183	0.000
$v_w = 1.33\ m/s$						
a)	-25370	592	-156.2	-3238	827	0.2586
b)	-16870	1015	-171.0	-5189	-280	0.051
c)	-10560	317	-95.2	-1943	928	0.004
d)	-19750	1395	-101.9	1401	1733	0.024
$v_w = 1.68\ m/s$						
a)	-42270	1695	-222.1	-4856	833	0.000
b)	-14410	306	-120.1	-1787	805	0.000
c)	5360	-1181	-119.0	-2972	1000	0.000
d)	37030	-9176	-185.1	-5022	524	0.346

Bibliography

[1] Abdulhadi, H. M., D. C. Kerrigan, and P. J. LaRaia: 1996, 'Contralateral shoe-lift: effect on oxygen cost of walking with an immobilized knee'. *Archives of Physical Medicine and Rehabilitation* **77**(7), 670–672.

[2] Ackermann, M. and H. Gros: 2005, 'Measurements of Human Gaits'. Zwischenbericht ZB-144, Institute B of Mechanics - University of Stuttgart, Stuttgart.

[3] Ackermann, M. and W. Schiehlen: 2006a, 'Dynamic Analysis of Human Gait Disorder and Metabolical Cost Estimation'. *Archive of Applied Mechanics* **75**(10-12), 569–594.

[4] Ackermann, M. and W. Schiehlen: 2006b, 'Prosthesis design by robotic approaches, Part 2: Optimization Approach'. In: T. Zielinska and C. Zielinski (eds.): *ROMANSY 16 - Robot Design, Dynamics, and Control*. Wien, pp. 329–336.

[5] Ackermann, M. and W. Schiehlen: 2007, 'Physiological methods to solve the force-sharing problem in biomechanics'. In: *Proceedings of ECCOMAS*. to appear.

[6] Alt, W., H. Lohrer, and A. Gollhofer: 1999, 'Functional Properties of Adhesive Ankle Taping: Neuromuscular and Mechanical Effects Before and After Exercise'. *Foot & Ankle International* **20**(4), 238–245.

[7] Anderson, F. C. and M. G. Pandy: 1999, 'A dynamic optimization solution for vertical jumping'. *Computer Methods in Biomechanics and Biomedical Engineering* **2**, 201–231.

[8] Anderson, F. C. and M. G. Pandy: 2001, 'Dynamic optimization of human walking'. *Journal of Biomechanical Engineering* **123**(5), 381–390.

[9] Anderson, F. C. and M. G. Pandy: 2003, 'Indivual muscle contributions to support in normal walking'. *Gait & Posture* **17**(2), 159–169.

[10] Annegarn, J.: 2006, 'Scaling in human simulation models: developing an isometric strength scaling model from easy accedssible data'. Master's thesis, Maastricht University - Faculty of Health Science.

[11] Audu, M. L. and D. T. Davy: 1985, 'The influence of muscle model complexity in musculoskeletal motion modeling'. *Journal of Biomechanical Engineering* **107**, 147–157.

[12] Bell, A. L., R. A. Brand, and D. R. Pedersen: 1989, 'Prediction of hip joint centre location from external landmarks'. *Human Movement Science* **8**, 3–16.

[13] Bell, A. L., D. R. Pedersen, and R. Brand: 1990, 'A comparison of the accuracy of several hip center location prediction methods'. *Journal of Biomechanics* **23**(6), 617–621.

[14] Berbyuk, V.: 1995, 'Multibody systems modeling and optimization problems of lower limb prostheses'. In: D. Bestle and W. Schiehlen (eds.): *Proceedings of the IUTAM Symposium on Optimization of Mechanical Systems*. Stuttgart/Germany, pp. 25–32.

[15] Bessonnet, G., P. Seguin, and P. Sardain: 2005, 'A Parametric Optimization Approach to Walking Pattern Synthesis'. *The International Journal of Robotics Research* **24**(7), 523–536.

[16] Bestle, D.: 1994, *Analyse und Optimierung von Mehrkörpersystemen*. Berlin: Springer-Verlag.

[17] Bhargava, L. J., M. G. Pandy, and F. C. Anderson: 2004, 'A phenomenological model for estimating metabolic energy consumption in muscle contraction'. *Journal of Biomechanics* **37**(1), 81–88.

[18] Blajer, W. and W. Schiehlen: 1992, 'Walking without impacts as a motion/force control problem'. *Journal of Dynamic Systems, Measurement, and Control* **114**, 660–665.

[19] Blumentritt, S., H. W. Scherer, J. W. Michael, and T. Schmalz: 1998, 'Transfemoral amputees walking on a rotary hydraulic prosthetic knee mechanism: a preliminary report'. *Journal of Prosthetics and Orthotics* **10**(3), 61–70.

[20] Cappello, A., A. Cappozzo, U. d. Croce, and A. Leardini: 1997, 'Bone Position and Orientation Reconstraction Using External Markers'. In: P. Allard, A. Cappozzo, A. Lundberg, and C. L. Vaughan (eds.): *Three-dimensional Analysis of Human Locomotion*. John Wiley & Sons, pp. 147–171.

[21] Cappozzo, A., U. d. Croce, and L. Lucchetti: 1997, 'Gait Data: Terminology and Definitions'. In: P. Allard, A. Cappozzo, A. Lundberg, and C. L. Vaughan (eds.): *Three-dimensional Analysis of Human Locomotion*. John Wiley & Sons, pp. 129–146.

[22] Chandler, R. F., C. E. Clauser, J. T. McConville, R. M. Reynolds, and J. W. Young: 1975, 'Investigation of inertial parameters of the human body'. Technical report.

[23] Chapra, S. C. and R. P. Canale: 1985, *Numerical Methods for Engineers*. New York: McGraw-Hill.

[24] Cole, G. K., A. J. van den Bogert, W. Herzog, and K. G. M. Gerritsen: 1996, 'Modeling of force production in skeletal muscle undergoing stretch'. *Journal of Biomechanics* **29**(8), 1091–1104.

[25] Crowninshield, R. D. and R. A. Brand: 1981, 'Physiologically based criterion of muscle force prediction in locomotionl'. *Journal of Biomechanics* **14**(11), 793–801.

[26] da Silva, M. P. T. and J. A. C. Ambrosio: 2004, 'Human motion analysis using multibody dynamics and optimization tools'. Ph.D thesis, Instituto de Engenharia Mecânica, Lisboa, Portugal.

[27] Davy, D. T. and M. L. Audu: 1987, 'A dynamic optimization technique for the muscle forces in the swing phase of the gait'. *Journal of Biomechanics* **20**(2), 187–201.

[28] de Leva, P.: 1996, 'Adjustments to Zatsiorsky-Seluyanov's segment inertia parameters'. *Journal of Biomechanics* **29**(9), 1223–1230.

[29] Delp, S. L.: 1990, 'Surgery simulation: a computer graphics system to analyze and design musculoskeletal reconstructions of the lower limb'. Ph.D thesis, Department of Mechanical Engineering, Stanford University.

[30] Delp, S. L. and J. P. Loan: 2000, 'A computational framework for simulation and analyzing human and animal movement'. *IEEE Computing in Science and Engineering* **2**(2), 46–55.

[31] Dempster, W. T.: 1955, 'Space requirements of the seated operator: geometrical, kinematic, and mechanical aspects of the body with special reference to the limbs'. Technical Report 55-159, University of Michigan.

[32] Durkin, J. L. and J. J. Dowling: 2003, 'Analysis of body segment parameter differences between four human populations and the estimation errors of four popular mathematical models'. *Journal of Biomechanical Engineering* **124**, 515–522.

[33] Garcia, M., A. Chatterjee, A. Ruina, and M. Coleman: 1998, 'The Simplest Walking Model: Stability, Complexity, and Scaling'. *Journal of Biomechanical Engineering* **120**, 281–288.

[34] Gerritsen, K. G. M., A. J. van den Bogert, M. Hulliger, and R. F. Zernicke: 1998, 'Intrinsic muscle properties facilitate locomotor control – a computer simulation study'. *Motor Control* **2**, 206–220.

[35] Gruber, S.: 2004, 'Zur Dynamik und Regelung zweibeiniger Gehmaschinen'. PhD thesis, Institute B of Mechanics - University of Stuttgart, Düsseldorf. VDI Verlag.

[36] Gruber, S. and O. Ludwig: 2002, 'Analyse der Armbewegung beim menschlichen Gehen'. Technical Report ZB-130, Institut B für Mechanik.

[37] Gruber, S. and W. Schiehlen: 2002, 'Biped walking machines: a challenge to dynamics and mechatronics'. In: H. A. Mang, F. G. Rammerstorfer, and J. Eberhardsteiner (eds.): *WCCM V, Fifth World Congress on Computational Mechanics*. Vienna, Austria. paper 81246.

[38] Hanada, E. and D. C. Kerrigan: 2001, 'Energy consumption during level walking with arm and knee immobilized'. *Archives of Physical Medicine and Rehabilitation* **82**(9), 1251–1254.

[39] Hansen, A. H., D. S. Childress, S. C. Miff, S. A. Gard, and K. P. Mesplay: 2004, 'The human ankle during walking: implications for the design of biomimetic ankle prostheses'. *Journal of Biomechanics* **37**, 1467–1474.

[40] Hanson, J. and H. E. Huxley: 1953, 'Structural basis of the cross-striations in muscle'. *Nature* **172**, 530–532.

[41] Hase, K. and H. Yamazaki: 1997, 'Development of three-dimensional whole-body musculoskeletal model for various motion analyses'. *JSME International Journal - Series C* **40**(1), 25–32.

[42] Hatze, H.: 1971, 'Was ist Biomechanik'. *Leibesübungen, Leibeserziehung* **25**, 33–34.

[43] Hatze, H.: 1976, 'The complete optimization of a human motion'. *Mathematical Biosciences* **28**, 99–135.

[44] Hatze, H.: 2002, 'The fundamental problem of myoskeletal inverse dynamics and its implications'. *Journal of Biomechanics* **35**, 109–115.

[45] Hatze, H. and J. D. Buys: 1977, 'Energy-Optimal controls in the mammalian neuromuscular system'. *Biological Cybernetics* **27**, 9–20.

[46] He, J., W. S. Levine, and G. E. Loeb: 1991, 'Feedback gains for correcting small perturbations to standing posture'. *IEEE Transactions on Autonomic Control* **36**, 322–332.

[47] Herzog, W.: 1999, 'Muscle'. In: B. M. Nigg and W. Herzog (eds.): *Biomechanics of the musculo-skeletal system*. New York: John Wiley & Sons, 2nd edition, Chapt. 2.7, pp. 148–188.

[48] Herzog, W.: 2000, 'Considerations on the mechanisms of muscular contraction'. In: W. Herzog (ed.): *Skeletal Muscle Mechanics*. New York: John Wiley & Sons, Chapt. 1.

[49] Hill, A. V.: 1938, 'The heat of shortening and the dynamic constants of muscle'. *Proceedings of the Royal Society of London, Series B, Biological Sciences* **126**(843), 136–195.

[50] Ho Hoang, K.-L.: 2005, 'Anwendung der inversen Dynamic an Versuchsdaten aus einem Gehversuchslabor'. Studienarbeit STUD - 220, Institute B of Mechanics - University of Stuttgart.

[51] Hsu, M.-J., D. H. Nielsen, J. Yack, D. G. Shurr, and S.-J. Lin: 2000, 'Physiological comparisons of physically active persons with transtibial amputation using static and dynamic prostheses versus persons with nonpathological gait during multiple-speed walking'. *Journal of Prosthetics & Orthotics* **12**(2), 60–67.

[52] Huxley, A. F.: 1957, 'Muscle structure and theories of contraction'. *Progress in Biophysics and Biophysical Chemistry* **7**, 255–318.

[53] Huxley, H. E. and J. Hanson: 1954, 'Changes in the cross-striations of muscle during contraction and stretch and their structural interpretation'. *Nature* **173**, 973–976.

[54] Inman, V. T., H. J. Ralston, and F. Todd: 1994, 'Human Locomotion'. In: J. Rose and J. G. Gamble (eds.): *Human Walking*. Baltimore: Williams & Wilkins, 2nd edition, Chapt. 1, pp. 1–22.

[55] Jaegers, M. H. J., L. D. W. Vos, P. Rispens, and A. L. Hof: 1993, 'The relationship between comfortable and most metabolically efficient walking speed in persons with unilateral above-knee amputation'. *Archives of Physical Medicine and Rehabilitation* **74**(5), 521–525.

[56] Jinha, A., R. Ait-Haddou, and W. Herzog: 2006, 'Predictions of co-contraction depend critically on degrees-of-freedom in the musculoskeletal model'. *Journal of Biomechanics* **39**, 1145–1152.

[57] Johansson, J. L., D. M. Sherrill, P. O. Riley, P. Bonato, and H. Herr: 2005, 'A Clinical Comparison of Variable-Damping and Mechanically Passive Prosthetic Knee Devices'. *American Journal of Physical Medicine & Rehabilitation* **84**(8), 563–575.

[58] Klute, G. K., C. F. Kallfelz, and J. M. Czerniecki: 2001, 'Mechanical properties of prosthetic limbs: adapting to the patient'. *Journal of Rehabilitation Research and Development* **38**(3).

[59] Komi, P. V., J. T. Viitasalo, R. Rauramaa, and V. Vihko: 1978, 'Effect of isometric strength training on mechanical, electrical, and metabolic aspects of muscle function'. *European Journal of Applied Physiology* **40**(1), 45–55.

[60] Kreuzer, E. and G. Leister: 1991, 'Programmsystem NEWEUL'90'. Anleitung AN-24, Institute B of Mechanics, University of Stuttgart.

[61] Kuo, A. D.: 1998, 'A least-squares estimation approach to improving the precision of inverse dynamics computations'. *Journal of Biomechanical Engineering* **120**, 148–159.

[62] Kuo, A. D.: 2001, 'A simple model of bipedal walking predicts the preferred speed-step length relationship'. *Journal of Biomechanical Engineering* **123**, 264–269.

[63] Lehmann, J., R. Price, S. Boswell-Bessete, A. Dralle, K. Questad, and B. deLateur: 1993, 'Comprehensive analysis of energy storing prosthetic feet: Flex-Foot and Seattle Foot versus standard SACH Foot.'. *Archives of Physical Medicine and Rehabilitation* **74**, 1225–31.

[64] Lewis, F. L., C. T. Abdallah, and D. M. Dawson: 1993, *Control of Robot Manipulators*. Macmillan Publishing Company.

[65] Lu, T. W. and J. J. O'Connor: 1999, 'Bone position estimation from skin marker coordinates using global optimisation with joint constraints'. *Journal of Biomechanics* **32**(2), 129–134.

[66] Lutzenberger, C.: 2001, 'Dynamik des menschlichen Ganges'. PhD thesis, Technical University of Munich.

[67] Macfarlane, D. J.: 2001, 'Automated metabolic gas analysis systems'. *Sports Medicine* **31**(12), 841–861.

[68] MacFarlane, P. A., D. H. Nielson, D. G. Shurr, K. G. Meier, R. Clark, J. Kerns, M. Moreno, and B. Ryan: 1997, 'Transfemoral amputee physiological requirements: comparisons between SACH Foot and Flex-Foot walking'. *Journal of Prosthetics & Orthotics* **9**(4), 138–143.

[69] Mansour, J. M. and M. L. Audu: 1986, 'The passive elastic moment at the knee and its influence on human gait'. *Jounal of Biomechanics* **19**(5), 369–373.

[70] Martin, P., G. D. Heise, and D. W. Morgan: 1993, 'Interrelationships between mechanical power, energy transfers, and walking and running economy'. *Medicine & Science in Sports & Exercise* **25**, 508–515.

[71] McGeer, T.: 1990, 'Passive Dynamic Walking'. *The International Journal of Robotics Research* **9**(2), 504–524.

[72] Menegaldo, L. L., A. T. Fleury, and H. I. Weber: 2003, 'Biomechanical modeling and optimal control of human posture'. *Journal of Biomechanics* **36**(11), 1701–1712.

[73] Menegaldo, L. L., A. T. Fleury, and H. I. Weber: 2004, 'Moment arms and musculotendon lengths estimation for a three-dimensional lower-limb model'. *Journal of Biomechanics* **37**(9), 1447–1453.

[74] Menegaldo, L. L., A. T. Fleury, and H. I. Weber: 2006, 'A 'cheap' optimal control approach to estimate muscle forces in musculoskeletal systems'. *Journal of Biomechanics* **39**, 1787–1795.

[75] Michael, J. W.: 1999, 'Modern prosthetic knee mechanisms'. *Clinical Orthopedics and Related Research* **361**, 39–47.

[76] Minetti, A. E. and R. M. Alexander: 1997, 'A theory of metabolic cost for bipedal gaits'. *Journal of Theoretical Biology* **186**, 467–476.

[77] Mochon, S. and T. A. McMahon: 1980, 'Ballistic Walking'. *Journal of Biomechanics* **13**, 49–57.

[78] Nagano, A. and K. G. M. Gerritsen: 2001, 'Effects of neuromuscular stregth training on vertical jumping performance - a computer simulation study'. *Journal of Applied Biomechanics* **17**(2), 113–128.

[79] Nagurka, M. L. and V. Yen: 1990, 'Fourier-Based Optimal Control of Nonlinear Dynamic Systems'. *Journal of Dynamic Systems, Measurement, and Control* **112**, 17–26.

[80] Neptune, R. R. and M. L. Hull: 1998, 'Evaluation of performance criteria for simulation of submaximal steady-state cycling using a forward dynamic model'. *Journal of Biomechanical Engineering* **120**, 334–341.

[81] Neptune, R. R., S. A. Kautz, and F. E. Zajac: 2001, 'Contributions of the individual ankle plantar flexors to support, forward progression and swing initiation during walking'. *Journal of Biomechanics* **34**(11), 1387–1398.

[82] Neptune, R. R. and A. J. van den Bogert: 1998, 'Standard mechanical energy analyses do not correlate with muscle work in cycling'. *Journal of Biomechanics* **31**(3), 239–245.

[83] Neptune, R. R., I. C. Wright, and A. J. van den Bogert: 2000, 'A method for numerical simulation of single limb ground contact events: application to hee-toe running'. *Computer Methods in Biomechanics and Biomedical Engineering* **3**, 321–334.

[84] Nigg, B. M.: 1999, 'Introduction'. In: B. M. Nigg and W. Herzog (eds.): *Biomechanics of the Musculo-Skeletal System*. New York: Wiley, 2nd edition, Chapt. 1, pp. 1–48.

[85] Pandy, M. G., F. Anderson, and D. G. Hull: 1992, 'A parameter optimization approach for the optimal control of large-scale musculoskeletal systems'. *Journal of Biomechanical Engineering* **114**, 450–460.

[86] Peasgood, M., J. McPhee, and E. Kubica: 2005, 'Stabilization and energy optimization of dynamic walking gait simulation'. In: *Proceedings of IDETC/CIE2005*, Vol. 1.

[87] Radcliffe, C. W.: 1994, 'Prosthesis'. In: J. Rose and J. G. Gamble (eds.): *Human Walking*. Baltimore: Williams & Wilkins, 2nd edition, Chapt. 8, pp. 165–199.

[88] Ralston, H. J.: 1976, 'Energetics of human walking'. In: R. M. Herman et al. (ed.): *Neural Control of Locomotion*. New York: Plenum Press, pp. 77–98.

[89] Reinbolt, J. A., J. F. Schutte, B. J. Fregly, B. I. Koh, R. T. Haftka, A. D. George, , and K. H. Mitchell: 2005, 'Determination of patient-specific multi-joint kinematic models through two-level optimization'. *Journal of Biomechanics* **38**(3), 621–626.

[90] Riener, R. and T. Edrich: 1999, 'Identification of passive elastic joint moments in the lower extremities'. *Journal of Biomechanics* **32**(5), 539–544.

[91] Rose, J., H. J. Ralston, and J. Gamble: 1994, *Human Walking*, Chapt. 3, pp. 47–72. Willians & Wilkins, 2nd edition.

[92] Royer, T. D. and P. E. Martin: 2005, 'Manipulations of Leg Mass and Moment of Inertia: Effects on Energy Cost os Walking'. *Medicine & Science in Sports & Exercise* **37**(4), 649–656.

[93] Saidouni, T. and G. Bessonnet: 2003, 'Generating globally optimised sagittal gait cycles of a biped robot'. *Robotica* **21**, 199–210.

[94] Saziorski, W. M., A. S. Aruin, and W. N. Selujanow: 1984, *Biomechanik des menschlichen Bewegungsapparates*. Berlin: Sport Verlag.

[95] Schiehlen, W.: 1997, 'Multibody System Dynamics: Roots and Perspectives'. *Multibody System Dynamics* **1**, 149–188.

[96] Schiehlen, W.: 2005, 'Recent Developments in Multibody Dynamics'. *Journal of Mechanical Science and Technology* **19**(1), 227–236.

[97] Schiehlen, W. and P. Eberhard: 2004, *Technische Dynamik*. Stuttgart: Teubner, 2. edition.

[98] Schirm, W.: 1993, *Symbolisch-numerische Behandlung von kinematischen Schleifen in Mehrkörpersystemen*, No. 106 in Reihe 12. Düsseldorf: VDI-Verlag.

[99] Schmalz, T., S. Blumentritt, and R. Jarasch: 2002, 'Energy expenditure and biomechanical characteristics of lower limb amputee gait: The influence of prosthetic alignment and different prosthetic components'. *Gait & Posture* **16**(3), 255–263.

[100] Shan, G. and C. Bohn: 2003, 'Anthropometrical data and coefficients of regression related to gender and race'. *Applied Ergonomics* **34**(4), 327–337.

[101] Siegler, S. and W. Liu: 1997, 'Inverse dynamics in human locomotion'. In: P. Allard, A. Cappozzo, A. Lundberg, and C. L. Vaughan (eds.): *Three-dimensional Analysis of Human Locomotion*. New York: John Wiley & Sons, pp. 191–209.

[102] Söderkvist, I. and P. A. Wedin: 1993, 'Determining the movements of the skeleton using well-configured markers'. *Journal of Biomechanics* **26**(12), 1473–1477.

[103] Spägele, T.: 1998, 'Modellierung, Simulation und Optimierung menschlicher Bewegung'. Ph.d. thesis, Institute A of Mechanics, University of Stuttgart.

[104] Stadler, W. (ed.): 1988, *Multicriteria Optimization in Engineering and in the Sciences*. New York: Plenum Press.

[105] Stein, R. B., M. K. Lebiedowska, D. B. Popovic, A. Scheiner, and H. J. Chizeck: 1996, 'Estimating mechanical parameters of leg segments in individuals with and without physical disabilities'. *IEEE Transactions on Rehabilitation Engineering* **4**(3), 201–211.

[106] Strang, G.: 1980, *Linear algebra and its applications*. New York: Academic Press, 2nd edition.

[107] Strobach, D., A. Kecskemethy, G. Steinwender, and B. Zwick: 2005, 'A simplified approach for rough identification of muscle activation profiles via optimization and smooth profile patches'. In: *Proceedings of MULTIBODY DYNAMICS 2005, ECCOMAS Thematic Conference*.

[108] Stryk, O. v.: 1998, 'Optimal Control of Multibody Systems in Minimal Coordinates'. *Zeitschrift für Angewandte Mathematik und Mechanik* (3), 1117–1120.

[109] Sutherland, D. H., K. R. Kaufman, and J. R. Moitoza: 1994, *Human Walking*, Chapt. 2, pp. 23–44. Baltimore: Williams & Wilkins, 2nd edition.

[110] Sutherland, J. L., D. H. Sutherland, K. R. Kaufman, and M. Teel: 1997, 'Case Study Forum: Gait Comparison of Two Prosthetic Knee Units'. *Journal of Prosthetics & Orthotics* **9**(4), 168–173.

[111] Thelen, D. and F. C. Anderson: 2006, 'Using computed muscle control to generate forward dynamic simulations of human walking from experimental data'. *Journal of Biomechanics* **39**, 1107–1115.

[112] Thelen, D. G., F. C. Anderson, and S. L. Delp: 2003, 'Generating dynamic simulations of movement using computed muscle control'. *Journal of Biomechanics* **36**, 321–328.

[113] Tsai, C. S. and J. M. Mansour: 1986, 'Swing phase simulation and design of above knee prostheses'. *Journal of Biomechanical Engineering* **108**, 65–72.

[114] Tsirakos, D., V. Baltzopoulos, and R. Bartlett: 1997, 'Inverse optimization: functional and physiological considerations related to the force-sharing problem'. *Critical Reviews in Biomedical Engineering* **25**(4-5), 371–407.

[115] Umberger, B. R., K. G. M. Gerritsen, and P. E. Martin: 2003, 'A model of human muscle energy expenditure'. *Computer Methods in Biomechanics & Biomedical Engineering* **6**(2), 99–111.

[116] van den Bogert, A. J. and B. M. Nigg: 1999, 'Simulation'. In: B. M. Nigg and W. Herzog (eds.): *Biomechanics of the musculo-skeletal system*. New York: John Wiley & Sons, 2nd edition, Chapt. 4.9, pp. 594–616.

[117] van Soest, A. J. and M. F. Bobbert: 1993, 'The contributions of muscle properties in the control of explosive movements'. *Biological Cybernetics* **69**(3), 195–204.

[118] Vaughan, C. L., J. G. Andrews, and J. G. Hay: 1982, 'Selection of body segment parameters by optimization methods'. *Journal of Biomechanical Engineering* **104**, 38–44.

[119] Volle, A.: 1998, 'Ein biomechanisches Modell des menschlichen Körpers'. Zwischenbericht ZB-100, Institute B of Mechanics, University of Stuttgart.

[120] Wasserman, K., J. E. Hansen, D. Y. Sue, R. Casaburi, and B. J. Whipp: 1999, *Principles of exercise testing and interpretation*. Lippincott Willians & Wilkins, 3rd edition.

[121] Waters, R. L. and S. Mulroy: 1999, 'The energy expenditure of normal and pathologic gait'. *Gait and Posture* **9**(3), 207–231.

[122] Winter, D. A.: 1991, *The biomechanics and motor control of human gait: normal, elderly and pathological*. Waterloo: University of Waterloo Press, second edition edition.

[123] Winter, D. A.: 2005, *Biomechanics and Motor Control of Human Movement*. Hoboken, New Jersey: John Wiley & Sons, third edition edition.

[124] Winters, J. M.: 1990, 'Hill-based muscle models: a system engineering perpective'. In: J. M. Winters and S. L.-Y. Woo (eds.): *Multiple Muscle Systems*. Springer-Verlag, Chapt. 5, pp. 69–93.

[125] Witkin, A. and M. Kass: 1988, 'Spacetime constraints'. In: *Computer Graphics (Proc. Siggraph 1988)*, Vol. 22. pp. 159–168.

[126] Wolf, S. and O. Rettig, 'Normal gait data for 26 subjects measured in the gait analysis laboratory of the "Orthopädischen Universitätsklinik Heidelberg"'. personal communication.

[127] Wolf-Heidegger, G.: 1989, *Atlas of Human Anatomy*. Basel, Switzerland: Karger, 4th edition.

[128] Yamaguchi, G. T.: 1990, 'Performing whole-body simulations of gait with 3-D, dynamic musculoskeletal models'. In: J. M. Winters and S. L.-Y. Woo (eds.): *Multiple Muscle Systems*. New York: Springer-Verlag, Chapt. 43, pp. 663–679.

[129] Yamaguchi, G. T., D. W. Moran, and J. Si: 1995, 'A computationally efficient method for solving the redundant problem in biomechanics'. *Journal of Biomechanics* **28**, 999–1005.

[130] Yoon, Y. S. and J. M. Mansour: 1982, 'The passive elastic moment at the hip'. *Journal of Biomechanics* **15**(12), 905–910.

[131] Zahalak, G. I.: 1990, 'Modeling muscle mechanics (and energetics)'. In: J. M. Winters and S. L.-Y. Woo (eds.): *Multiple Muscle Systems*. Springer-Verlag, Chapt. 1, pp. 1–23.

[132] Zajac, F. E.: 1989, 'Muscle and Tendon: properties, models, scaling, and application to biomechanics and motor control'. *CRC Critical Reviews in Biomedical Engineering* **19**(4), 359–411.

[133] Zajac, F. E., R. R. Neptune, and S. A. Kautz: 2003, 'Biomechanics and muscle coordination of human walking Part II: Lessons from dynamical simulations and clinical implications'. *Gait & Posture* **17**(1), 1–17.

[134] Zarrugh, M. Y. and C. W. Radcliffe: 1976, 'Simulation of swing phase dynamics in above-knee prostheses'. *Journal of Biomechanics* **9**, 283–292. experimental data for the hip movement of amputees in Fourier Series.

[135] Zatsiorsky, V. M.: 1998, *Kinematics of Human Motion*. Human Kinetics.

[136] Zatsiorsky, V. M.: 2002, *Kinetics of Human Motion*. Human Kinetics.

[137] Zlatnik, D.: 1998, 'Intelligently controlled above knee prosthesis'. Ph.D. thesis nr. 12814, Swiss Federal Institute of Technology, Zürich.

[138] Zmitrewicz, R. J., R. R. Neptune, and K. Sasaki: 2006a, 'Mechanical energetic contributions from individual muscles and elastic prosthetic feet during symmetric unilateral transtibial amputee walking: a theoretical study'. *Journal of Biomechanics.* in press (10.1016/j.jbiomech.2006.07.009).

[139] Zmitrewicz, R. J., R. R. Neptune, J. G. Walden, W. E. Rogers, and G. W. Bosker: 2006b, 'The effect of foot and ankle prosthetic components on braking and propulsive impulses during transtibial amputee gait'. *Archive of Physical Medicine and Rehabilitation* **87**, 1334–1339.